NATIONAL INSTITUTE FOR FUSION SCIENCE

Proceeding of A3 Foresight Program Seminar on Critical Physics Issues Specific to Steady State Sustainment of High-Performance Plasmas 1-4 December, 2015, Gotemba, Japan

Edited by Shigeru MORITA, Liqun HU and Yeong-Kook OH

(Received - Jun. 30. 2016)

NIFS-PROC-101

Sep. 09. 2016

Proceeding of A3 Foresight Program Seminar on Critical Physics Issues Specific to Steady State Sustainment of High-Performance Plasmas

1-4 December, 2015, Gotemba, Japan

Edited by

Shigeru MORITA, Liqun HU and Yeong-Kook OH

Abstract

The A3 Foresight Program titled by "Critical Physics Issues Specific to Steady State Sustainment of High-Performance Plasmas", based on the scientific collaboration among China, Japan and Korea in the field of plasma physics, has been started from August 2012 under the auspice of the Japan Society for the Promotion of Science (JSPS, Japan), the National Research Foundation of Korea (NRF, Korea) and the National Natural Science Foundation of China (NSFC, China). The main purpose of this project is to enhance joint experiments on three Asian advanced fully superconducting fusion devices (EAST in China, LHD in Japan and KSTAR in Korea) and other magnetic confinement devices to solve several key physics issues on steady state sustainment of high-performance plasmas. The eighth meeting of the A3 program was held in Gotemba, Japan, 1-4 December 2015, as the seventh A3 seminar on the collaborative research, which was hosted by National Institute for Fusion Science, to check and review on-going joint research activities including scientific results during past three years and to discuss the future plan. New proposals based on the A3 collaborative research and oral presentations by young scientists were also encouraged. The topics in the seminar include steady state sustainment of magnetic configurations, edge and divertor plasma control and confinement of alpha particles.

Key words: superconducting fusion device, magnetic confinement, toroidal plasmas, high-performance plasmas, steady state sustainment, edge plasma, divertor plasma, edge stability, high-energy particle, alpha particle and fusion plasma simulation.

Organization Committee

Shigeru MORITA (National Institute for Fusion Science, Japan)
Liqun HU (Institute of Plasma Physics, Chinese Academy of Sciences, China)
Yeong-Kook OH (National Fusion Research Institute, Korea)

Program Committee

Shigeru MORITA (National Institute for Fusion Science, Japan)
Liqun HU (Institute of Plasma Physics, Chinese Academy of Sciences, China)
Yeong-Kook OH (National Fusion Research Institute, Korea)
Satoru SAKAKIBARA (National Institute for Fusion Science, Japan)
Kato DAIJI (National Institute for Fusion Science, Japan)
Naoko ASHIKAWA (National Institute for Fusion Science, Japan)
Satoshi OHDACHI (National Institute for Fusion Science, Japan)
Mitsutaka ISOBE (National Institute for Fusion Science, Japan)
Yasushi TODO (National Institute for Fusion Science, Japan)

Conference Secretariats

Makoto ASAI (National Institute for Fusion Science, Japan)
Hideo HOSOKAWA (National Institute for Fusion Science, Japan)
Shaohua DONG (Institute of Plasma Physics, Chinese Academy of Sciences, China)
Noh-Yeong OH (National Fusion Research Institute, Korea)

Preface

The first meeting of A3 foresight program on Plasma Physics hosted by NFRI (Korea) was held in Jeju Island, Korea on 22nd August, 2012 as coordinator meeting to initiate the A3 program. The first seminar hosted by NIFS (Japan) and the second seminar hosted by ASIPP (China) were held in Kushiro, Japan during 22-25 January, 2013 and in Beijing, China during 20-23 May, 2013, respectively. Concrete planning of collaborative research was made and possible scientific progresses done in steady state sustainment of high-performance plasmas were also discussed in two seminars. Many young scientists were joined in these seminars. The third seminar hosted by NFRI was held in Gyeongju, Korea, during 3-4 November, 2013 to report the progress and achievement in on-going A3 collaboration. The fourth seminar hosted by NIFS and the fifth seminar hosted by ASIPP were held in Kagoshima, Japan, during 23-26 June, 2014 and in Nanning, China, during 6-9 January in 2015 to discuss achievements and summarize intermediate report within the A3 scientific framework, respectively.

The seventh A3 seminar hosted by NIFS was held in Gotemba, Japan, 1-4 December 2015, following the sixth A3 seminar in Chuncheon, Korea, 19-22 May 2015, to check and review the on-going A3 collaboration including scientific results during the past three years and to discuss the future plan. The presentations in the seminar are consisted of four categories;

I. Steady state sustainment of magnetic configurations,
II. Edge and divertor plasma control
  IIa. Transport of edge and divertor plasmas
  IIb. Stability of edge plasma
III. Confinement of alpha particles
IV. Theory and simulation.

In the seminar totally 43 participants were attended (19 from Japan, 13 from China and 11 from Korea) and 40 reports were presented. As a special topics in this seminar, a session on new divertor experiments and a session on Ph.D. students learning in graduate school were set up to step up the A3 activities.

The seminar was completed with great success, clarifying significant progress in collaborative researches along A3 program physics categories mentioned above and also contributing to the fostering of young scientists and Ph.D students. The organizing and program committees are deeply grateful to all participants and acknowledge foundation of three countries (NSFC in China, JSPS in Japan and NRF in Korea) for strong and continuous supports. Based on their supports and corporation the seminar

was steadily and successfully concluded.

Shigeru MORITA, Liqun HU and Yeong-Kook OH

Chairpersons of the Organizing Committee


The 8th A3 Foresight Program Workshop
December 1st –4th, 2015 Gotemba, Japan
Sponsored by Japan Society for the Promotion Science, Natural Science Foundation of China and National Research Foundation of Korea
日中韓フォーサイト事業
A3 Foresight Program
独立行政法人
日本学術振興会
Japan Society for the Promotion of Science

Contents

◆Session 10

Current Status of Scintillator-Based Fast-Ion Loss Detector Project in Magnetic Confinement Fusion Experimentsin Japan, Korea, and China

ISOBE Mitsutaka[1,2)], KIM Junghee[3,4)], ZHANG Yipo[5)], CHANG Jiafeng[6)], OGAWA Kunihiro[1,2)], KIM JunYoung[4)], and LIU Yi[5)]

[1)]National Institute for Fusion Science, 322-6, Toki, 509-5292, Japan

[2)]SOKENDAI (The Graduate University for Advanced Studies), 322-6, Toki, 509-5292, Japan

[3)]National Fusion Research Institute, 34133 Daejeon, Korea

[4)]Korea University of Science and Technology, 34133 Daejeon, Korea

[5)]Southwestern Institute of Physics, PO Box 432, Chengdu, 610041, China

[6)]Institute of Plasma Physics, Chinese Academy of Science, Hefei 230031, China

Abstract The scintillator-based fast-ion loss detector (FILD) project in Japan, Korea, and China has been accelerated in the collaboration framework of A3 foresight program to enhance comprehensive understanding fast-ion behaviors in magnetic confinement fusion.The FILDs in LHD heliotron, KSTAR, HL-2A, and EAST tokamaks are successfully working as a result of joint work and physics experiments on fast ions, such as effects of Alfvénic mode, tearing mode, resonant magnetic perturbation field, and disruption on fast-ion behaviors are ongoing.

1. Introduction

Good confinement of fast ions in fusion plasmas is crucial to the success of the fusion reactor since fusion-born α particles play an essential role in steady state sustainment of a future burning plasma as a primary heating source. Although unfavorable effects on fast-ion orbit caused by axisymmetry breaking of the system is one of the oldest issues in fusion, attention is now being focused on it again because the non-axisymmetric three-dimensional (3-D) perturbed field produced by resonant magnetic perturbation (RMP) is often superposed to mitigate edge localized mode (ELM) in recent experiments. Fast-ion-driven magnetohydrodynamics (MHD) instabilities such as toroidal-Alfvéneigen mode (TAE) [1] and energetic-particle continuum mode (EPM) [2] are also of great concern since those instabilities can potentially lead to redistribution and/or loss of fast ion. For the reasons above mentioned, tight collaboration on fast-ion physics in fusion were initiated in 2012 in three Asian countries of Japan, Korea, and China in the support of the A3 foresight program on critical physics issues specific to steady state sustainment of high-performance plasmas [3]. A primary purpose of our joint work is to obtain comprehensive understanding of fast-ion transport and/or loss caused by 3D field and/or fast-ion-driven MHD instabilities in toroidal fusion plasmas. Our immediate goal in the early stage of this program is to set up scintillator-based fast-ion loss detectors (FILDs) onto four major fusion devices in East Asia, i.e., the LHD heliotron [4,5], the KSTAR [6], the HL-2A [7], and the EAST [8] tokamaks. The FILD is a type of magnetic spectrometer for charged particles, providing energy and pitch-angle (velocity component) of escaping fast ions as a function of time simultaneously. Note that the FILD was originally developed at the Princeton Plasma Physics Laboratory for escaping charged fusion products in the TFTR tokamak [8-11]. After the shut down of TFTR, the technology of FILD was transferred to CHS at the National Institute for Fusion Science (NIFS) for escaping beam ion diagnostics [12,13]. At present, the FILD has become a fundamental diagnostic tool for escaping fast-ion diagnostics and has been widely used in many magnetic confinement fusion devices [14-19].

As a result of intensive joint collaboration in the framework of the A3 foresight program, installation of the FILD onto four major devices in East Asia was completed in 2014. In LHD, TAE and/or EPM-induced fast-ion losses have been intensively studied by using the FILD [20-22]. Effects of resonant magnetic perturbation (RMP) field on fast-ion behavior have been also investigated [23]. The KSTAR FILD is successfully working. A study on behavior of fast ions due to RMP field is in the center of attention in KSTAR [24, 25]. In HL-2A, fast-ion losses induced by tearing modes, long-lived mode, sawtooth crash, and disruption have been observed [26]. A recent important step in our work is that the operation of the FILD on

EAST has begun. The localized bright spot appears on the screen while neutral beam (NB) is tangentially injected and disappears after NB is turned off as expected. In this paper, current status on the FILD projects in Japan, Korea and China, and representative results obtained from ongoing activities are shown.

2. Experimental setup and representative results

2.1 FILD onLHD

The LHD FILD project was initiated in 2001 after the successful operation of the FILD in CHS[27]. As a result of continuous efforts to improve the detector performance, the LHD FILD has reached the existing system schematically depicted in Fig. 1. Because significant radial transport of co-going transit beam ions due to TAE bursts was recognized by a neutral particle analyzer having a tangential line of sight [28], the FILD was designed to detect escaping co-going transit beam ions whose orbitsdeviate substantially from magnetic flux surfaces.The scintillation light image on the ZnS (Ag) screen due to impact of escaping beam ions is transferred by using a long image bundle fiber of 35 m and is focused on to the image intensifier connected to the CMOS camera placed in the basement. This designissued from a great concern about irradiation effects of neutron and x-ray ontohighly integrated electronics of the FILD in a deuterium discharge planned in LHD.Because the CMOS camera employed in LHD is not fast enough to follow rapid events such as beam ion transport due to TAE bursts, fast-photomultiplier tube (PMT) array consisting of 16 tubesis employed at the same time.

The LHD is equipped with intense NB injection heating system, i.e., three negative-ion source based NB injectors,here called N-NBIs (E_b/P_{nb}=180 keV/~5 MW for each) in the tangential direction and two positive-ion source based NB injectors (E_b/P_{nb}=40 keV/~6 MW for each) in the perpendicular direction. In addition to high-power NB heating, beam ions provided by N-NBIs can be super Alfvénicif the toroidal magnetic field strength B_t is lower than 1 T.For this reason, fast-ion-driven MHD instabilities have been often observed while high-energy tangential NBs are injected into low-B_t(< ~1 T) plasmas [29].

Figure 2 shows typical time evolutions of the FILD signals in the N-NB heated discharge of LHD. Recurrent magnetic fluctuation bursts of which frequency ranges from ~20 kHz to ~35 kHz are observed. Because beam ions are super Alfvénic and the mode frequency is in the TAE gap on the shear Alfvén continua, the observed mode is recognized as TAEs. Correlated with the TAE bursts, periodic increases of fast-ion loss flux reaching the FILD are recognized. The FILD indicated that energy and pitch-angle of escaping beam ions are 100~180 keV and 30~40 degrees, respectively. It is interesting to note that two bright spots appear on the scintillator screen while TAEs are destabilized whereas a single weal spot is seen while TAEs are not present. The observation tells us that TAEs induced beam ions having particular pitch-angles.

2.2 FILD on the KSTAR

Experimental studies on the energetic-particle physics of KSTAR plasmas have been conducted since the 2011 campaign by starting development of the fast-ion loss detector (FILD). The KSTAR FILD [6] is based on the TG-Green ($SrGa_2S_4:Eu^{2+}$) scintillator plate exhibiting the energy and the pitch-angle of the escaping fast ions. The FILD-1 head which is controlled by the linear manipulator system (Fig. 3 (a)) has the shaped front surface of the graphite protector in order to avoid the excessive heat load that can cause unexpected emission from the scintillator due to thermal stimulation. In particular, scintillator material was coated on the thick stainless steel plate to block the hard X-ray whose energy is below 1 MeV. The FILD-2 system depicted in Fig. 3(b) is located at a different toroidal location (I-port) which is equipped 135°apart from the FILD-1 position (C-port). Since availability of the port at the I-port is very poor, flexible in-vessel wound fiber guide (made by Schott) has been inserted into the special housing. Imaging test with the in-vessel halogen lamp (Fig. 3(b)) shows the clear picture of the scintillator plate through the narrow viewport. All the optical systems are made of the commercial lens sets to expedite development except the optical-fiber components to be connected to the PMT array (FILD-1) and the APDCAM (FILD-2). The focus of all the channels connected to the PMT array via a 16channel fiber bundle are checked by means of backward lighting from the end of the fiber bundle to the scintillator plate inside the FILD head (Fig. 3(a)). It has been found that the period of the optical alignment to guarantee the clear focus on the PMT array can be longer than one week during the experimental campaign. This means that the optical systems of the KSTAR FILDs are more or less free from vibration or displacement of tokamak body.

The KSTAR FILD system has shown various physical phenomena such as fast-ion loss behaviors related to the edge magnetic perturbations [24, 25, 30], tearing modes [25], and others. In particular, resonant magnetic perturbation (RMP) intending ELM mitigation and/or suppression could change local fast-ionloss intensity significantly [30]. Fig. 4 shows the example of the fast-ion loss intensity changes depending on the directions

of the radial magnetic perturbations (B_r). Outward B_r at the FILD head location increases the fast-ion loss signal, however, inward B_r decreases fast-ion loss signal intensity significantly. By changing the "phasing" of the RMP coil current polarity with the fixed helicity (e.g. n=1 or 2), toroidal localization of the fast-ion loss depending on the RMP helicity have been identified [24, 25]. Further analyses based on full 3-D orbit simulations with Lorentz-Orbit (LORBIT) code [31] have been performed to confirm the toroidal variation of the loss patterns. As described in Fig. 4(b), LORBIT simulations show the outward B_r makes clear intersections between the fast-ion orbits (blue dots) and the FILD-head, and vice versa.
Moreover, fast-ion orbits become stochastic at the edge region as shown in Fig. 4(b). Flexibility of RMP configuration on KSTAR and diagnostic capability of KSTAR enable extending the physics studies on the interactions between the fast-ion orbits and the RMP-stimulated edge stochasticity as well as radial perturbations. Besides the RMP-associated fast-ion loss, fast-ion loss correlated with the core MHD instability such as tearing mode is observed on the spectrogram of the PMT signal sensitive to the low pitch-angle side implying the resonant interaction with the core magnetic perturbations (Fig. 4 (c)) [25].

2.3 FILD on the HL-2A

A new scintillator-based FILD has been developed and operated in the HL-2A tokamak to measure the losses of NB ions, as shown in Fig. 5. The probe is capable of traveling across an equatorial plane port and sweeping the aperture angle rotationally with respect to the axis of the probe shaft by two-step motors in order to optimize the radial position and the collimator angle. The light pattern on the scintillator plate is measured with a PMT array and a high-speed video camera. The PMT array can detect the total loss rate of fast ions as a function of time with frequency response up to 1 MHz. The camera provides a slow video of the fast-ion-loss image but with a high energy and pitch-angle resolution.
Characteristics of fast-ion losses induced by various MHD instabilities, such as tearing mode (TM), long-lived mode (LLM), sawtooth crash, and disruption, have been observed and experimentally investigated in the HL-2A tokamak. Figure 6 shows the time evolution of the images of fast-ion losses due to TM. From Fig. 6 (t2) and (t3), it can be seen that another luminous spot appears on the scintillator plate during TM. Along with the disappearance of the TM, the spot dims and then vanishes, as shown in image (t4). It is therefore reasonably concluded that the second light spot strongly correlates with TM, that is, the fast-ion loss event is induced by TM. Moreover, the spot becomes brighter as the TM amplitude becomes stronger, suggesting that the fast-ion losses increase with the increase of TM amplitude. The energy and pitch-angle of the lost fast ions induced by TM are 30 keV and 60°, respectively. Compared with TM and LLM, the fast-ion losses induced by sawtooth crash have a broad range in energy and pitch-angle. There may be some interactions between fast ions and magnetic disturbance, which cause the losses with the wide range of energy and pitch-angle. During disruptions, the total neutron emission rate drops by ~90% as a result of the strong fast-ion losses. The possible reasons for this phenomenon are the strong magnetic perturbations and the drastic change of the fast-ion transport. In addition, the clear experimental evidences of drastic losses of fast ions during disruptions have been obtained.

2.4 FILD on the EAST

The FILD in EAST is the newest in our activities. The EAST FILD project was initiated in 2011 in the collaboration between NIFS and the Institute of Plasma Physics, Chinese Academy of Science. In 2012, the FILD position suitable for escaping beam-ion detection was carefully investigated for EAST by using the LORBIT code [31]. Subsequently, the detailed design of the probe head section was carried out. As a result of efforts mentioned above, the specific FILD design was performed in 2013 and then the FILD was installed onto EAST in 2014.
A photograph of the FILD on EAST is shown in Fig. 7. The FILD is placed ~15 cm above from the equatorial plane of the tokamak. It can be inserted almost vertically into the vacuum chamber. It is also designed so as to rotate the probe head section. In EAST, the ZnS(Ag) scintillation phosphor was chosen. The EAST FILD is now equipped with only a fast camera. To follow rapid events such as beam-ion loss due to TAE and/or EPM, the measurement section has been upgraded lately by usingPMT array consisting of 25 channels. In EAST, the tangential NB injection heating began in 2014. Localized bright spot on the scintillator screen due to impact of escaping beam ions appeared while NB was injected as shown in Fig. 8. The FILD indicates that energy of measured escaping beam ion matches that of beam injection energy (E_b~40 keV). Bright spot appears when NB is turned on and disappears when NB is turned off. Also, measured pitch-angle is reasonable in terms of orbit topology of beam ions in EAST. Therefore, it can be reasonably concluded that measured bright spot is due to impact of escaping beam ions.

3. Summary

The A3 foresight program has accelerated close collaboration for fast-ion diagnostics development in Japan, Korea, and China. The FILDs have been setup onto LHD, KSTAR, HL-2A, and EAST as a result of joint work in the early stage of the program. Our efforts have been made to reveal 3-D magnetic field effects on confinement property of fast ions and fast-ion lossescaused by MHD instabilities resonant and non-resonant with fast ions. The FILDs developed in this project are successfully working.In LHD, the TAE has been often destabilized by super-Alfvénic beam ions, expelling beam ionsin particular range of pitch-angles.In KSTAR, it has been identified that toroidal localization of the fast-ion loss depends on the RMP helicity. In HL-2A, fast-ion losses induced by various MHD instabilities, such as tearing mode, long-lived mode, sawtooth crash, and disruption, have been characterized. As for EAST, the FILDarenow ready for stepping into physics experiments on fast ions. In the latter half stage of the program, joint experiments will be conducted to reveal common physics issues related to fast ions in tokamak and helical devices.

Acknowledgments

This work was supported by the JSPS-NRF-NSFC A3 Foresight Program in the Field of Plasma Physics (NSFC : No.11261140328, and NRF : No. 2012K2A2A6000443).

REFERENCES

[1] Cheng C.Z. and ChanceM.S., Phys. Fluids,**29** (1986) 3695.
[2] Chen Liu, Phys. Plasmas,**1**(1994) 1519.
[3] Eds. Morita S., Hu L., and Oh Y.-K., Proceedings of A3 Foresight Program Seminar on Critical Physics Issues Specific to Steady State Sustainment of High-Performance Plasmas, 22-24 January, 2013, Kushiro, Japan. NIFS-PROC-92.
[4] Ogawa K. et al., J. Plasma Fusion Res. SERIES,**8** (2009) 655.
[5] IsobeM. et al.,Fus. Sci. Technol.,**58** (2010) 426.
[6] Kim Jungheeet al., Rev. Sci. Instrum.,**83** (2012) 10D305.
[7] Zhang Yipoet al., Rev. Sci. Instrum.,**85**(2014) 053502.
[8] Ogawa K. et al., Proceedings of A3 foresight program seminar on critical physics issues specific to steady state sustainment of high-performance plasmas, 23-26 June, 2014, Kagoshima, Japan.NIFS-PROC-97, p.81.
[9] Zweben S.J., PhysicaScripta,**T16** (1987) 119.
[10] Zweben S.J.,Nucl. Fusion,**29**(1989)825.
[11] Darrow D.S. et al., Rev. Sci. Instrum.,**66** (1995) 476.
[12] Darrow D.S. et al., J. Plasma Fusion Res. SERIES,**1** (1998) 362.
[13] IsobeM. et al., Rev. Sci. Instrum.,**70** (1999) 827.
[14] Werner A. et al., Rev. Sci. Instrum.,**72** (2001) 780.
[15] BaeumelS. et al.,Fus. Eng. Des.,**74**(2005)853.
[16] Darrow D.S., Rev. Sci. Instrum.,**79** (2008) 023502.
[17] García-Muñoz M. et al., Rev. Sci. Instrum.,**80** (2009) 053503.
[18] Fisher R.K. et al., Rev. Sci. Instrum.,**81** (2010) 10D307.
[19] Pace D.C. et al.,Rev. Sci. Instrum.,**83** (2012)973501.
[20] IsobeM. et al., Contrib. Plasma Phys.,**50**(2010) 540.
[21] Ogawa K. et al.,Nucl. Fusion,**52**(2012)094013.
[22] Ogawa K. et al., Plasma Phys. Control. Fusion,**56** (2014) 094005.
[23] Ogawa K. et al., Plasma and Fusion Research,**9**(2014)3402097.
[24] Kim Jun Young et al., 41st European Plasma Physics (EPS) Conference on Plasma Physics, Berlin, 23-27, June, 2014. **P4.607**.
[25] Kim Junghee et al., 14th IAEA Technical Meeting on Energetic Particles in Magnetic Confinement Systems, 1-4, September, 2015, Vienna, Austria. **O-9**.
[26] Zhang Y.P. et al.,Nucl. Fusion,**55**(2015)113024.
[27] SaidaT. et al., Advanced Diagnostics for Magnetic and Inertial Fusion (Kluwer Academic/PlenumPublishers, New York, 2002) p. 133.
[28] OsakabeM. et al.,Nucl. Fusion,**46**(2006)S911.

[29] ToiK. et al., Plasma Phys. Control. Fusion,**53** (2011) 024008.
[30] García-Muñoz M. et al.,Nucl. Fusion,**53**(2013)123008.
[31] IsobeM. et al., J. Plasma Fusion Res. SERIES,**8**(2009)330.

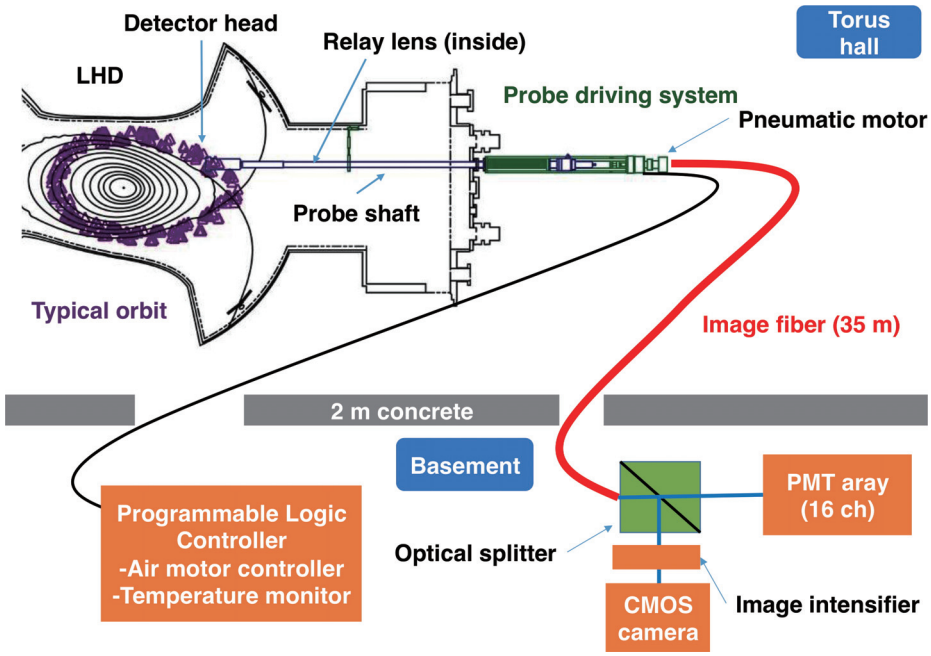

Fig.1 Schematic drawing of scintillator-based FILD system on the LHD heliotron. The FILD can be remotely controlled from the LHD operation room.

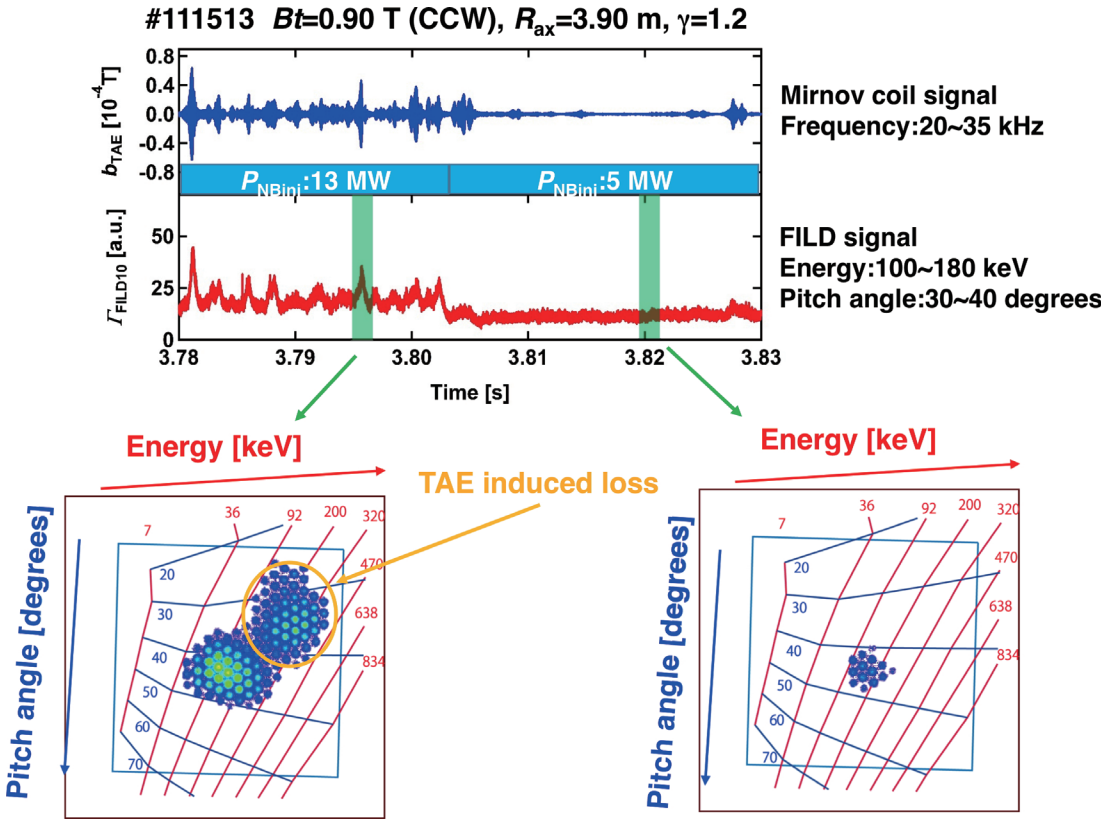

Fig. 2 Typical time evolutions of magnetic fluctuation and escaping beam ion flux measured with the PMT in a TAE discharge of LHD. Energy and pitch-angle of escaping beam ions measured with the FILD are also shown.

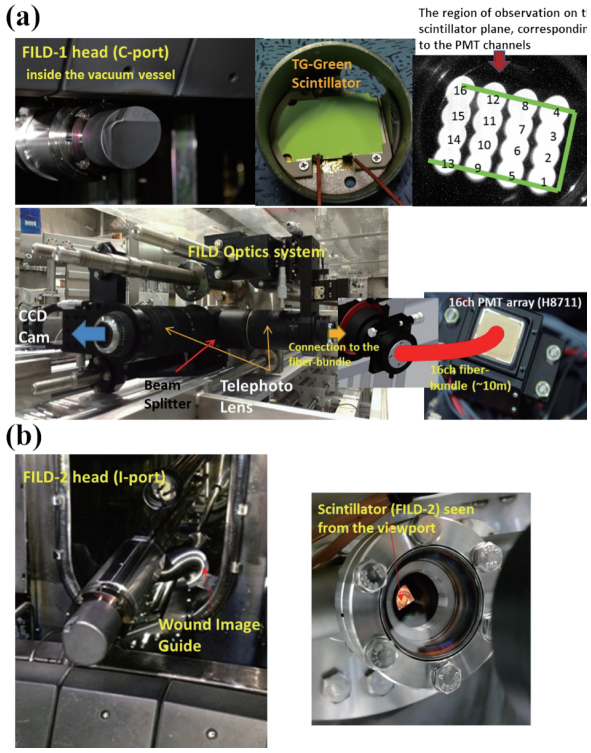

Fig. 3 Scintillator based FILD systems are installed on KSTAR tokamak. (a) FILD-1 system controlled by the manipulator at C-port consists of the CCD camera part and the fast-measurement system (PMT array). (b) FILD-2 system at I-port will be used for the study on fast-ion loss interplaying with non-axisymmetric fields.

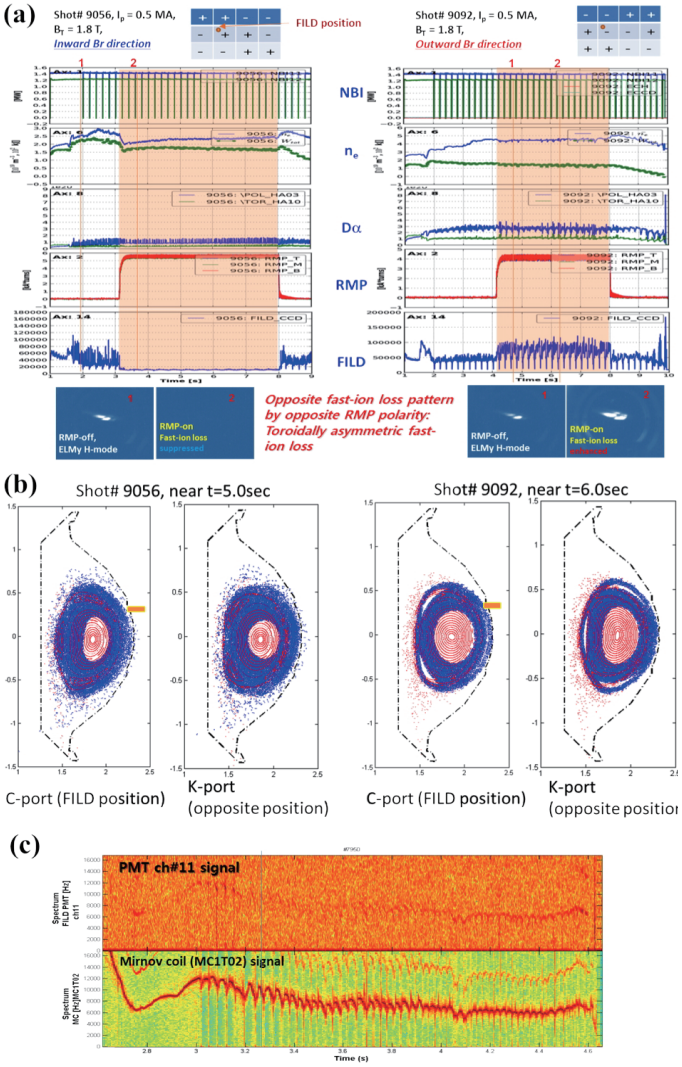

Fig. 4 (a) Fast-ion loss behaviors associated with opposite magnetic perturbation directions are captured on the FILD CCD images. (b) LORBIT simulations confirm toroidal localization of the fast-ion losses. (c) Spectrogram of PMT#11 signal shows clear correlation with the tearing mode.

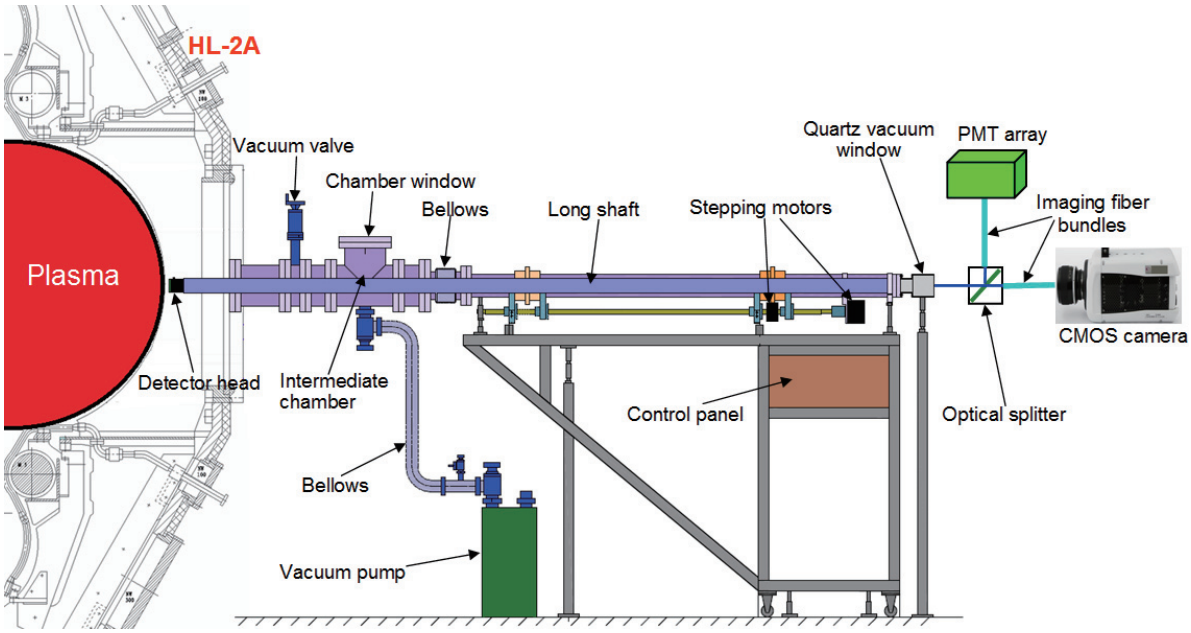

Fig. 5. Schematic overview of the FILD in the HL-2A tokamak.

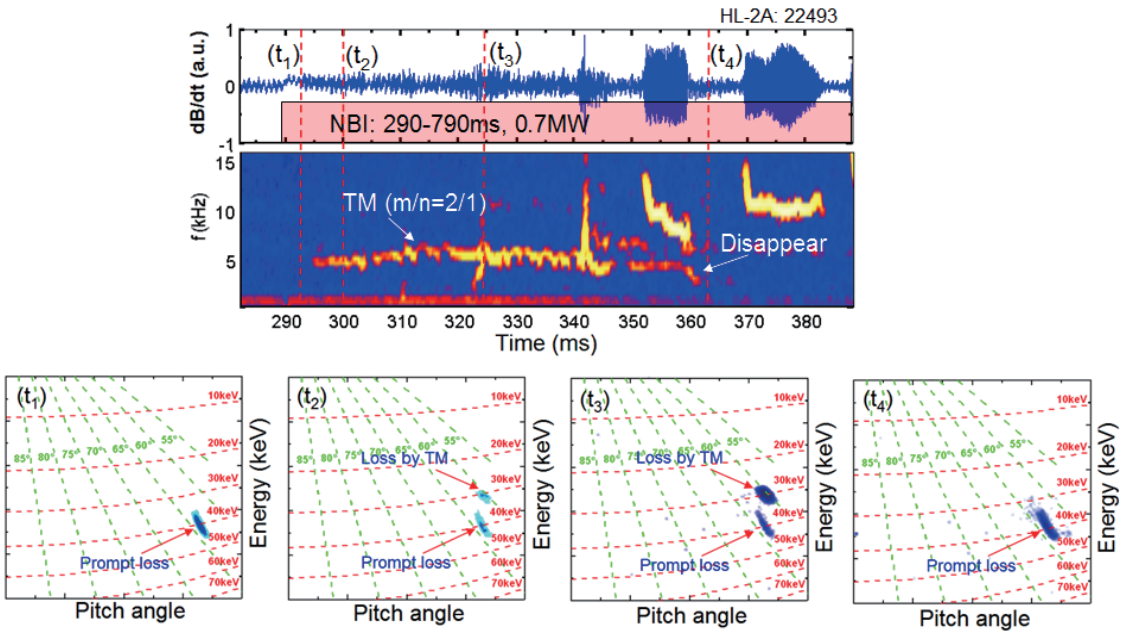

Fig. 6. Typical fast-ion losses induced by tearing mode in the HL-2A tokamak.

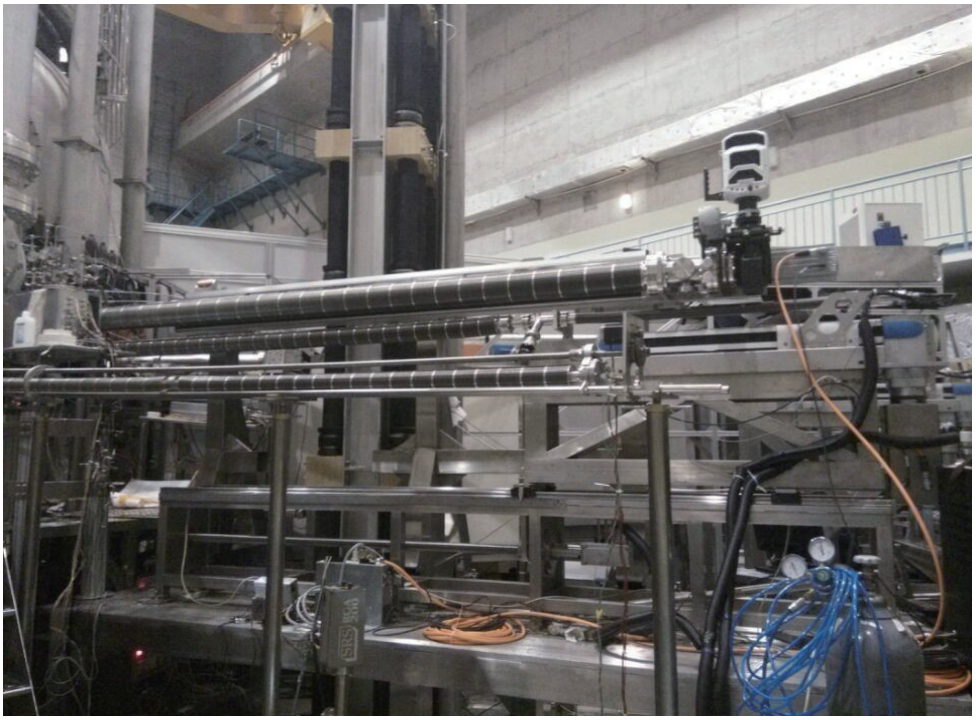

Fig. 7 External appearance of FILD on the EAST tokamak.

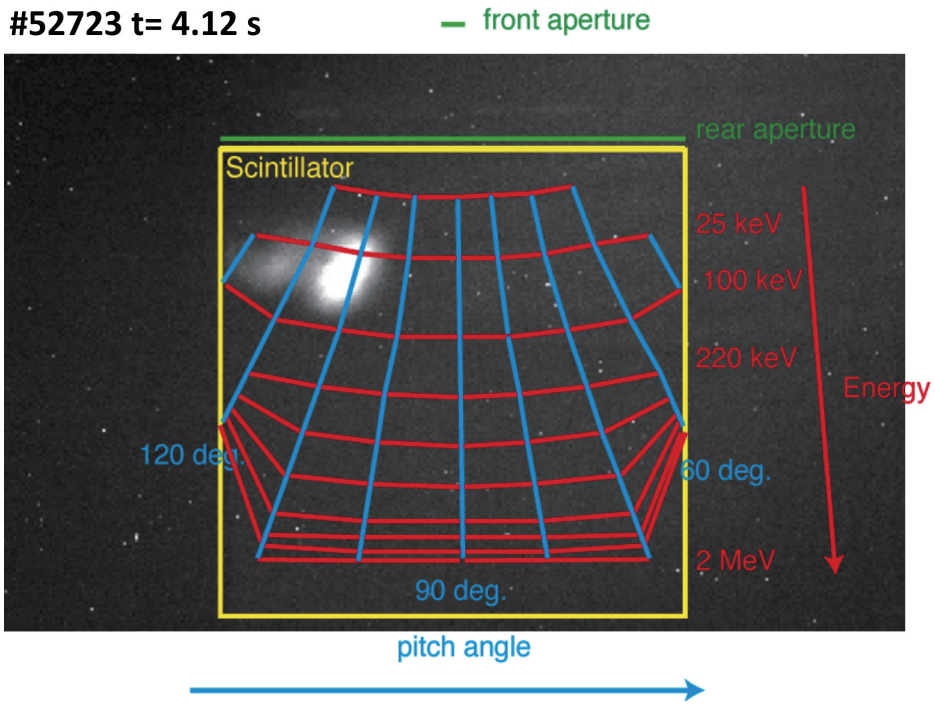

Fig. 8 Localized bright spot on the scintillator screen due to impact of escaping beam ions in the EAST tokamak.

14.1 MeV neutron measurement result in KSTAR deuterium plasma

Jungmin Jo[a], M. S. Cheon[b], Kyoung-Jae Chung[a,*] and Y. S. Hwang[a]

[a]*Department of Energy System Engineering, Seoul National University, Seoul, Republic of Korea*
[b]*ITER Korea, National Fusion Research Institute, Daejeon, Republic of Korea*
**Corresponding author: jkjlsh1@snu.ac.kr*

Measurement on 14.1 MeV d-t neutrons has been carried out for KSTAR deuterium plasmas using Neutron Activation System (NAS) with copper and silicon samples. A High Purity Germanium (HPGe) detector was used to count gamma rays from the activated samples. Background gamma rays radiated from activated surrounding materials near the counting station which activated by thermalized fusion neutrons were compensated. Due to the long plasma discharge duration nearly 60 seconds at the maximum in KSTAR, decay of activated silicon sample during the neutron irradiation has been considered. The analysis data from the activation measurement obtained during the 2015 KSTAR campaign show that the average neutron production rate was about $2\times10^{11}\ n/s$ for neutral beam heated plasma discharges. This measurement result will be used for the triton burnup studies in KSTAR.

Keywords: KSTAR, neutron activation system, 14.1 MeV neutron, deuterium plasma

1. Introduction

The detection of 14.1 MeV d-t neutrons in the deuterium plasmas in fusion device is of considerable interest as this can provides triton burnup probability. The triton burnup probability, i.e. the ratio between the number of burned up tritons and birth tritons, depends upon the slowing-down time and confinement of the tritons. A knowledge of the behavior of 1 MeV fusion tritons plays an important role due to their behavior similar to fusion alpha particles which provide plasma heating in burning d-t plasma. The cross-sections for two different d-d reaction branches are nearly the same, so that triton burnup ratio can be easily calculated from the ratio of the d-t and d-d neutron yield [1, 2].

Two neutron flux monitors, a fission chamber and a He-3 proportional counter are being used to measure d-d neutron yield from KSTAR plasma. Thus by measuring 14.1 MeV d-t neutrons with neutron activation system (NAS) triton burnup ratio can be determined in KSTAR. Considering relatively low expected d-t neutron yield in KSTAR deuterium plasmas and perturbing effect on sample gamma counting from background gamma rays, appropriate sample materials, silicon, copper, aluminum and iron are selected and their gamma counting strategies are established [3]. In this paper, among the selected sample material, copper and silicon sample were used for d-t neutron measurement due to their high activation cross-sections and relatively short half-life. To accurately measure the activity of each samples, background gamma rays, competition reactions and activity attenuation during and after the neutron irradiation are compensated.

2. Basic theory

The nuclear activation technique is a simple methods for measuring the total neutron yield, i.e., time integrated fusion power, from fusion devices. The activation technique has a strong point of intrinsic satisfactory of reliability, accuracy and linearity over several orders of neutron emission. Appropriate materials are transferred by using a pneumatic transfer system to the irradiation end close to the plasma and irradiated during the plasma discharge [4]. After the irradiation, it is retrieved to counting station then the neutron induced gamma activity of the sample is assayed. It provides the total number of activated atoms, N_{total}, during neutron irradiation time. It is related to the total yield of the fusion device through the equation [4]:

$$\mathrm{Y} = N_{total}/(\,P_m\,N_{sample}), \tag{1}$$

where, Y is the total neutron yield, N_{sample} is the number of atoms of the isotope of interest in the sample, and P_m is the activation coefficient. The activation coefficients is described as [5],

$$P_m = f\int_0^{Emax}\phi(E)\sigma(E)\,dE, \tag{2}$$

where f is the fraction of neutrons from the plasma incident on the sample, $\sigma(E)$ is the neutron activation cross section, and $\phi(E)$ is neutron spectrum at the sample position normalized to one source neutron [5]. Activation coefficient can be determined by using neutron transport calculations. Due to the activity of irradiated samples decay with time, through the following procedure, we can derive the total number of activated atoms during neutron irradiation time.

The total number of activated atoms N_{total} is given by [6]:

$$\mathrm{N}_{total} = \mathrm{R}\,t_0, \tag{3}$$

where R is reaction rate $[\,s^{-1}\,]$ and t_0 is neutron irradiation time.

If we assume that reaction rate R is constant and burn-up of target nuclei is negligible, the number of activated nuclei, N, can be written as:

author's email: wh1223@snu.ac.kr

$$N(t) = \frac{R}{\lambda}\left(1 - e^{-\lambda t}\right), \quad (4)$$

where λ is the decay constant of the daughter nuclide.

Basically, the activity, A, of the sample at certain time is given by:

$$A(t) = \lambda N(t). \quad (5)$$

Thus, right after the irradiation, i.e. at t_0, the activity is,

$$A(t_0) = \lambda N(t_0) = R\left(1 - e^{-\lambda t_0}\right) \equiv A_0. \quad (6)$$

And this can be determined from gamma counts from activated sample, C, which is measured during the time interval $\Delta t = t_2 - t_1$,

$$C = \alpha_\gamma \varepsilon \int_{t_1}^{t_2} A_0 e^{-\lambda t}\, dt = \alpha_\gamma \varepsilon A_0 \frac{e^{-\lambda t_1}(1 - e^{-\lambda \Delta t})}{\lambda}, \quad (7)$$

where α_γ is gamma abundance and ε is gamma detection efficiency.

Thus, from equations (3), (4), (6), and (7), the total number of activated atoms can be written as:

$$N_{total} = \frac{t_0}{(1 - e^{-\lambda t_0})} \frac{C\lambda}{\alpha_\gamma \varepsilon e^{-\lambda t_1}(1 - e^{-\lambda \Delta t})}. \quad (8)$$

If $t_0 \ll 1/\lambda$, it can be simplified as following,

$$N_{total} = \frac{C\lambda}{\alpha_\gamma \varepsilon e^{-\lambda t_1}(1 - e^{-\lambda \Delta t})}. \quad (9)$$

3. Experimental setup

The layout of the KSTAR NAS is depicted in Fig. 1(a) [7]. The position of irradiation station is located inside the vacuum vessel at "F" equatorial port. Counting system and pneumatic transfer system located beneath the KSTAR tokamak. Since 2011 KSTAR campaign, it has been successfully operated with indium samples which gives d-d neutron yield of KSTAR deuterium plasmas [7]. The measurement result of NAS with indium sample during the 2015 KSTAR campaign is shown in Fig. 1(b).

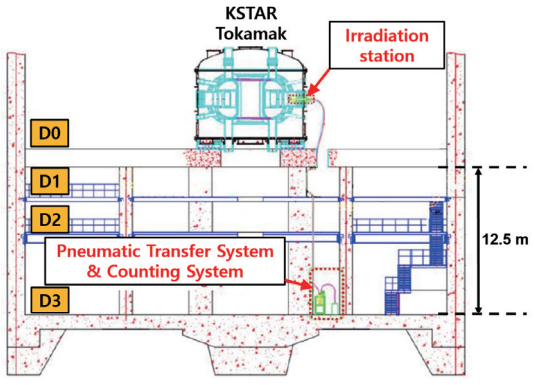

(a)

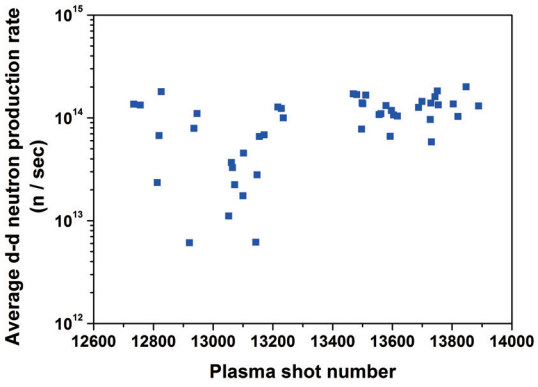

(b)

Fig. 1 (a) Layout of the KSTAR NAS, (b) Average d-d neutron production rate measured by the KSTAR NAS during 2015 KSTAR campaign.

Si, Cu, Al and Fe can be used for NAS sample materials and their neutron induced reactions are appropriate to measure d-t neutron in KSTAR environment. The neutron induced reactions and characteristics of each samples are listed in Table 1 [3].

Table 1. Candidate neutron induced reactions for 14.1 MeV neutron measurements.

Reaction	Isotopic abundance (%)	Half-life	E_γ (keV)	Gamma abundance (%)
^{28}Si(n,p)^{28}Al	92.2	2.24 m	1779	100
^{63}Cu(n,2n)^{62}Cu	69.2	9.75 m	511	195
^{27}Al(n,α)^{24}Na	100	15.2 h	1368.6	100
^{56}Fe(n,p)^{56}Mn	91.7	2.58 h	846.8	100

All these materials are widely used in many fusion devices because they have high activation cross sections at d-t neutron energy and completely discriminate against d-d neutrons intrinsically due to their reaction threshold energies are exceed d-d neutron energy. In KSTAR use of these materials requires more careful handling due to rather close position of the counting system with the tokamak. Sample gamma counting can be affected by the background gamma rays radiated from surrounding structures activated by fusion neutrons and also thermalized fusion neutrons themselves. Some of gamma peaks are exactly the same with gamma rays from sample materials. Therefore, to compensate background gamma ray appropriately, sample and background gamma spectrum have to be counted in the same shot interval of usually 10 minutes in KSTAR. Among these 4 materials, copper and silicon have a short minimum required counting time, thus it is possible to use in every plasma discharges. Since, there is no interfering reactions to be considered and it has short half-life of 2.24 minute, silicon is the most appropriate material. In this experiment, both silicon and copper are used for the cross calibration purpose.

Copper sheet (99.96% purity, Nilaco) has been used for the fabrication of copper samples. The mass of copper sample was 10 g. In copper case, activated copper

sample radiates 511 keV annihilation radiation after decays with positron emission. Because all the nuclides that decays with positron emission or radiates high energy gamma rays over 1022 keV can produce annihilation radiation, it is hard to identify the origin of background annihilation radiation. Furthermore, from the 8 times of sequentially measured background annihilation radiation result during the 10 minutes of shot interval, the decay characteristics is not an exponential shape, i.e. many kinds of radiation sources and/or complicated chain reactions are expected. However, fortunately, it barely changes during the 10 to 15 minutes of shot interval. Thus, it is possible to be assumed as constant during usual shot interval of 10 to 15 minutes for KSTAR. For copper samples, twice measurements with sufficiently long time interval are required due to the competing reactions: $^{65}Cu(n,2n)^{64}Cu$ and $^{63}Cu(n,\gamma)^{64}Cu$. Therefore, totally 4 times of measurements are required including background gamma ray measurement. For the convenience in calculation, the counting time is set to be the same in all cases as 250 seconds.

Silicon crystal rod (99.999% purity, Goodfellow) has been used for the fabrication of silicon sample. The mass of silicon sample was 14 g. In silicon case, activated silicon sample radiates 1779 keV gamma ray. In this case, there is exactly overlapped background gamma ray peak from the surrounding aluminum which is activated by thermalized fusion neutrons. It produces exactly the same daughter nuclide ^{28}Al. Fortunately, there is no other possible nuclides which radiates gamma ray of this energy, thus we can compensate it easily after the consideration of exponential decay. In KSTAR long pulse scenario, plasma discharge duration time is nearly 60 seconds at the maximum. Thus it is comparable to the half-life of ^{28}Al, 2.24 minutes. So not only decays of daughter nuclide after the plasma discharge, but also decays during the plasma discharge are considered.

Energy and efficiency calibration of 511 keV gamma energy for copper sample were performed by using ^{22}Na (511 keV, 1270 keV) standard gamma source. In silicon case, 1779 keV, due to the limitation of our practical conditions, alternative methods are used for energy and efficiency calibration. Energy calibration was performed with activated aluminum sample which is irradiated typical KSTAR neutral beam heated plasma. As described previous paragraph it produces exactly same daughter nuclide via $^{27}Al(n, \gamma)^{28}Al$ reaction. Detection efficiency at this gamma energy has been obtained from extrapolated efficiency curve which determined from two standard gamma source ^{133}Ba (303, 356, 384 keV) and ^{22}Na. Efficiency characteristic curve of P-type germanium detector was considered to determine appropriate extrapolation function. It will be re-calibrated soon with yttrium standard gamma source.

.

4. Experimental results

Measurement results of d-t neutron yield during the neutral beam heated plasmas by using copper and silicon are shown in Fig. 2(a) and Fig. 2(b), respectively. In Fig. 2, error bars denote only gamma counting errors. There are large counting errors in copper sample case compare with silicon sample case. This is due to the relatively small signals compare with that of competing reactions and the accumulated errors from the two times of measurements. Error decreases as increasing d-t neutron yield. Both measurement results show that d-t neutron yield in neutral beam heated KSTAR deuterium plasma is around from 1×10^{11} to 1×10^{13} n/shot.

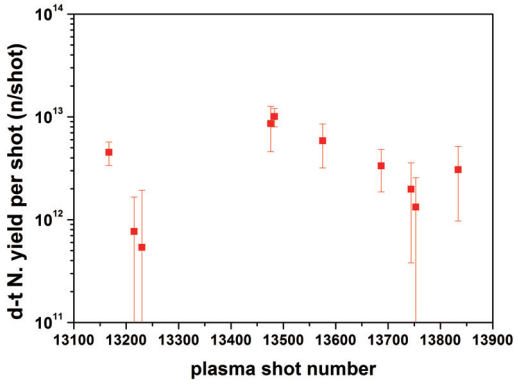

(a)

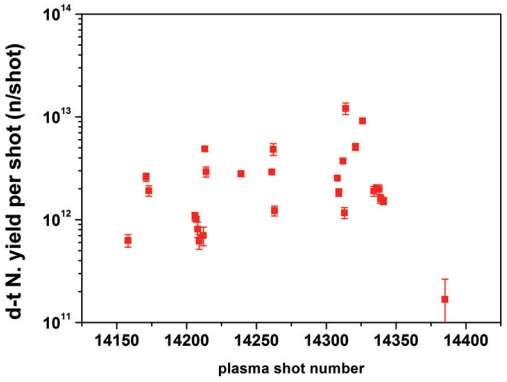

(b)

Fig.2 (a) d-t neutron yield from copper sample (b) d-t neutron yield from silicon sample

The average d-t neutron production rate from copper and silicon sample are shown in Fig. 3(a) and Fig. 3(b) respectively. The average d-t neutron production rate is about 1×10^{10} to 1×10^{12} n/s. It is around 1% of the average d-d neutron production rate.

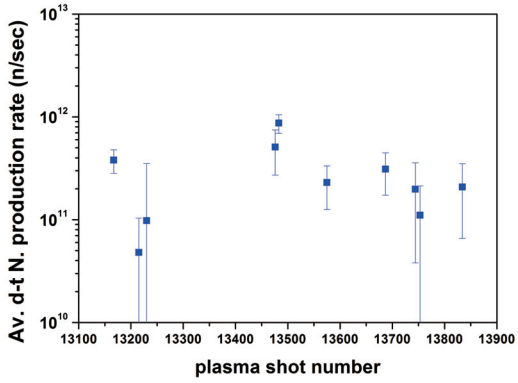

(a)

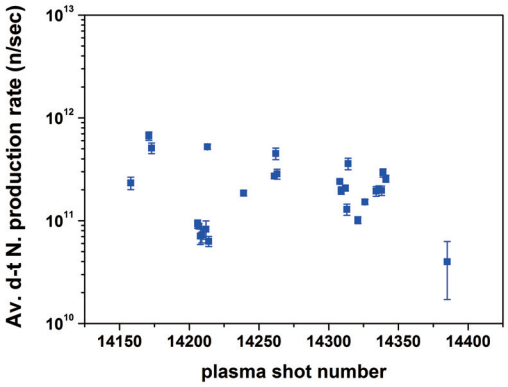

(b)

Fig.3 (a) average d-t neutron production rate from copper sample (b) average d-t neutron production rate from silicon sample.

For the cross calibration purpose, copper and silicon sample were irradiated in the same shot simultaneously. In this sample copper was situated in front of silicon. Due to the self-absorption effect, it is expected that the measurement result from silicon sample might be lower than that of copper sample. From the neutron transport calculation result using MCNP-5[8], 4 % and 13 % of attenuation are expected inside the copper and silicon sample respectively. The attenuation increases linearly with increase in sample thickness, keeping the normalized neutron spectrum unchanged. Thus if the measurement was ideal, the neutron yield from silicon sample should be lower than that of copper sample by around 5%. However in the experimental result the difference is bigger than expectation, as listed in Table 2.

Table 2. d-t neutron measurement result from copper and silicon composite sample.

Shot #	Copper	Silicon
	d-t neutron yield (n/shot)	d-t neutron yield (n/shot)
14262	8.39×10^{12}	4.86×10^{12}
14314	2.01×10^{13}	1.21×10^{13}

The measurement result from silicon sample in shot # 14262 and # 14314 are lower than copper sample around 58% and 60% respectively. Considering 13% of counting errors, the difference is nearly consistent for two cases. The large difference between the calculated and measured values might be mainly caused by inaccurate detection efficiency calibration of silicon sample. After the efficiency calibration with yttrium standard gamma source, it is expected that the difference between the calculation and experiment can be reduced.

5. Summary and conclusion

The 14.1 MeV d-t neutron yield has been measured with copper and silicon samples. The measured average d-t neutron production rate was about 2×10^{11} n/s in both copper and silicon cases. The counting errors in copper sample is relatively large compared with silicon case. The difference between the measurement results from silicon and copper is considerably larger than the calculation result from neutron transport code. It might be mainly caused by inaccurate detection efficiency calibration in 1779 keV gamma ray. After accurate calibration of the detection efficiency of 1779 keV gamma ray, the measurement result from silicon sample will become more reliable. This measurement result will be used for the triton burnup studies in KSTAR, together with measurement result from neutron flux monitors.

References

[1] G. Sadler, O. N. Jarvis, P. van Belle, M. Pillon, Use of the ^{28}Si(n,p)^{28}Al reaction for the measurement of 14 MeV neutrons from fusion plasmas, *Review of Scientific Instruments* **61**, 3175(1990).

[2] W. W. Heidbrink, G. J. Sadler, The behaviour of fast ions in tokamak experiments, *Nuclear Fusion* **34**, 535 (1994).

[3] Jungmin Jo, M. S. Cheon, Kyoung-Jae Chung, Y. S. Hwang, Sample design and gamma-ray counting strategy of neutron activation system for triton burnup ratio measurements in KSTAR, submitted to Fusion Engineering and Design (2015).

[4] L. Bertalot, A. L. Roquemore, M. Loughlin, B. Esposito, Calibration of the JET neutron activation system for DT operation, *Review of Scientific Instruments* **70**, 1137(1999).

[5] M. J. Loughlin, N. Watkins, L. Bertalot, B. Esposito, A. L. Roquemore, Neutron transport calculations in support of neutron diagnostics at JET, *Review of Scientific Instruments* **70**, 1126(1999).

[6] M. Hoek, T. Nishitani, Y. Ikeda, A. Morioka, Initial results from neutron yield measurements by activation technique at JT-60U, JAERI-M 94-002, (1994).

[7] M.S. Cheon, Y.S. Lee, A. C. England, H.S. Kim, S. Pak, C.R. Seon, H.G. Lee, Diagnostic neutron activation system for KSTAR, *Journal of Instrumentation* **7**, C05009 (2012).

[8] X-5 MONTE CARLO TEAM collaboration, *MCNP — a general Monte Carlo N-particle transport code, version* 5, Los Alamos National Laboratory, Los Alamos U.S.A. (2000).

Fast ion loss associated with RMP penetration

Jun Young Kim[a], Junghee Kim[a,b], T. N. Rhee[b], Won-Ha Ko[a,b],
S. W. Yoon[b], Y. M. Jeon[b], M. Isobe[c] A. Shimizu[c] and k. Ogawa[c]

[a]Korea University of Science and Technology, Daejeon, Korea
[b]National Fusion Research Institute, Daejeon, Korea
[c]National Institute for Fusion Science, Toki-shi, Japan
Email: nature1981@nfri.re.kr

Since Resonant magnetic perturbation (RMP) demonstrate edge localized mode (ELM) suppression and/or mitigation in DIII-D and KSTAR, RMP became a most promising tool for ITER to control ELM. However, enhancement of fast ion loss has been observed in KSTAR during RMP application and it became very crucial to understand the fast ion loss behavior in the presence of the non-axisymmetric magnetic field. In order to investigate the behaviors of the fast ions during RMP in KSTAR plasmas, fast-ion loss detectors (FILD) have been used intensively. In order to investigate relation between axisymmetric breaking and fast ion loss behavior, various spectrum of RMP has been applied. In addition, to control the RMP penetration, plasma rotation speed has been modulated using ECH heating. It has been observed that n=1 static RMP induced toroidally asymmetric fast ion loss with 90 degree of phase difference with maximum radial magnetic perturbation intensity. In addition, fast ion loss during RMP is following a power law to the level of toroidal rotation speed.

1. Introduction

Since DIII-D and KSTAR demonstrate ELM suppression using resonant magnetic perturbation (RMP), it became one of the most optimistic methods for ELM mitigation and/or suppression in ITER for reduction of the thermal load on a divertor. However, unwanted fast ion loss enhancement at a toroidally local position during RMP application has been reported from both numerical simulation works and experimental results. [1~5] In KSTAR 2015 experimental campaign, fast ion losses have been measured at a fixed toroidal position using fast ion loss detector (FILD) while various spectral of static RMP is applied. The measurement results show that the fast ion loss in RMP applied plasma is toroidally localized depending on a RMP polarity. In addition, in RMP applied plasma, it has been observed that the fast ion loss rate has a dependency in toroidal rotation speed, which could be related with screening of external perturbation field penetration by the fast rotating plasma [6]. Since the reliable prediction of fast ion loss positions becomes a crucial issue on potential damage to the first wall [7], more detailed research on the fast ion transport related to non-axisymmetric perturbation and/or Plasma locking should be analyzed and controlled. To investigate fast ion loss behavior during RMP, scintillator based fast-ion loss detectors (FILD) have been used at the peripheral of confined plasmas to understand

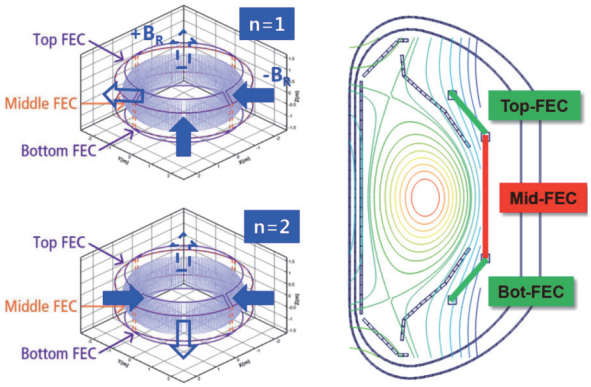

Figure 1. KSTAR field error correction (FEC) coils for magnetic resonant perturbation (RMP). It consists of Top, Middle and bottom coils and divided into 4 sections in toroidal direction. This configuration of RMP coil can produce n=1, 2 and mixture of n=1 and 2 of perturbation field.

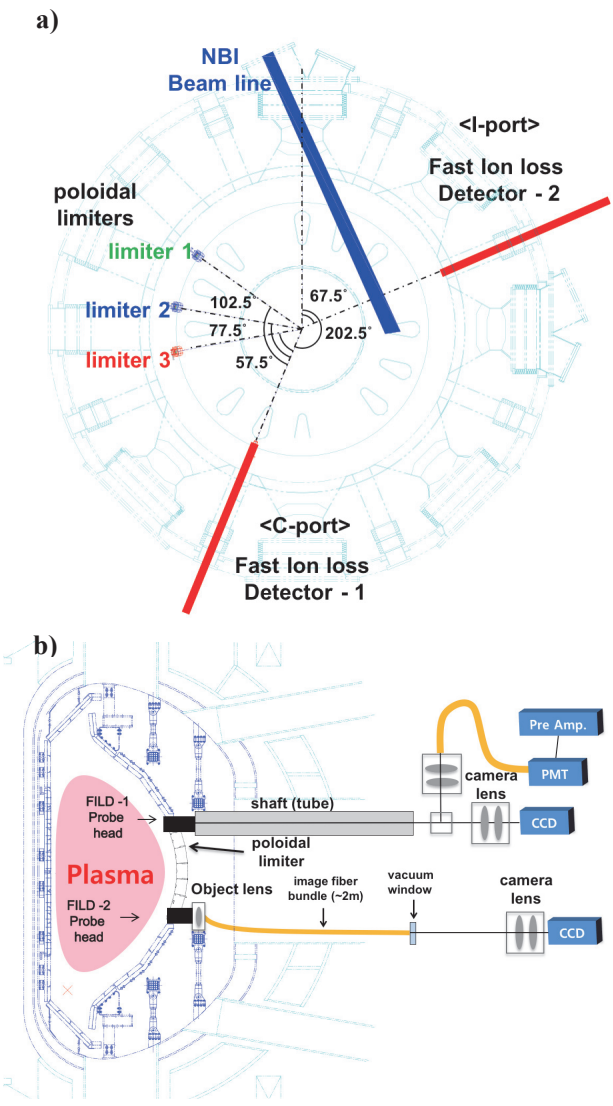

Figure 2. KSTAR scintillator based fast ion loss detectors (FILD) positions in a) toroidal view b) polodal projections.

the loss mechanisms of fast-ions.

2. RMP coils and fast ion loss detectors

KSTAR Field error correction (FEC) coils have been utilized for the magnetic resonant perturbation (RMP) [8]. FEC coils are consisted with total 12 coils that are 4 sections in toroidal direction and each section has top, middle and bottom coil. By using this configuration of coils, n=1 or n=2 or mixture of n=1 and n=2 perturbations are applicable. Also three rows of the FEC coils can provide various poloidal magnetic spectra.

In 2015 KSTAR campaign, two FILD system are operated. FILD-1 is installed at the upper mid-plane (44cm above the mid-plane) of the C-port which is separated 202.5 degree from NBI in toroidal direction. The FILD-1 system consists of the probe head, the mounting system and the image detection system. The probe head of the FILD consists of a scintillator plate, aperture and collimator slits and a graphite thermal shield. The aperture of the three-dimensional collimator is aligned parallel to the local magnetic field. The three-dimensional collimator is acting as a magnetic mass spectrometer and it disperses the incident fast-ions on the scintillator plate according to their energies and pitch-angles. The perpendicular velocity component of a fast-ion to the magnetic field line is directly related to the gyro-radius of the lost ion and the distance from the collimator to the scintillator strike point is proportional to its gyro-radius. Pitch-angle is a ratio between the parallel and the perpendicular components of the total velocity of a fast-ion to the external magnetic field, and in a similar manner, as the pitch-angle varies, the ion will strike the different position on the scintillator even though the total ion energy is same. Consequently, it is possible to determine the pitch-angle and gyro-radius of escaping fast-ions from the measurement of the strike position on the scintillator. The mounting system enables controlling the radial position of the probe head by moving the shaft tube back and forth using an air motor. A graphite shield covers up the probe head of FILD system to protect the internal components from the excessive heat load. The graphite cover is shaped according to the plasma boundary to reduce the perpendicular heat load on to the protection cover. TG-green was chosen as a scintillator material for better emitting efficiency and it is coated on the stainless steel substrate. Cubic beam splitter divides scintillation light from the fast-ion bombardment into two and the CCD camera (~200 fps) utilized with a telescopic camera lens to captures one of the rays from beam splitter. Another ray is focused on the optical fiber

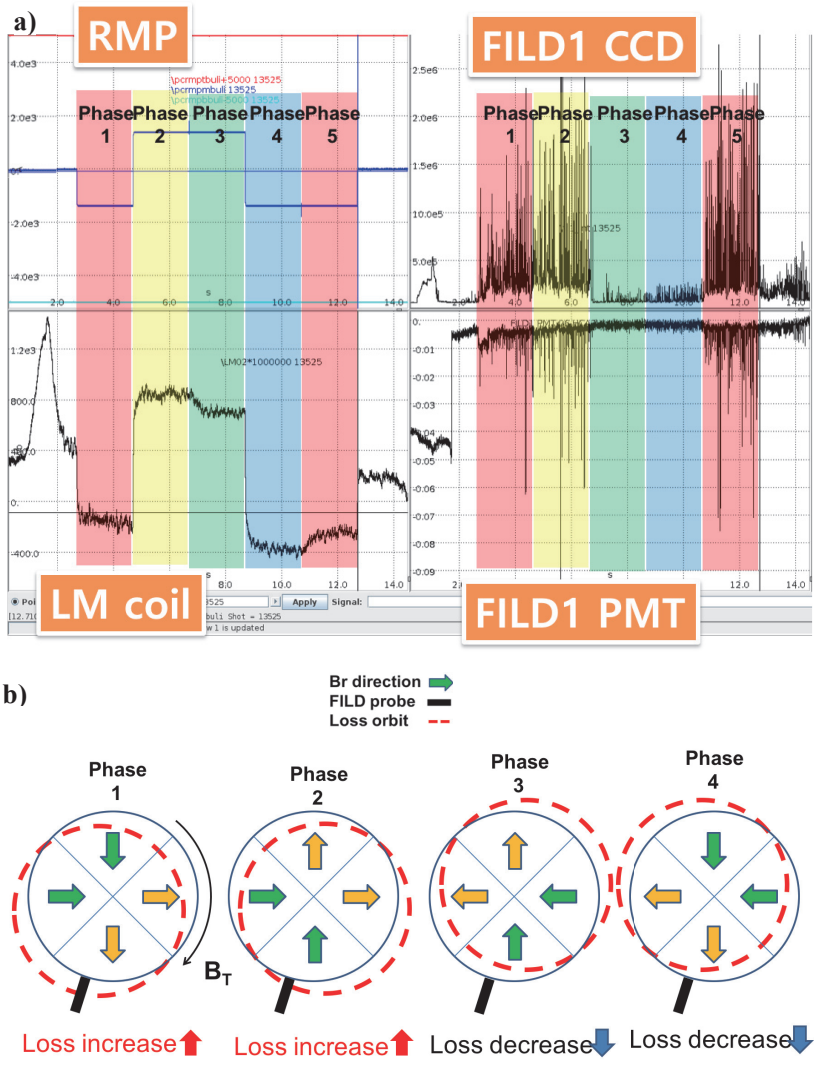

Figure 3. Fast ion loss during n=1 static RMP. a) Toroidal phase of n=1 RMP is shifted in count clockwise direction for 90 degrees, for 5 times; from phase 1 to 5. b) Maximum fast ion loss rate in n=1 RMP shows 90 degrees of toroidal phase difference compared to maximum perturbation field strength

bundle and it is connected to the 16-channel photomultiplier tube (PMT) for fast measurement (up to 2MHz) of fast ion loss fluctuation. FILD-2 is also a scintillator based fast ion loss detector, but its probe-head is fixed at R=2.3m radial position. It is installed at I-port, lower mid-plane which is toroidally separated from for 135 degrees from FILD-1.

3. Experimental results of fast ion loss measurement during RMP

n=1 RMP with only middle coil has been used to investigate the localized and/or toroidal asymmetric fast ion loss by RMP. Both static and sinucoidally rotating RMP has been tested. In case of static RMP, toroidal phase of n=1 RMP is shifted in count clockwise direction for 90 degrees, for 5 times; from phase 1 to 5. So the phase 1 and 5 are the same. Since FILD1 is placed at C-port, middle RMP coil current between B- and F-port can be compared with locked mode coil at E-port. Negertive sign of the RMP coil current produce an 'outward δB_r' and positive sign of the RMP coil current produce an 'inward δB_r'. The response of the locked mode coil is well corresponding with the B-F middle RMP coil current throughout all five phases. (Fig. 3a upper left and lower left) However, in case of fast ion loss response which is measured by FILD-1 CCD and PMT (Fig. 3a upper right and lower right) showed phase difference with RMP coil current sign and locked mode signal. For phase 1, RMP coil current and locked mode signal represent the direction of δB_r at FILD probe to be outward. Meanwhile, fast ion loss rate from the CCD and PMT showed an enhancement both in signal base level and amplitude of loss peaks by ELM bursts, in a comparison with before-RMP. However, in phase 2, even thought the direction δB_r has changed to inward, fast ion loss rate is kept enhanced. After one more rotation to phase 3, the direction δB_r at FILD probe is sustained as inward, but the fast ion loss rate is significantly reduced both in base line and peak amplitudes. In phase 4, δB_r direction is changed to outward and fast ion loss rate is still remained as suppressed. In order to understand the observation, fast ion orbit drift by perturbation field should be considered. (Fig. 3b) Fast ion orbit could be drift away by the

direction and amplitudes of δB_r. For example, n=1 RMP configuration will superpose an outward δB_r throughout half of toroidal angle and the other half of toroidal position will have inward δB_r on a magnetic equilibrium. A fast ion travels in outward δB_r region, ion orbit will be drift way to outward as long as it sees outward δB_r. At the position when the direction of δB_r is changed to inward, the outward displacement of ion orbit becomes maximum. Even thought the fast ion entered inward δB_r region, the ion will continually drift to inward direction, starting from maximum out displacement position. This can explain the cases of phase 2 and 4. Consequently, maximum fast ion loss rate in n=1 RMP shows 90 degrees of toroidal phase difference compared to maximum perturbation field strength.

To investigate the effect of the toroidal rotation on the external field screening effect and fast ion loss rate, electron cyclotron heating (ECH) has been used to change the rotation speed while the RMP is applied. During shot number 11465, n=2 middle coil was turned on during plasma current plate-top region. 110 Ghz and 170 Ghz ECH has been launched to reduce the toroidal rotation velocity. Both in L- and H-modes, toroidal rotation dependency on the fast-ion loss has been shown clearly. As rotation increases, fast-ion loss decreases. In a low rotation or locking plasma, fast-ion loss level is enhanced and the possibility of severe damage on the first-wall and in-vessel components is increasing.

4. Summary

Toroidally 90 degrees of phase difference between the maximum perturbation field by n=1 RMP and the maximum loss orbit displacement has been observed. In addition, by changing RMP coil polarity, toroidally asymmetric fast ion loss can be regulated. It seems that the toroidal rotation and fast ion loss rate closely related. As rotation speed is increasing, fast ion loss rate is decreasing. Shielding effect of as external perturbation (RMP) field penetration needs to be more investigated. Toroidally asymmetric and localized fast ion loss due to RMP should be avoided to prevent the damage to the wall or vacuum vessel. Also low toroidal rotation velocity could enhance the fast ion loss rate and it could harm the fusion performance.

Acknowledgement
This research was supported by Ministry of Science, ICT, and Future Planning under KSTAR project and was partly supported by the JSPS-NRF-NSFC A3 Foresight Program (NRF No. 2012K2A2A6000443).

References
[1] K. Tani *et al*., Nucl.Fusion **52**, 013012 (2012).
[2] K. Shinohara *et al*., Nucl. Fusion **52**, 094008 (2012).
[3] J. Kim *et al*., Rev. Sci. Instrum. **83**, 10D305 (2012).
[4] M. Garcia-Munoz *et al*., Nucl. Fusion **53**, 123008 (2013).
[5] J. Kim *et al*., 10th ITPA Energetic Particles Topical Group Meeting (2013).
[6] Y. Q. Liu *et al*., Plasma Phys. Control. Fusion 54 (2012) 124013
[7] C.Z. Cheng, *et al*., in Fusion Energy 1996 (Proc. 16th Int. Conf. Montreal, 1996), Vol. **2**, IAEA, Vienna (1997) 953
[8] Y.M. Jeon *et al.,* Phys. Rev. Lett. **109,** 035004 (2012)

PROGRESS OF ITER RADIAL X-RAY CAMERA DIAGNOSTIC

L.Q. Hu[1], K. Chen[1], Y. Chen[1], S. Li[1], J.Shen[1], X. Sheng[1], L.Niu[1], Y. Cheng[1], J.Zhao[1]

[1]Institute of Plasma Physics, Chinese Academy of Sciences, Hefei 230031, China

Abstract

The Radial X-ray Camera (RXC) is designed to measure the poloidal profile of the plasma x-ray emission with high spatial and temporal resolution. Its primary diagnostic role includes measuring low (m,n) magnetohydrodynamics (MHD) modes, sawteeth, disruption precursors and ELMs. The camera consists of two subsystems, i.e. in-port and ex-port cameras which view the outer and core region respectively through vertical slots in the diagnostics shield module of an equatorial port plug. The detailed camera design is in progress including design of camera structure, electronics, data acquisition and control, calibration and pretest on EAST tokamak. The sight path and neutron shielding have been optimized. The design of secondary vacuum, heat insulation, cooling, positioning and calibration have been carried out. The structure analysis results for external camera indicated that even under 5 times gravity acceleration, the maximum stress was still below the allowable stress. The heat analysis result indicated that the maximum temperature on the detector box was about 56°C which was within the detector operation temperature limit. Neutronics analysis result indicated that the detectors can be operated during the whole Deuterium-Deuterium (D-D) phase without detector replacement. The electronics group and Instrumentation and Control (I&C) group have also made good progress.

1. Introduction

The ITER Radial X-ray Camera (RXC) is being designed by China [1]. The Camera is applied to measure the poloidal profile of the plasma x-ray emission with high spatial and temporal resolution. Its primary diagnostic role includes measuring low (m,n) MHD modes, sawteeth, disruption precursors and ELMs. RXC also provides supplementary measurements of plasma position, radiative power, runaway electrons, impurity content, etc. [2].

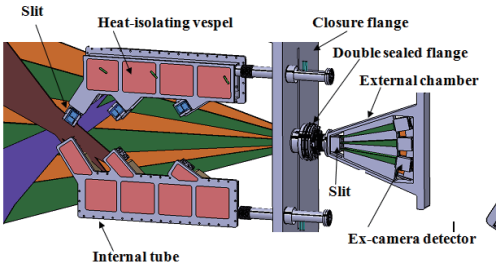

Fig.1 Overall view of the internal and external cameras

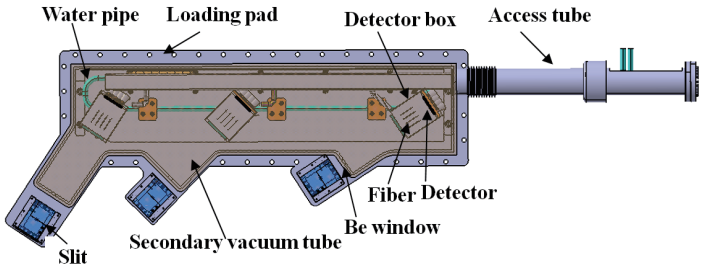

Fig.2 Overview of internal camera structure

RXC is installed on the middle Diagnostics Shield Module (DSM) of Equatorial 12 Port Plug (PP) which is shared by RXC, Glow Discharge Cleaning system (GDC) and Hard X-ray Camera (HXC) [3]. The camera consists of two subsystems, i.e. in-port and ex-port cameras which view the outer and core region respectively through vertical slots in the DSM of an equatorial port plug [1]. External detector chamber and internal detector tube have secondary vacuum housed with beryllium window assemblies for separation between tokamak vacuum and secondary vacuum. Internal detectors are installed on light-weight removable support frame within tube to facilitate detector maintenance. Besides, due to high environment

temperature during baking, dedicated cooling for in-port detectors is required. The necessity of cooling for ex-port detectors depends on environment temperature which will be estimated. An overall view of the current internal and external cameras is shown in the Fig.1. Along with the change of camera configuration, detailed design has been carried out including design of structure, electronics, I&C, calibration and pretest on EAST tokamak. Technical details of the design are described as follows.

2. Design of camera structure

2.1. Design of internal camera structure

Each internal arm contains three detector arrays viewing the outer plasma region. The three detector arrays share a common secondary vacuum tube. As shown in Fig.2, all detectors, signal cables, pipes, etc. are housed in secondary vacuum tube connected to the closure flange through an access tube lip-welded to the flange. The beryllium windows form the boundary of secondary vacuum and sit behind slits. The internal camera tube is divided into 3 parts. The 1st part contains loading pad, slit parts and dovetail groove guide. The 2nd part, including support pad for loading detectors, cooling pipe and cables, is located on the loading pad with dovetail groove. The 3rd part consists of shielding shells to conserve secondary vacuum and shield neutron radiation. The 3rd part is welded with the loading pad conjointly forming the vacuum boundary. Besides, for the sake of thermal isolation, the material vespel is envisaged to cover the tube surface to preclude strong heat flux from entering the tube.

The detectors are housed in dedicated box for better EM shielding and easier cooling operation. Sandwich-like structure is used for better detector cooling. Theupper part is detector box, middle one is copper layer with cooling pipe, and bottom part is heat insulator layer employed to efficiently restrain the heat from the support pad. All cables running out from detector box are routed along the water tube for cooling. The cables will be considered to house in cable tray for better EM shielding.

For cooling, from the point of view of safety, the non-activated Chilled Water System (CHWS) with inlet temperature 6°C cannot be directly used for detector cooling [4]. A heat exchanger has to be used in which the cooling water in secondary loop of heat exchanger penetrates the closure flange into the detector tube in secondary vacuum. In the design of heat exchanger, cooling power in the secondary loop is an important parameter considering that the environment temperature around internal tube in baking mode is 240°C (±10°C) and all surfaces in contact with torus vacuum must reach at least 120°C [4].

For detector calibration, four channels of optical fiber transmitting light are arranged to illuminate the detector active surface. In order to measure detector background noise and heat drift, the first and last channels of each detector chip are blind. In addition, as the beryllium window which plays the role of vacuum sealing and light filtering is a critical component of RXC, two types of Be window have been designed and tested. The test result showed that for 80 μm Be foil with optical area of 60 mm×25 mm, both sides of two kinds of window assemblies can bear the pressure difference of one atmospheric pressure and 240°C (Ref. 5) baking for 2 hours [5]. The Be window tested is comparable (dimension, thickness, bonding technology) with the one foreseen on ITER diagnostic.

2.2. Design of external camera structure

The external camera system presented in Fig.1 contains double sealed flange, external camera chamber, beryllium window, three detector boxes located in one vertical plane and three detector boxes in another toroidally-shifted vertical plane. The LOS of six detector arrays together constitutes the LOS of whole external camera viewing central plasma. The toroidal shift arrangement of detectors is better for neutron shielding.

What deserves mention is that double Be window structure is envisaged for safety consideration.

Preliminary progress on this issue has been achieved. Several solutions on the external camera with standard flange and double window have been considered, two of which as shown in Fig.3 are probable solutions. In the left solution, the beryllium window is welded or bolted onto a vacuum flange which is connected to main vacuum extension tube, and there is a piece of bellows used to fix the alignment of external camera which is close to the camera flange. One or two supporting frame connected to the rear flange of the port plug will support the camera and be used to adjust the alignment. Note that beryllium window, flanges, bellows and chain clamp are part of secondary vacuum boundary. Compared with the first one, the main difference of solution 2 in the right of Fig.3 is that external camera flange is directly connected with Be window flange instead of through chain clamp flange.

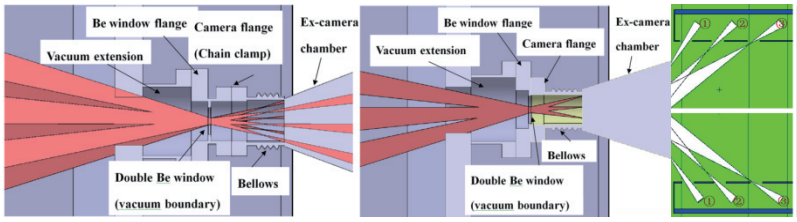

Fig.3 Beryllium assembly in the external RXC

Detector Location	Total Neutron Flux 1 ($n \cdot cm^{-2} \cdot s^{-1}$)	Total Neutron Flux 2 ($n \cdot cm^{-2} \cdot s^{-1}$)
Up-1	1.40×10^{8}	3.22×10^{6}
Up-2	3.36×10^{5}	1.37×10^{6}
Up-3	5.74×10^{5}	1.02×10^{6}
Down-1	1.84×10^{8}	2.36×10^{6}
Down-2	3.74×10^{5}	1.24×10^{6}
Down-3	4.36×10^{5}	8.91×10^{5}

Fig.4Neutronic analysis result of internal camera

3. Load analysis

Thermal analysis has been done for internal camera with a simplified model in which the whole support pad is copper layer and unconcerned parts such as slits are neglected. The absorbed energy of the whole structure is supposed equal to the heat flow, following which the temperature of the outlet of cooling water is got. Based on another two assumptions that the inlet temperature of cooling water is 35°C and the environment temperature during baking is 250°C, the analysis result has been acquired showing that the maximum temperature on the detector box is about 56°C which is within the detector operation temperature limit.

Acceleration analysis for external camera has been carried out as well for displacement and stress distributions under the condition of only gravity acceleration and 5 times gravity acceleration based on the assumed acceleration limit the external camera experiences. The results show that the maximum displacement is 0.22 mm and 1.33 mm for gravity accelerationand 5 times gravity acceleration respectively. The maximum stress is 21.92 MPa and 114.31 MPa respectively. The maximum stress is below the allowed threshold 122 MPa [6].

To ensure the silicon photodiode array in the RXC can survive in extremely strong neutron irradiation environment in ITER D-D, it is necessary to consider neutron shielding and evaluate the shielding efficiency during the camera structure design. By applying the standard neutronics analysis model provided by ITER organization, the neutron flux distribution of the camera is analyzed for D-D phase, and corresponding silicon photodiode detector lifetime of internal camera in D-D phase is estimated. The analysis result indicates that the detector closest to the plasma exceeds the damage limit 1.5×10^{13} n/cm^2/s (Ref. 7) in the end of D-D phase [4]. Therefore, it is necessary to optimize the camera model to satisfy the requirement of neutron shielding. In the optimization, the camera LOS is adjusted. The detector closest to the plasma is moved towards the closure flange. Besides, the space outside light path is filled with B4C material to enhance neutron shielding. The analysis results corresponding to detector locations are shown in Fig.4. “Flux 1” and “Flux 2” represent the flux before and after optimization respectively. It is seen that the neutron flux on camera detectors decreases by an order of magnitude for the two detectors closest to plasma. Consequently, the expected shielding requirement is achieved and it is believed that the detector can

survive in the whole D-D phase. It should be stressed that safety factor, i.e. uncertainty, has not been multiplied in Fig.4.

4. Function pretests on EAST tokamak

Two kinds of cameras have been tested on EAST tokamak for RXC Research and Development (R&D). The first one is to test new large-area detector for soft x-ray measurement in ITER and single detector located behind the diode array as blind channel. The active area of diode array detection unit is 12 mm × 2 mm and that of single detector is 14 mm × 14 mm. For the diode array, two adjacent channels are connected together to form a larger-area channel to test the feasibility. The gain of the amplifier used for photocurrent amplification is 10^7 and the bandwidth is 100 kHz. During experiments the camera with 8 channels works as steadily as that of normal EAST soft x-ray cameras used for physics study. The signal noise is about 50 mV which means 5 nA (50 mV divided by gain 10^7) noise on photocurrent signal (signal level can be as large as 100 nA or more) and the signal noise from other detector types is about 20 mV meaning 20 nA noise current because of gain 10^6.

The second one aims to explore the grounding scheme in tokamak environment similar to ITER and to explore the detector cooling scheme. Note that electronics is grounded by connecting with cryostatin ITER grounding scheme, while electronics of EAST normal soft X-ray arrays is isolated from cryostat. The basic features of this camera are: replaceable detector housing for future testing, test of cooling capability and JET-like grounding (electronics is also grounded by connecting with cryostat as ITER, but grounding scheme is more detailed) [4]. 24 channels of the detector are used for this camera. With a housing used for EM shielding, the detector, electrically isolated from the port, is installed inside a long tube with a flange connected and electrically isolated to the port flange and is close to the first wall through 4.3 m long vertical port. The detector cathode and cable shielding layer are directly electrically connected with the tube for grounding. The detector housing is connected with a copper plate with water pipe running through. The signal cables are attached around the outlet water pipe for cooling. The data acquisition system is isolated from electronics system with optical isolator.

During 180°C baking, the temperature around the detector can be as low as 30°C. As the tube is not electrically connected to the port flange, the noise amplitude is less than 50 mV observed through the acquired signal with amplifier 4×10^5 gain and 100 kHz bandwidth using differential circuit scheme. However, as the tube is connected to the port flange, the noise amplitude is about 100 mV, the cause of which is still under study. Besides, it is found the signal is susceptible to ICRF (Ion Cyclotron Resonant Frequency) disturbance. As ICRF is launched, the signal waveform is similar to ICRF waveform and disturbance amplitude can be as large as 0.5 V, which results in signal-noise ratio less than 1. This is probably due to the fact that the detector cathode is exposed to ICRF radiation through cathode-housing-tube connection. It is thought that another layer of shielding separated from the tube or disconnecting the cathode from the tube is needed to protect the detector cathode from direct ICRF exposure. A test is planned for the improved shielding scheme to confirm that the noise will be reduced. The test result will be consideredin the detailed design of ITER RXC EM shielding.

Instrumentation & control (I&C) has also been tested on EAST for various kinds of networks required by ITER RXC, for performance of I&C system in on-site complex EM environment, and for real-time data calculation and uploading. The test used full ITER type cubicle containing ITER type CPU chassis, I/O chassis, data acquisition (DAQ) cards, Control, Data Access and Communication (CODAC) system and Linux drive. The I&C system works steadily during EAST experiments. 46 signals are acquired withsampling rate 250 kHz which can be raised to 1 MHz for physical study. Synchronous Databus

Network (SDN) function is replaced by saving data function because of no SDN network available, where the DAQ card used is PXIe-6368 (Ref. 8) and the software environment is CODAC Core System 4.3. All data is transferred to the data server and saved in MDSPlus data format [9]. The response time is about 300 μs from triggering data acquisition to saving data including centroid computation. The test result implies that RXC I&C system can provide real-time data with quite short response time.

5. Summary

In summary, preliminary design of RXC has produced useful results. The beam path and neutron shielding have been optimized. The internal and external cameras are designed in detail with favored configuration for easier assembly and maintenance. It is proposed to use double beryllium window for safety instead of two valves in order to save space and facilitate operation and maintenance in the external camera. The structure analysis results for external camera indicated that even under 5 times gravity acceleration, the maximum stress was still below allowable stress. The neutronics analysis result indicated that the detectors can be operated during the whole D-D phase without detector replacement. In order to measure background noise and accommodate detector position error, the concepts of blind channel and overlap channels have been implemented in the design. Besides, two set of Be windows with good pressure-resistant performance have been designed and tested. The electronics and I&C group have also made good progress. The electronics group has carried out the design of pre-amplifier, main amplifier and communication and interface circuit. The test results of different circuit scheme indicated maximum noise level can be less than 10 nA.

These design provide solid basis for further RXC design: identification of all interfaces; solution of the space clash with other surrounding systems in the frame of Port Integration; optimization of the layout of cameras; confirmation of space allocation for candidate advanced detectors; etc. The design scheme of camera electronics will be improved and fixed with enough consideration of radiation hardness. The preamplifier will be placed in Port Interspace and main amplifier in Port Cell to reduce radiation dose absorbed. Two solutions have been envisaged to improve the lifetime of electronics in D-D phase: using radiation-hard amplifiers or shielding cabinet with a programmable amplifier interface and remote control function.

It is believed that the progress of RXC will push the setup of RXC prototype and determination of various interfaces at the earliest time, which will provide solid base for the future manufacturing.

Acknowledgements

Thanks to people in ITER Organization and other organizations or institutes supporting RXC design.Special thanks to Robin Barnsley, Antoine Sirinelli, Barry Alper and Michael Walsh.

Reference

[1] A. E. Costley et al, “Measurement Requirements and the Diagnostic System on ITER:Modifications Following the Design Review,”*22nd IAEA Fusion Energy Conference*, Geneva, 2008.

[2] S. Wang et al., “Electromagnetic behavior on ITER radial soft x-ray camera,”*2013 IEEE 25th Symposium on Fusion Engineering (SOFE)*, San Francisco, 2013.

[3] G. Vayakis et al., “Current status of ITER diagnostics development,”*26th ITPA Spring Meeting*, Pohang, 2014

[4]L. Hu et al., “Progress on the ITER Diagnostic-Radial X-Ray Camera”,*25th IAEA Fusion Energy Conference*, Saint Petersburg, Russian Federation, October 13-18, 2014, FIP/P4-2.

[5]Z. Chen, et al.,Fusion Eng. Des.**88**(2013)3280.
[6] ASME Boiler and Pressure Vessel Committee on Materials, *2013 ASME Boiler & Pressure Vessel Code*, Vol. II, Part A, p. 360-390, TheAmerican Society of Mechanical Engineers, New York, NY (2013).
[7]B. Alper, et al.,Rev. Sci. Instrum.**68** (1997) 778.
[8] PXIe-6368, http://sine.ni.com/nips/cds/view/p/lang/en/nid/209218.
[9] MDSplus, http://www.mdsplus.org

ECH system performance in KSTAR 2015

Sangwook Jung[a], M. Joung[a], J.H.Jeong[a], S.J.Wang[a], J. W. Han[a], J.G.Gwak[a], Y. K. Oh[a], K. Sakamoto[b], K. Kajiwara[b], Y. Oda[b], J. Hosea[c], R. Ellis[c]

[a] *National Fusion Research Institute, Daejeon, Korea*
[b] *Japan Atomic Energy Agency, Naka, Japan*
[c] *Princeton Plasma Physics Laboratory, Princeton, USA*
Email: woogijung@nfri.re.kr

1. Introduction

ECH systems of the KSTAR firstly are used for assisting reliable start up and flux saving by on-axis heating. And the systems are also used for various physics experiments: MHD instability control, steady state operation, particle transports, impurity control, and etc. To try those experiments, there were two ECH systems in this year's campaign: one was 110 GHz Gyrotron system, and the other was 170 GHz Gyrotron system. 110 GHz Gyrotron system can inject 0.3 MW of microwave for 2 sec. This was usually used assisting start up of plasma. 170 GHz system can inject around 1 MW of microwave for 50 sec from 2.3 T to 3.5 T of torodial magnetic field. The 170 GHz system was used assisting start up, on- and off-axis heating and current driving for instability control. The 110 GHz system's operation have been finished in this year's campaign. From next year campaign, a new gyrotron system will be launched for the KSTAR. The gyrotron has two operation frequencies, 105 GHz and 140 GHz. The system can inject 1 MW of microwave for 300 sec into the KSTAR. In order to inject high power up to megawatt and long pulse, active cooled launchers were installed for two systems.

A ECH system in KSTAR have been operated since 2008. In 2008, 84 GHz, 0.1 MW gyrotron was used for pre-ionization and assisting start up. In 2009, 110 GHz, 0.3 MW gyrotron had launched and operated for assisting start up. At 2011, 170 GHz, 1 MW gyrotron system operation was started. The ECH systems of KSTAR has gradually been increasing the power from 0.1 MW to 1 MW. In last year's campaign, we had success to inject EC wave for 41sec. And in this year, the wave injection duration was enhanced to 50 sec.

2. Experimental result

There are two methods to make high quality plasma with a ECH system. One is injecting EC power as much as possible. And the other is to make EC waves absorbed into a plasma as much as possible. In order to increased the injection power, one makes RF source's power increased. But the power is not possible to increased infinitely. The output power is limited by vacuum power tubes performances. And the other method is an increasing transmission efficiency. But waveguide's materials have their own resistance, so the RF made from a gyrotron has lost their power during transmitted to a plasma. Those things can't approve a plasma quality by limitation of increasing injection power. The other way is enhancing absorption efficiency. The method of changing absorbing efficiency is polarization angle control. Effective polarization angle is easily calculated by ray tracing codes.

The injection polarization angle was controlled by the use of polarizer system. There

are two miter bend components. The polarizers are different sinusoidal grooved mirror. To array in series, accurate polarization and ellipticity are obtained. There were five shots to compare absorbing efficiency. Every shot had varied the polarization angle from -0.96° to 90°. Polarization angle and ellipticity was calculated by ECHres code. X-mode was expected at -0.96° of the angle and -0.45 of ellipticity, and O-mode was expected at 90° of the angle and -0.45 of ellipticity. Other two shots are 30°, 45° of angle with same ellipticity. Another one is same angle with X-mode but different ellipticity, 0 of ellipticity. From ECE 48 signals, the plasma temperature variations were obtained. Highest temperature was found when calculated X-mode. Second harmonic X-mode EC power of 550 kW increased ECE intensity by 25% than O-mode.

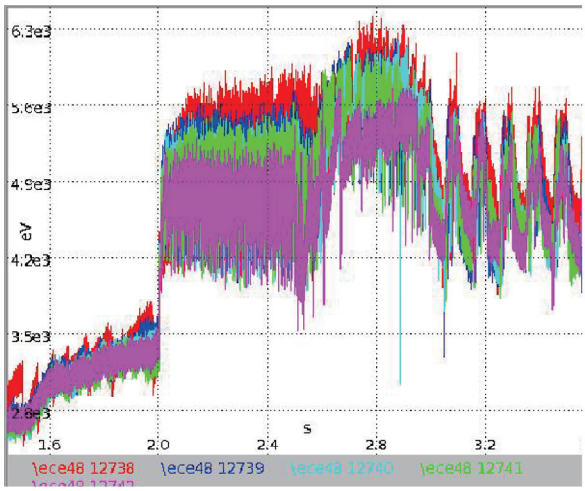

Figure 1. ECE intensity data

In last year's campaign, long pulse injection, 41 sec, had been succeeded. The active cooling launcher is an important component to inject long pulse. In 2014 campaign, temperature of two mirrors on launcher was saturated at around 20 sec after starting shot. The temperature saturation was observed from difference temperature between input and output water. The saturated difference is 2.4°C at fixed and steerable mirrors. From 2014 campaign's results, the active cooling launcher is adaptable for CW operation. In this year's campaign, long pulse injection for 50 sec was succeeded. In this year's long pulse operation, two launcher mirrors saturated temperature differences are 2.8°C at fixed mirror and 3.6°C at steerable mirror. Because steerable mirror's temperature difference is higher than before, flow rate of coolant is slower than 2014 campaign. To prevent damage to welded inlet and outlet bellows due to excessive pressure, the rate was decreased. The welded bellows was adopted to improve steering speed.

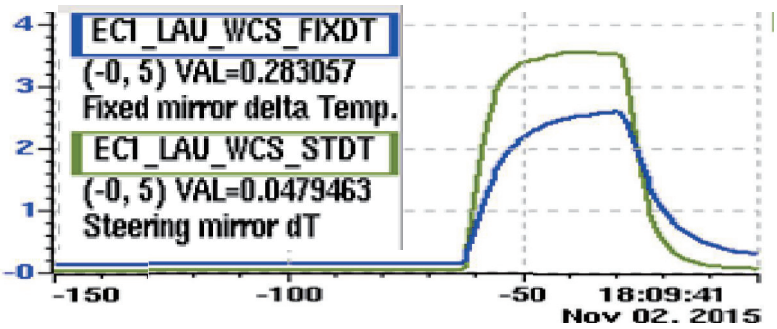

Figure 2. Laucher mirrors' temperature difference

3. Upgrade plan

The 110 GHz ECH system operation had been finished in 2015. A new ECH system will be operated for KSTAR campaign. A new gyrotron is installed in the heating room of the KSTAR building. The gyrotron has two operating frequencies: 105 GHz and 140 GHz. It can inject 1MW of EC wave into the KSTAR for 300 sec. EC wave from the gyrotron will be transmitted by corrugated waveguide and figure 3 is a schematic of the new ECH system from the gyrotron to KSTAR tokamac. The EC wave will be transmitted by corrugated waveguide. Table 1 was expected transmission efficiency and injection power. The expected efficiency is 87% at 105 GHz and 85% at 140 GHz. The output power of the gyrotron is 0.8 MW at 105 GHz and 0.95 MW at 140 GHz. Consequently, the expected injection power is 696 kW at 105 GHz and 808 kW at 140 GHz. Because the new system uses same port with 110 GHz system, the waveguide was changed from ϕ31.75 mm to ϕ63.5 mm to enhance transmitted microwave power capability. A cathode power supply can apply -55 kV and 50 A. Its modulation frequency is up to 60 Hz. A body power supply can apply 40 kV and 150 mA. It can modulate up to 5 kHz.

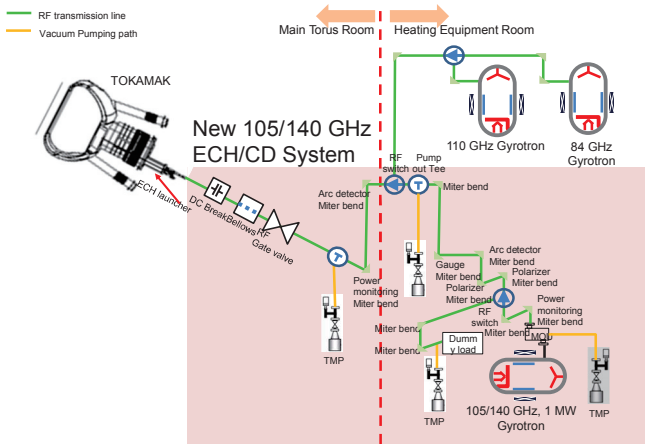

Figure 3. Schematic of the new 105/140 GHz ECH system.

Table 1. Expected injection power of the new ECH system

Frequency (GHz)	105	140
Output power after gyrotron window (kW)	800	950
Output power after MOU (kW)	750	900
Transmission efficiency without miter bend offset angle and misalignment (%)	91	92
Expected transmission power without misalignment (kW)	728	875
Offset angle loss at miter bend (%)/typcally 1.5mrad	4.39	7.71
Transmission efficiency with misalignment (%)	87	85
Expected transmission power with misalignment (kW)	696	808

Now, we are developing new launchers. To protect from heat, the launchers' cooling channel should be made as close as possible. To make complicated cooling structure, metal 3D printing technique is applied. The launcher mirror was imported from PPPL in this year. The launcher will be installed for 2016 KSTAR campaign. KSTAR have a plan which is to enhance ECH injection power up to 6 MW. A part of the plan is a two channel launcher. The launcher can inject 2 MW of EC wave by connected with two gyrotrons.

LHCD study toward to high performance plasma in EAST

B J Ding, for EAST Team and collaborators

Institute of Plasma Physics, Chinese Academy of Sciences, Hefei 230031, P R China

Abstract

A 4.6 GHz lower hybrid current drive (LHCD) system has been firstly commissioned in EAST in 2014 campaign. Effect of turbulence on plasma-coupling and the comparison between 2.45 GHz and 4.6 GHz are compared, suggesting a better coupling for 4.6 GHz LHW. Studies show that compared to H-mode, the plasma-wave coupling indicated by the mean reflection coefficient is better in the case of L-mode plasma, suggesting the lower density in the case of H-mode. Compared to 2.45 GHz LHW, 4.6 GHz LHW has a better capability on current drive, plasma heating, confinement improvement, modifying current profile, possibly due to less parametric instability in this case.

1. Introduction

Lower hybrid current drive (LHCD) [1–3] plays a key role in controlling current profile in tokamak experiments aimed at achieving important goals relevant to fusion plasma. Lower hybrid wave (LHW)-plasma coupling and current drive (CD) at high density, related to turbulence, are two important issues in achieving lower hybrid current drive (LHCD) high confinement plasma. In fusion plasmas, intermittent density fluctuations were observed in nearly all the devices where Langmuir probe measurements were performed. The statistical properties of the turbulent signals in four different type devices (Tore Supra with circular cross-section limiter-bounded plasma [4], Alcator C-Mod with a divertor configuration [5], MAST with vacuum chamber walls far from the plasma last closed flux surface [6] and the PISCES linear plasma device [7]) are found to be identical allowing to conclude that intermittent convective transport by avaloids is universal in the sense that it occurs and has the same properties in many confinement devices with different configurations[8]. Since density fluctuation is edge region will affect the grill density, the LHW-plasma coupling is easily to be influenced by such burst behaviour. Also, it is reported [9-12] that the density fluctuations has some effect on wave propagation and current drive capability. In turn, it could be possible that the LHW may affect the turbulence. In Tore-supra, study [13] shows that the effect of ICRH on turbulence takes place in the vicinity of the active antenna but not necessarily magnetically connected to it. In addition, how to improve the CD capability at high density is a challenge, including looking for a suitable condition for good CD effect.

In EAST, both 4.6 GHz/6 MW and 2.45 GHz/4 MW LHCD system have been installed. Related experimental results at high density have been reported in Refs [11, 12, 14-19]. Since LHW-plasma coupling and LHW propagation are both related with LHW frequency, it is necessary to investigate the related physics with these two systems.

2. Relationship between fluctuation and coupling

As we know, density profiles in front of the LHW launcher are the important factors affecting the

LHW-plasma coupling characteristics [20-23]. Such density is affected by the turbulence and edge localized mode (ELM) behaviour, since they will give rise to the increase of edge density. To investigate the LHW-plasma coupling, the probability distribution function (PDF) of reflection coefficient (RC) and raw ion saturation signals, showing a statistics property of the coupling and density fluctuation, are utilized. Investigating the PDF's of turbulent fluctuations in general was emphasized by the Kolmogorov article, often called K41 [24], in which he assumed that fluctuations are random. Because the PDF of a random variable is Gaussian, it was rather straightforward to check this hypothesis by mainly using the normalized third order moments of the fluctuating signal. For a signal denoted by x, the skewness factor is defined as $\langle x^3\rangle/\langle x^2\rangle^{3/2}$ and is equal to 0 for a Gaussian distribution reflecting its symmetry around the average value. Figure 1 is the typical plasma wave form of 4.6 GHz LHCD, including L-mode, ELMy H-mode and ELM-free mode. The PDF of RC in the above three modes are plotted in Fig. 2. It is shown that the averaged RC (<RC>: around the peak value of RC) in L-mode is lower than that in H-mode, implying better coupling in L-mode discharge. Though the averaged RC are very similar for the ELMy and ELM-free plasma, the little difference in skewness is still observed. The positive value means the counts of distribution in the range of RC> <RC> is higher than that in the range of RC <<RC>, whereas the negative valve means the opposite behaviour. This suggests that ELMy behaviour leads to the increase of grill density compared to the ELM-free case.

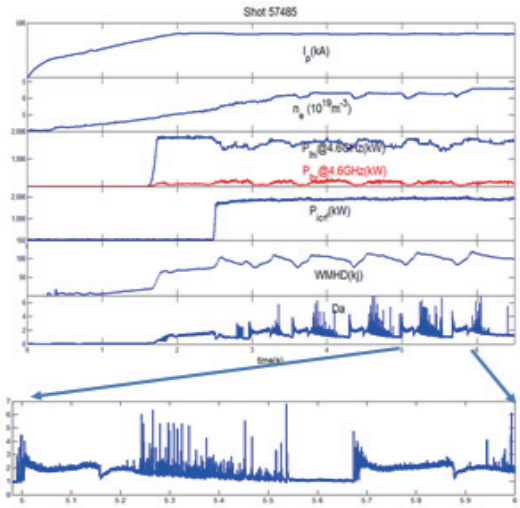

Fig. 1 Typical LHCD H-mode waveform

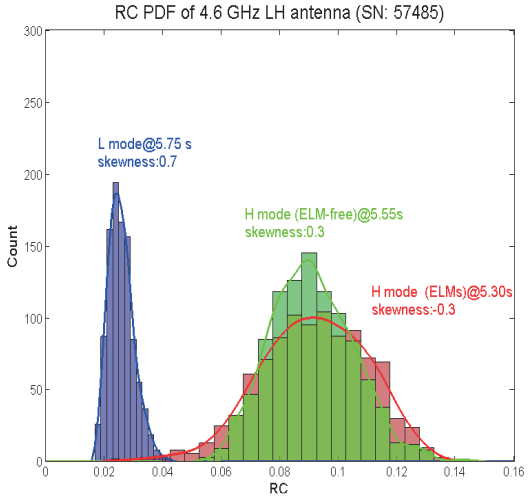

Fig. 2 PDF of RC

Figure 3 shows the PDF of raw ion saturation current reflecting density fluctuation measured by Langmiur probes installed at the mouth of LHCD antenna. It is seen that in L-mode and ELMy plasma, an obvious positive skewness is observed, meaning a strong deviation from Gaussian distribution at the positive fluctuation. Also, a longer tail in the positive part in ELMy plasma, suggesting ELM leads to the density increase with the burst. In addition, in the ELM-free plasma, the PDF is very close to Gaussian distribution, implying less 'blob' compared to the other two cases.

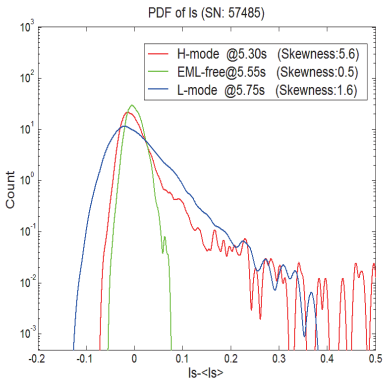

Fig. 3 PDF of ion saturation

3. LHCD characteristic comparison between 4.6 GHz and 2.45 GHz LH waves

Many parameters may affect LHCD effect, such as wall condition, magnetic configuration, target plasma, and so on. In order to rule out such effects, two different frequency waves with the same power (P_{LH} = 1.05 MW) were injected successively in one discharge with almost constant density ($n_{e\_av} = 2.0 \times 10^{19} m^{-3}$) and the typical waveform are shown in Fig. 4. It is seen the difference in residual voltage (V_{loop}) and ECE super-thermal T_e is obvious between two waves, which definitely justifies better CD efficiency for 4.6 GHz waves. The residual voltages are 0.49 V and 0.36 V respectively for current drive with 2.45 GHz and 4.6 GHz. Better plasma heating effect for 4.6 GHz can be obtained from the time evolution of plasma stored energy (W_{MHD} ~ 68.3 kJ and 74.8 kJ, respectively for 2.45 GHz and 4.6 GHz). Also, the internal inductance is higher with the 4.6 GHz LH wave injection, meaning the peaker power deposition. This is in agreement with the line integrated measured HXR profile (Fig. 5). The plasma rotation is observed during LHCD application. For similar power input, measurements show larger rotation change with 4.6 GHz. Seen from the IR picture shown in Fig. 6, the bright belt is observed in the bottom of the divertor for both 2.45 GHz and 4.6 GHz LHW plasma and the brightness with 4.6 GHz is stronger. Such belt should not be the hot spot since the belt is symmetric in toroidal direction. The temperature induced from IR is also shown in Fig.4, showing higher temperature with 4.6 GHz LHW, possibly due to larger stored energy and stronger heat transport. A comparison of frequency spectra between two waves is illustrated in Fig. 7, from which it is seen that more significant broadening occurs for 2.45 GHz case, indicating stronger PI behaviour. This possibly explain the better CD effect with 4.6 GHz LH wave.

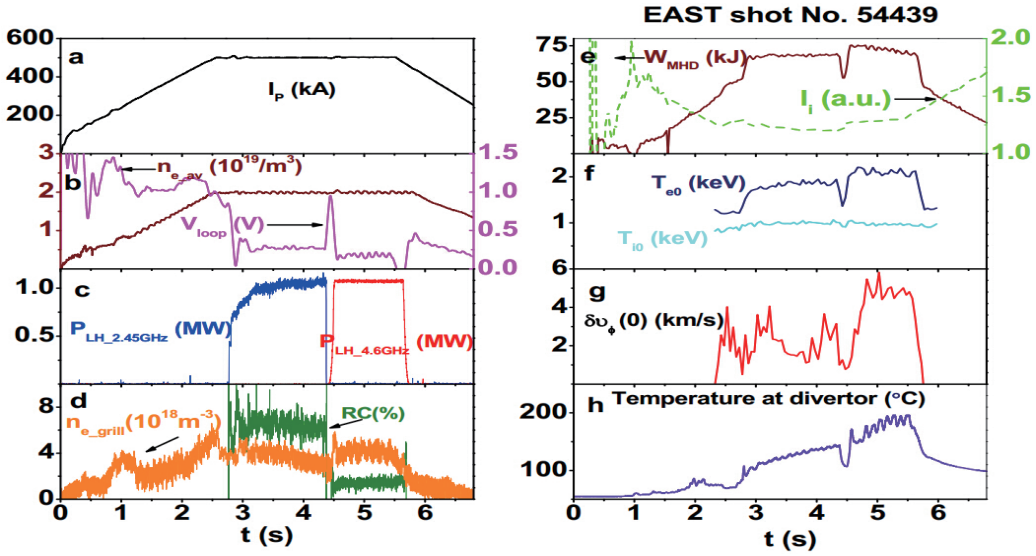

Fig .4 Typical waveform for comparison 2.45 and 4.6 GHz LHCD characteristic

The PDF of the RC is plotted in Fig. 8, showing that the averaged RC with 4.6 GHz is lower and the coupling is better, which is in agreement with the RC shown in Fig. 4. Though this is conflict with the lower density requirement for coupling with higher frequency, which is indicated by a cut-off density determined by $n_{e,co} = (\omega^2 m_e)/(4\pi e^2)$, where /ω/ is the wave frequency, /m/$_e$ is the electron mass and /e/ is the electron charge, it is in agreement with the higher grill density with 4.6 GHz LHW measured by

Langmuir probe, possibly implying the stronger ionization capability of 4.6 GHz LHW. The distribution is almost Gaussian, which is different from shown in Fig.2. The possible reason could be different experiment conditions.

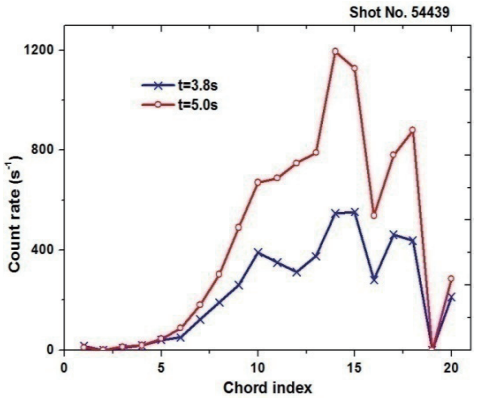

Fig. 5Line integration of HXR

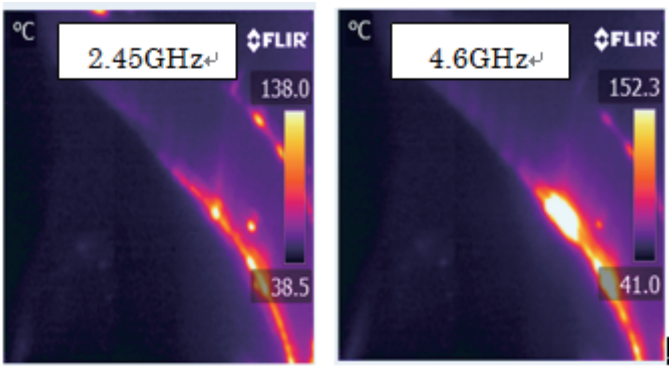

Fig. 6 IR picture of the divertor

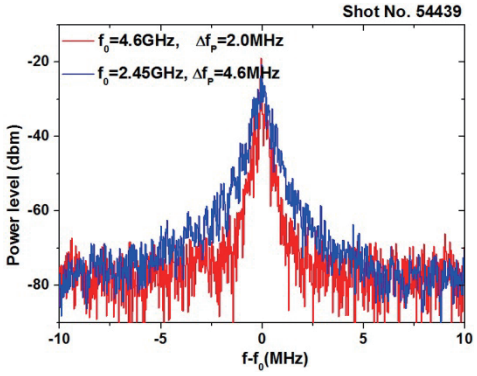

Fig. 7 PI signal by RF antenna

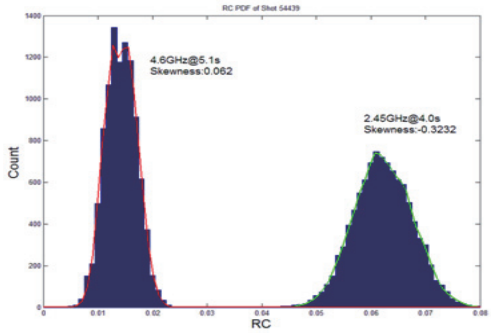

Fig. 8 PDF comparison of RC

Next, we would like to investigate the dependence of CD capability on the line averaged density with the two frequency wave. Usually, hard X-ray (HXR) from fast electrons generated by LH waves is taken as a significant feature of the LH driven current and the HXR count rate can also be taken as a proxy for the density of the fast electron. Although the CD efficiency cannot be obtained quantitatively from the HXR count rate, we can use it to assess the relative change of CD efficiency. Unfortunately, the hard X-ray results for the 4.6 GHz case are not available. Therefore, we use the non-thermal ECE instead, which is also sensitive to fast electrons, since they are both available for the cases and the trends of dependence of HXR and ECE temperature on the density are almost same with 2.45 GHz LH plasma, which can be seen in Fig. 9. It is seen that the variations of both HXR count rates and ECE temperature conform to the 1 / n_{e_av} scaling with the density smaller than 2.0×10^{19}m^{-3}, but for higher density they fall much more steeply than 1 / n_{e_av} indicating anomalous loss of CD efficiency. First of all, it must be pointed out that during the density ramped up, the accessibility condition is satisfied, because of the sufficiently high values of launched refractive index ($N_{//0}$ = 2.1) and toroidal magnetic field (B_t = 2.3 T). For the case of 4.6 GHz, the ECE temperature does not drop quickly until up to density of 2.0×10^{19}m^{-3}. Results clearly show that, with 4.6 GHz LH wave, the density at which the fast electron emission deviates from the curve of 1/n is larger

than that with 2.45 GHz, implying better CD effect of 4.6 GHz. It can be also seen that the difference in current drive between two waves becomes more significant with density increasing.

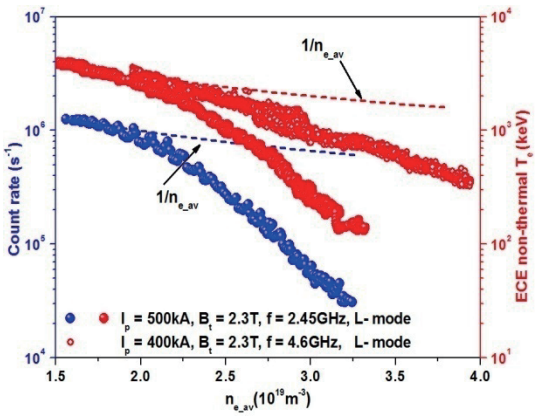

Fig.9 Normalized HXR counts and ECE temperature as a function of density

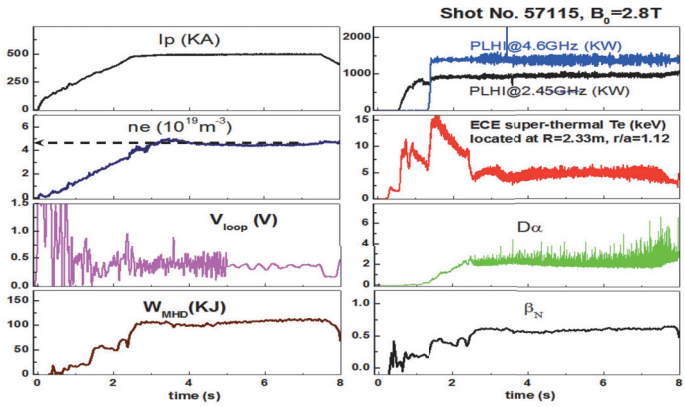

Fig.10 Typical LHCD H-mode plasma at high density

By means of 4.6 GHz and 2.45 GHz LHCD system, H-mode plasma is obtained at relatively high density. The typical wave form is shown in Fig.10 Seen from ECE, even if at n~4.5 × 10^{19}m^{-3}, part of current is driven by LHW since ECE could come from the fast electron emission generated by LHW.

Next we would like to roughly compare the effect of LHW on confinement with the two systems. It is analyzed by investigating the effect of LH power on stored energy and the results are shown in Fig.11, in which $P_{tot} = P_{OH} + P_{LH\text{-}2.45} + P_{LH\text{-}4.6} + P_{ICRH}$. It is seen that, for a same injected power, the stored energy decrease with increasing $P_{LH\text{-}2.45}$, whereas for the case of 4.6 GHz, it seems opposite, or at least the stored energy doesn't decrease with increasing $P_{LH\text{-}4.6}$. This implies 4.6 GHz LHW has a better effect on confinement than 2.45 GHz one.

Since PI behaviour is less with 4.6 GHz LH wave, such PI behaviour could be responsible for the lower CD effect with 2.45 GHz LH wave. Therefore, high LH frequency wave is preferred in the LHCD experiment at high density.

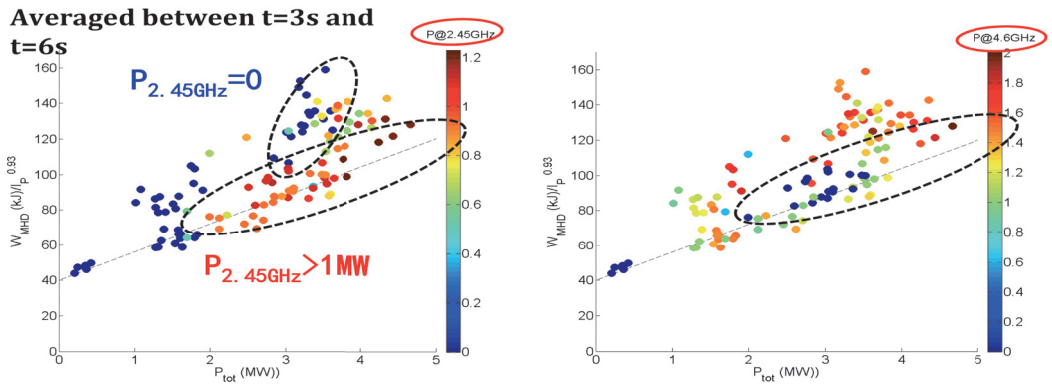

Fig. 11 Dependence of stored energy on LH power variation ((a) 2.45 GHz, (b) 4.6 GHz)

Conclusions

Effect of turbulence on plasma-coupling and the comparison between 2.45 GHz and 4.6 GHz are

compared by investigating the statistics property of RC and ion saturation, suggesting a better coupling for 4.6 GHz LHW. Studies show that compared to H-mode, the plasma-wave coupling indicated by the mean reflection coefficient is better in the case of L-mode plasma, suggesting the lower density in the case of H-mode. Results show that, compared to 2.45 GHz LHW, 4.6 GHz LHW has a better capability on current drive, plasma heating, confinement improvement, modifying current profile, being nearly in agreement the less parametric instability in this case.

Acknowledgements:

This work is supported by the National Magnetic Confinement Fusion Science Program of China (Grant No. 2015GB102003, 2013GB106001, 2013GB112003), the National Natural Science Foundation of China under Grant No. 11175206, 11305211 and 11275233, Hefei Science Center CAS (2015HSC-UE005), and the JSPS-NRF-NSFC A3 Foresight Program in the field of Plasma Physics (NSFC No. 11261140328). It is partly supported by the China-France Collaboration program.

References:

[1] N. J. Fisch, Phys. Rev. Lett. 41 (1978) 873.

[2] S. Bernabei, et al Phys. Rev. Lett. 49 (1982) 1255.

[3] N. J. Fisch, Rev. Mod.Phys. 59 (1987)175.

[4] Tore Supra Team, Nuclear Fusion, 40 (2000) 1047

[5] B. LaBombard, et al., Phys. Plasmas 8 (2001) 2107

[6] A. Sykes, et al., Phys. Plasmas 8 (2001) 2101

[7] D. Geobel, et al., Rev. Sci. Istrum. 56 (1985) 1717

[8] Y. Ghassan, et al., Phys. Plasmas 10 (2003) 419.

[9] Y. Peysson, J. Decker, L. Morini, et al Plasma Phys. Contr. Fusion 53 (2011) 124028.

[10] P. T. Bonoli and E. OTT, Phys. Fluids25 (1982) 359.

[11]B J Ding, et al., Nucl. Fusion 53 (2013) 113027.

[12] B J Ding, et al., Nucl. Fusion 55 (2015) 093030.

[13] G.Y. Antar, M. Goniche, A. Ekedahl and L. Colas, Nucl. Fusion 52 (2012) 103005.

[14] F K Liu, B J Ding, et al., Nucl. Fusion 55 (2015) 123022

[15] B.J. Ding, et al Phys. Plasma 19 (2012) 122507

[16] B. J. Ding. et al Phys. Plasma 18 (2011) 082510

[17] L.Zhang, et al Phys. Plasma 20 (2013) 062507

[18] E.H. Kong, et al Plasma Phys. Control. Fusion 55 (2013) 065008

[19] M. H. Li, et al Phys. Plasmas 21 (2014) 062510.

[20] J. Stevens, et al Nucl. Fusion 21(1981) 1259.

[21] M. Preynas, et al Nucl. Fusion 51 (2011) 023001.

[22] M. Brambilla, Nucl. Fusion 16 (1976) 47.

[23] M. Preynas, et al Nucl. Fusion 53 (2013) 013012

[24]A. N. Kolmogorov, C. R. Acad. Sci. URSS 30 (1941) 301.

Preparation and improvement for NBI system to LHD deuterium experiment

K. Tsumori[1,2], M. Osakabe[1,2], K. Nagaoka[1,2], K. Ikeda[1], M. Kisaki[1], H. Nakano[1,2]
O. Kaneko[1,2], and Y. Takeiri[1,2]

[1]National Institute for Fusion Science, Toki 509-5292, Gifu, Japan

[2]SOKENDAI (Graduate University for Advanced Studies), Toki 509-5292, Gifu, Japan

Abstract

Preparations for two positive-ion- and three negative-ion-based neutral beam injectors (NBI) start to adjust the beam specification for LHD deuterium experiment. One of the positive-ion-based NBI (p-NBI) is increased the maximum beam energies from 40 keV to 60 keV and another one 60 keV to 80 keV. Injection powers are expected to increase from 6 to 9 MW. On the other hand, the negative-ion-based NBI (n-NBI) beamlines are not upgraded the beam energies and the current density of deuterium negative ion (D^-) becomes $1/2^{1/2}$ times lower than that of hydrogen negative ion (H^-) due to Child-Langmuir's law at the same accelerator configurations and energies. In order to improve the injection power, an accelerator with multi-slot grounded grid (MSGG), which is installed the negative-ion-based NBI #1 and the maximum injection power is ~7 MW, will be adopted for the other two n-NBI systems. Active caesium (Cs) control and suppression of co-extracted electron are also considered for n-NBI ion sources.

1. Introduction

Neutral Beam Injector (NBI) is a reliable and powerful device for plasma heating and current drive [1-4]. NBI has also contributed to investigate the plasma physics in fusion plasma machines [5-8]. Due to the reliability NBI systems are planned to install in ITER as the main heating devices [9]. In National Institute for Fusion Science (NIFS), two p-NBI systems and three n-NBI ones are installed at the Large Helical Device (LHD). Energy of neutral beams provided with the p-NBIs are 40 keV and injected beams heat background ions confined in LHD with the ion heating ratio of ~50 %. On the other hand, the n-NBIs have provided neutral beams with higher energy of 180 keV to play important roles to generate peaked temperature profile to generate high ion temperature plasmas [10]. Because of the beam energy, the negative-ion-based beams have also contributed to increase the β value and density in super-dense core plasma [11].

Deuterium plasma experiment is the next plan to improve the plasma performances of LHD. The mission values of ion temperature, plasma β and the plasma triple product are 10 keV, 5 % at troidal field strength of 1 T and 1 x 10^{20} m^{-3}•keV•sec. In order to achieve those mission values, upgrading modifications to NBI systems are required. In this article, we describe the upgrades to the deuterium experiment are described.

In following sections, we describe introduction of NIFS NBI systems, the influences of mass difference to form hydrogen and deuterium ion beams due and improvement to keep the injection power of negative-ion-based NBI.

2. LHD NBI Systems

Figure 1 shows a schematic of LHD NBI systems, which are three tangential n-NBI and two perpendicular p-NBI systems. The nominal values of beam energies and powers are 40 keV and 6 MW for p-NBI and 180 keV and 5 MW for n-NBI, respectively. All the systems have successfully achieved those design values in LHD hydrogen-plasma experiment. As the next step of LHD project, deuterium-beam injection is scheduled for LHD NBI. The beam energies of two p-NBIs are enhanced from 40 keV up to 60 and 80 keV to increase the p-NBI beam power. On the other hand, the energies of n-NBIs is planned to keep the present values of 180 keV.

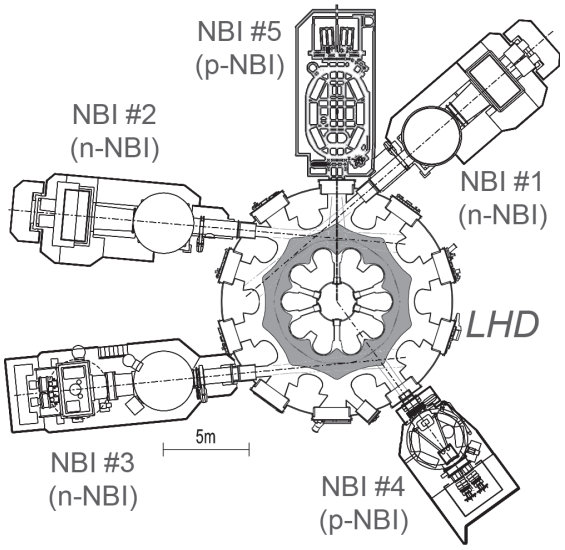

Fig. 1. Schematic view of p-NBI and n-NBI configurations from upper side of LHD. Three tangential beamlines of n-NBI and two perpendicular p-NBI are installed.

The ion and electron heating rates of p- and n-NBI are indicated in Fig. 2 [12] with respect to the ratio of beam energy to critical one. The symbols of "H-H", "D-D" and "D-H" in brackets show "hydrogen beam into hydrogen target plasma", "deuterium beam into deuterium target plasma" and "deuterium beam into hydrogen target plasma", respectively. As shown in this graph, the ion heating rates of p-NBI with the energy of 40 keV (H-H) to that of 60 keV (D-D) increase from ~50 % to ~65 %. The ratio reaches ~80 % with the condition of 60 keV (D-H). By keeping the energy of n-NBI beams for deuterium injection, the ion-heating rate increases from ~32 % (H-H) to ~35 % (D-D) and ~50 % (D-H). In hydrogen-beam injection into D plasmas, more ion-heating efficiencies can be obtained in both cases of p-NBI and n-NBI. By increasing the energy of p-NBIs, the injection powers are expected to increase from 6 MW to 9 MW. Improvement of ion-heating efficiencies and increase of p-NBI power are considered to achieve the ion temperature of 10 keV. In addition, plasma confinement is possible to be improved owing to isotope effect in deuterium plasma.

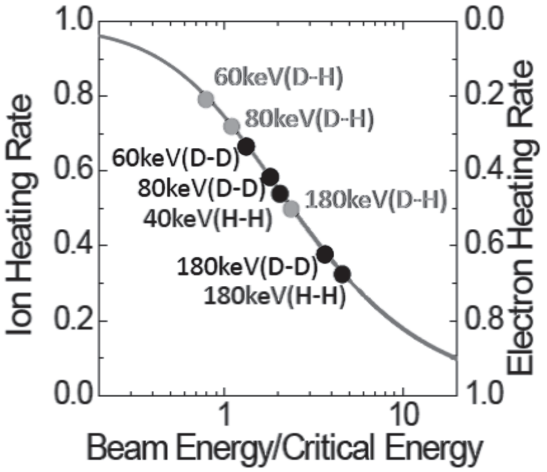

Fig. 2. Ion and electron heating rate with respect to the ratio of beam energy to critical energy. The rates are indicated for p-NBI with the beam energy of 40, 60 and 80 keV in the condition of (H-H) H beam into H target plasma, (D-D) D beam to D target plasma and (D-H) D beam to H target plasma. The energy of n-NBI will be kept at 180 keV [12].

3. Difference of Hydrogen and Deuterium Beams

Ignoring the difference of plasma flux toward beam extraction region, the largest difference of beam

formations of hydrogen and deuterium ions appears in the mass term of Child-Langmuir's law as shown in eq. (1).

$$J_i = \frac{4}{9}\sqrt{2e/m_i}\,\frac{E_{ext}^{3/2}}{d_{ext}^{1/2}} \tag{1}$$

where, J_i, e and m_i are ion current density, elementally electric charge and ion mass, respectively. E_{ext} and d_{ext} are the electric field to extract ion beam and the electrode gap, respectively. In the same extraction field and gap, the current density of deuteron beam becomes $2^{-1/2}$ times smaller than that of proton due to $m_i^{-1/2}$ term in eq. (1). In the case of the positive ion source, the reduction can be compensated with decreasing the extraction gap and/or with increasing the strength of extraction field, E_{ext} by enhancing the extraction voltage. Margin of the voltage holding capability during beam extraction is not so large, and frequent voltage breakdowns are expected in the extraction electrode gap too shorter than the present configuration. Beam energy of NBI #4 is set from 40 to 60 keV and the electrode gap is fixed 6 to 8 mm. The energy and gap of NBI #5 is increased to 80 keV and 8 mm, respectively.

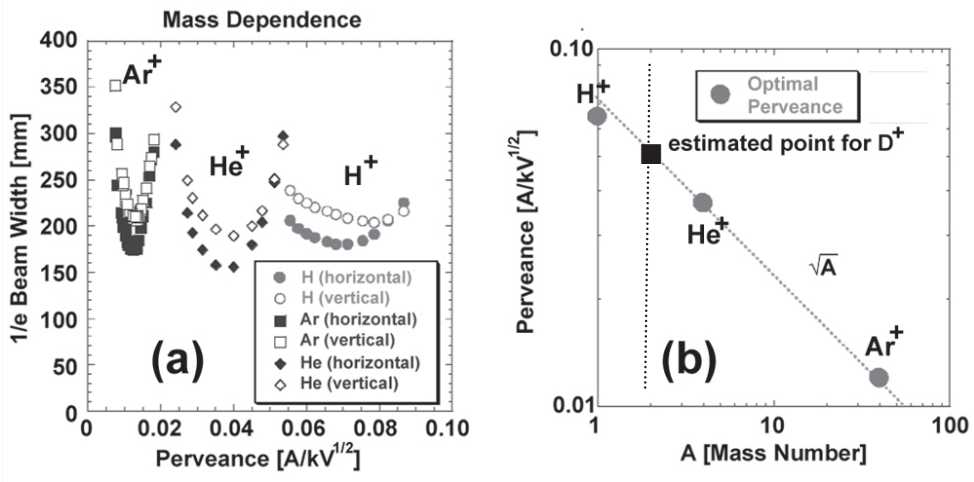

Fig. 3. (a) Perveance dependence of 1/e beam widths of H^+, He^+ and Ar^+. Horizontal and vertical widths are indicated with filled and open plats, respectively. (b) Optimal beam widths of H^+, He^+ and Ar^+ beams. Estimated point for D^+ is shown as a plot of "■" [13].

Mass dependence of optimal beam width is related to perveance matching and it is necessary to confirm. Perveance dependences of 1/e beam widths of H^+, He^+ and Ar^+ beams are shown in Fig. 3(a), and the minimal beam widths corresponding to the optimal perveances with respect to ion mass numbers are indicated in Fig. 3(b) [13]. The optimal perveances are almost on a line except for H^+, which is involving the influence of molecular ions. Estimated point of D^+ is shown as "■" in the figure.

4. Deuterium-Negative-Ion Beams

Negative ion extraction is subject to Child-Langmuir's law as well as positive ion beam. The beam energy of D^- is fixed at present value of 180 keV to improve ion-heating ratio, and thus D^- current is required to enhance to obtain higher injection power. Increase the extraction electric field by reducing the gap distance is one of the methods to increase the D^- current density. This method, however, is not applicable due to the following reason. Accelerator of n-NBI consists of plasma grid (PG), extraction grid

(EG) and grounded grid (GG). When the extraction field (E_{ext}) is increased to enhance the D^- current density, acceleration field (E_{acc}) need to be proportionally increased to satisfy the beam focal condition indicated in eq. (2).

$$E_{acc} / E_{ext} = const. \quad (2)$$

The field strength of E_{acc} is more than 2.5 kV/mm at present and it is considered close to a limit of voltage breakdowns at the electrode gap between EG and GG.

Additionally, it has been described in some articles that current ratio of co-extracted electron decreases in D^- extraction [14, 15]. The reduction of D^- current due to mass difference and increase of co-extracted electron current is necessary to be solved simultaneously. Experiments to investigate those problems are scheduled to achieve with following three subjects.

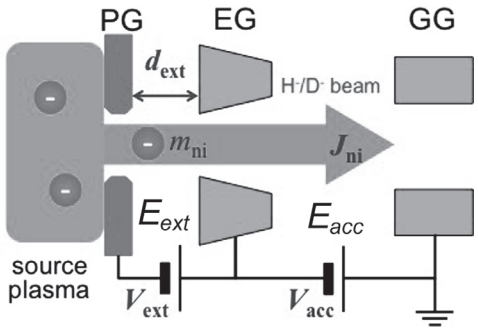

Fig. 4. Schematic view of beam acceleration of negative ion source.

（a） Adoption of the beam accelerator with multi-slot grid installed in NBI #1 to NBI #2 and 3,

（b） Improvement for Cs recycling by heating side and back-plate walls to enhance D^- current.

（c） Enhancement of magnetic field on the plasma side of PG using ferromagnetic materials.

Concerning the first item, the maximum injection power of 6.9 MW has been obtained for 1.6 sec. using NBI-#1 sources installed an accelerator with multi-slot grounded grids (MSGG) [16]. The NBI can inject stable beams with the power of 6.4 MW for H^- beam acceleration per beamline, and total injection power of 13.6 MW (3 beamlines x 6.4 MW / $\sqrt{2}$) can be obtained by replacing the conventional accelerators with multi-rounded aperture grounded grid of NBI #2 and #3 to those with MSGG. Beam experiment with replacing the accelerator has been carried out with use of NBI #3. As the result, conditioning time for voltage holding and beam extraction are reduced. The arc efficiency, which is defined as a ration of extracted H^- current to input discharge power, became twice higher in the case of MSGG accelerator. The result is hopeful to increase the injection power in D^- acceleration.

Appropriate supply of Cs vapour is considerably effective to enhance negative ions and to suppress co-extracted electrons, while best condition to produce negative is difficult to find. One of the reasons is that the Cs vapour pressure is passively evaporated from the inner walls of arc chamber by irradiated with plasma light and hot particles. Heat flux onto each wall of the chamber is not the same and condensed Cs distributed on the side and back-plate walls in our ion source [17]. The Cs layers on those walls are obviously much thicker than the other inner parts. In order to control the Cs pressure actively, a hot-water circulator is prepared to keep the temperature of side and back-plate walls warmer and to evaporate Cs on them. This experiment on active Cs control will be conducted on next June.

The last item of the list above is related to the production of negative-ion plasma involving very low electron density [18]. This plasma is produced in so-called beam extraction region between magnetic filter and PG, and the region is surrounded with multi-layered magnetic fields induced by filter and electron

suppression magnets. Especially, it has been observed the plasma includes electron density less than 1 % to H^- density at the region with stronger magnetic field. Such plasmas are very suitable to enhance negative ion and to reduce co-extracted electrons at the same time. Enhancement of magnetic field on the plasma side of PG is possible by replacing the SG made of molybdenum to ferromagnetic material. This concept of the magnetic enhancement is shown in Fig. 5. Returning magnetic field at the downstream of beam "pulled" toward ferromagnetic SG and shorted in the grid. Consequently, disconnection due to the ferromagnetic SG induces a new loop on the plasma side and the new loop enhances the magnetic field near PG. Three different grids and the magnetic field distributions are shown on the left hand side of Fig. 6(a), (b) and (c), which are configurations with Mo-SG, with Fe-SG and additional Fe rods on PG and Fe-SG, respectively.

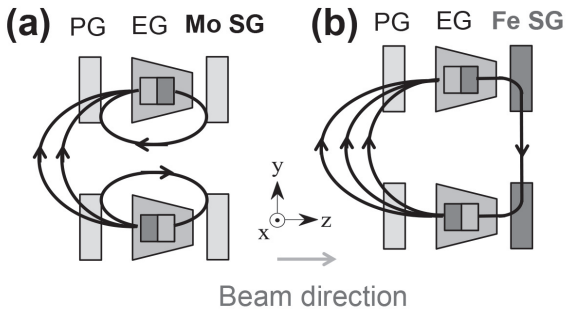

Fig. 5. Enhancement of magnetic strength using steering grid made of ferromagnetic material. (a) normal steering grid made of Mo and (b) modified steering grid made of Fe.

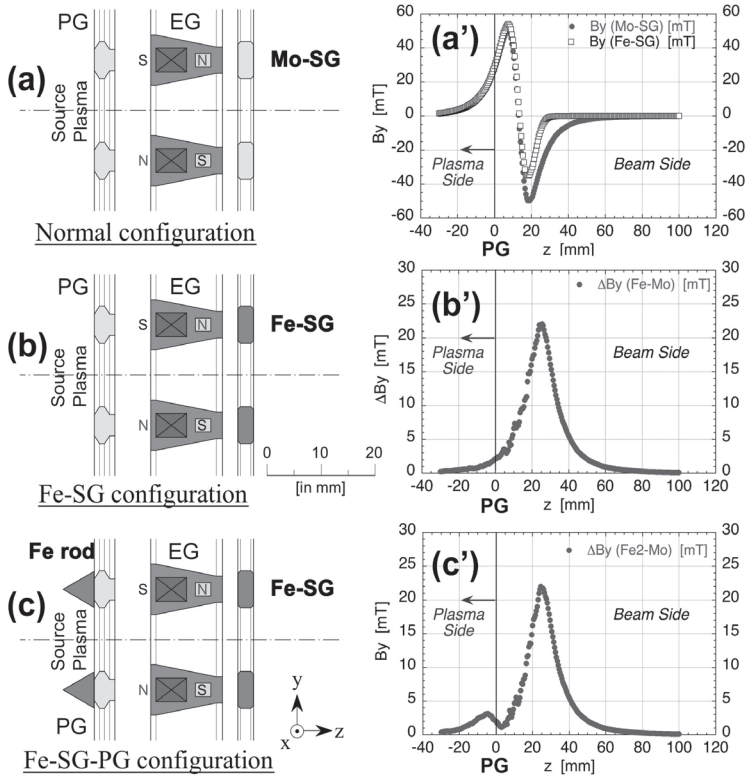

Fig. 6. Three beam accelerator having the configurations with (a) Mo-SG, (b) Fe-SG and (c) Fe-SG and Fe-rods on PG. The y components of the magnetic fields configured with (a) and (b) are shown in (a') for comparison. The plots in (b') and (c') show subtractions of magnetic distributions of (a) from (b) and (c), respectively.

Notice that the scales of the plots on the right hand side are compressed to show the tail part of electron deflection magnets installed in EG. The magnetic fields are simulated with TOSCA provided by Vector Field [19]. In Fig. 6(a'), plots with solid circles and open squares correspond to the field distributions in y direction, *B*y, in normal (Mo-SG) and Fe-SG configurations. Centre of the electron deflection magnet is

located at zero-crossing point near 16 mm. It is clear that the returning field of Fe-SG configuration reduces the *B*y amplitude and thickness. Reduced *B*y component is directed towards Fe-SG and converted to *B*z to conserve total magnetic flux. Subtracted *B*y field of the normal (a) from (b) Fe-SG configurations is indicated in Fig. 6(b'). Beam direction is parallel to z axis, whose origin corresponds to the plasma-facing surface of PG. The magnetic field increase becomes ~8 % higher than normal configuration. The *B*y field near PG can be enhanced by aligning ferromagnetic rods parallel to the lines of electron deflection magnets and on PG surface as shown in Fig. 6(c). Difference of *B*y field subtracted of (a) from (c) configurations is plotted in Fig. 6(c'). As seen in this figure, magnetic thickness in y direction on plasma side increases more comparing the case of just installing Fe-SG and that from (c) to (a) configurations in Fig. 6(c'). As the next step, we have started the beam simulation to compare the beam characteristics under those configurations.

After further investigation of three methods listed in the items of (a) to (c), we are going to combine the configuration to optimize the enhancement of D^- current.

Acknowledgements

This work was partly supported by the JSPS-NRF-NSFC A3 Foresight Program in the field of Plasma Physics (NSFC: No.11261140328, NRF: No.2012K2A2A6000443).

References

[1] A.Bar-Shalom, M.Klapisch and J.Oreg, J.Quant.Spectr.Radiant.Trans. 71 (2001) 169.
[2] F. Wagner, Plasma Phys. Control. Fusion 49 (2007) B1–B33.
[3] T. Ohkawa, Nucl. Fusion 10, 185 (1970).
[4] M. Kuriyama, N. Akino, T. Aoyagi, et al., J. Nucl. Sci. and Technology. **35** (1998) 739.
[5] Y. Takeiri, O. Kaneko, K. Tsumori, et al., Fusion Sci. Tchnol, 58 (2010) 482.
[6] S. Yamamoto, K. Toi, S. Ohdachi, Proceedings of 29th EPS Conference on Plasma Phys. and Contr. Fusion Montreux, 17-21 June 2002 ECA **26B**, P-1.079 (2002).
[7] D. Ćirić, A.D. Ash, B. Crowley, et al., Fusion Engineering and Design, **86** (2011) 509
[8] Y. Kamada, Y. Ishida, S. Neyatani, et al., J. Nucl. Sci. and Technology. **39** (1999) 1627.
[9] ITER Physics Expert Group on Energetic Particles, Heating and Current Drive, ITER Physics Basis Editors, Nuclear Fusion **39** (1999) 2495.
[10] K. Nagaoka, K. Ida, M. Yoshinuma, Nuclear Fusion, **51** (2011) 083022.
[11] J. Miyazawa, R. Sakamoto, S. Masuzaki, et al., et al., Nuclear Fusion, **48** (2008) 015003.
[12] M. Osakabe, M.Yokoyama, K.Nagasaki, et al., the 25th International Toki Conference, **I-1**, November 3-6, 2015, Toki-city, Gifu, JAPAN. (to be published in Plasma and Fusion Res.)
[13] H. Nakano, M. Osakabe, K. Tsumori, et al., Rev. Sci. Instrum, **81** (2010) 02B116.
[14] M. Kashiwagi, N. Umeda, H. Tobari, et al., Rev. Sci. Instrum, 85 (2014) 02B320.
[15] U. Fantz, B. Heinemann, D. Wünderlich, et al., Rev. Sci. Instrum. **87** (2016) 02B307.
[16] K. Tsumori, M. Osakabe, O. Kaneko, et al., Rev. Sci. Instrum. **79** (2008) 02C107.
[17] K. Tsumori, O. Kaneko, Y. Takeiri, et al., AIP conference proceedings **1390** (2011) 517.
[18] K. Tsumori, H. Nakano, M. Kisaki, et al., Rev. Sci. Instrum, 83, (2012) 02B116.
[19] Opera FEA, http://operafea.com/

Improved plasma equilibrium control by using a newly developed, self-proven controller design method

Y.M. Jeon[1], S.H. Hahn[1], H.S. Han[1], M.H. Woo[1], Jayhyun Kim[1], S.W. Yoon[1], N.W. Eidietis[2], A.W. Hyatt[2], M. Lanctot[2], D. Mueller[3], M.L. Walker[2], D.A. Humphreys[2]
[1]*National Fusion Research Institute, Daejeon, Korea*
[2]*General Atomics, San Diego, USA*
[3]*Princeton Plasma Physics Laboratory, Princeton, USA*
Email : ymjeon@nfri.re.kr

A self-consistent and self-decoupled controller design method for tokamak plasma equilibrium control is newly developed by using a free boundary tokamak equilibrium solver. By this method, a specific controller can be obtained independently on the other controllers, i.e. self-decoupled, and the plasma responses to the control action are included self-consistently. Also the controllability of obtained controllers is to be self-proven. Application of newly designed isoflux controllers to KSTAR equilibrium control shows excellent control performances with fully decoupled plasma responses.

1. Introduction

For the successful operation of magnetically confined fusion plasmas such as in ITER and DEMO, the reliable control of plasma boundary or shape is a fundamental but essential element. Moreover, the emergence of an innovative divertor configuration, for instance a snowflake [1] or super-X divertor [2], makes it challenging, particularly in a superconducting coil system as like KSTAR tokamak. In this regard, a new intuitive and direct method for optimal design of decoupled plasma shape controller is proposed and applied to KSTAR. Typically the plasma shape controller is designed by a matrix inversion of a shape response matrix, which is obtained by examining the plasma shape responses to small variations of coil currents through experiments or equilibrium dynamics modeling. In the new method, the shape controller matrix is directly formed from a series of free boundary equilibria, without any matrix inversion. In this method, it is obviously shown that the plasma response is taken into account self-consistently and the decoupled controllability is self-proved automatically. As a practical application, fully decoupled MIMO isoflux shape controllers are designed and applied to KSTAR by this new method. Furthermore, it is shown with the most importance that the control actions can be greatly reduced by this MIMO isoflux shape controllers, compared with those by the SISO-type controllers.

KSTAR has 14 up-down symmetric superconducting (SC) poloidal field (PF) coils for the control of plasma current and shape, 2 up-down anti-series connected in-vessel vertical control (IVC) coils for fast vertical instability control, and 2 up-down series connected in-vessel radial control (IRC) coils for fast radial position control. Fig. 1 shows both slow SC PF coils and fast IVC/IRC copper coils, with a reference plasma equilibrium shape and surrounding conducting structures (double wall vacuum vessel and in-vessel passive stabilizers). Note that ITER has a similar coil system to that in KSTAR, so that the controller design method introduced in this article can be applied directly.

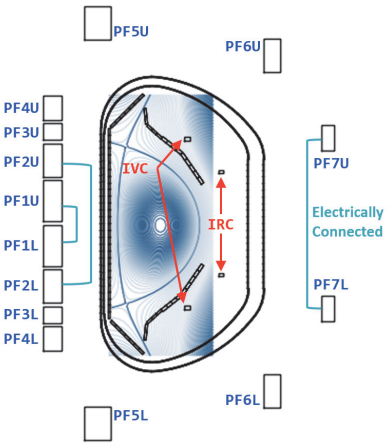

Fig. 1. KSTAR coil system for magnetics control

In Section 2 and 3,the conventional design approach

and new design approach are explained and compared. In Section 5, the experimental results of using newly designed controllers will be discussed, followed by the summary.

2. Conventional design approach for isoflux shape controllers

Since the plasma shape control is a typical multi-input, multi-output (MIMO) control problem, controller decoupling is an important issue. To deal with this issue in a logical manner, the MIMO controller design problem can be described as a minimization problem as like,

$$\min_{\Delta \mathbf{I_{PF}}} \left[\sum_{k}^{N_{iso}} \left\{ \sum_{i}^{N_{PF}} G(R_k, Z_k; R_i, Z_i) \cdot \Delta \mathbf{I_{PF,i}} - \Delta\psi_k \right\}^2 + \sum_{k}^{N_{XP}} \left\{ \sum_{i}^{N_{PF}} G_{B_P}(R_k, Z_k; R_i, Z_i) \cdot \Delta \mathbf{I_{PF,i}} - \Delta B_{P,k} \right\}^2 + \left\{ \sum_{i}^{N_{PF}} G(R_c, Z_c; R_i, Z_i) \cdot \Delta \mathbf{I_{PF,i}} - \Delta\psi_c \right\}^2 + \gamma^2 \sum_{i}^{N_{PF}} \left(\Delta \mathbf{I_{PF,i}} \right)^2 \right] \quad (1)$$

where N_{iso}, N_{XP}, and N_{PF} are the numbers of isoflux boundary points, X-points, and PF coils, respectively. The first term of square-sum is total flux errors on the isoflux boundary points, the second term is total magnetic field strength errors on X-points, and the third term is the flux linkage error on the effective plasma center position for I_P control. The last term is included for the regulation of solution. The $G(R_k,Z_k;R_i,Z_i)$ gives a poloidal magnetic flux from a source (R_i,Z_i) to a target (R_k,Z_k) location. Similarly the $G_{BP}(R_k,Z_k;R_i,Z_i)$ gives a poloidal magnetic field strength. And$\Delta\psi_k$, $\Delta B_{P,k}$, and $\Delta\psi_c$ are the control errors of poloidal magnetic flux on k-th isoflux points, of poloidal magnetic field strength on k-th X-points, and of flux linkage on effective plasma center, respectively. Note that in this conventional approach, the plasma is assumed to be invariant to the change of external coil currents so that the control errors, i.e.$\Delta\psi_k$, $\Delta B_{P,k}$, and $\Delta\psi_c$, can be completely compensated by the external control action, ΔI_{PF}.

Thus, we can obtain a set of decoupled isoflux controllers and for instance, the X-point controllers are shown in Fig. 2. In both R_x and Z_x controllers, the variations on PF1 and PF2 are to keep the inner gap unchanged and the variations on PF6 and PF7 are to keep the outer gap unchanged. Therefore, the main components of R_x and Z_x controllers are the variations on PF3, PF4, and PF5, marked with green-colored dotted circles. That is, the PF4 plays a key role on R_x control, while the PF5 does on Z_x control. Note that it is well consistent with what we expect intuitively.

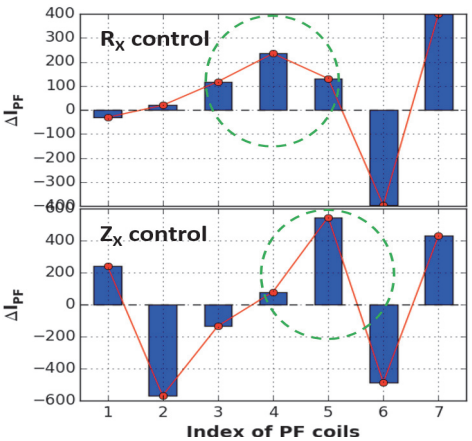

Fig. 2. X-point control vectors obtained via the conventional design

However, in practice, the plasma shape responses are not exactly consistent with this interpretation. The actual plasma responses in experiments are that a certain amount of PF5 changes do not make a corresponding change on Z_x, while the $R_x$is controlled well by PF4. Therefore, we should understand what causes this inconsistency and figure out an improved or alternative way of controller design.

3. New design approach with self-proven plasma responses

In order to resolve the X-point (R_x and Z_x) control issue, which has been a major control issue in KSTAR, we have developed a new approach for a design of decoupled shape controllers. The key idea is to include the plasma (shape and position) responses in a controller design. Remind that in Eq. (1), there is no plasma response taken into account. To describe the plasma response self-consistently on the design, we utilize a free-boundary tokamak equilibrium solution. In a solution of free-boundary tokamak equilibrium, there are two types of equilibrium problem [2]. One is so called, '*ideal free*' boundary tokamak equilibrium, in which external equilibrium fields by PF coils are given as an input and the plasma shape is obtained as a result of solution. The other is so called, '*semi free*' boundary tokamak equilibrium, in which the desired plasma shape is specified as an input and the external equilibrium coil currents required to form the specified plasma shape are obtained as a result. For the controller design, we can use the '*semi free*' boundary tokamak equilibrium, while the '*ideal free*' equilibrium can be used for the controller validation. For the numerical solution of these free-boundary tokamak equilibrium problems, we used TES code [2].

To understand the procedure of decoupled controller design by using the '*semi free*' boundary tokamak equilibrium, let's consider one free-boundary tokamak equilibrium as a reference. This reference equilibrium gives a reference set of external equilibrium coil currents ($\mathbf{I_{PF0}}$) to form the reference plasma shape. Then re-calculate the semi free boundary equilibrium with a small finite deviation on the target plasma shape and with the initial coil currents given same as those in the reference. For instance, ΔR_x=+2cm. The resultant external equilibrium coil currents ($\mathbf{I_{PF1}}$) should be slightly different from those in the reference. The difference of the equilibrium coil currents ($\mathbf{\Delta I_{PF}} = \mathbf{I_{PF1}} - \mathbf{I_{PF0}}$) is the required changes of coil currents to make the desired change of plasma shape (here, ΔR_x=+2cm with all other shapes unchanged). Therefore, this$\mathbf{\Delta I_{PF}}$ is the final R_x control vector, which is completely decoupled with other shape controls. In a similar way, we can design any type of decoupled plasma shape controller. The resultant R_x and Z_x controllers are shown in Fig. 3, compared with those (of Fig. 2) from the conventional design approach. Surprisingly it shows thatPF5 is not effectiveon $Z_x$control but rather effective onR_x control, while PF4 is effective on Z_x control. Also note that the obtained R_x(or Z_x) controller by new method is quite similar to the Z_x (or R_x) controller by conventional method.

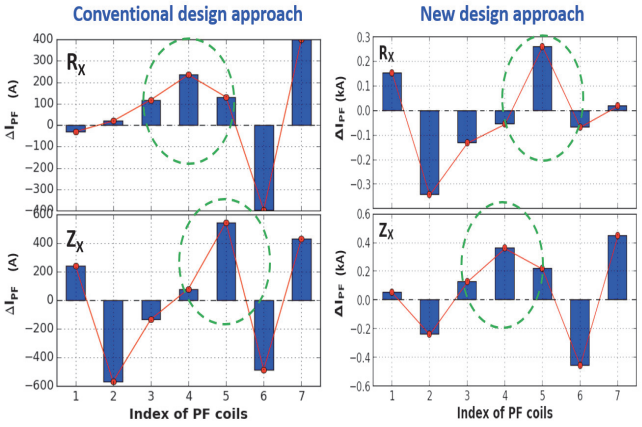

Fig. 3. Comparison of X-point controllers designed by 'conventional approach' (left) and 'new approach' (right)

4. Experimental validations of new design approach

X-point controllers obtained by the new design method showed completely opposite compositions compared with those by the conventional design method, as shown in Fig. 3. Therefore it is important to judge experimentally which controller is correct or effective in practical plasma operation. Based on the control experience in KSTAR during last several years, it is concluded that the conventional (or intuitively designed) X-point controllers did not provide a sufficient control performance or capability. On the contrary, the new X-point controllers, designed by the new design method, showed remarkable improvements on control performances. One representative X-point control result is shown in Fig. 4. As marked with red shaded area, the control errors of R_x and Z_x were quickly converged to zero

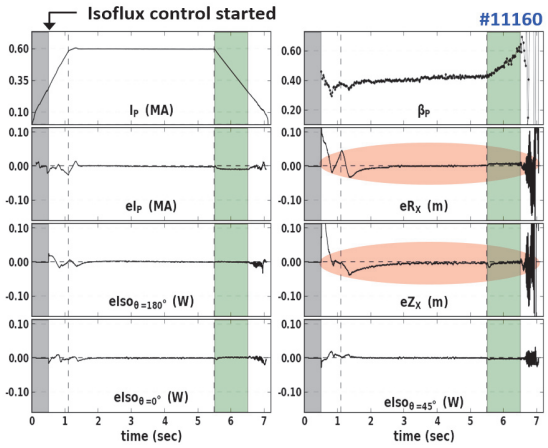

Fig. 4. Control performances by using SISO-type X-point controllers

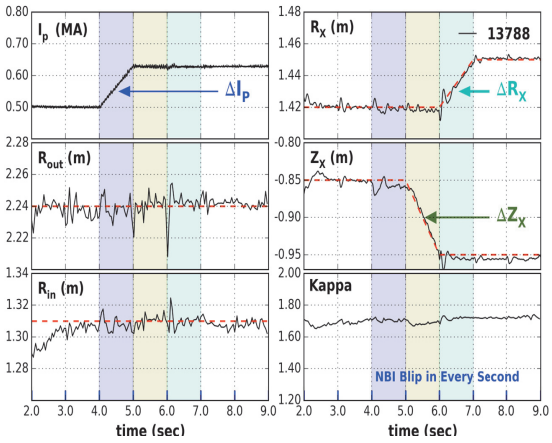

Fig. 5. Fully decoupled control performances by using MIMO isoflux controllers

and sustained even during Ip ramp-down (green shaded area). Note that in this discharge, the R_x control was consisted with PF5 only and the Z_x controller was done with PF4 only (i.e. SISO-type controllers),to validate the correctness of newly designed controller (see Fig. 3). Further optimization of decoupled shape control have been examined by applying the full MIMO isoflux controllers, and it turned out that the required coil current changes (control cost) can be substantially reduced and the controller coupling can be minimized, compared with SISO-type controllers. The best representative control performance is shown in Fig. 5, where MIMO isoflux controllers obtained by the new design method were applied. In every control events, i.e. I_p increase (4~5 sec), R_x increase (5~6 sec), and Z_x decrease (6~7 sec), each control variables were well controlled with minimal disturbances on the other controls.

By virtue of substantial improvements of isoflux shape control, the KSTAR plasma operation has been improved and extended from various aspect. The long pulse operation has been explored in routine with full shape control up to ~60 sec (almost to the limit of current hardware system) with I_P=0.6 MA, B_T=2.9 T, P_{AUX}~5.0 MW. A fully non-inductive, steady state operation has been achieved for the first time in KSTAR with I_P=0.4 MA, B_T=2.9 T, P_{AUX} ~6.0 MW.

5. Summary

In last 2015 KSTAR campaign, the plasma equilibrium magnetics control has been substantially improved by introducing a newly developed design method for decoupled isoflux shape control. The new method provides a direct and logically intuitive controller design including self-consistent and self-proven plasma responses. The newly designed isoflux controllers showed excellent control performances with fully decoupled plasma responses. Note that the introduced new design method for decoupled MIMO shape controller can be applied directly to the controller design in ITER and beyond.

Acknowledgement

This research was supported by Ministry of Science, ICT, and Future Planning under KSTAR project through A3 Foresight Program.

References

[1]D. D. Ryutov, Phys. Plasmas **14**, 064502 (2007).
[2]M. Kotschenreuther, P. M. Valanju, S. M. Mahajan and J. C. Wiley, Phys. Plasmas **14**, 072502 (2007).
[3]Y.M. Jeon,J. Korean Phys. Soc., **67**, 5, p843-853 (2015)

Experimental Results of Helicon Wave Coupling in KSTAR Plasmas

S. J. Wang, H. H. Wi, H. J. Kim, M. Joung, J. H. Jeong, J. H. Kim, and J.G. Kwak
National Fusion Research Institute, Daejeon, Korea
Email : sjwang@nfri.re.kr

For efficient off-axis current drive in fusion reactor, high frequency helicon wave current drive has been suggested. [1] It has been found that high frequency fast wave, frequency just below LH (lower hybrid) resonance frequency in the middle of plasma, can drive plasma current in the mid-radius of high electron beta plasmas in modern medium and large size tokamak due to moderate optical thickness and wave alignment nature of helicon wave in helical magnetic field. KSTAR is an ideal machine to test and to use off-axis current drive capability of helicon wave because it has adequate machine parameters and it will have high electron beta plasmas in near future with additional ECH power. To test the feasibility of helicon wave system in KSTAR, low power mock-up TWA (travelling wave antenna) system has been designed, fabricated and tested in plasmas. [2] In the experiment, power coupling coefficient defined by the ratio of radiated power to injected power was measured. It has been found that the coupling factor can be easily controlled by controlling radial outer gap of plasma without loss of plasma confinement in some extend. Coupling control by local gas puffing is also effective; however there is a slight degradation of confinement. The antenna has Faraday shield to suppress O-mode polarization which may launch slow wave. If both fast and slow waves are coupled to plasma from antenna, the coupling should be minimized if tilting angle of Faraday shield is aligned to static magnetic field assuming that the Faraday shield works correctly and slow wave coupling is much larger than fast wave coupling. However, the effect of alignment has not been found during magnetic pitch angle scan. It might be concluded that the slow wave coupling compared to fast wave coupling is not large if above assumptions are reasonable. During the transition to ELMy H-mode plasma from L-mode, slight degradation of coupling without noticeable increase of reflection to RF source was found due to the characteristics of TWA, however too much coupling and the bursts of reflection were found during ELM burst. The overall coupling is found to be too much compared to the initial expectation made from EM calculation and bench-top simulation. Too much coupling makes maintaining peak $n_{||}$ hard because TWA requires small loading resistance per each radiating element compared to mutual reactance between adjacent elements.

1. Helicon Antenna System

TWA is an antenna system made of seven mutually coupled radiating elements driven by 500 MHz RF power. As shown in figure 1, the TWA is basically 2 ports loss system having input port connected to power source and output port connected to dummy load. A fraction of power applied to the current carrying element is radiated and the remaining fraction of power is transferred to the next. At the last elements, remaining power is dumped to the matched dummy load. Therefore, with appropriate mutual inductance ωM and loading resistance R_L, the impedance at the input port can be maintained within the range for tolerable reflection regardless of R_L change if R_L is small enough compared to mutual reactance, $\omega M >> R_L$.

Frequency scanned low RF power and measurement of forward volage V_f, reflected voltage V_r, and transmitted voltage V_t are done by network analyzer. Using the measured complex voltages, the coefficients of transmission $T=P_t/P_f$, reflection $R=P_r/P_f$, and

absorption or radiation $A=P_a/P_f=1-(T+R)$ can be calculated, where P_t, P_f and P_r are transmitted, forward and reflected powers, respectively. Another important measurement is phase deference Φ between V_f and V_t, which is directly related to parallel refractive index $n_{||} = (2\pi n+\Phi)c/(L\omega)$, where L is the length of the effective radiation zone of TWA and n is a fringe number.

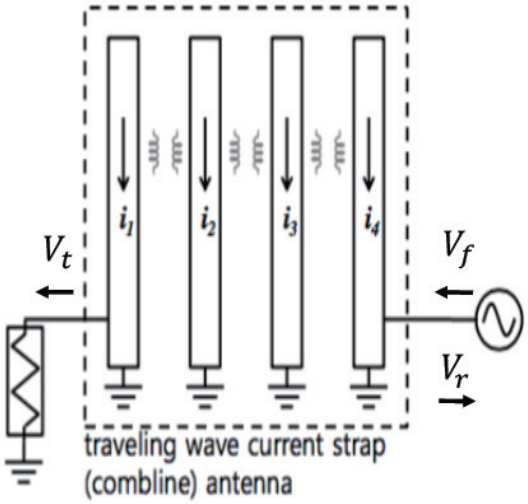

Figure 1. Schematics of travelling wave antenna. (Only four radiating elements among the seven are shown.)

Figure 2 shows installed TWA in KSTAR vacuum vessel 30 cm above mid-plane and 1 cm behind poloidal limiter. By installing at the top of LH launcher, utilizing Langmuir probes and local gas puffing nozzle attached at the LH launcher is possible though magnetic field lines are not connected to the TWA.

Figure 2. Mockup TWA installed 30 cm above mid-plane.

Figure 3 shows the frequency scanned coefficients of T and R in vacuum or with plasma. R remains below -20 dB regardless of plasma existence while T reduces from -10 dB

to -30 dB in frequency range of 490-500 MHz. Note that loss of thin cables connecting antenna and probes are un-calibrated. This results shows that the TWA works as intended.

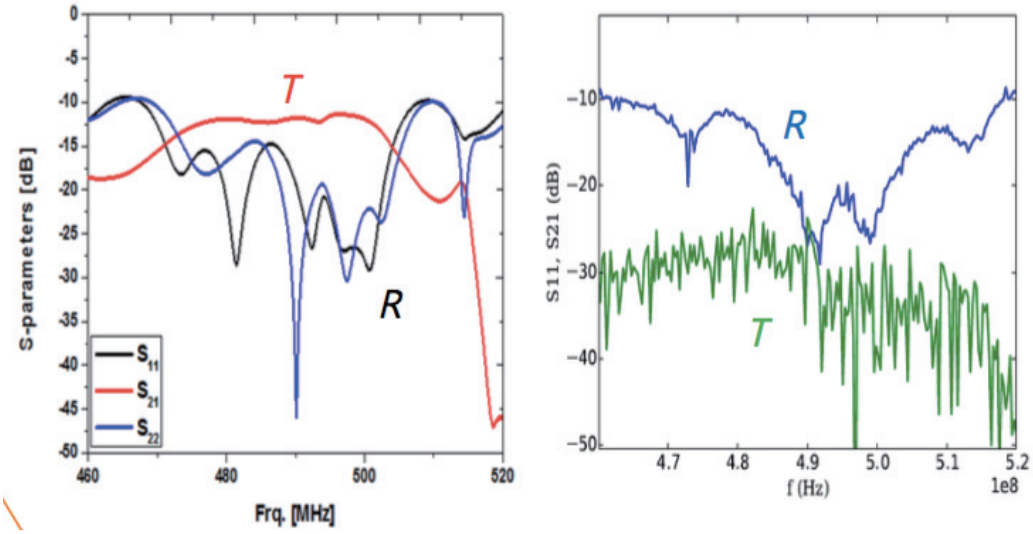

Figure 3. Coefficients of reflection R and transmission T. Left figure is in vacuum without plasma and right figure is with plasma.

2. Coupling Measurements

In H-mode plasma, coupling was controlled by controlling radial outer gap Gap_{out} defined by the distance between LCFS and poloidal limiter at outer mid-plane. During the Gap_{out} scan from 8 cm to 3 cm, coupling *A* increases from 0.4 to 0.9 and the the shortest distance between LCFS and the center of antenna surface also change from 10 cm to 6 cm as in figure 4 left. The Gap_{out} control for enhancing *A* is quite effective as there no degradation of H_{89} factor is observed in this range of scan.

Another useful method for enhancing coupling for RF heating such as ICRF and LH is local gas puffing with nozzles at the position of magnetic connection. In spite of no magnetic connection between LH puffing nozzle and TWA, the strong enhancement of A with gas puffing is observed in H-mode plasma at 2.9 T as in figure 5 right. However, during gas puffing, slight decrease of H_{89} and increase of average density are observed.

TWA has tilted Faraday shield to suppress O-mode polarization which could launch slow wave. If slow wave coupling is dominant or strong enough, coupling *A* would be minimized when slow wave is suppressed with aligning the tilting angle of Faraday shield with magnetic pitch angle at the antenna surface. Figure 5 shows that there is no noticeable change of *A* when magnetic pitch angle passes Faraday shield tilting angle, 10 degrees. It may be possible that the suppression of slow wave is not so sensitive to the change of pitch angle from 8 degrees to 12 degrees. If it is true, the range of magnetic pitch angle should be expanded. Reversing pitch angle would be a suitable choice of experimental condition if other relevant parameters can be fixed.

Plasma L/H-mode transition makes slight decrease of the baseline of coupling *A* and no meaningful increase of the baseline of reflection *R*. Also, no meaningful change of phase difference Φ is observed. However, large increases of *A, R* and fluctuation of phase difference are observed during ELM bursts. It should be careful for the quantity of phase changes during almost 100% of coupling *A* because large phase error is expected with small transmission.

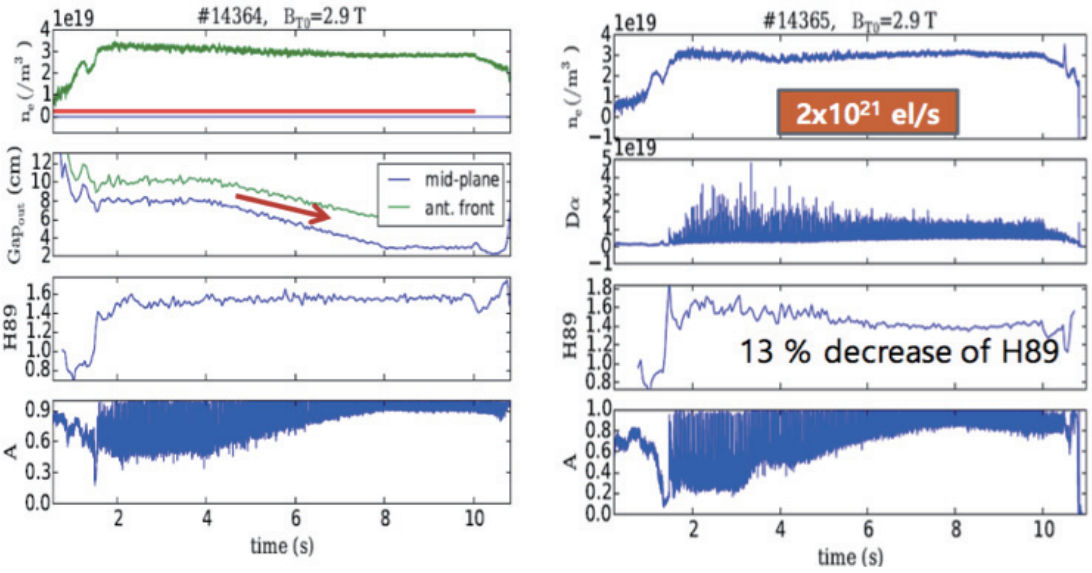

Figure 4. (LEFT) Coupling A changes from 0.4 to 0.9 during radial outer gap scan in H-mode plasmas at 2.9 T of B_{T0}. No degradation of H_{89} factor or increase of average density is observed. (RIGHT) Local gas puffing is tried to enhance coupling A in H-mode plasma. Slight decrease of H_{89} factor is observed with slight increase of average density during gas puffing period.

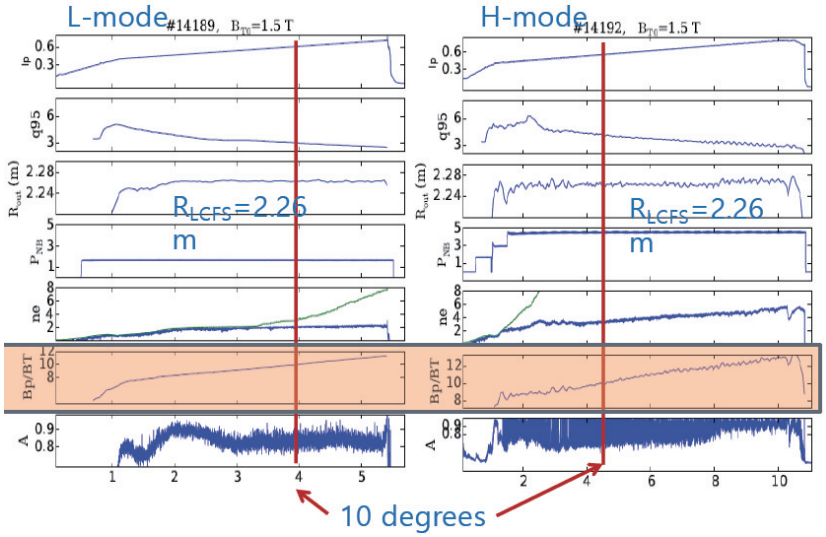

Figure 5. Magnetic pitch angle scan. Bp/BT is a pitch angle at the front center of antenna in degree.

Figure 7 shows phase difference Φ as a function of coupling A in H-mode plasma and EM calculation for the antenna with artificial absorber. In spite of the large difference of coupling at the same gap distance, phase-coupling relations agree very well. Above certain value of A, $A > 0.7$ in this case, phase difference decreases rapidly. It means that deviation of $n_{||}$ from designed value in large absorption is unavoidable. TWA requires small loading resistance compared to mutual reactance between radiating elements, $\omega M >> R_L$, for minimal change of reflection and radiation spectrum. Therefore, it is necessary to limit the coupling by optimizing coupling capability of TWA for proper operation.

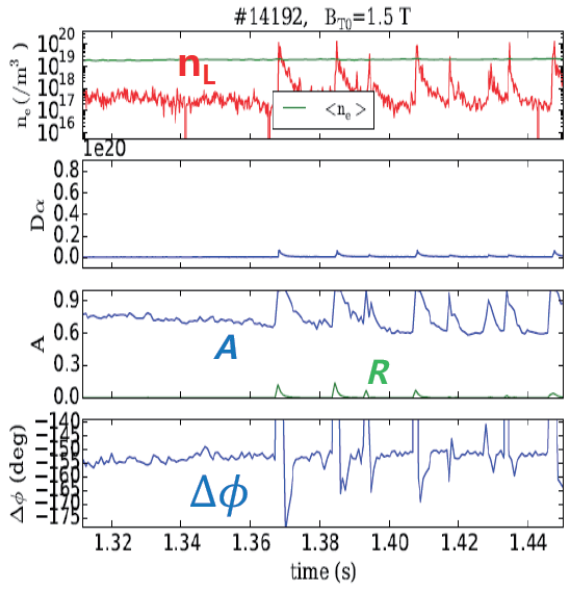

Figure 6. The baseline of coupling A slightly decreases when plasma transited to EMLy H-mode however, there is no noticeable increase of baseline reflection *R*. ELM bursts cause large spikes of *A*, *R*, and sharp fluctuation of phase difference.

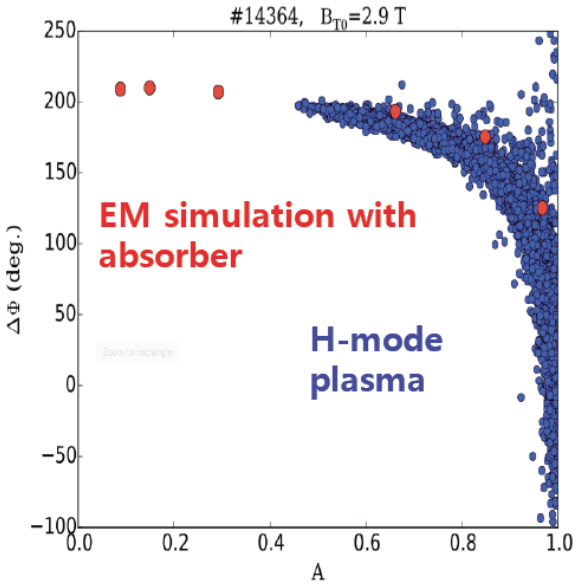

Figure 7. Phase difference as a function of *A*. Red dots are simulated data and blue dots are data obtained in ELMy H-mode plasma.

3. Conclusion

TWA mock-up antenna installed at the KSTAR reveals high couplings in both L- and H-mode plasmas. The coupling can be easily controlled by radial outer gap without degradation of plasma confinement or local gas puffing with slight decrease of plasma confinement. Magnetic pitch angle scan does not show any evidence of large slow wave coupling. The antenna system is load resilient in L/H transition, however too much coupling is observed during ELM bursts. Almost 100% coupling causes spikes of reflection and fluctuations of transmission phase. It is necessary to limit coupling by optimizing antenna system, reducing coupling per unit antenna length.

Acknowledgement

This research was partly supported by the JSPS-NRF-NSFC A3 Foresight Program (NRF No. 2012K2A2A6000443 and NSFC No. 11261140328).

References

[1] V. L. Vdovin, Plasma Physics Reports, **39**, 95 (2013)

[2] S. J. Wang *et al.*, 21st Topical Conference on RF Power in Plasmas, Lake Arrowhead, *Proceedings will be published* (2015)

Flow velocity and ion temperature of carbon impurities measured using VUV spectroscopy in the ergodic layer of LHD

T. Oishi[1,2], S. Morita[1,2], S. Y. Dai[1,3], M. Kobayashi[1,2], G. Kawamura[1], X. L. Huang[1], H. M. Zhang[2], Y. Liu[2], M. Goto[1,2] and the LHD Experiment Group[1]

[1]National Institute for Fusion Science, Toki 509-5292, Gifu, Japan

[2]Graduate University for Advanced Studies, Toki 509-5292, Gifu, Japan

[3]School of Physics and Optoelectronic Technology, Dalian University of Technology, Dalian 116024, PR China

Abstract

Spatial profiles of vacuum ultraviolet (VUV) lines from impurities emitted in the ergodic layer of the large helical device (LHD) were measured by a space-resolved VUV spectroscopy using a 3 m normal incidence spectrometer in wavelength range of 300-3200 Å. Carbon impurity flows were derived by the Doppler shift of the CIV spectra with the wavelength of 1548.20 × 2 Å. The flows projected along the major radius clearly had outboard direction at the top and bottom edges in the ergodic layer. Direction of the flows agrees with simulation results by a three-dimensional simulation code EMC3-EIRENE indicating flows which drive the impurity screening phenomena.

1. Introduction

Stochastization of edge magnetic fields is extensively studied not only for the ELM mitigation but also for the plasma detachment and the impurity transport. The ergodic layer of the large helical device (LHD) consists of stochastic magnetic fields with three-dimensional structure intrinsically formed by helical coils, while well-defined magnetic surfaces exist inside the last closed flux surface [1]. It is therefore extremely important to study the impurity behaviour and transport in the ergodic layer and to compare with those in the scrape-off layer of tokamaks. Recently, reduction of the parallel impurity transport, so called "impurity screening", has been studied in LHD [2]. A transport model for the impurity behavior in the ergodic layer has been proposed considering the parallel momentum balance on impurity ions along a magnetic field line connecting the core plasma and the divertor plate based on the following equation;

$$m_Z \frac{\partial V_{Z//}}{\partial t} = -\frac{1}{n_Z}\frac{\partial T_Z n_Z}{\partial s} + ZeE_{//} + m_Z \frac{V_{i//} - V_{Z//}^{imp}}{\tau_s} + 0.71Z^2 \frac{\partial T_e}{\partial s} + 2.6Z^2 \frac{\partial T_i}{\partial s}, \qquad (1)$$

where five terms in the right-hand side are contributions of impurity ion pressure gradient, parallel electric field, friction force between bulk ions and impurity ions, electron thermal force, and ion thermal force, in the order. Among these terms, the friction force terms and the ion thermal force term are the dominant terms. When the ion density gradient increases, the friction force increase resulting the impurity flow is directed toward divertor plates, which means the impurity screening. On the other hand, when the ion

temperature gradient increases, the ion thermal force increases resulting that the impurity flow is directed toward the core plasmas, which means the impurity accumulation. However, the impurity flow in the ergodic layer has not been yet measured experimentally even though it is considered to be a key mechanism to determine impurity distributions. Therefore, a precise profile measurement of the impurity flow is truly required to examine the validity of the theoretical modelling on the impurity transport in stochastic magnetic field layer.

2. Measurements of emission intensity, ion temperature and flow velocity of the carbon impurity

A space-resolved vacuum ultraviolet (VUV) spectroscopy using a 3 m normal incidence spectrometer is utilized to measure impurity emission profile in the edge and divertor plasmas of LHD in wavelength range of 300 - 3200 Å [3]. Figure 1 shows the observation range of VUV spectroscopy on the poloidal cross section at horizontally-elongated plasma position of LHD with the magnetic axis of R_{ax} = 3.6 m.

We conducted an experiment with a magnetic configuration with R_{ax} = 3.6 m and B_t = 2.75 T. The averaged electron density n_e was scanned from 2.0 to 6.5 × 10^{13} cm^{-3}. Figure 2 (a) shows the vertical profiles of CIV line intensity with the wavelength of 1548.20 × 2 Å for n_e = 2.0, 4.0, and 6.0 × 10^{13} cm^{-3}. It is known that the spatial profile of the CIV intensity has a steep peak in the ergodic layer. CIV emission is released only in the outermost region of the ergodic layer in LHD plasmas because the low ionization energy of 65eV for C^{3+} ions causes less fractional abundance in the core plasma. Therefore, the peak of the intensity profile outside LCFS shown in Fig. 2 (a) is a result of line integration in a long path along the sightline through the ergodic layer at the bottom edge of the holizontally-elongated elliptical plasma. Figure 2 (b) shows the profiles of ion temperature T_i derived from the Doppler broadening of CIV spectra. The T_i profile also indicates the edge T_i in the ergodic layer at corresponding vertical position. T_i has a negative correlation with n_e.

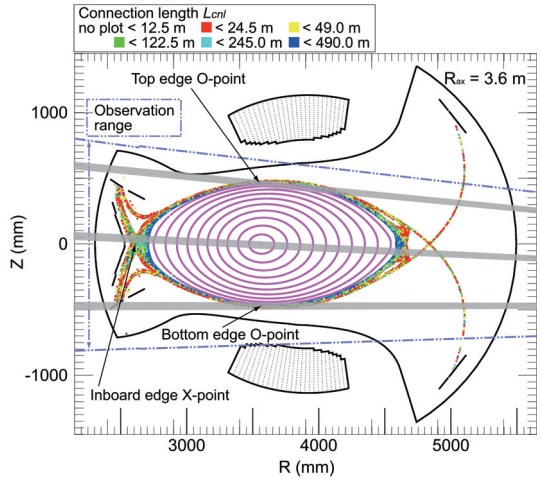

Fig. 1. The observation range of VUV spectroscopy shown on the poloidal cross section of LHD.

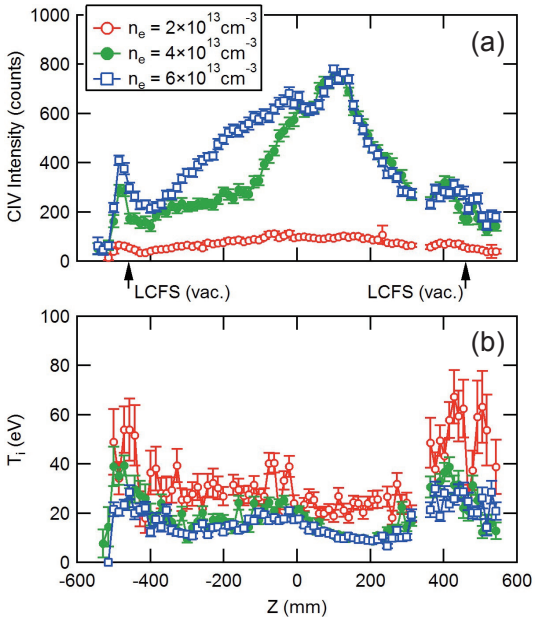

Fig. 2. Vertical profiles of (a) CIV line intensity and (b) ion temperature derived from the Doppler broadening of CIV spectra.

Figure 3 shows a vertical profile of relative flow with $n_e = 6.3 \times 10^{13}\mathrm{cm}^{-3}$. The relative flows were derived by the Doppler shift of the CIV spectra taking the spectra measured in a plasma termination phase as references of the flows. Positive values in the vertical axis indicate increment of flows directing toward the outer horizontal diagnostics port, which corresponds to radially outboard direction. The measured flow velocity in Fig. 3 is projection of the flow along the observation chord which can be approximately considered to be the direction of the plasma major radius. From the figure it is found that the flow direction is the same, i.e. the outboard direction, for both the top (Z = 480 mm) and bottom (Z = -480 mm) edges of the ergodic layer. In addition, electron density dependences of the flow at the top and bottom edges of the ergodic layer indicated that the flow velocity increased with the density, as predicted by the theoretical model in which the friction force between impurity and bulk ions is more effective at higher electron density range. We also investigated emission intensities of carbon lines for the charge states of from CIII to CVI. CIII and CIV emitted from outer region of the ergodic layer increase while CV and CVI from inner region decrease in higher density ranges. This result indicates enhancement of the impurity screening and has no argument with enhancement of friction-force dominated carbon flow.

3. Interpretation of the observed flow structure

The carbon flow measured with spectroscopic method for the first time is compared with the impurity transport simulation based on a three-dimensional simulation code EMC3-EIRENE. The simulation is carried out under the same discharge condition as the result in Fig. 3. Figure 4(a) shows the simulation result of C^{3+} impurity flow parallel to magnetic field lines, $V_{//}$ [4]. The simulation result indicates that the toroidal component of $V_{//}$ blue-colored at the top edge is directed in the clock-wise (CW) direction while that orange-colored at the bottom edge is directed in the counter-clock-wise (CCW) direction. Figure 4(b) illustrates the magnetic field lines in the ergodic layer only for the upper half of the plasma. As stated above, the simulated parallel flow show in Fig. 4(a) has the toroidal component in CW direction at the top edge. This means that the radial component of the parallel flow, V_R, is directed toward the outboard direction as shown in Fig. 4(b). Also at the bottom edge, V_R is directed toward the outboard direction because the toroidal component of $V_{//}$ is directed in CCW direction as shown in Fig. 4(c). In summary, the toroidal component of $V_{//}$ has an opposite direction between the top and bottom edges, while the major radius component of $V_{//}$ has the same direction toward outboard side. This structure of the flow agrees qualitatively with the experiment.

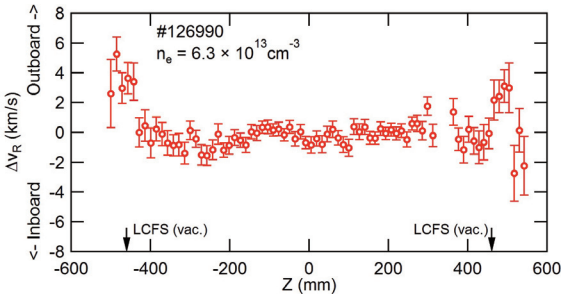

Fig. 3. Vertical profile of relative flow along the observation chords with $n_e = 6.3 \times 10^{13}\mathrm{cm}^{-3}$ taking the spectra measured in a plasma termination phase as references of the flows.

4. Summary

Spatial profiles of VUV lines from impurities emitted in the ergodic layer of LHD were measured by a space-resolved VUV

spectroscopy using a 3 m normal incidence spectrometer in wavelength range of 300-3200 Å. Carbon impurity flows were derived by the Doppler shift of the CIV spectra with the wavelength of 1548.20 × 2 Å. The flows projected along the major radius clearly had outboard direction at the top and bottom edges in the ergodic layer. Direction of the flows agrees with simulation results by a three-dimensional simulation code EMC3-EIRENE indicating flows which drive the impurity screening phenomena.

Acknowledgements

The authors thank all the members of the LHD team for their cooperation with the LHD operation. This work is partially conducted under the LHD project financial support (NIFS14ULPP010). This work was also supported by Grant-in-Aid for Young Scientists (B) 26800282 and partially supported by the JSPS-NRF-NSFC A3 Foresight Program in the Field of Plasma Physics (NSFC: No.11261140328, NRF: No.2012K2A2A6000443).

References

[1] T. Morisaki, K. Narihara, S. Masuzaki *et al.*, J. Nucl. Mater. **313–316** (2003) 548.

[2] M. Kobayashi, S. Morita, C. F. Dong *et al.*, Nucl. Fusion **53** (2013) 033011.

[3] T. Oishi, S. Morita, C. F. Dong *et al.*, Appl. Opt. **53** (2014) 6900.

[4] S. Y. Dai, M. Kobayashi, G. Kawamura *et al.*, *submitted to* Nucl. Fusion.

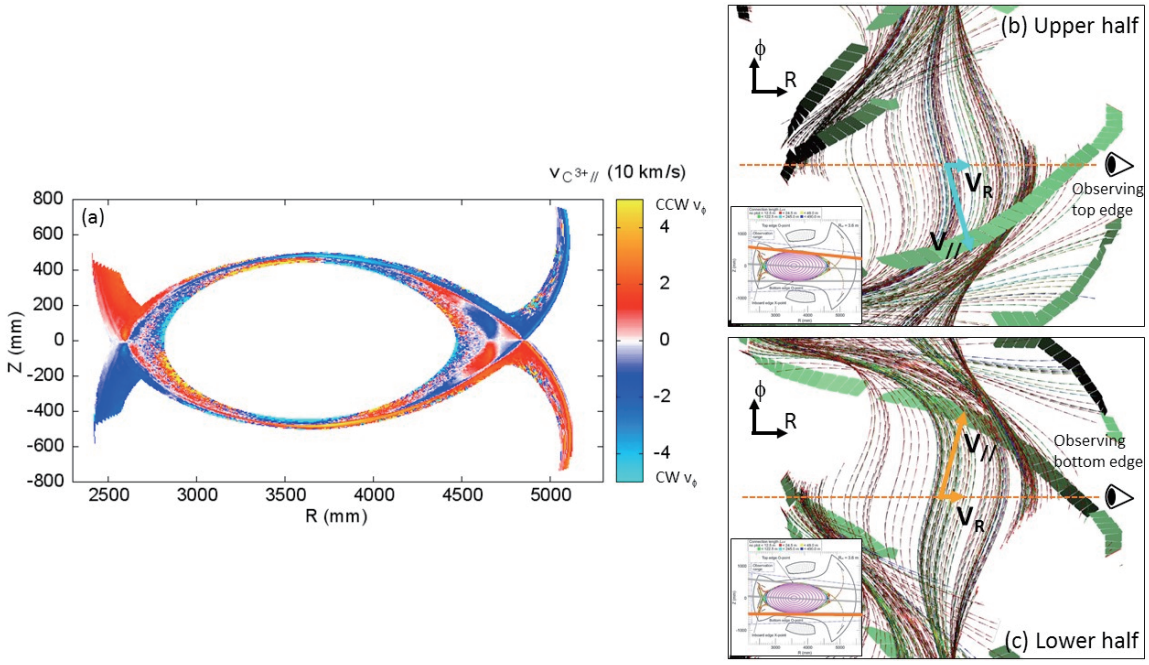

Fig. 4. (a) Simulation result of C^{3+} impurity flow parallel to magnetic field lines calculated by a three-dimensional simulation code EMC3-EIRENE. Schematic drawing of the parallel flow $V_{//}$, its radial component V_R, magnetic field lines in the ergodic layer and observation chord located at the plasma edge for (b) upper half and (c) lower half of the plasma.

Edge particle confinement and operational range in LHD discharges with stochastic magnetic field layer

S.Morita[1,2], T.Oishi[1,2], X.L.Hunag[2], H.M.Zhang[2], Y.Liu[2] and M.Goto[1,2]

[1]National Institute for Fusion Science, Toki 509-5292, Gifu, Japan

[2]SOKENDAI (Department of Fusion Science, Graduate University for Advanced Studies), Toki 509-5292, Gifu, Japan

Abstract

In LHD confinement improvement has been observed in magnetic configuration with thick stochastic magnetic field layer called ergodic layer, e.g. R_{ax}=3.90 m configuration, when NBI power input ($P_{NBI}\geq$7 MW) is reduced to a considerably low level (P_{NBI}~1 MW). The energy confinement time τ_E, increases from 20 ms to 80 ms after reducing P_{NBI}, while T_e decreases from 1.8 keV to 1 keV. A specific feature of the discharge is focused on the density behavior. The density gradually increases with time response of ~300 ms from 1.5x10^{13}cm^{13} to 3.5x10^{13}cm^{-3} after reducing the P_{NBI}. The reason is discussed with edge particle confinement time which has been evaluated from toroidal and poloidal Hα measurements.

1. Stochastic magnetic field layer (ergodic layer) in LHD

In LHD the LCFS is defined by outermost flux surface on which the deviation of the magnetic field line is less than 4 mm while it travels 100 turns along the torus. When the point of sight in Figs. 1 (b) and (d) moves from the core region to edge region outside the LCFS, the magnetic field lines created by a set of helical coils change into open magnetic field. The open magnetic field line in the space outside the LCFS still goes in the toroidal direction. However, the open magnetic field line suddenly changes the direction toward helical coils, when the point of sight gets further away from the LCFS and approaches the helical coil. The field line simply begins to link two positions on the first wall with extremely short magnetic field connection length. It is called 'open field layer', which is understood as an area outside the shaded elliptical area in Figs. 1(b) and (d). The magnetic field connection length, L_c becomes much shorter (L_c<10 m) in the open field layer and monotonically decreases as a function of Z. Any significant plasma cannot be sustained in the open field layer due to a rapid transit time of particles. At the entrance of the open field layer, then, two divertor plates are directly connected by the field lines. Here, we define a space surrounded by the field line connecting divertor plates as 'geometric confinement region' which is denoted by an elliptical solid line with shaded area. The geometric confinement region (GCR) is basically determined by the position of helical coils, but fairly insensitive to coil currents of other poloidal and vertical magnetic coils in general high-B_t operation. As a result, the geometric confinement region outside the core region defined by LCFS, which is denoted by a filled area inside the GCR, becomes 'stochastic region' consisting of stochastic magnetic field lines with a variety of L_c ($10 \leq L_c \leq 2000$ m), which corresponds to 0.5-100 toroidal turns of the LHD torus. Therefore, when the magnetic axis position is shifted outwardly, i.e. R_{ax}=4.0m in Fig. 1(c), the ergodic layer becomes much thicker compared with

inward-shifted magnetic axis position of R_{ax}=3.60 m in Fig. 1(a).

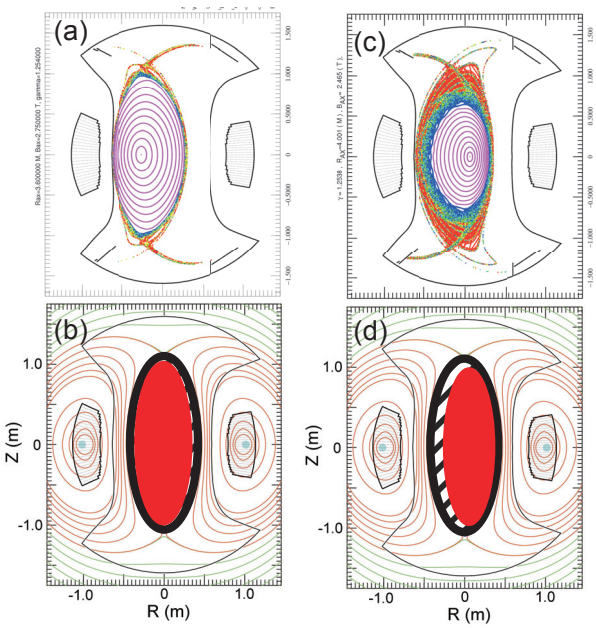

Fig.1 Edge stochastic magnetic field layer at (a) inward- (R_{ax}=3.6 m) and (b) outward-shifted (R_{ax}=4.0 m) magnetic axes and geometric confinement region (shaded area) and core plasma region within ρ=1 (filled area) at (b) R_{ax}=3.6 m and (d) R_{ax}=4.0 m.

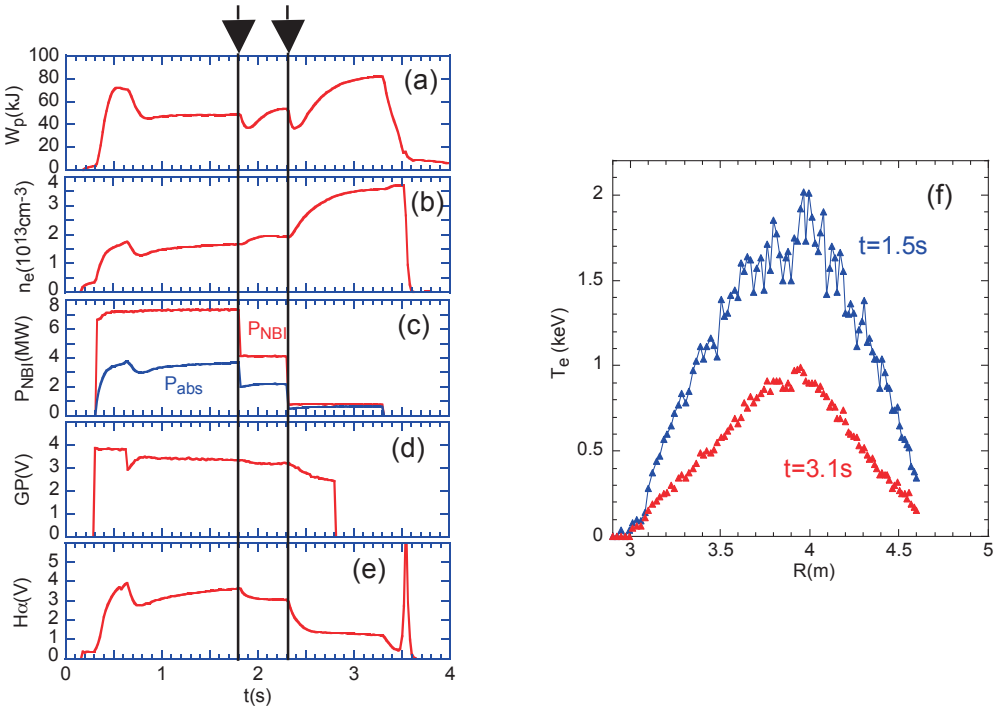

Fig.2 (a)-(e) Confinement improvement of LHD discharges with thick stochastic magnetic field layer at outward-shifted magnetic axis of R_{ax}=3.9 m and (f) radial profiles of T_e at t=1.5 and 3.1 s in NBI discharges. Two arrows at t=1.8 and 2.3 s indicate timing of P_{NBI} reduction.

2. LHD discharges at R_{ax}=3.90 m with P_{NBI} reduction

NBI discharges are carried out in outward-shifted configuration at R_{ax}=3.9 m plasma axis position

with thick ergodic layer, as shown in Fig.2. The NBI power input is reduced two times during the discharge at t=1.8 and 2.3 s as denoted with two arrows. After reducing P_{NBI}, the density gradually increases with time response of ~300 ms and the plasma stored energy, W_p, also increases, while the Hα signal intensity decreases. It clearly indicates an improvement in both the energy and particle confinements. Figure 2 (f) shows T_e profiles before and after the P_{NBI} reduction at t=1.5 and 3.1 s, respectively. Since the Ti seems to be unchanged, i.e. T_i~Te at t=3.1 s, the increase in W_p mainly originates in increases in the density and the ratio of T_i to T_e.

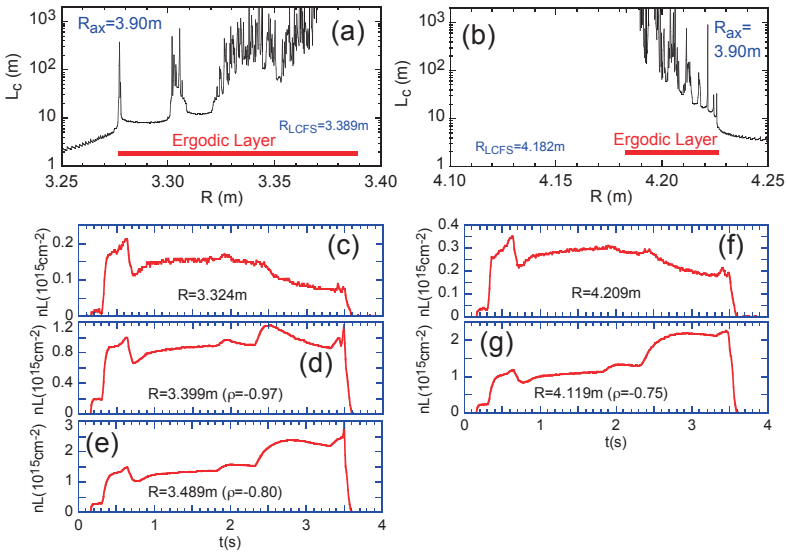

Fig.3 Magnetic field connection length at (a) inboard and (b) outboard sides in vertically elongated plasma cross section of R_{ax}=3.90 m magnetic configuration and (c) - (g) temporal behavior of edge density.

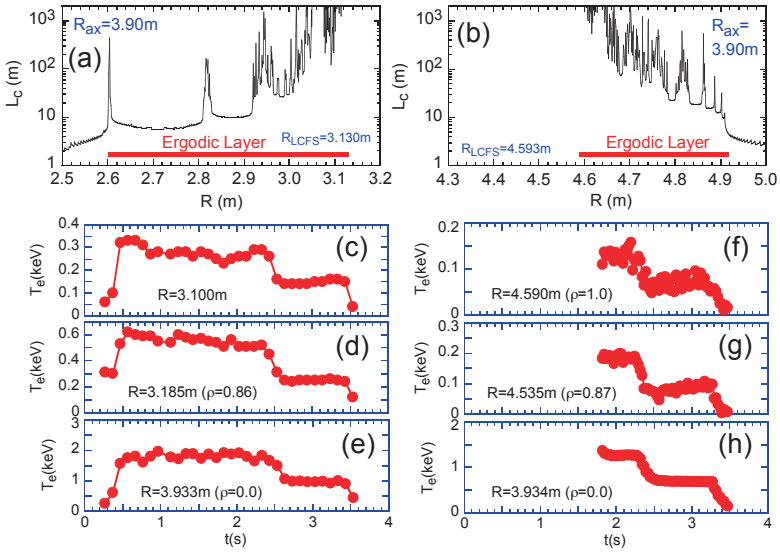

Fig.4 Magnetic field connection length at (a) inboard and (b) outboard sides in horizontally elongated plasma cross section of R_{ax}=3.90 m magnetic configuration and (c) - (h) temporal behavior of edge temperature.

Temporal behaviors of edge n_e and T_e are shown in Figs. 3 and 4, respectively. The chord-integrated density, nL, in Fig.3 is vertically measured with 12 channel FIR interferometer at vertically elongated plasma cross section, while the Te is horizontally measured with Thomson scattering system at horizontally elongated plasma cross section. Therefore, the L_c profiles along major radius direction shown in Figs. 3(a) and (b) and Figs. 4(a) and (b) have a different scale in the axis of abscissa. Seeing the edge density behavior in Figs. 3(c)-(g), we understand that the density in the plasma core at $\rho \leq 1$ increases after the P_{NBI} reduction but the density in the ergodic layer at $\rho > 1$ decreases. On the contrary, the edge temperature decreases in all plasma positions.

The density behavior after the P_{NBI} reduction is summarized as a parameter of R_{ax} position in Fig. 5(a). The axis of ordinate in the figure is normalized at t=2.3 s where the P_{NBI} is reduced. It is clear that the density increase after t=2.3 s is enhanced when the R_{ax} position is outwardly shifted. The ergodic layer thickness, λ_{erg}, is largely affected by the R_{ax} position. Then, the density increase rate is plotted against the λ_{erg} as shown in Fig. 5(b). Here, the axis of ordinate is expressed by a ratio of density at t=2.75s after the P_{NBI} reduction to the density at t=2.30s before the P_{NBI} reduction. The result indicates a clear correlation between the density increase and λ_{erg}.

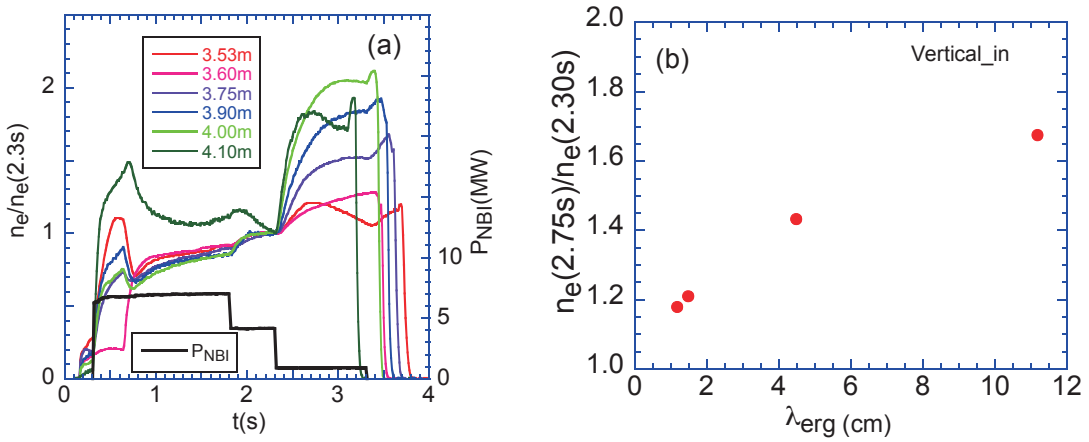

Fig.5 (a) Density rise normalized at t=2.3s as a parameter of R_{ax} position and (b) density rise after P_{NBI} reduction at t=2.75 s normalized by density before P_{NBI} reduction at t=2.30 s as a function of ergodic layer thickness, λ_{erg}, at inboard side of vertically elongated plasma cross section.

3. Edge particle confinement time

In LHD Hα emissions have been measured in several toroidal positions as a discharge monitor, i.e. 44 channel vertical parallel array at horizontally elongated plasma cross section, two 30 channel poloidal arrays at vertically elongated plasma cross section and 10 channel toroidal array. Particle confinement time, τ_p, is then evaluated by integrating the Hα emissions over the whole plasma surface based on the following equation;

$$\tau_p = N/\Phi_{in}, \qquad (1)$$

where N is the total ion number given by $N=\int \pi r^2 \times 2\pi R \times n_i(r) dr$ and Φ_{in} the total ion flux given by $\Phi_{in}=\int \varphi_{in}(\theta,\phi) ds$. The $\varphi_{in}(\theta,\phi)$ [particles/cm^2.s] calculated from Hα intensity and ionization event is the local ion flux at poloidal and toroidal angles of θ and ϕ, respectively.

The result is plotted against edge T_e at ρ=1 in Fig. 6(a). Two different groups are seen in the figure, i.e. high- and low-recycling discharges. The R_{ax}=3.53 and 3.60 m configurations with thinner λ_{erg} show low-recycling discharges. The R_{ax}=3.75, 3.90 and 4.00 m configurations with thicker λ_{erg} show high-recycling discharges, while the low-recycling is observed in low temperature discharges at $T_e l_{\rho=1} < 0.1$ keV. It means that most of particles in magnetic configuration with thick λ_{erg} do not enter the core plasma and simply coming back to divertor plates after ionizing at the peripheral region of the ergodic layer.

In order to explain the particle behavior before and after the P_{NBI} reduction ionization lengths, λ_i, of hydrogen molecules and atoms are calculated as shown in Fig. 6(b). Since the ergodic layer thickness in R_{ax}=3.90 m configuration is 5-10 cm which depends on the poloidal location, the divertor recycling is dominant when the edge T_e at outer region of the ergodic layer is high, e.g. 20 eV. But, once the edge T_e decreases, e.g. below 10 eV, the λ_i quickly becomes long and the value tends to exceed 10 cm. It means the discharge can have a good fueling efficiency when the edge T_e is low. Therefore, the low energy confinement appeared in the magnetic configuration with thick ergodic layer can be concluded in its high-recycling, although the poor deposition of NBI beam and smaller plasma radius are also a reason why the discharge performance is low in outward-shifted magnetic configurations in LHD.

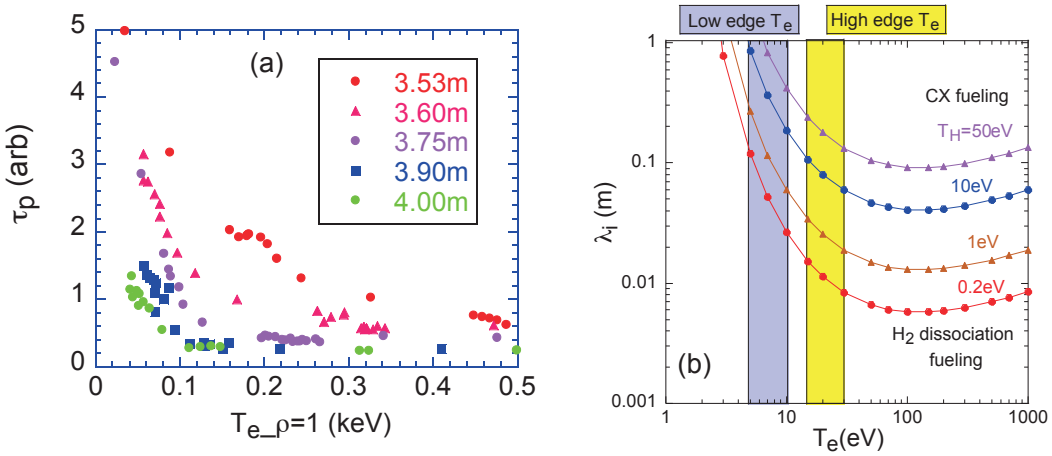

Fig.6 (a) Edge particle confinement time, τ_p, against T_e at ρ=1 as a parameter of R_{ax} position and (b) ionization length of hydrogen neutral and molecule against T_e as a parameter of neutral and molecule energies.

Acknowledgements

The authors thank all the members of the LHD team for their cooperation through the LHD experiment. This work was partially carried out under the LHD project financial support (NIFS15ULPP010) and partly supported by the JSPS-NRF-NSFC A3 Foresight Program in the field of Plasma Physics (NSFC: No.11261140328, NRF: No.2012K2A2A6000443).

Experimental results of deposited tungsten targets exposed to deuterium plasmas in KSTAR

N. Ashikawa[1,2], K. Katayama[3], S. Saito[4], S.H. Son[5], M.K. Bae[5], J.G. Bak[5], S.H. Hong[5], Y.W. Yu[6], F. Ding[6]

[1]*National Institute for Fusion Science, Toki, Japan*
[2]*SOKENDAI, Toki, Japan*
[3]*Kyushu University, Kasuga, Japan,*
[4]*NIT Kushiro College, Kushiro, Japan*
[5]*National Fusion Research Institute, Daejeon, Korea*
[6]*Institute of Plasma Physics Chinese Academy of Science, Hefei, China*

E-mail:ashikawa@LHD.nifs.ac.jp

1. Introduction

Areas of controllable wall retention are limited region (not fully thickness of walls) in fusion devices [1-3]. Hence, to understand a range of controllable thickness into plasma facing materials (PFMs) is important. However, tools of wall retention are limited, such as baking, wall conditioning discharges for the PFMs.

Tungsten (W) is a candidate material for plasma-facing components because of low solubility and low sputtering yield for hydrogen isotopes. During fusion plasma discharges, the W surface will be modified due to sputtering and re-deposition. The deposited W layer has a structure different from the original W material. Therefore, the evaluation of tritium retention in not only original materials but also in deposited layers is required. Moreover, tritium desorption property from deposited W layers has to be also understood for tritium recovery. Lab-scale experiments on hydrogen isotope behavior in deposited W layer formed by plasma sputtering has been performed in Kyushu University. However, in order to discuss tritium behavior in deposited W layers formed in a fusion reactor, the characterized deposited layer should be exposed to energetic particles having energy distribution in the fusion experimental devices. In this work, the common target materials of deposited W layers produced by hydrogen plasma sputtering in Kyushu University are exposed to deuterium plasma in EAST and KSTAR, and surface analyses are planned in Kyushu University and NIFS. An advantage of this deposited W layer is to use characterized target materials with the known parameters. Amounts of tritium inventory on deposited W layer on the plasma facing materials are evaluated and the proper tritium recovery method will be proposed. The obtained results will be useful also for understanding hydrogen isotope retention in fusion devices.

2. Experimental setup

Figure 1 shows the schematic drawing of cross-section at the equatorial plane in KSTAR. The poloidal electric probe system is located at the low field side around the equatorial planes at different positions on torus and measured particle fluxes [4]. Poloidal limiter probes array

locates about 160~170 mm away from the last closed flux surface (LCFS) and 74 mm behind the poloidal limiter. The deposition probe system is located at the section C in KSTAR [5]. The head position of the deposition probe system is about 10 cm below from the equatorial plane. At this position, target samples did not attach to plasmas directly. Three samples holders were set on the circular plate of 78 mm diameter, it was made by the stainless steel 316, and this was connected to the deposition probe system. Fig.2 shows a picture of sample holders. In this experiment, bulk W, deposited W on the bulk W, titanium, silicon, and stainless steel 316 targets were installed in the sample holders. In addition, three kinds of different W targets, Nilaco Corp., A.L.M.T. Corp., EAST-divertor type, were used. Two thermocouples were connected to side planes of sample holders, but data could not be detected due to damages of these thermocouples.

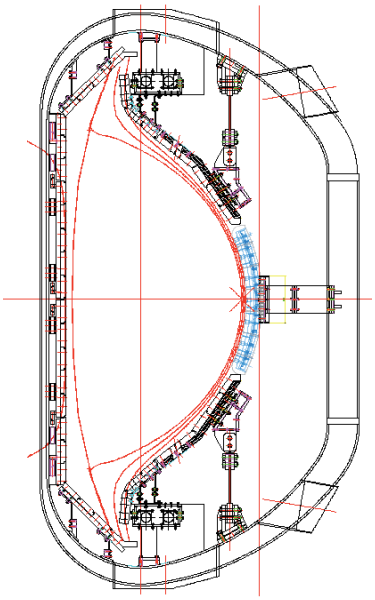

Fig.1 Poloidal cross section and poloidal probe system at the equatorial plane in KSTAR

Samples exposed to deuterium plasmas during two experimental date in KSTAR. Typical plasma duration is about 30 seconds and plasma shot numbers are from 13775 to 13851. Effective plasma discharges are about 25 shots and an effective exposure time during H-mode plasmas was counted about 120 seconds in this experiment. Particle fluxes were measured by the poloidal limiter probes around the equatorial plane and a distance from the LCFS to the head of probes is similar to that from the LCFS to the surface of target materials. From analytical results, particle fluences of 1E23 D^+/m^2 were calculated using above total exposure time.

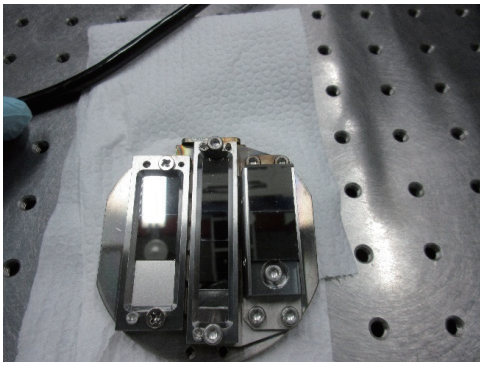

Fig.2 A picture of the sample holder in KSTAR.

X-ray photoelectron spectroscopy (XPS) analyzed surface contaminations and their chemical bindings on the target materials. An Al X-ray source of 400 W and a spot size of 800 μm were used. An argon (Ar) ion gun was used to etch the target samples and analysis of their depth profiles.

Total deuterium retention after plasma exposures was evaluated by thermal desorption spectrometry (TDS) measurements. The thermal desorption of molecules was measured by quadrupole mass spectroscopy (QMS). In laboratory experiments, it was reported that results of deuterium retention show clearly fluence dependences. As additional experiments, common tungsten target materials exposed to deuterium plasmas in tokamaks, EAST and KSTAR, in this A3 collaboration work. The first experiment in EAST was done in 2013 and KSTAR experiment was done in 2015.

3. Results and discussion

Surface contaminations on target material of stainless steel were measured by XPS, after deuterium plasma exposures. Major impurity contaminations on the surface of target materials are oxygen and carbon due to air contaminations. Fluorine (F) intensity was observed on the surface of the stainless steel target before Ar ion gun sputtering as shown in Fig.3 (a). A source of fluorine was considered due to a melting materials of insulator by a heating of plasma radiation. After short Ar ion gun sputtering, fluorine was not observed and only carbon impurity was remained as shown in Fig.3 (b). In this result, it was estimated that surface temperature of target materials, in particular, target samples at the upper side of the holder in Fig.2, was increasing a little during plasma exposures. The distance to the PCFS is estimated as shorter than that at the bottom side. Fig.3 (b) shows that impurity contaminations from erosion of plasma facing materials are negligible.

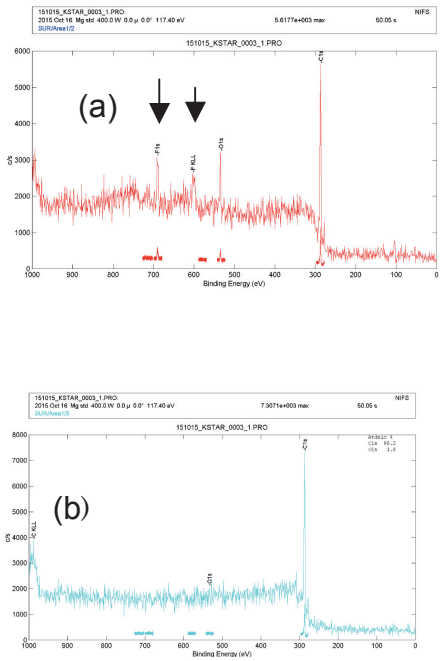

Fig.3 XPS survey scans at (a) before Ar ion gun sputtering and (b) after Ar ion gun sputtering on the stainless steel target material. Two arrows indicate F peaks.

Fig. 4 shows fluence dependences of deuterium retention on various W in the laboratory experiments. A temperature range of target materials was selected from 500 K to 573 K. These results of deuterium retention show clearly fluence dependences. As additional experiments, common W targets were exposed to deuterium plasmas in tokamaks, EAST and KSTAR (this experiment), and a fluences were about 1E22 D^+/m^2 and 1E23 D^+/m^2, respectively. Amounts of particle fluences in EAST were an estimation due to low sensitivity of probes on the target sample holders in EAST. In Fig.4, an analytical result of deuterium retention in EAST was plotted. Particle fluences in KSTAR experiment was of one order of magnitude higher than that of EAST experiment. Reasonable amounts of fluences were obtained in KSTAR for data set of deuterium retention vs fluences at difference tokamaks.

Bulk W samples with and without deposited W layers were exposed to deuterium plasma in EAST, 2013. Initial amounts of hydrogen were implanted by working gassed during sputtering to make deposition layer and a ratio between tungsten and hydrogen, H/W, is 0.032. These amounts of W/H before and after plasma exposures are the same. Retained deuterium after plasma exposure was implanted by deuterium plasma and the ratio between tungsten and deuterium, D/W, is 0.002. The retained deuterium in deposited W layer is at least one order of magnitude higher than that in bulk W [6]. In general, metal oxide layers on metal targets are regarded as one of trapping sites for hydrogen isotopes. In this experiment, initial oxide layers produced by air contaminations were removed during plasma exposures and influences of oxide layers for deuterium trappings are a few in this experiment. As other possibility of trapping sites for deuterium isotopes, a grain boundary is considered in W. Deuterium trapping site into deposited W layers will be discussed later with a comparison with a

numerical simulation.

4. Summary

Deuterium retention on deposited W targets exposed to deuterium plasmas have been investigated. Deuterium plasmas experiments of KSTAR were successfully done in 2015. Particle fluxes from deuterium plasmas were measured by poloidal probe system and total fluences are calculated. Fluences of KSTAR experiment was of one order of magnitude higher than that of EAST. Reasonable amounts of fluences were obtained in this KSTAR experiment for data set of deuterium retention vs fluences in difference tokamaks. Impurity contaminations on the target materials were negligible. A surface temperature will increase during plasma exposures. Analyses of deuterium retention after KSTAR plasma exposures is planned soon.

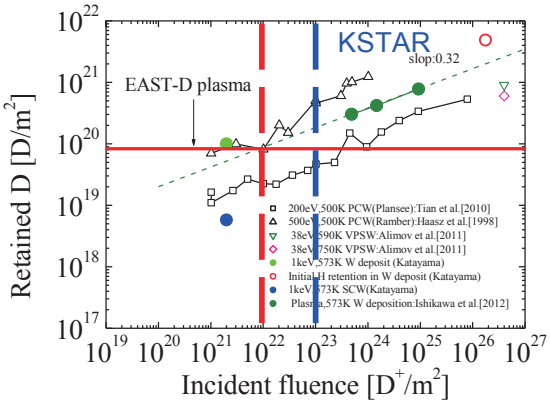

Fig.4 Deuterium retention vs fluences on deposited W targets. Temperature range is from 500 K to 573 K.

A comparison with simulation and analytical results for deuterium retention has been discussed as future works. Required parameters of target materials are incident energies of energetic particles and grain sizes measured by SEM. It is planned that simulations of a depth profile of working gasses and isotope exchanges in target materials.

5. Acknowledgements

This research was partly supported by the JSPS-NRF-NSFC A3 Foresight Program in the field of Plasma Physics (NSFC: No.11261140328, NRF: No.2012K2A2A6000443) and NIFS budget KUHR010 and ULFF004.

[1] J.S.Hu et al., Fusion Engineering and Design, 84(2009) 2167.
[2] T. Wauters at al., 39th EPS Conference on Plasma Phys., Stockholm, July 2-6, 2012.
[3] N. Ashikawa et al.,Plasma and Fusion Research, 6, (2011) 2402138.
[4] J.G. Bak, Y.S. Ho,H.S. Kim, et al., Contrib. Plasma Phys., 53(2013) 69.
[5] S.K.Hong, et al., Fusion Sci. and Tech., 63 (2015) 36.
[6] K.Katayama, N. Ashikawa, et al., Annual report of NIFS (2012 April - 2013 March).

Key issues of plasma surface interactions on EAST

J.L. Chen*, R. Ding, H. Xie

Institute of Plasma Physics, Chinese Academy of Sciences, Hefei 230031, P.R.China

The plasma facing components (PFCs) will experience strong plasma surface interactions (PSI) especially in long pulse and high performance plasma [1]. The lifetime of the wall components can be seriously reduced by the substantial particle and heat fluxes, and the impurities eroded from the wall can be transported long distance to the plasma and badly influence the plasma performance. Therefore, study the physical mechanism of plasma wall interaction (PWI) as well as the edge plasma behavior is quite necessary. The Experimental Advanced Superconducting Tokamak (EAST) was built to achieve long pulse and high performance plasma to study the physics and engineering issues relevant to the next-step long pulse fusion devices such as ITER and DEMO [2]. There are many PSI issues capable to be studied in EAST such as: practical test of W divertor and experiment for ITER, excessive heat load control, particle exhaust and impurity control as well as edge recycling and density control. In the following, more detailed information about EAST capabilities in PSI studies and some main recent research activities will be introduced.

The upper divertor of EAST tokamak has been upgraded from carbon to ITER like tungsten PFC in 2014. Three different plasma facing materials are currently in use at EAST: graphite for the lower divertor, tungsten for the upper divertor, and molybdenum for the first wall [3]. The upgraded ITER like W monoblock upper divertor can sustain about 8.4 MW/m^2 heat load with cooling water of 20 Celsius degree and 15s/15s on/off cycles. During the test, the mock up can even survive up to 1000 cycles with surface temperature up to 1150 Celsius degree. With the tungsten divertor, practical test of W divertor in tokamak and experiment for ITER is available to be performed in EAST. Currently, there are multiple PSI diagnostics in EAST such as IR imaging for upper divertor, W source spectroscopy for uppter tungsten divertor, visible spectroscopy for plasma and impurities near MAPES head, thermocouples and probes embedded in MAPES sample and LIBS and LIAS for first wall at high field side. A new upper cryo-pump has been installed recently, thus with the upper and lower in vessel cryo-pumps the particle exhausting rate can reach to about 110 m^3/s for D_2. Heat and particle flux diagnostics include the IR thermography and divertor embedded Langmuir probe arrays. The divertor surface temperature and target heat flux can be measured by IR camera with field of view of 47°×58°, temporal resolution of 8.7 ms with full frame, and spatial resolution of 4 mm. The divertor probe arrays can measure target plasma density, temperature and particle fluxes. Location the probe arrays at D and O ports makes toroidal asymmetry study available. The data measured by divertor embedded Langmuir probes can help to do the PWI, divertor and 3D physics studies. In the following the wall conditionings (WCs) on EAST will be briefly introduced. First, 200-250 Celsius degree is used for first wall baking. And then, discharge cleaning is performed to control impurity and recycling by glow discharge (GDC), high frequency glow discharge (HF-GDC), ion cyclotron (ICWC) and electron cyclotron. In order to control the impurity and H/D radio, boronization and siliconization are used as film coating on the EAST first wall. Lithium is also used in EAST by evaporation and powder or granule injection to control impurity and recycling as well as ELM pacing. At mid-plane of H port locates the material and plasma evaluation system (MAPES). Different kind of samples for

PWI study can be pulled by the system to the scrape off layer (SOL) of plasma for short sequences of plasma exposure. The system can handle as much as 20kg material with the remote control system and independent pumping system. Currently, MAPES has been upgraded with water cooling and heating system, and also gas puffing system. There are also various diagnostics on the MAPES such as Langmuir probes, spectroscopy and thermal couples.

Recently, edge magnetic topology in EAST has been found to be changed by low hybrid wave (LHW) induced by both 4.6 GHz and 2.45 GHz systems [4]. There are several helical current sheets induced by low hybrid current drive (LHCD) which lead to splitting of strike point and expand plasma wetted areas on the divertor region. Also, active control of divertor footprint pattern with resonant magnetic perturbation (RMP) has been performed in EAST. The results show that splitting of strike points in both L and H modes were observed. Toroidal asymmetry of footprint pattern was demonstrated in the experiment. Similar results are normally observed with LHW heating in EAST. Different experiments about regulating edge divertor conditions to control the power deposition on divertor in LHW-heated plasmas have been performed, such as super-sonic molecular beam injection (SMBI) into pedestal, argon seeding into divertor region [5], and normal gas puffing to control density and fluxes. In the divertor Ar impurity seeding experiment, 20% Ar with 80% D_2 has been puffed into the H mode plasma with neutral beam injection (NBI) power of 1.4 MW. Significant decrease of divertor particle flux and target temperature has been observed during Ar seeding. Moreover, much less disruption with impurity seeding in high plasma density discharges has been observed. However, still high high radiation in pedestal region has been found. Therefore, in the near future, Ne and N_2 impurity seeding are planned to integrate with high performance.

The heat and particle flux to PFCs during edge local mode (ELM) in H mode discharges can be much higher. Study of characteristics of ELM is essential in current devices. In and out divertor asymmetry during type I ELM has been analyzed in EAST. Strong dependence on Bt direction was exhibited by ELM in-out asymmetry, which is affected by classical drift and ballooning-like transport instability. The EAST experiments show that the particle flux favors inner divertor with normal toroidal magnetic field (Bt), while it favors outer divertor with reversed Bt. Study of plasma flows by high field side (HFS) and low field side (LFS) Langmuir probes (LPs) indicate that PS flow is dominant for the in-out asymmetry. Lithium technology has been developed in EAST for the purpose of reducing recycling, suppressing impurities, decreasing the ratio of H/(H+D) (to get effective ion cyclotron resonance heating (ICRH) coupling), and mitigating ELMs. Lithium coating conditioning can get as high as 94% of Lithium coverage in the vacuum vessel of EAST. And real-time Lithium injection has been performed to facilitate long pulse H-mode with or without ELMs. Lithium radiative shielding effectiveness on particle and heat flux during Li discharge has also been studied. During the experiment, there is strong interaction between Li and plasma with green radiative loop form at the same height with flowing liquid lithium (FLiLi). Plasma density and stored energy are increased, with reduction of ion saturation current at outer strike point (OSP) and increasing of power deposition width. With real time Li aerosol injection, steady state ELM-free H mode of 18 s has been achieved in EAST [6]. The Li injection can effectively suppress ELMs and then reduce heat load on targets. The long pulse ELM free H mode is accompanied by a strong edge coherent mode (ECM), which provides continues

exhaust of energy and particles in the absence of ELMs. It is a new way to facilitate ECM and achieve steady state ELM free H-mode plasmas.

As mentioned before, upper divertor of EAST has been upgraded to ITER like W divertor. Some experiments and physics related to the W in tokamak have been analyzed. The experiments indicate that W source increases during NBI heating, and AXUV signal near upper divertor rises corresponding to the increased WI signal. During type I ELMs, strong W source appears together with other impurities such as carbon, Lithium, and so on. The experiment also shows that the inter-ELM W sputtering depends on the electron temperature. The poloidal distribution of intra ELM W influx presents a significant increase at strike point region, corresponding to Te distribution at divertor. Experiments in EAST also show that W erosion mitigated by Li powder injection because active Li injection decrease recycling and edge neutral pressure and radiation cooling of divertor plasma reduces W erosion considerably.

Besides, there are many PWI related experiments have been performed on MAPES, such as migration experiments for ITER first wall (FW) [7], optimization of castellation structure for ITER, impurity deposition and fuel retention in gaps, deuterium retention in different W materials, deposition mitigation for first mirror, flowing liquid lithium limiter experiments. Also some experiment proposals are going to be performed in the near future like ripple effect on plasma performance using test blanket module (TBM) mockup, ICRF cleaning experiments, $^{13}CH_4$ injection experiments and erosion and deposition of W. Also, the in-situ wall characterization using laser induced breakdown spectroscopy (LIBS) in EAST has detected the depth profile of Li layer and H/D retention in the Li-co-deposited layer.

In conclusion, EAST capabilities on PSI study and main recent research activities relate to excessive control of heat load, particle exhaust and impurity and edge recycling and density has been introduced. In the near future, there are also many research plans related to PSI study will be performed. For the task of steady state divertor heat flux control, the experiment proposals are focus on radiative divertor with neon seeding from divertor and argon seeding from LFS mid-plane, synergy effect of divertor condition with LHW/RMP induced edge magnetic topology change, and fish tailing divertor with high frequency strike point sweeping. On the aspect of particle exhaust and low Z impurity control, dedicated experiments are proposed such as integration of cryo-pumping with in-out divertor particle flux asymmetry, optimization of divertor configuration to find strike point for best exhaust, and increase the closure of top divertor by dome optimization. While for the PSI studies under long pulse with mixed W/C environments, currently we have the research plans like W production, transport and control, exhaust, erosion, re-deposition, retention and C/W material migration; high frequency small ELMy H mode scenario, periodically remove core impurity; core tungsten exhaust with ECRH/ICRH, integration with core confinement.

Acknowledgements

The authors gratefully acknowledge supports by National Magnetic Confinement Fusion Science Program under Contract No.2013GB105003 and National Natural Science Foundation of China under contract No.11175205.

References

[1] J. Roth, E. Tsitrone, A loarte et al., J. Nucl. Mater. 390-391 (2009) 1-9.

[2] H.Y. Guo, X. Gao, J. Li et al., J. Nucl. Mater. 415 (2011) S369-S374.

[3] D. M. Yao, G.N.Luo, S.J. Du et al., Fus. Eng. and Design. 98-99 (2015) 1692-1695

[4] Y. Liang, X. Z. Gong, K. F. Gan et al., Phys. Rev. Lett. **110** (2013) 235002.

[5] H.Y. Guo, J. Li, B.N. Wan et al, Physics of Plasmas 21 (2014) 056107.

[6] J.S. Hu, Z. Sun, H.Y.Guo et al. Phys. Rev. Lett. 114 (2015) 055001.

[7] R.Ding, R.A.Pitts, D. Borodin et al, Nucl. Fusion 55 (2015) 023013.

Impurity transport study using Al injection with laser blow-off in the HL-2A ECRH plasma

Z.Y.Cui[1], K.Zhang[1], P.Sun[1], C.F.Dong[1], B.Z.Fu[1], P.Lu[1], X.T.Ding[1], S.Morita[2], S.D.Song[1], Y.Xu[1], Q.W.Yang[1] and X.R.Duan[1]

[1]Southwestern Institute of Physics, P. O. Box 432, Chengdu 610041, China

[2]National Institute for Fusion Science, Toki 509-5292, Gifu, Japan

Abstract

Impurity transport has been studied with trace impurity injection into the electron cyclotron resonance heating (ECRH) L-mode plasmas in the HL-2A tokamak. The effect of ECRH on impurity transport is investigated with scanning the ECRH deposition position in range ρ_d ~0-0.7. The progression of injected aluminum ions is monitored by the soft x-ray (SXR) arrays and bolometer arrays, for both having good temporal and spatial resolutions. The decay time during the decrease phase of the SXR after impurity injection clearly decreases with shifting the radial deposition position of ECRH inwards. This indicates that the impurity transport is clearly changed with changing the ECRH heating position. Based on the simulation with a one dimensional impurity transport code STRAHL, the diffusion coefficient is strongly increased with ECRH when compared with ohmic discharge. The convection velocity changes the sign from the negative (inward direction) in the ohmic discharge to the positive (outward direction) in the ECRH discharge. The enhancement of impurity transport becomes more significant and the impurity density profile becomes slightly hollow with central ECRH. It is instead peaked in the center when the ECRH deposits away from the plasma center.

1. Introduction

Impurities in fusion devices play a crucial role in plasma performances since they can enhance the radiation losses and affect the plasma stability. Especially, the discharge would be disrupted when the high Z impurities are accumulated in the plasma center. This could cause a serious damage to the first wall in the fusion reactor. Therefore, controlling impurities in the plasmas is an urgent and critical issue for ITER. In the current experiments, on the other hand, auxiliary heating, ECRH has a beneficial effect on the reduction of impurity content in the plasmas [1]. An increase in the central impurity diffusivity and a suppression of the convective pinch has been observed, sometimes even the rise to an outward impurity convection [2, 3]. However, the interaction of plasma facing components with edge plasma and non-thermal electrons become usually stronger when ECRH is applied. It might cause a careful concern for ITER in which a high-Z material such as tungsten is used as plasma facing components. Therefore, understanding impurity behaviors and physics behind is extremely required.

In this paper, the effect of ECRH on impurity transport is studied by using the laser blow-off (LBO) technique in the HL-2A tokamak (R/a = 165/40 cm). The impurity transport coefficients are determined using a 1D impurity transport code STRAHL [4]. Impurity transport with relation to the ECRH

deposition position has been studied. The comparison of impurity transport behaviors between the ECRH and ohmic discharge are also carried.

2. Experiment with trace impurity injection in the ECRH plasma

In HL-2A, aluminum as the trace impurity has been injected by LBO technique in the ECRH and ohmic discharges. The ECRH power deposition was scanned from the plasma center to the edge. The plasma parameters of these discharges are identical except the toroidal magnetic field. The time evolution of the main plasma parameters are shown in Fig. 1, where the ECRH power P_{ECRH}, toroidal magnetic field B_t, line-averaged electron density n_e, the central chord-integrated soft x-ray emission and bolometer signal are plotted from the top to the bottom. The temporal and spatial resolutions of soft x-ray arrays (5×20 channels) are 10 μs and 2.5 cm, respectively, and of the bolometer arrays (3×16 channels) are 50 μs and 2.5 cm, respectively. Al is injected at t = 600 ms. B_t shown in Fig. 1(b) is changed from 1.22 T to 1.41 T which corresponds to the change of ECRH power deposition position in the range ρ_d = 0, 0.13, 0.27, 0.41, 0.63, 0.70. Here, ρ_d is the normalized minor radius of the ECRH power deposition position. It shows that the injection of Al does not disturb the plasma parameter in any noticeable way, seeing in Fig. 1(c) on the observation of n_e as an example. By contrast, the characteristics of the Al injection can be clearly seen from the soft x-ray and bolometric signals. This means the amount of trace impurity is well controlled.

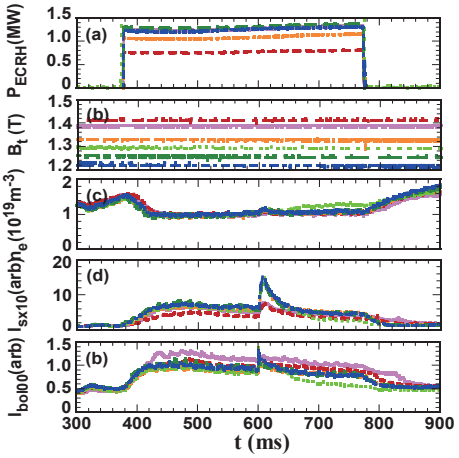

Fig.1 Time evolution of main plasma parameters in six discharge with ECRH deposition position scan.

The expansion of central chord-integrated soft x-ray emission during the time of Al injection is presented in Fig. 2(a) for the six discharges with ECRH. After Al injection, the intensity of soft x-ray increases firstly and then decreases gradually. However, it behaves differently when the ECRH power deposition changes. Seeing in the figure, when the ECRH is deposited in the central region (ρ<0.5) the increase and decrease of the SXR is obviously quicker than that with ECRH depositing at the outer part of plasma (ρ>0.5). After the SXR reaches its maximum, its intensity decreases exponentially. The decay time τ_d can be estimated by fitting the central chord SXR with a formula $I = I_0 e^{-t/\tau_d}$. The obtained τ_d is plotted in Fig. 2(b) as a function of the ECRH deposition position. It clearly shows that τ_d is much smaller with $\rho_d < 0.5$ than that with $\rho_d > 0.5$. This indicates the transport property of the injected Al impurity has been significantly changed with central ECRH, compared with the ECRH deposition position being far away from the plasma center. On the other hand, τ_d is generally larger than 90 ms for the ohmic discharge with the similar plasma parameters. The observations mean that the ECRH can strongly enhance impurity transport, especially with the central ECRH.

3. Simulation with 1D impurity transport code

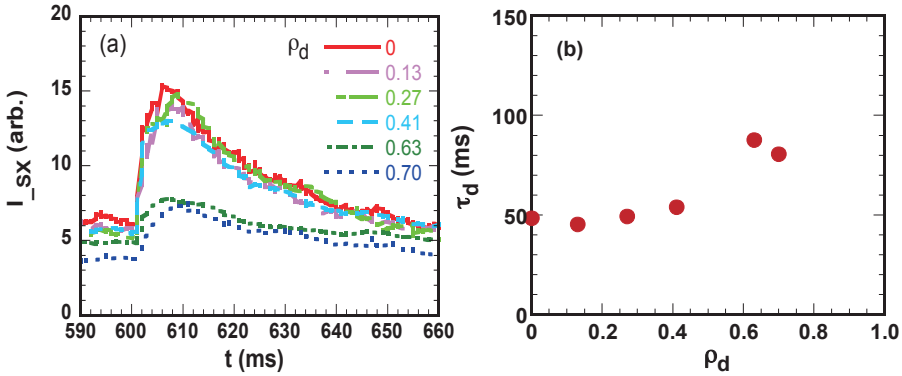

Fig.2 (a) Time trace of the core SXR signals after Al injection and (b) plot of decay time during the decrease phase of SXR as a function of ECRH deposition locations.

In order to quantitatively obtain the impurity transport coefficients, diffusion coefficient D and convection velocity V, a one dimensional impurity transport code STRAHL [4] has been applied. The measured plasma parameters of these discharges, especially the electron density and temperature profiles, are used as the input data in the code. The STRAHL code starts from an initial guess of the transport coefficient radial profiles. It solves the coupled continuity equations and reconstructs the emission measurements. Then the transport coefficients are modified iteratively until the difference between the reconstructed signals and the measured ones is minimized. The comparison between the simulation and the experiments are shown in Fig. 3, where the obtained transport coefficients for the best fitting are also plotted in the right panel. The result with the ECRH deposited at $\rho_d = 0.63$ is presented in the figure as an example. It shows that the diffusion coefficient profile, D(r), is strongly increased, especially in the outer part of plasma, while the convective velocity profile, V(r), is negative (inward direction) at the central region and positive (outward direction) in the outer part of plasma. Compared with the neoclassical transport coefficients simultaneously calculated in the code, the D and V are strongly increased with ECRH. That means the impurity transport is significantly enhanced with ECRH. The obtained D and V are also in good agreement with previous results [3, 5].

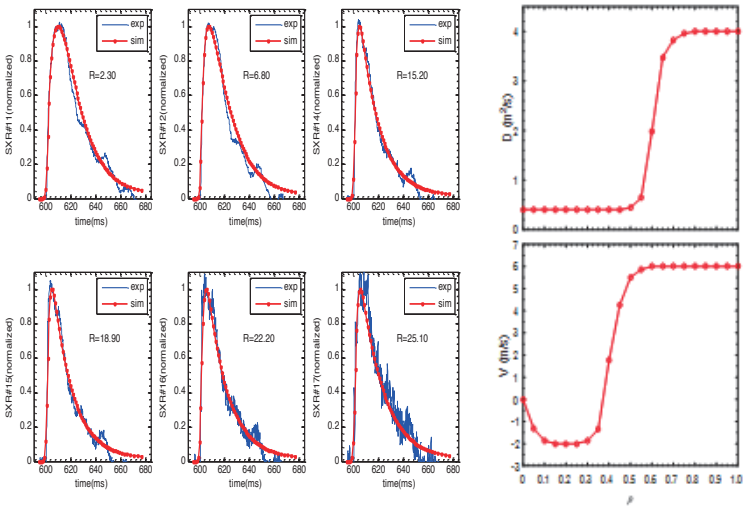

Fig. 3. Time evolution of soft x-ray brightness in different channels in the ECRH discharge. The background emission before LBO has been subtracted. The right panel is the obtained diffusion coefficient and convection velocity for the best fitting.

The simulations results of the discharges with scanning ECRH power deposition are summarized in Fig. 4. Seeing in Fig. 4(a),

both D and V are increased when the deposition position of ECRH shifts towards the plasma center. The V reverses to the outward direction (positive) with ECRH. However, it directs inwards (negative) in the ohmic discharges (not shown here). In Fig. 4(b), the calculated Al density profile is plotted with relation to three ECRH deposition locations. It also shows that the impurity density profile becomes slightly hollow with on-axis ECRH, while it is peaked in plasma center with off-axis ECRH. This confirms that the impurity density peaking can be effectively controlled with central ECRH.

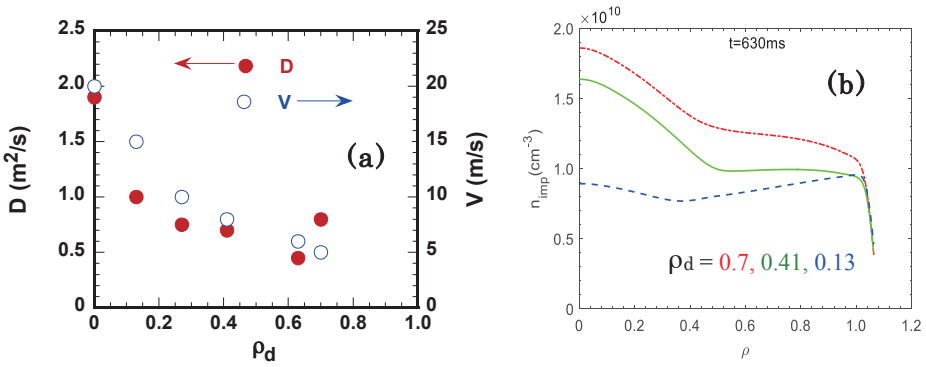

Fig. 4 Plot of (a) obtained impurity transport coefficients as a function of ECRH deposition locations and (b) impurity density profiles with ρ_d=0.7, 0.41 and 0.13.

4. Summary

The effect of ECRH on impurity transport has been studied using LBO technique with Al injection. The impact of ECRH power deposition position on impurity transport has been investigated. The experiment shows that the impurity transport has been strongly enhanced when ECRH is applied, comparing to the ohmic discharge. The decay time during the decrease phase of the SXR after Al injection obviously decreases with inwards shifting the ECRH deposition position. The simulation result shows that the convection velocity changes from the inward direction in the ohmic discharge to the outward direction in the ECRH discharge. Both diffusion and outward convection are increased with ECRH. The increment of D and V becomes more significant with on-axis ECRH than that with off-axis ECRH. The density profile of Al become slightly hollow with on-axis ECRH but it peaks in the core with off-axis ECRH. That means the impurity control with central ECRH is more efficient.

Acknowledgements

This work was partly supported by the National Natural Science Foundation of China (grant no. 11375057 and no. 11175061), Chinese National Magnetic Confinement Fusion Science Program (no. 2014GB108003), and the JSPS-NRF-NSFC A3 Foresight Program in the field of Plasma Physics (NSFC: No.11261140328, NRF: No.2012K2A2A6000443).

References

[1] R.Dux, et al., Plasma Phys. Control. Fusion **45**(2003)1815.

[2] J.Hong, et al., Nucl. Fusion **55**(2015)063016.

[3] X.W.Cui, Z.Y.Cui, B.B.Feng, et al., Chin. Phys. B **22**(2013)125201.

[4] R.Dux, 2006 Technical Report No 10/30 IPP Garching Germany.

[5] Z.Y.Cui, S.Morita, H.Y.Zhou, et al., Nucl. Fusion **55**(2013)093001.

Comparison of impurity transport among different LHD configurations based on radial profiles of Fe n=3-2 L_α transition array

X.L.Huang[1], S.Morita[1,2], T.Oishi[1,2], I.Murakami[1,2],M.Goto[1,2], H.M.Zhang[2] and Y.Liu[2]

[1]National Institute for Fusion Science, Toki 509-5292, Gifu, Japan

[2]SOKENDAI (Graduate University for Advanced Studies), Toki 509-5292, Gifu, Japan

Abstract

Using the space-resolved extreme ultraviolet (EUV) spectrometer working in the wavelength range of 10-130 Å, the radial profiles of Fe n = 3–2 L_α transition array consisting of emissions from ionization stages of Ne-like Fe^{16+} through Li-like Fe^{23+} ions are simultaneously measured. Based on the density profiles of Fe ions, the radial structure of transport coefficients, i.e. diffusion coefficient and convective velocityare analyzedwith help of a one-dimensional impurity transport code. The impurity transportatahollow n_e profile is then compared in three magnetic configurations with R_{ax} = 3.6 m, 3.75 m and 3.9 m.Comparison of transport coefficients at different R_{ax} shows both the diffusion coefficient and the convective velocity have the smallest value at R_{ax} = 3.75 m. Outward convection is usually observed near the plasma center. However, the convection can change its direction below a threshold of normalized density gradient. The threshold of the normalized density gradient is larger at R_{ax} = 3.75m and R_{ax} = 3.9m.

1. Introduction

Radial transport of impurity ions still remains several important issues in magnetically confined fusion devices, since the plasma performance is significantly affected by the radiation loss and fuel dilution caused by the impurity.In the Large Helical Device (LHD), the density profile can exhibit a variety of distributions of a peaked, flat or hollow shape, depending on plasma parameters such as B_t, T_e, and n_e. Therefore, it is of great importance to investigate the corresponding impurity transport in the plasma core of LHD [1]. As a typical phenomenon in the impurity transport it is reported that the impurity accumulation can be also observed in LHD as well as tokamaks, in which the transport is analyzed based on an assumption of the radial structure of convective velocity when a centrally peaked density profile occurs in high-density LHD discharges [2]. Formation of the hollow or flat density profile in the LHD is quite unique compared to the tokamak. Therefore, LHD plasmas give a good opportunity for studying the impurity transport through analysis of the radial structure in the transport coefficient, in particular, in relation to the density and temperature gradients. Analysis on the detail structure of transport coefficients is essential for understanding of the radial transport. On the other hand, the impurity transport could also depend on the magnetic configuration. When the position of magnetic axis changes, the helical ripple varies and thus affects the neoclassical transport.Comparison of the impurity transport coefficients among different LHD configurations will beuseful to clarify the contribution of neoclassical and anomaloustransport in impurity flux.

It should be noted that the iron transport can be analyzed along the minor radius without any assumption on the radial structure of transport coefficients because the Fe L_α transition with several ionization stages is emitted over wide range of the radial plasma location.

2. Experimental setup

The extreme ultraviolet (EUV) system used in the present study working in the wavelength range of 10-130Å mainly consists of an entrance slit, a spatial-resolution slit, a gold-coated concave varied-line-spacing (VLS) laminar-type holographic grating with a groove density of 2400 per mm and a charge-coupled device (CCD) detector with 1024 × 255 pixels (26μm×26μm/pixel) [3]. The EUV spectrometer is installed on a mid-plane port at the backside of a rectangular vacuum extension chamber. Figure 1shows theschematic of the EUV system

The elevation angle of the central viewing chord is exactly aligned to make possible the vertical profile measurement at upper half of the elliptical plasma, i.e. Z = 0–50 cm, as shown in Fig. 1(a). A relatively long distance between the spectrometer and the plasma is necessary for observing the vertical plasma range of 50 cm. In practice the distance between the central plasma position and the entrance slit of the spectrometer is set to 9157 mm when the plasma axis position is R = 3.90 m. Since the distance between the entrance slit and the CCD detector is roughly 470 mm, which is a weak function of wavelength, we obtain a multiplication factor of 19.5. EUV radiation emitted from LHD plasmas passes through the entrance slit and reaches the grating adjusted at the angle of incidence of 88.6◦. The iron radiation diffracted on the grating is focused on the focal plane and recorded by the CCD detector. The large angle of incidence is necessary for observing the EUV light in such a short wavelength range with high throughput.

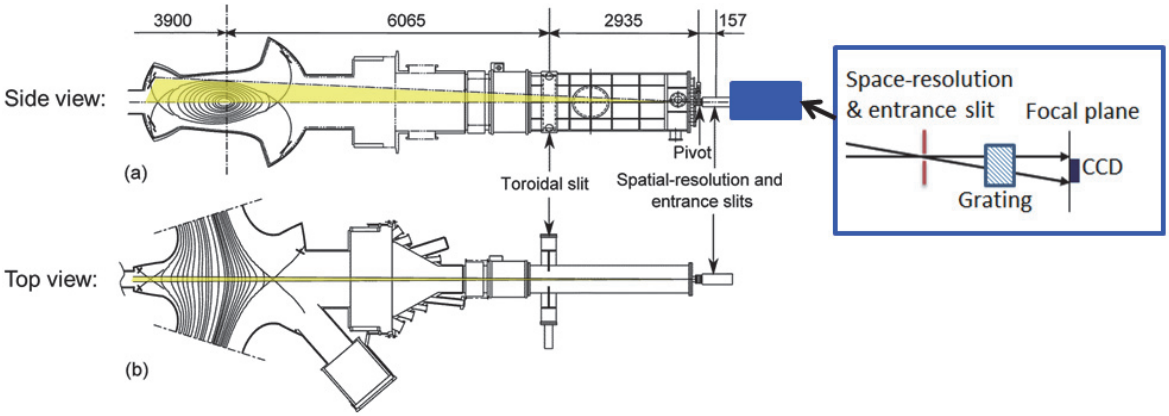

Fig.1Schematic of short-wavelength space-resolved EUV system.

3. Spectrum and radial profiles of Fen = 3–2 L_α transition array

Iron spectrum of the n = 3-2 L_α transitions between 10 and 20 Å has beenmeasured by injecting an iron impurity pellet. A typical result is shown in Fig. 2. A lot of L_α transitions from highly ionized Fe ions are observed in thespectrum. Since several Fe lines are blended with other Fe lines at severalwavelength intervals, the spectrum appears with structure like pseudo continuum. Inparticular, it is enhanced in the

wavelength range of 12-16 Å. The reason may becaused by a lack of the spectral resolution. It is often hard to distinguish the spectralline individually. Nevertheless, the ionization stage of Fe L_α transitions basicallyincreases step-by-step when the wavelength decreases from 20 Å to 10 Å. Theresultant spectrum at such a narrow wavelength interval then exhibits Fe transitions ina variety of ionization stages of Ne-like to Li-like ions, i.e., FeXVII to FeXXIV.

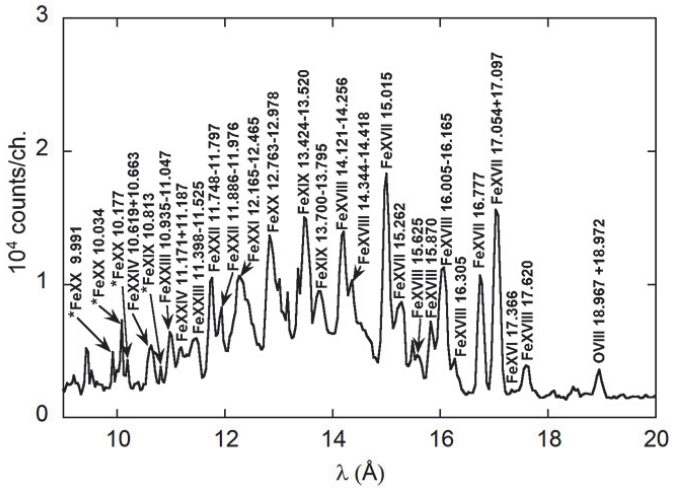

Fig.2Fe n = 3–2 L_α spectrum measured after iron impurity pellet injection in NBI discharge with central electron temperature of 3keV. The asterisks (*) before wavelengths denote that two or more lines are blended into the same wavelength position.

Figure 3 shows typical chord-integrated intensity profiles of FeXVII (Fe^{16+}) to FeXXIV (Fe^{23+}) which are observed after iron pellet injection. The iron density profile in each ionization stage is derived with the local emissivity profile reconstructed from the measurement taking into account the elliptical magnetic surface calculated with VMEC code and the density and temperature profiles.The peak position of each profile moves insidewith increasing ionization stage. The FeXXIII and FeXXIV indicate an almost flat profile in thevicinity of plasma center reflecting a hollow iron density profile.

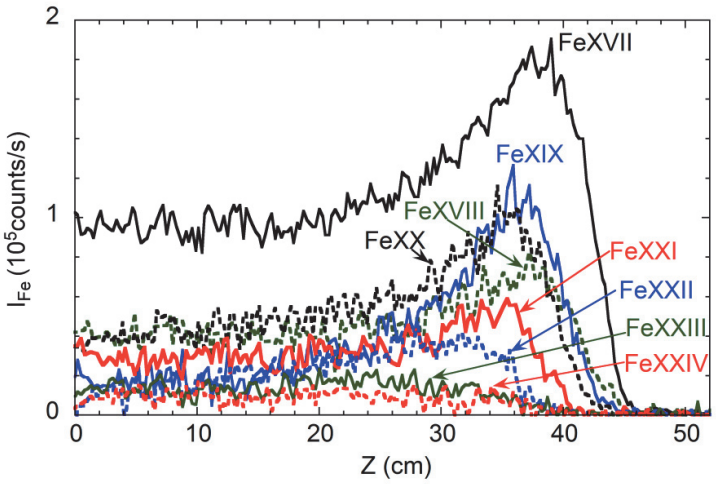

Fig.3Chord-integrated radial intensity profiles for L_α emissions of FeXVII to FeXXIV.

4. Impurity transport simulation

A one-dimensional impurity transport code is employed to determine the transport coefficient [4]. It is assumed that the impurity ions satisfy the following equations of transport and continuity.

$$\Gamma_I^K = -D\frac{\partial n_I^K}{\partial r} + Vn_I^K \quad (6.1)$$

$$\frac{\partial n_I^K}{\partial t} = -\frac{1}{r}\frac{\partial}{\partial r}r\Gamma_I^K + n_e\left[S_I^{K-1}n_I^{K-1} - \left(S_I^K + \alpha_I^K\right)n_I^K + \alpha_I^{K+1}n_I^{K+1}\right] \quad (6.2)$$

where $\Gamma_I^K, n_I^K, D, V, S_I^K$ and α_I^K are the particle flux, the ion density, the diffusion coefficient, the convective velocity, the ionization rate coefficient and the recombination coefficient of impurity ions in the Kthionization stage, respectively. Positive values of V stand for outward and inward convection.

Updated rate coefficients for ionization and recombination have been included in the present transport code [5-7]. With given transport coefficients and radial profiles of plasma parameters, the code yields the impurity ion density profile in all ionization stages as a function of time. The transport coefficient near the emissivity peak can be determined by comparing the emissivity profile between the experiment and the simulation. In order to determine the transport coefficient at the whole plasma radius, the iron emission is simultaneously analyzed in several ionization stages. The minimization of deviation between measured and simulated impurity profiles and time evolution of Fe emissions can determine the transport coefficient profile.

5. Comparison of impurity transport at different R_{ax}

Pellet injection experiments have been carried out in LHD for comparison of iron impurity transport at different magnetic axis position R_{ax} = 3.6m (inward shifted configuration), 3.75m (standard configuration) and 3.9m (outward shifted configuration) with magnetic field B_t = 2.5-2.7T.Figure 4(a) shows the typical temperature and density profiles in the three magnetic configurations. It should be noted that the density profiles are all hollow and peaked near ρ = 0.8. The time evolution of FeXVIII and FeXXI emissions is shown in Fig. 4 (b) and (c).The FeXVII emission are distributed near the last closed flux surface (LCFS) while the FeXXI emission are close to the plasma center. The decay time of the emissions reflects the confinement time of the corresponding impurity ions. The confinement time of Fe ions is longer near the plasma center than that in the edgein the cases ofR_{ax}= 3.6 m and 3.75 m while impurity accumulation seems to appear in the R_{ax}=3.9m case.Among the three magnetic configurations, the impurity confinement time is the shortest at R_{ax} = 3.6 m and increases with the magnetic axis shifting outwards.

Previous analysis [8] shows that the diffusion coefficient increases with increasing minor radius. This could explain the longer confinement time in the plasma center. On the other hand,an outward convective velocity is obviously observed in the core plasma region at ρ< 0.8. The convective velocity changes from outward to inward at certain radial plasma location in the peripheral region where the density gradient changes the sign, i.e. from positive to negative. This suggests the convective velocity is correlated with the density gradient.

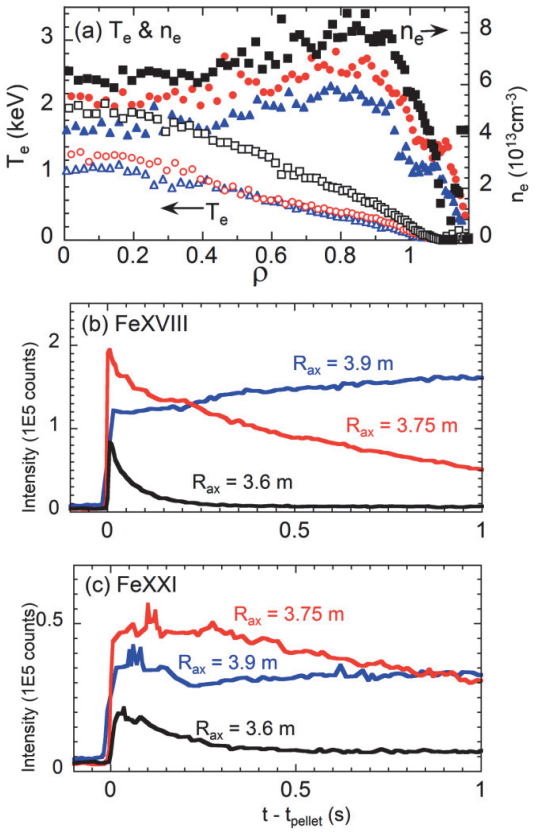

Fig. 4 (a) Electron temperature (hollow symbols) and density (solid symbols) profiles for the cases ofR_{ax} = 3.6m (sqaures), Rax = 3.75m (circles), Rax = 3.9m (triangles); time evolution of (b) FeXVII and (c) FeXXI emissions at R_{ax} = 3.6m (black lines), Rax = 3.75m (red lines), Rax = 3.9m (blue lines)

Transport coefficients at ρ = 0.5 of a hollow density profile are compared among the three magnetic axes. Figure 5 shows the diffusion coefficient D as a function of electron density. The diffusion coefficient has the smallest value at R_{ax} = 3.75m, whereas the neoclassical theory predicts the particle transport is most reduced at inward shifted configuration (R_{ax} = 3.6m). This suggests an important role of anomalous transport. There is no significant difference in the diffusion coefficient between R_{ax} = 3.9m and 3.6m. Figure 6 shows the convective velocity as a function of normalized density gradient ($(dn_e/n_e)/dr$) because the convection strongly depends on the density gradient as discussed above. The values of the convective velocity in the three configurations have similar results to the diffusion coefficient. However, the convective velocity can be zero or negative at the normalized density gradient below a threshold value. This threshold seems to be larger at R_{ax} = 3.75 m and R_{ax} = 3.9 m. This means the impurity accumulation may easily occur when the density increases. This result of the convective velocity could well explain the difference in confinement time of impurity ions in the three magnetic configurations as shown in figure 4. Further analysis will be performed in the near future to clarify the driving mechanisms of the difference in the impurity transport under the three magnetic configurations.

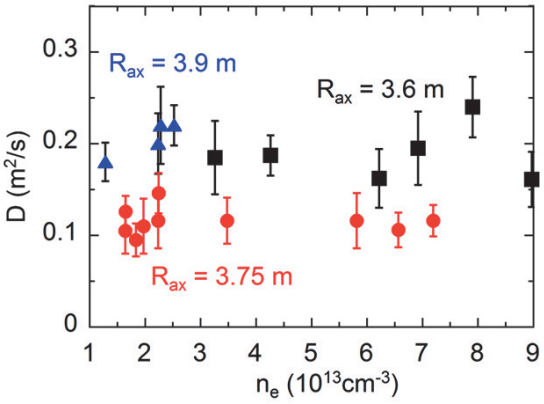

Fig. 5 Diffusion coefficient at ρ= 0.5 as a function of density for the cases of R_{ax}= 3.6m (squares), 3.75m (circles) and 3.9 m (triangles).

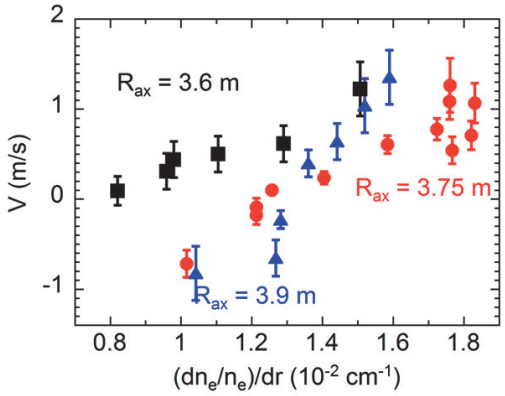

Fig. 6 Convective velocity at ρ= 0.5 as a function of density for the cases of R_{ax}= 3.6 m (squares), 3.75 m (circles) and 3.9 m (triangles).

6. Summary

With help of the transport code, the transport coefficients are successfully obtained analyzing radial profiles of Fe n=3-2 L_α transition array measured in LHD. Decay time analysis of Fe emissions with a hollow density profile indicates the impurity confinement time at plasma center is longer than that near the plasma edge at R_{ax} = 3.6 m and 3.75 m while impurity accumulation is observed in theR_{ax} =3.9 m case. The impurity confinement time increases when the magnetic axis moves outwards.The diffusion coefficient is found to be smallest at R_{ax} = 3.75 m in contrast with the prediction of R_{ax} = 3.6 m. The convective velocity increases with increasing normalized density gradient. When the density gradient decreases, the convective velocity could become negative even at a hollow density profile.The threshold of the normalized density gradient at which the outward convection is appeared seems to be larger at R_{ax} = 3.75m and R_{ax} = 3.9m. The result of transport coefficients can well explain the difference in the confinement time of impurity ions observed in the pellet injection experiments.

Acknowledgements

The authors thank all the members of the LHD experiment group for their cooperation including technical supports.This work was partly supported by the JSPS-NRF-NSFC A3 Foresight Program in the field of Plasma Physics (NSFC: No.11261140328, NRF: No.2012K2A2A6000443).

References

[1] S. Morita *et al.*, Plasma Sci. Technol. **11**(2009) 402.

[2] C. F. Dong *et al.*, Plasma Sci. Technol.**15**(2013) 230.

[3] X.L.Huang*et al.*, Rev. Sci.Instrum.**85** (2014) 11E818.

[4] T. Amano, J. Mizuno, and J. Kako, Simulation of impurity transport in tokamak, Int. Rep. IPPJ-616, Institute of Plasma Physics, Nagoya University (1982).

[5] N. R. Badnell, Astrophys. J. Suppl. Ser. **167**(2006) 334.

[6] N. R. Badnell*et al.*, Astron. Astrophys. **406**(2003) 1151.

[7] K. P. Dere, Astron. Astrophys**466**(2007) 771.

[8] X. L. Huang *et al.*,Poceedingsof 42nd EPS Conference on Plasma Physics, (2015) P4.183.

Electron stochastic motions in the presence of lower hybrid waves

Yueheng Huang[1, 2, 3], Nong Xiang[1, 3], Guozhang Jia[1, 3], Dehui Li[1, 3]

1 Institute of Plasma Physics, Chinese Academy of Sciences, Hefei 230031, China

2 University of Science and Technology of China, Hefei 230026, China

3 Center for Magnetic Fusion Theory, Chinese Academy of Sciences, Hefei 230031, China

Xueyi Wang[4], and Yu Lin[4]

4 Physics Department, 206 Allison Laboratory, Auburn University, AL 36849-5311, USA

Abstract:

The interactions between electrons and multiple electrostatic plane waves with different phase velocities. It is well known that as the resonance overlap occurs, the motions of trapped electrons become stochastic which results in electron heating. However, in these studies the evolution of the wave field is not taken into account. In this work, the interactions between electrons and multiple lower hybrid waves are investigated via particle-in-cell (PIC) simulations based on GEFI framework [Yu Lin, Xueyi Wang, Zhihong Lin and Liu Chen, Plasma Phys. Control. Fusion 47, 2005, 657]. It is shown that the orbits of trapped electrons in each wave field are altered in the presence of other lower hybrid waves. As a result, the damping of this wave is significantly enhanced. As the resonances overlap, a corresponding plateau of the electron distribution function can be formed. The results are helpful to understand the interactions of lower hybrid waves and plasmas during lower hybrid current drive in Tokamaks.

I. Introduction

Tokamak steady-state operations require efficient non-inductive plasma current drive. Lower hybrid (LH) wave current drive (LHCD) is currently the most efficient method to drive the plasma current and is able to provide a continuous off-axis toroidal current for plasma control ［1-4］. In present-day LHCD experiments, the input power of the LH wave is typically up to a few mega-watts. It can be expected that nonlinear plasma-wave interactions could be very significant. In fact, different nonlinear processes have been observed in many LHCD experiments [4-6]. It is well known that LH wave energy is absorbed by electrons via Landau damping, and achieving an efficient electron Landau damping is a key for LHCD. If the wave amplitude is finite, the effect of the perturbed orbit needs to be taken into account which may cause the wave amplitude oscillates as the time is longer than the bouncing period of the trapped electron [7, 8].

For charged particles of a plasma moving in the fields of two plane waves, it refers to a two-degree-freedom Hamiltonian system, large scale stochasticity (L.L.S) emerge as the resonances overlap (stochastic layers overlap actually) [9, 10], this stochasticity may lead to particle diffusion and heating. Stochastic heating (or acceleration) have been studied by many works. Menyuk et al [11] investigated the interaction of electrons with a Langmuir wave by

self-consistent and non-self-consistent simulations. It is found that the wave propagating obliquely with respect to a magnetic field has many resonances. When the resonances overlap, there is a transition between regular and stochastic particle motion, leading to a strong decrease in the final wave amplitude. Karney [12, 13] studied the stochastic ion heating by a LH wave. It is found that, for ions with $v_\perp \geq \omega/k_\perp$ in the field of a LH wave and a constant background magnetic field, the motion is stochastic when resonances overlap in surface of section plots. However, the published works so far are not based on self-consistent treatment.

In this work the interactions of electrons with multiple lower hybrid waves is studied via GEFI code [14].

II. Simulation model and results

The simulation is carried out in a one-dimensional domain (x direction). The boundary conditions are periodic. The plasma is uniform, and initial distribution function of the particles is Maxwellian. The main parameters are set as follows. The mass ratio is $m_i/m_e = 1836$. The equilibrium density is $n_{e0} = n_{i0} = 2.28\times10^{19} m^{-3}$. The electron and ion thermal speeds are $V_{the} = \sqrt{T_e/m_e}, V_{thi} = \sqrt{T_i/m_i}$, where the temperature are $T_e = T_i = 0.512\text{keV}$. The background magnetic field, is assumed to be in the x-y plane, B_{0x} = 0.11T, B_{0y} =1.53 T, accordingly, $k_p/k_\perp = 0.075$. The length of the plasma is $L = 235.3\rho_e$. The cell number is 128, and the particle number per cell is 20000. The time step is $\Delta t = 1/\Omega_{ce}$

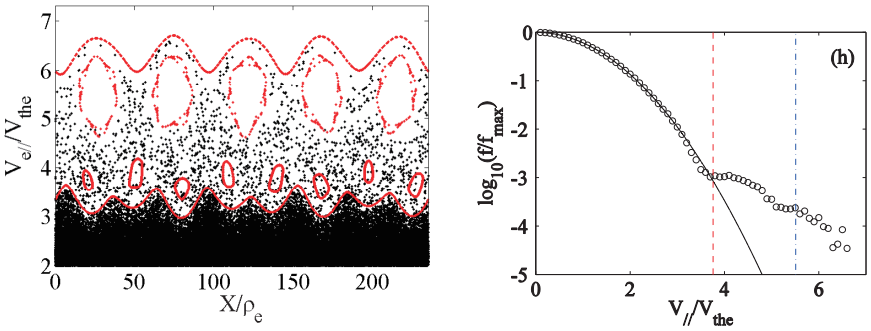

Fig.1. Phase plot of electrons and the electron distribution function for s =1.07.

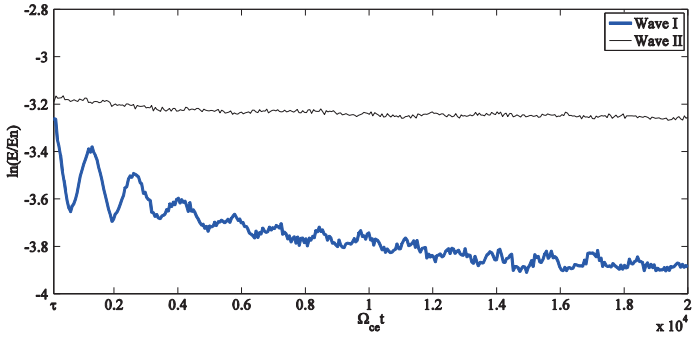

FIG. 2.The outline of time evolution of the two LH waves' electric field in nonlinear regime, thick blue lines for Wave I and thin black lines for Wave II(τ=111Ω_{ce}^{-1}, $E_n = V_{the}B_0 = 1.46\times10^7 V/m$)for s=1.07.

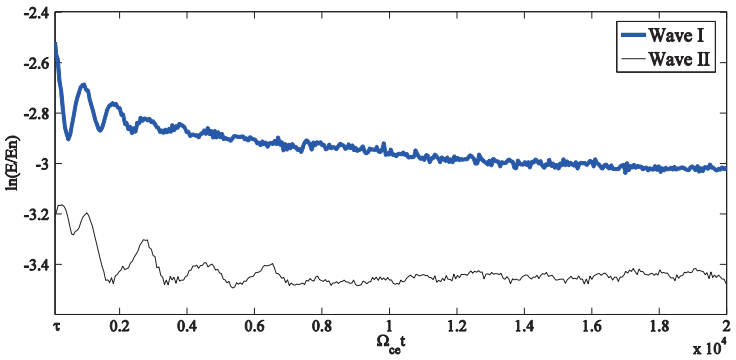

FIG. 3.The outline of time evolution of the two LH waves' electric field in nonlinear regime, thick blue lines for Wave I and thin black lines for Wave II(τ=111Ω_{ce}^{-1}, $E_n = V_{the}B_0 = 1.46\times10^7\ V/m$) for s=1.36.

Firstly, we show the result for s=1.07. We use the Poincaré section to estimate whether the motion of an electron with a certain position in phase space will be regular or chaotic at $t = 0$, eight high dense clusters of electrons within the stochastic sea are shown in Fig. 1 and few electrons are in the islands in which the electrons maymove regularly.

In Fig. 2, the amplitude of Wave I oscillates for several period which is mainly modulated by the initial high dense clusters of electrons. But the clusters would not hold for so long time and the wave energy would damp because of the chaotic phase mixing process. Finally the amplitude approaches an asymptotic constant*ln* (E_1/E_n) =-3.9 which is lower than that in case 1. The damping is enhanced by chaotic phase mixing of the chaotic orbits. On the other hand, The amplitude of Wave II is also affected slightly by a few electrons with velocities close to V_{p2}. Fig. 3 shows the evolution of E_1 and E_2 in the natural logarithm scale. The amplitude of Wave I oscillates several period and *ln* (E_1/E_n) approachs to -4.4. On the other hand, the amplitude of Wave II oscillates more obviously than that in case 2 because there are more considerable electrons with velocities close to V_{p2} which can be seen in the corresponding parallel velocity distribution.

III. Summary

When the amplitude of the off-resonant wave is larger and the two resonances overlap, the L.L.S emerges in Poincaré surface of section. The damping of Wave I is enhanced, but Wave II is slightly affected because the number of the electrons close to V_{p2} is not enough.

As the two resonances overlap more strongly, the size of stochastic regions become larger thus leading stronger diffusion in phase space. The plateau in the electron velocity distribution function is more significantly broadened and the damping is greatly enhanced. For the parameters similar to Tokamak experiment plasma, 40~60 percent of the energy could be absorbed by the electrons in the nonlinear wave-particle process. This process may not be

ignored in LHCD experiment. It should be noted that there are only two LH waves in the simulation, this study could be partially give a simple physics picture of wave-particle interactions in LHCD experiments with high input wave power. Fully understanding of such nonlinear processes with more LH waves will be studied in future works.

Acknowledgment : This work is supported partially under the JSPS-NRF-NSFC A3 Foresight Program in the field of Plasma Physics (NSFC No.11261140328).

References

1. Fisch, N.J., *Confining a Tokamak Plasma with Rf-Driven Currents.* Physical Review Letters, 1978. **41**(13): p. 873-876.
2. Fisch, N.J., *Theory of Current Drive in Plasmas.* Reviews of Modern Physics, 1987. **59**(1): p. 175-234.
3. PATRICK H. DIAMOND, S.-I.I., KIMITAKA ITOH, *MODERN PLASMA PHYSICS*, in *Volume 1: Physical Kinetics of Turbulent Plasmas*. 2010, Cambridge University Press.
4. Cesario, R. and V. Pericoliridolfini, *Study of the Parametric-Instabilities in the Lower Hybrid Frequency-Range in the Ft Tokamak.* Nuclear Fusion, 1987. **27**(3): p. 435-445.
5. Cesario, R., et al., *Plasma edge density and lower hybrid current drive in JET (Joint European Torus).* Plasma Physics and Controlled Fusion, 2011. **53**(8).
6. Baek, S.G., et al., *Measurements of ion cyclotron parametric decay of lower hybrid waves at the high-field side of Alcator C-Mod.* Plasma Physics and Controlled Fusion, 2013. **55**(5).
7. Oneil, T., *Collisionless Damping of Nonlinear Plasma Oscillations.* Physics of Fluids, 1965. **8**(12): p. 2255-&.
8. Wharton, C.B., J.H. Malmberg, and T.M. Oneil, *Nonlinear Effects of Large-Amplitude Plasma Waves.* Physics of Fluids, 1968. **11**(8): p. 1761-&.
9. Zaslavsk.Gm and Filonenk.Nn, *Stochastic Instability of Trapped Particles and Conditions of Applicability of Quasi-Linear Approximation.* Soviet Physics Jetp-Ussr, 1968. **27**(5): p. 851-&.
10. Escande, D.F., *Large-Scale Stochasticity in Hamiltonian-Systems.* Physica Scripta, 1982. **T2**: p. 126-141.
11. Menyuk, C.R., *Effect of a Transition between Regular and Stochastic Electron Motion on the Evolution of an Obliquely Propagating Langmuir Wave.* Physics of Fluids, 1983. **26**(3): p. 705-723.
12. Karney, C.F.F., *Stochastic Ion Heating by a Lower Hybrid Wave.* Physics of Fluids, 1978. **21**(9): p. 1584-1599.
13. Karney, C.F.F., *Stochastic Ion Heating by a Lower Hybrid Wave .2.* Physics of Fluids, 1979. **22**(11): p. 2188-2209.
14. Lin, Y., et al., *A gyrokinetic electron and fully kinetic ion plasma simulation model.* Plasma Physics and Controlled Fusion, 2005. **47**(4): p. 657-669.

Simulations of Energetic Particle Driven Geodesic Acoustic Mode in 3-dimensional LHD Equilibrium

H.Wang[1], Y.Todo[1,2] and Y.Suzuki[1,2]

[1]National Institute for Fusion Science, Toki 509-5292, Gifu, Japan

[2]SOKENDAI (Graduate University for Advanced Studies), Toki 509-5292, Gifu, Japan

Abstract

The first simulation results of energetic particle driven geodesic acoustic mode (EGAM) in 3-dimensional Large Helical Device (LHD) equilibrium are investigated with a hybrid simulation code for energetic particles and magnetohydrodynamics (MHD). In this work, the EGAM in 3-dimensional helical configuration and the EGAM in tokamak configuration are compared. MEGA, which is a hybrid code for energetic particles interacting with a magnetohydrodynamic fluid, is used for the simulations. It is demonstrated that the EGAM in LHD is a combination of m/n=0/0 (strong), 1/0 (medium) and 2/10 (weak) components, which is different with that in tokamak. The 2/10 component appears from the 3-dimensional LHD configuration.

1. Introduction

Geodesic acoustic mode (GAM) is an oscillatory zonal flow coupled with density and pressure perturbations in toroidal plasmas. Recently, energetic particle driven GAM (EGAM) has been observed in Large Helical Device (LHD) with neutral beam injection. The EGAM frequency chirping is observed, and the anomalous bulk ion heating during the EGAM implies EGAM channeling[1,2]. Understanding EGAM is important for magnetic confinement fusion where the energetic particles must be well confined for the bulk plasma heating. In order to reproduce realistic EGAM in LHD, and investigate the properties of stellarator EGAMs, the simulation under the condition of realistic 3-dimentional equilibrium data is implemented in the present work.

2. Simulation Model

MEGA code, which is a hybrid code for energetic particles interacting with a magnetohydrodynamic fluid, is used for the simulations[3-6]. The realistic 3-dimensional equilibrium data is based on an LHD discharge whose shot number is 109031, and this data is generated by HINT2 code at t=4.94 s. In the experiment, the EGAM activity is very strong at this moment, and the mode frequency chirps up[2]. The energy of neutral beam injection (NBI) is 170 keV. The energetic-particle distribution function is the slowing-down type, and the slowing-down time is 10 s. In addition, a Gaussian-type pitch angle distribution $f(\Lambda) = \exp[-(\Lambda-\Lambda_{peak})^2/\Delta\Lambda^2]$ is assumed for the energetic ions, where Λ is the particle pitch angle, $\Lambda_{peak} = 0.1$ represents the pitch angle for the distribution peak, and $\Delta\Lambda = 0.2$ is a parameter to control the distribution width. The safety factor q profile is normal shear case, q_0=2.8 on the magnetic axis, and q_{edge}=0.8 on the plasma edge.

3. Simulation Results

The EGAM in LHD is reproduced by MEGA code, as shown in Fig. 1. This figure shows the mode amplitude time evolution, and also the frequency spectrum analyzed by fast Fourier transform. The mode is oscillated, and it is excited in very short time, less than 0.2 ms. The mode frequency is 60 kHz in the linear phase, and chirps up to 80 kHz with chirping rate 15 kHz/ms. Figure 1(c) shows an experimental observation where the frequency chirping rate is also 15 kHz/ms. Figure 1(d) shows another experimental observation where the initial frequency is from 50 to 100 kHz. The simulated EGAM initial frequency is same as the experimental observation, the fast excitation and the high chirping rate are also roughly consistent with the experiment. In the simulation model, the NBI is not continually injected, but the mode amplitude keeps constant, does not decay. This happens because the mode can continually obtain the energy from particles in the chirping process.

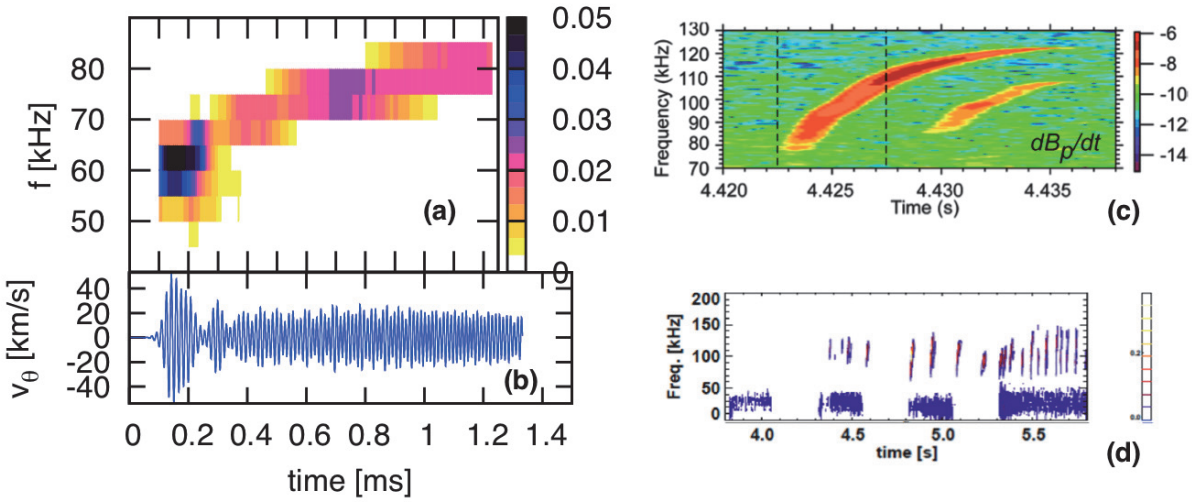

Fig.1 (a) The time evolution of simulated EGAM oscillation. (b) The frequency spectrum of simulated EGAM. (c) The frequency spectrum of experimental EGAM in LHD observed by T. Ido[1]. (d) The frequency spectrum of experimental EGAM in LHD observed by M. Osakabe[2].

The poloidal velocity v_θ of the mode in 3-dimentional case is shown in Fig. 2 (a)~(d). The mode is located near the magnetic axis, and the v_θ oscillation looks like a combination of m/n=0/0 (strong), 1/0 (medium) and 2/10 (weak) components. The ratio of the 2/10 component intensity to the 0/0 component intensity is about 17%, as shown in figure 2(e). The m/n=2/10 components exists due to the LHD configuration. In LHD, there are 10 twists in the toroidal direction, and there are 2 high field regions and 2 low field regions in the poloidal cross section. This is the first simulation of EGAM in the 3-dimentional LHD configuration. The mode number is different from the tokamak case, where the v_θ oscillation looks like a combination of m/n=0/0 and 1/0 components. In addition, it is found that the mode does not propagate radially in the linear phase, and propagates inward in the nonlinear phase.

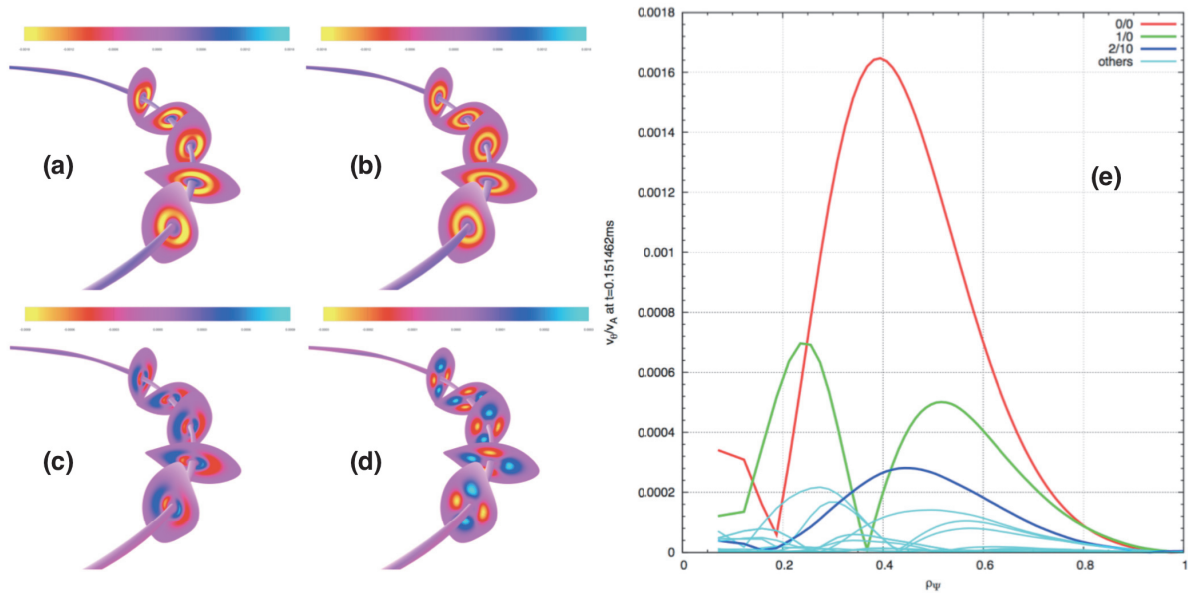

Fig.2 The 3-dimentional figure of poloidal flow of (a) all the components, (b) m/n=0/0, (c) m/n=1/0, and (d) m/n=2/10. Figure (e) shows the 2-dimentional figure of mode profile, where the intensity of m/n=2/10 mode is about 17% of m/n=0/0 mode.

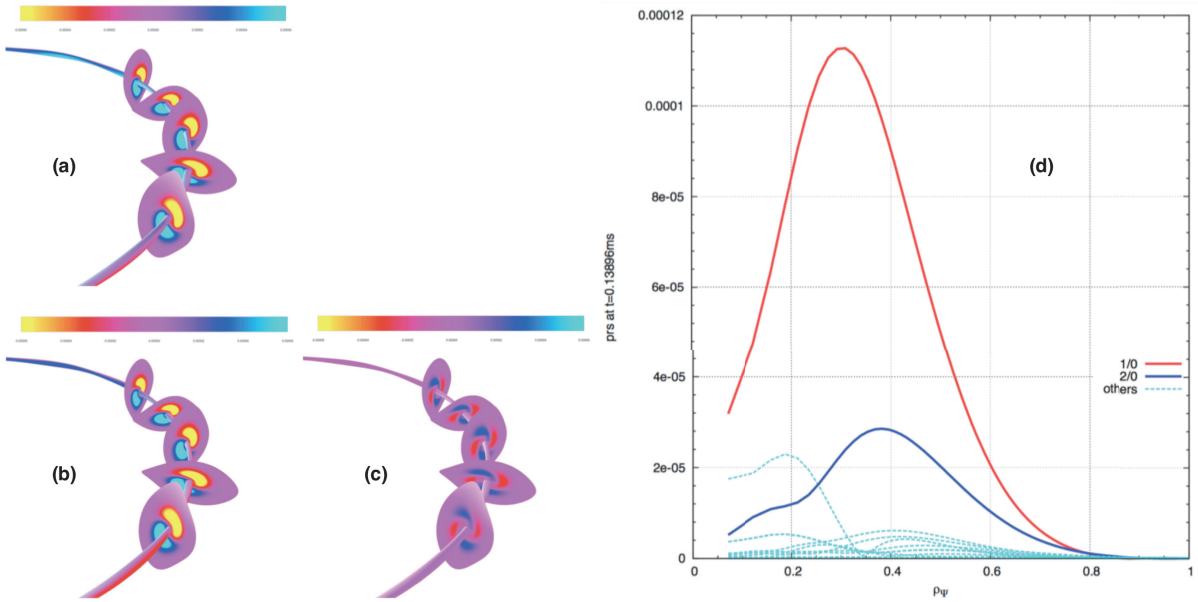

Fig.3 The 3-dimentional figure of pressure perturbation of (a) all the components, (b) m/n=1/0, and (c) m/n=2/0. Figure (d) shows the 2-dimentional figure of pressure perturbation profile.

The mode number of pressure perturbation is m/n=1/0, as shown in Fig. 3. This is similar with the tokamak case. In addition, the m/n=2/0 mode is also strong. The pressure perturbation rotates poloidally in the nonlinear phase, and the rotation direction changes periodically. This rotation is caused by the convection of EGAM, because the phase of pressure time derivative $\partial P/\partial t$ and the phase of v_θ are the same.

The energy transfer rate from the EGAM to the energetic particles in (Λ,E) space in the linear phase is shown in Fig. 4. The purple color represents the negative energy transfer, which means the energy transfer

from particles to the EGAM, destabilizing the mode. In contrast, the red color represents the positive energy transfer that stabilizes the mode. The particles with negative energy transfer rate is dominant, thus, the EGAM is excited on the whole. The stabilization region locates in E ~ 170 keV. This arises from the steep gradient in the distribution function, because the NBI energy is 170 keV. The particles with E ~ 90 keV and Λ ~ 0.5 supplies most of the energy to the mode, and the transit frequency of these particles are about 60 kHz, same as the mode frequency in the linear phase.

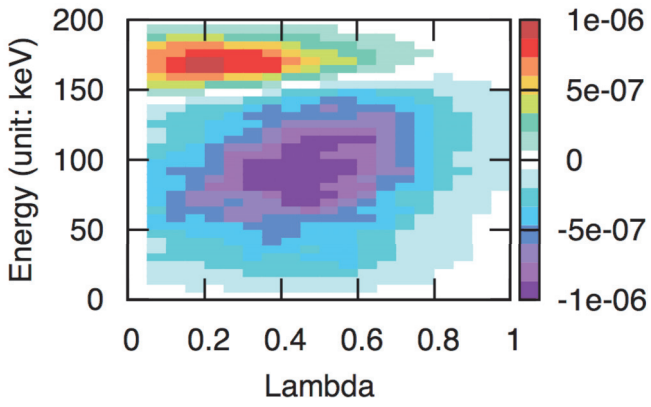

Fig.4 The energy transfer from the EGAM to the energetic particles in (Λ,E) space.

4. Summary

In summary, the first simulation results of energetic particle driven geodesic acoustic mode (EGAM) in 3-dimensional LHD equilibrium are investigated. The phenomenon of frequency chirping is reproduced. The v_θ oscillation is a combination of m/n=0/0 (strong), 1/0 (medium) and 2/10 (weak) components. This is different from the tokamak case. The pressure perturbation rotates with time evolution in the saturated phase. In the (Λ,E) phase space, the transit frequency of the particles in the most destabilization region is same as the mode frequency in the linear phase.

Acknowledgements

This work was partly supported by the JSPS-NRF-NSFC A3 Foresight Program in the field of Plasma Physics (NSFC: No.11261140328, NRF: No.2012K2A2A6000443).

References

[1] T. Ido, M. Osakabe, A. Shimizu, et al., Nucl. Fusion **55** (2015) 083024.

[2] M. Osakabe, T. Ido, K. Ogawa et al, 25th IAEA-FEC, 13-18 October 2014, St Petersburg, Russian Federation.

[3] Y. Todo, Phys. Plasmas **13** (2006) 082503.

[4] H. Wang and Y. Todo, Phys. Plasmas **20** (2013) 012506.

[5] H. Wang, Y. Todo, and C. C. Kim, Phys. Rev. Lett. **110** (2013) 155006.

[6] H. Wang, Y. Todo, T. Ido and M. Osakabe, Phys. Plasmas **22** (2015) 092507.

Resistive Interchange Mode destabilized by Helically Trapped Energetic Ions and its Effects on Energetic Ions and Bulk Plasmas

X.D. Du, K. Toi, M. Osakabe, S. Ohdachi, T. Ido, K. Tanaka, M. Yokoyama, M. Yoshinuma, K. Ogawa, M. Isobe, K. Nagaoka, T. Ozaki, S. Sakakibara, R. Seki, Y.Suzuki, K.Y. Watanabe and LHD Experiment Group

National Institute for Fusion Science, Toki 509-5292, Japan

Abstract

A resistive interchange mode of the $m = 1/n = 1$ structure (m, n: poloidal and toroidal mode numbers, respectively) with a bursting character and rapid frequency chirping in the range less than $10kHz$ is observed for the first time in the edge region of the net current-free, low beta LHD (Large Helical Device) plasmas during high power injection of perpendicular neutral beams. The mode resonates with the precession motion of helically trapped energetic ions (EPs), following the resonant condition. The radial mode structure is recognized to be similar to that of the pressure-driven resistive interchange mode, of which radial displacement eigenfunction quite localizes around the mode rational surface, and evolves into an odd-type (or island-type) during the late of frequency chirping phase.

1. Introduction

In this A3 seminar, we report the first observation of a bursting RIC destabilized by resonant interaction with helically trapped energetic ions (EPs) in LHD, named as the helically trapped energetic-ion-driven resistive interchange mode, or 'EIC'. The EICs are observed in the low frequency range ($f < 10kHz$), with rapid frequency chirping-down in low β plasmas ($\beta < 1\%$) where hydrogen neutral beam injection nearly perpendicular to magnetic field line (PERP-NBI) is applied [1]. The mode has an $m = 1/n = 1$ structure and localizes at the mode rational surface in the peripheral region of current-free plasma, where m and n are poloidal and toroidal mode numbers respectively. The eigenfunction shows a similar shape with the predicted eigenfunction of the RIC, which is clearly distinguished from the EP-driven internal kink mode in tokamak well known as 'fishbone' [2] or EP-driven external kink mode, so called EP-driven wall mode in JT-60U [3] or off-axis fishbone in DIII-D [4, 5]. In the peripheral region of the LHD plasma, the helical field ripple is large, i.e., $\epsilon_h \sim 0.25$. Consequently, energetic ions generated by PERP-NBI are deeply trapped in the helical ripple, called 'helically trapped energetic ions' [6]. These EPs is responsible for the mode destabilization.

2. Destabilization of the EIC

As shown in Fig. 1, the EICs are often observed in relatively low-density plasmas so-called high-Ti discharges with high power injections of both PERP-NBI and TANG-NBI of absorbed power of total $\sim 6MW$. The electron temperature T_e and density n_e typically have parabolic radial profiles, of which central values reach $T_{e0} \sim 3.5keV$ and $n_{e0} \sim 0.8 \times 10^{19} m^{-3}$, respectively. The volume-averaged toroidal beta

of bulk plasma β_{bulk}, evaluated from the YAG-laser Thomson Scattering system on the assumption that the electron and ion pressures are nearly the same, is fairly low due to the low electron density and high toroidal magnetic field strength. The volume-averaged beam beta perpendicular to magnetic field line $\beta_{h\perp}$ is comparable with β_{bulk} due to large slowing down time of helically trapped energetic ions. The $\beta_{h\perp}$ is estimated as $\beta_{h\perp} = \beta_{dia.} - \beta_{bulk}$, where the diamagnetic beta $\beta_{dia.}$ is obtained by a diamagnetic loop. It should be noted that $\beta_{h\perp}$ is dominated by the contribution from helically trapped EPs because that from passing EPs can be neglected.

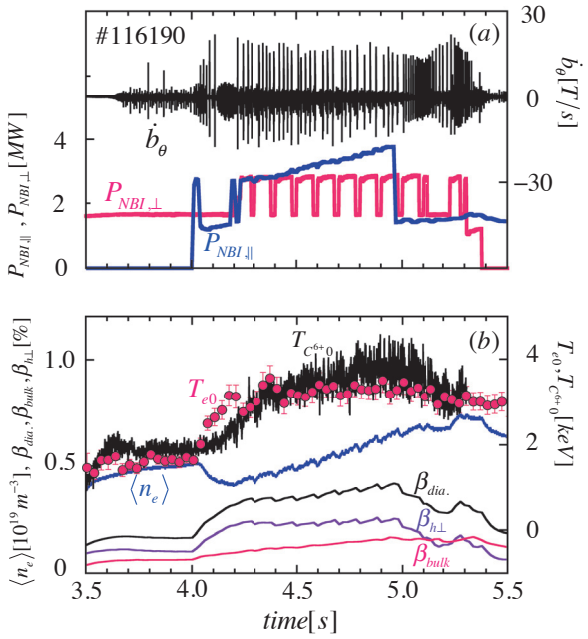

FIG.1 (a) Temporal evolutions of magnetic fluctuations measured by a magnetic probe signal (and absorbed powers of TANG-NBI and PERP-NBI. (b) Temporal evolutions of the central electron temperature, central carbon ion temperature, line-averaged electron density and volume-averaged bulk plasma beta derived from Thomson scattering diagnostics and volume-averaged beam beta perpendicular to magnetic field line derived from a diamagnetic loop.

As seen from Fig. 1(a), magnetic fluctuations of the EIC measured by a magnetic probe exhibit fishbone-shape oscillations, when $\beta_{h\perp}$ is large. The typical expanded waveform is shown in Fig. 2(a). A weak sinusoidal oscillation of $\sim 5kHz$ is observed from $t \sim 4.357s$ to $4.36s$, and grows rapidly in $\sim 0.2ms$ before the onset of an EIC burst. This oscillatory mode is thought to be a usual pressure-driven RIC. It suddenly evolves into the EIC having large amplitude and strongly distorted waveform. Here, the temporal frequency of the EIC is evaluated from each half period. The frequency from the trough to the crest is much larger than the one from the crest to trough in one period of oscillation, suggesting the strong distortion away from the sinusoidal oscillations. The frequency is also evaluated from one full period of oscillation, showing a characteristic of rapid chirping-down from $\sim 8.5\,kHz$ to $\sim 3.5\,kHz$ in $\sim 2ms$, accompanied with a gradual decay of the amplitude of magnetic fluctuations. Then, magnetic fluctuations disappear for a few ms just after the EIC burst. In addition, the Doppler frequencies arising from bulk plasma rotations in the poloidal and toroidal directions are evaluated from the rotations of C^{6+} ions measured by charge exchange spectroscopy (CXRS) using the PERP-NBI with $\sim 34keV$ proton beams. As seen from Fig. 2(b), the contribution from the Doppler frequencies to the observed frequency of the EIC is considerably small because the non-axisymmetric magnetic field structure brings about large parallel

viscosity and strongly slows down the toroidal and poloidal flows in peripheral region of LHD plasma. In other words, the EIC as well as the RIC do have the real frequency itself in the plasma frame. Moreover, according to the phase analysis of magnetic probe signals, both the RIC and the EIC with $m = 1/n = 1$ mode structure propagate in the electron diamagnetic drift direction poloidally and counter-B_t direction toroidally in the plasma frame, respectively. This is the same propagation direction of the usual pressure-driven RIC observed in various LHD plasmas.

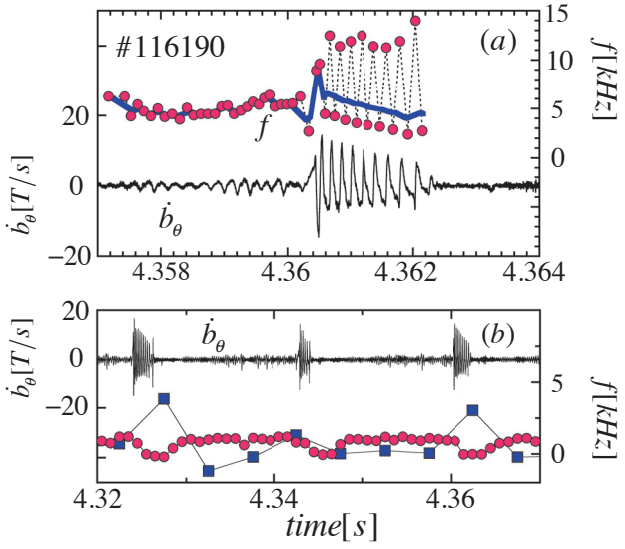

FIG.2 (a) Time evolution of the magnetic probe signal and the temporal frequency calculated by each half period of EIC (solid circle) and full period (line) for a typical EIC. (b) Magnetic probe signal with three EICs and the Doppler frequencies evaluated from poloidal (squares) and toroidal (circles) rotation velocities measured by CXRS at iota=1 location.

A specific experiment is conducted to destabilize the EIC by only PERP-NBI of initial beam energy $E_b = 34keV$, without any TANG-NBIs, shown in Fig. 3. In this experiment, electron cyclotron heating (ECH) with $77GHz$ is employed to maintain the plasma performance throughout the discharge. One PERP-NBI of $\sim 1.6MW$ deposition power is applied with full power modulation throughout the discharge and the other PERP-NBI of $\sim 1.6MW$ is superimposed during the short time window from $4.0s$ to $4.18s$, as shown in Fig. 3(d). Oscillatory mode destabilized weakly is observed in magnetic probes in the time interval from $t = 4.0s$ to $4.18s$ where two PERP-NBIs are overlapped, as shown in Fig. 3(b). The destabilization of the oscillatory mode is caused by the increase of $\beta_{dia.}$. In the latter half of the time interval, strong bursting events are detected in magnetic probes. As seen from the expanded view in Fig. 3(a), the oscillatory mode of $\sim 2kHz$ is firstly destabilized. Then, the magnetic fluctuation amplitude is suddenly enhanced with strongly distorted waveforms instead of sinusoidal oscillations, similar to the EICs observed in the so-called high-Ti discharge shown in Figs. 1 and 2. An important point is that the mode frequency suddenly jumps up to $\sim 8kHz$, and then rapidly chirps down to $\sim 2kHz$ in $\sim 2ms$. The Doppler frequency evaluated from the carbon toroidal flow measurement by CXRS is significantly small compared with the EIC mode frequency especially on the condition without the toroidal momentum input by TANG-NBI. In the low power phase of PERP-NBI after $t = 4.18s$, the bursting mode is no longer destabilized, as seen from Fig. 3(b). Note that two tiny tips of this phase in the probe signal are pick-ups due to PERP-NBI switch-off. This suggests that the EIC can be destabilized only by a large amount of helically trapped energetic ions produced with intense PERP-NBI.

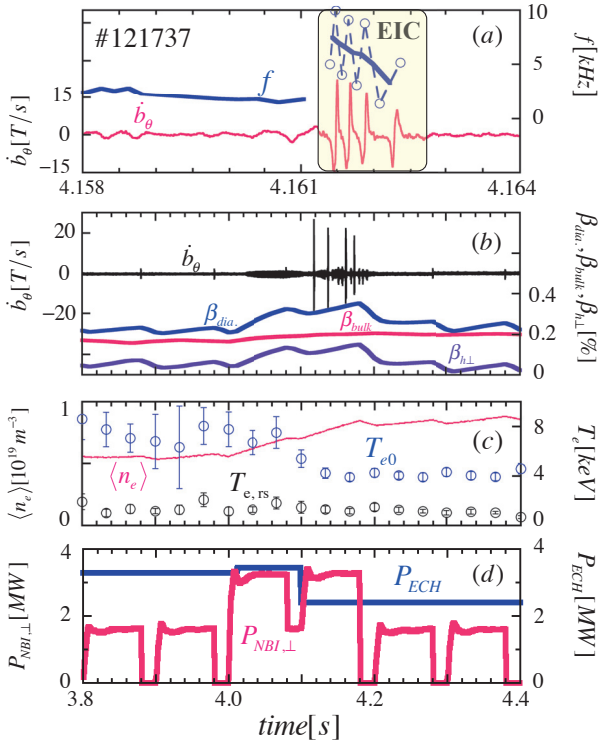

FIG.3 (a) An expanded view of magnetic probe signal and its frequency. (b) Time evolutions of magnetic fluctuation and volume-averaged bulk plasma beta derived from Thomson scattering diagnostics and volume-averaged beam beta perpendicular to magnetic field line derived from a diamagnetic loop, (c) electron temperature at the plasma center and that at iota=1 rational surface measured by Thomson scattering diagnostics together with the line-averaged electron density, and (d) absorbed power of ECH and that of PERP-NBI.

Acknowledgements

This work was partly supported by the JSPS-NRF-NSFC A3 Foresight Program in the field of Plasma Physics (NSFC: No.11261140328, NRF: No.2012K2A2A6000443).

References

[1] X.D. Du et al 2015 Phys. Rev. Lett. **114** 155003

[2] K. McGuire et al 1983 Phys. Rev. Lett. **50** 891

[3] G. Matsunaga et al 2009 Phys. Rev. Lett. **103** 045001

[4] M. Okabayashi et al 2011 Phys. Plasma **18** 056112

[5] W.W. Heidbrink et al 2011 Plasma Phys. Control. Fusion **53** 085028

[6] T. Watanabe et al 2006 Nucl. Fusion **46** 291

Locked mode stabilization by applying non-axisymmetric fields

J. Kim[1], Y. In[1], A.Y. Aydemir[1], J.-K. Park[2],
J.Y. Kim[3], J.G. Bak[1], C. Bae[1], and the KSTAR team

[1]National Fusion Research Institute, Daejeon, Korea
[2]Princeton Plasma Physics Laboratory, Princeton, Unites States of America
[3]University of Science and Technology, Daejeon, Republic of Korea

E-mail: jayhyunkim@nfri.re.kr

A synergistic effect of mixed non-axisymmetric (NA) field applications has been investigated in KSTAR ohmic plasmas. Since the use of two distinctly aligned NA field would provide broader island overlaps than that of a single NA field or non-resonant field on each individual island, such 3-D field configurations affect both NA field penetration and locking. Specifically, the NA error field penetration and locking could be understood by the torque imbalance between the intrinsic rotation in ohmic plasmas, and externally-driven magnetic braking. While the application of the n=1 NA field alone brings field penetration, locking, and then minor disruption, the addition of n=2 NA field appeared to have moved up the onset of n=1 EF penetration and locking, but to have either delayed or avoided the minor disruption. A preliminary analysis shows that such delay or avoidance of minor disruption was observed to be dependent on the pitch of the n=2 NA field. The magnetic diagnostics suggests that the n=2 NA field started to hinder the growth of n=1 locked mode, when the mode amplitude reached a certain level, which appears to be correlated with the n=2 NA field strength. Nonetheless, a fast mode growth resumes, just prior to a minor disruption. It seems that there exists 2nd threshold of EF penetration related to the disruption phenomena, similar to a locking threshold (*i.e.* 1st threshold). In comparison, the pure n=1 NA field case without n=2 field does not show any noticeable change of growth rate after locking, gradually increasing the locked mode amplitude towards minor disruption.

1. Introduction

Although the tokamak device is fundamentally based on toroidally axisymmetric field configuration, it has been demonstrated that a small amount of non-axisymmetric (NA) field could play a crucial role in performances such as transport characteristics and magneto-hydrodynamic stabilities. Recently, the effect of NA field has been studied intensively for suppressing edge localized mode [1] in addition to traditional interest on intrinsic error field (EF) [2]. Furthermore, it is expected that future fusion devices such as ITER may have to utilize various NA fields simultaneously, for different control purposes or better control action even within single control [3]. In those cases, the fields used in the controls have their own optimal spectra and affect each other as resonant and also non-resonant way. However, the influence due to the mutual interaction between them has not been fully understood yet [3, 4].

In this research, the locking and following disruption due to EF are mainly considered under the circumstance of mixed NA fields since these phenomena are closely related with the most urgent issues of ITER. Those are disruption avoidance and edge localized mode (ELM) suppression. Section 2 will briefly describe the experimental setup and the detailed result will be discussed in section 3. Finally, we will summarize the result with considering future work in section 4.

2. Experimental setup

2.1. Spectra of the applied fields

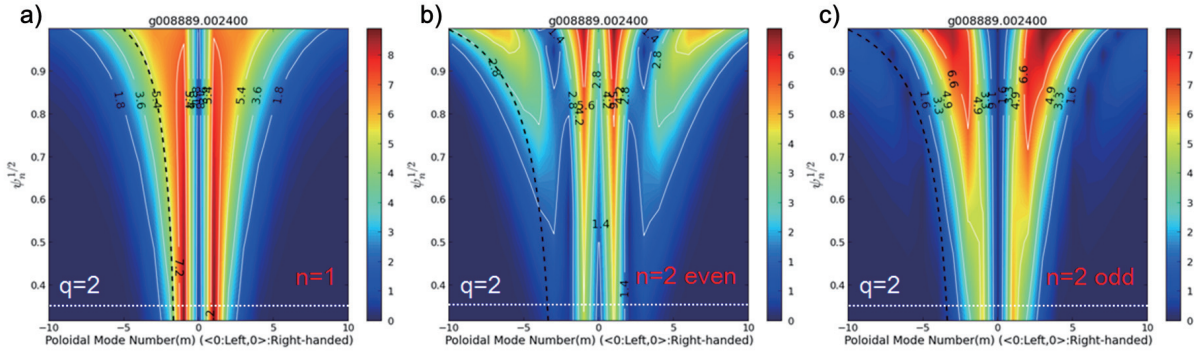

Fig. 1. Vacuum calculations of the applied NA fields. a) Spectrum of n=1 mid NA field, b) spectrum of n=2 even top/bottom NA field, and c) spectrum of n=2 odd top/bottom NA field. White dotted horizontal lines depict the q=2 surface.

As shown in figure 1a), n=1 middle FEC coil generates a spectrum which penetrates deep inside to the plasma core. When the strength of n=1 EF exceeds the threshold level of EF penetration, it causes the locking and disruption. It is widely known that low n EF (*i.e.* n=1 EF in this research) could result in the locking more easily than high n EF (*i.e.* n=2 EF). Thus the middle FEC coil is set to n=1 configuration in order to induce the EF penetration and locking while the off-mid-plane coils has n=2 configuration for investigating the influence of n=2 NA field on n=1 EF related phenomena.

Two different configurations were tested for the top and bottom FEC coils such as the even (*i.e.* same parity between top and bottom coils) and odd (*i.e.* opposite parity between top and bottom coils). Figures 1b) and 1c) exhibit their spectra, respectively. Near q=2 surface, n=2 even configuration dominantly produces non-resonant field in comparison with the target equilibrium field. On the other hand, n=2 odd configuration shows relatively resonant field spectrum.

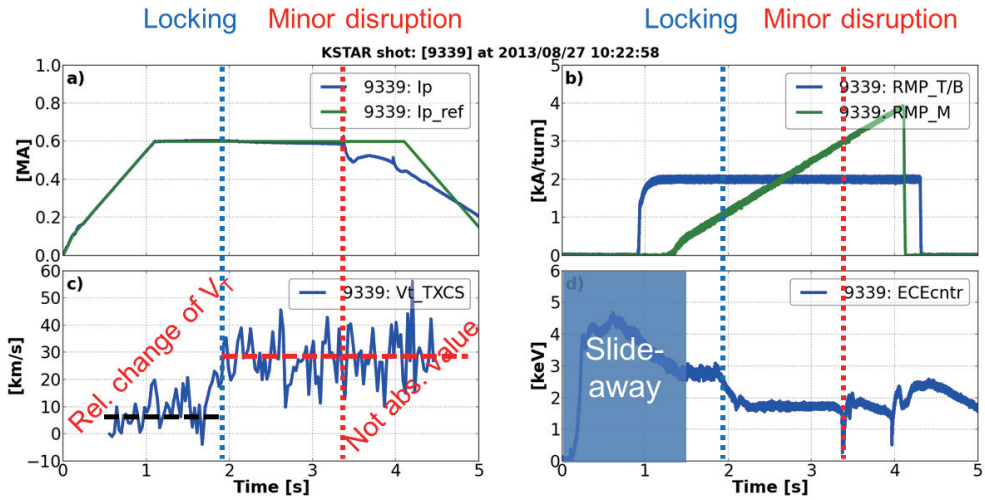

Fig. 2. Typical procedure of the EF penetration, locking, and minor disruption when n=1 and n=2 mixed NA fields are applied to ohmically heated plasmas. a) Plasma current, b) applied currents on FEC coils, c) core toroidal rotation, and d) core electron temperature.

3. Experimental result

3.1. Typical procedure of the EF penetration, locking, and minor disruption

Figure 2 illustrates a typical procedure of the simulated n=1 EF penetration with the underlying n=2 NA field. The middle FEC coil applied gradually increasing n=1 EF to cause error-field-induced locked mode as shown by green line of figure 2b). On the other hand, the n=2 NA field, which was applied by the top and bottom FEC coils, maintained constant level during the increase of the n=1 EF.

Locking and EF penetration were induced by the torque imbalance between the intrinsic rotation and external magnetic braking as depicted by the relative change of core toroidal rotation in figure 2c). Further increase of the n=1 EF resulted in minor disruption as marked by the red dotted vertical lines in figure 2. Sudden loss of the confinement is reflected in sharp drops of core electron temperature during the minor disruptions.

3.2. Locking threshold

As anticipated by the magnetic braking effect, the stronger n=2 NA field discharge exhibited earlier EF penetration and locking. The result seems to depend only on the n=2 NA field strength regardless of the pitch of the n=2 NA field (*i.e.* the even or the odd). Thus we conjecture that the effect of the n=2 NA field in the locking phenomena acts as non-resonant way such as the neoclassical toroidal viscosity damping [5].

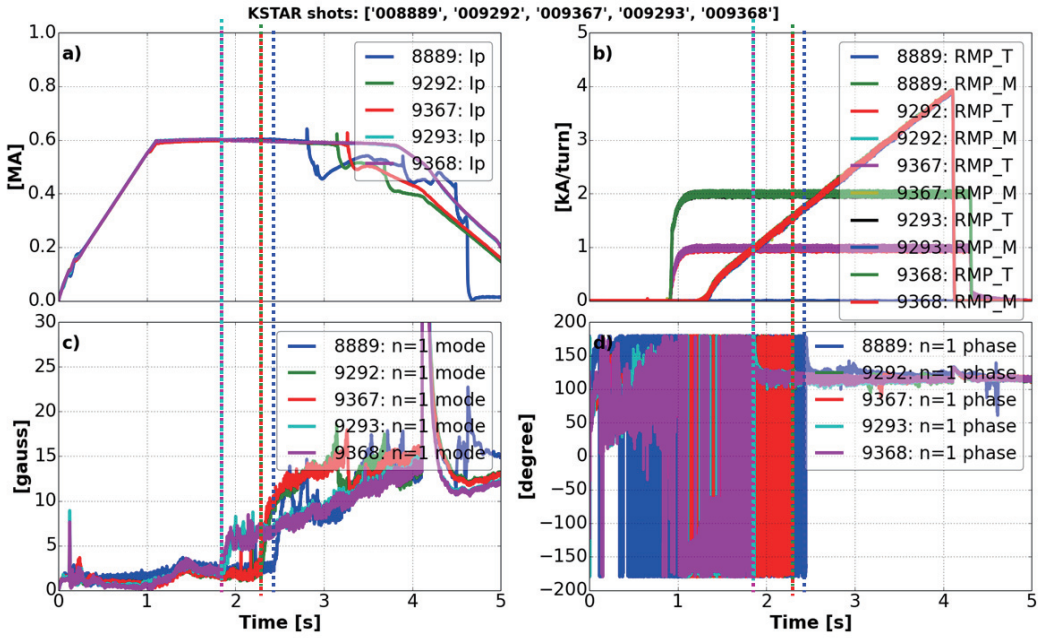

Fig. 3. Locking threshold of n=1 EF under the existence of n=2 NA field. a) Plasma currents, b) applied currents on FEC coils (increasing lines: n=1 middle FEC coil and the others: n=2 top/bottom FEC coils), c) n=1 mode amplitudes, and d) n=1 mode phases. Note that KSTAR shot no. 8889 has only n=1 EF without underlying n=2 NA field.

3.3. Disruption threshold

Figure 4 represents n=2 even NA field discharges with pure n=1 discharge and the amount of delay is proportional to the strength of n=2 even NA field. Analysis of the locked mode amplitude revealed that the n=2 NA field started to hinder the growth of n=1 locked mode when the mode amplitude reached certain level. The starting level of the hindrance appears to rely on the n=2 NA field strength as shown by figure 5b). More interestingly, the fast growth was recovered just before minor disruption. The yellow circle in figure 5b) depicts the final change of the growth rate. Thus it seems that there exists 2nd threshold of EF penetration related to the disruption phenomena like 1st threshold in the locking phenomena. Nevertheless,

the pure n=1 field case without n=2 field did not show clear change of the growth rate after locking and just exhibited gradual increase of the locked mode towards the minor disruption.

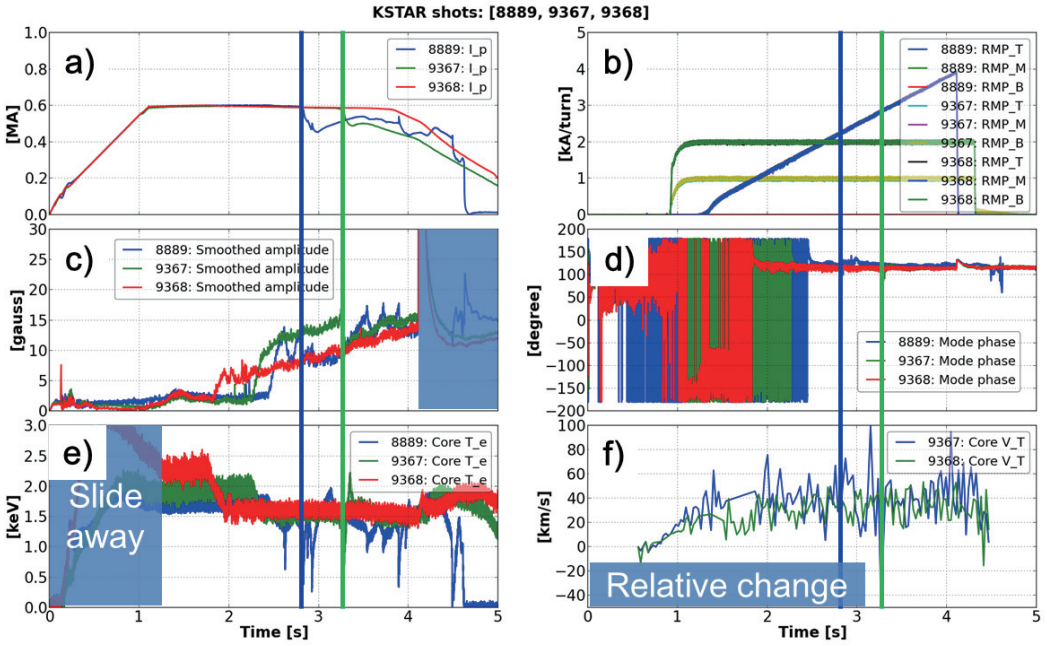

Fig. 4. (Minor) disruptions due to n=1 EF under the existence of n=2 even NA field. a) Plasma currents, b) applied currents on FEC coils, c) n=1 mode amplitudes, d) n=1 mode phases, e) core electron temperatures, and f) core toroidal rotations. Note that the strengths of n=2 even NA field are 0 kA/turn: KSTAR shot no. 8889 (*i.e.* pure n=1 EF as a reference shot), 1 kA/turn: KSTAR shot no. 9367, and 2 kA/turn: KSTAR shot no. 9368, respectively. The current waveforms of n=1 middle FEC coil are identical among the shots.

4. Summary

In this research, we investigated the interaction between distinctly aligned NA field with focusing on the EF penetration, locking, and disruption. As mentioned in the above, it was observed that the underlying NA field made the discharge more vulnerable to the EF penetration and locking phenomenon since the NA field causes global rotation damping towards the locking threshold of EF. It means that simultaneous applications of NA fields require more careful consideration between the intended control purpose, for instance, ELM suppression, and the unintended side effect, for instance, locking and H-L back transition.

On the other hand, it was revealed that the subsequent disruption was delayed or avoided by the deliberately aligned NA field. Although we still need to experiment the result in diverse discharge conditions, it could be possible to maintain the locked state of plasma within the intended control purposes. For example, the result might be applicable to secure the response time allowed to the disruption mitigation by applying a proper NA field when the locking signal is caught. It is definitely beneficial to ensure the safety of large tokamak devices such as ITER.

The research exhibits that there exist different thresholds in the locking and disruption phenomena and these thresholds are affected by the underlying NA field. Especially, the disruption threshold was not perceived in pure n=1 EF discharges and the underlying NA field uncovered the existence of it. In future work, we will make an effort to study the governing mechanism of the 2nd threshold.

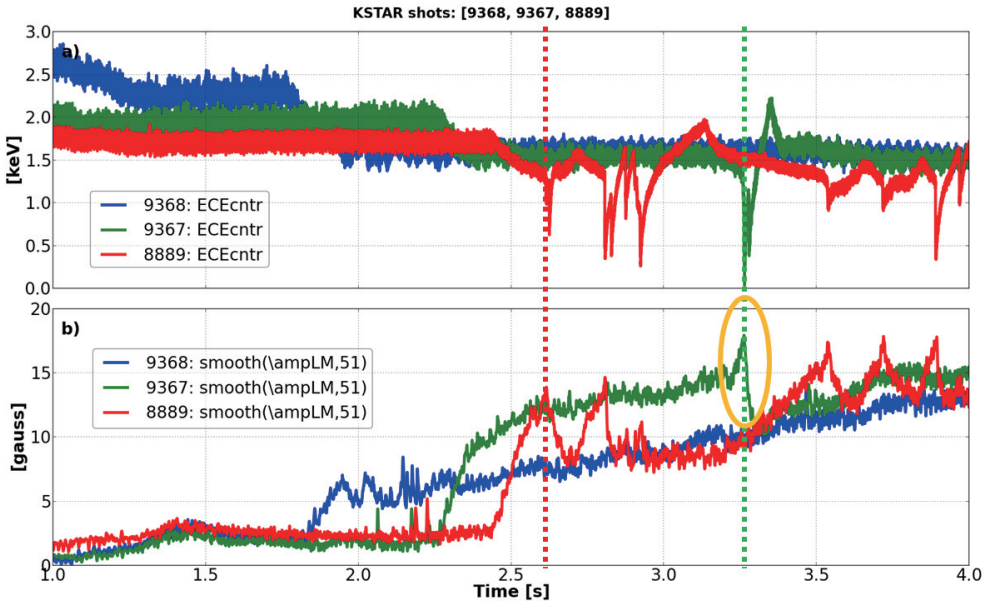

Fig. 5. Comparative study of the n=1 EF penetration depending on the underlying n=2 even NA field strength. Red line: no current on the n=2 FEC coil. Green line: 1 kA/turn current on n=2 FEC coil. Blue line: 2 kA/turn current on the n=2 FEC coil. a) Core electron temperature and b) n=1 locked mode amplitude.

Acknowledgement

This research was supported by Ministry of Science, ICT, and Future Planning under KSTAR project and was partly supported by the JSPS-NRF-NSFC A3 Foresight Program in the field of Plasma Physics (NSFC: No.11261140328).

References

[1] EVANS, T.E., et al., "Suppression of Large Edge-Localized Modes in High-Confinement DIII-D Plasmas with a Stochastic Magnetic Boundary", Phys. Rev. Lett. 92 (2004) 235003.

[2] PARK, J.-K., et al., "Sensitivity to error fields in NSTX high β plasmas", Nucl. Fusion 52 (2012) 023004.

[3] FENSTERMACHER, M.E., et al., "Effect of island overlap on edge localized mode suppression by resonant magnetic perturbations in DIII-D", Phys. Plasmas 15 (2008) 056122.

[4] COLE, A.J., et al., "Effect of Neoclassical Toroidal Viscosity on Error-Field Penetration Thresholds in Tokamak Plasmas", Phys. Rev. Lett. 99 (2007) 065001.

[5] SHAING, K.C., et al., "Neoclassical transport fluxes in the plateau regime in nonaxisymmetric toroidal plasmas", Phys. Fluids 29 (1986) 521.

Toroidal rotation and momentum transport studies in KSTAR

S. G. Lee[1], J. W. Yoo[2], L. Terzolo[1], Y. S. Kim[1], Z. Y. Chen[3], and KSTAR team

[1] National Fusion Research Institute, Daejeon, Korea
[2] Korea University of Science and Technology, Daejeon, Korea
[3] Huazhong University of Science and Technology, Wuhan, China

Email : sglee@nfri.re.kr

The toroidal rotation and momentum transport studies have been carried out in KSTAR tokamak. The impurity toroidal rotation has been observed in the core region from Doppler shift of helium-like argon x-ray line with various plasma discharges including a pure ohmic heating and auxiliary heating sources. In the ohmic plasmas, the direction and magnitude of the core rotation strongly depends on the plasma current, and the maximum core ion thermal Mach number is reached up to 0.25. In the neutral-beam injected H-mode plasmas, the central Mach number has been measured up to 0.8, which is faster than any other devices. Recently, the core toroidal rotation and ion temperature of a long-pulse plasma discharge are successfully measured up to 40 seconds.

1. Introduction

The toroidal rotation is one of the most important issues for the magnetically confined fusion plasma researches since it is essential for the stabilization of resistive wall mode and its shear plays an important role to improve plasma confinement by suppressing turbulent transport. The most advantage of KSTAR tokamak [1] for toroidal rotation studies is that it equips two main diagnostics including the high-resolution X-ray imaging crystal spectrometer (XICS) [2] and charge exchange spectroscopy (CES) [3]. The impurity toroidal rotation (V_φ) and ion temperature (T_i) are measured via the XICS and CES from a Doppler shift of the helium-like argon (Ar XVII) and hydrogen-like carbon (C VI) impurity lines, respectively. Detail description and experimental arrangement of the XICS and CES systems for KSTAR are well explained in Ref. 2 and 3, respectively. Simultaneous core V_φ and T_i measurements of different impurity species from the XICS and CES have shown in reasonable agreement with various plasma discharges in KSTAR [4]. Measurements of the direction and magnitude of the core rotation in plasmas with pure ohmic heating during the plasma current flat-top have been performed on many tokamaks, and the results of these measurements have been compared in Ref. 5. In NBI heated plasmas, the toroidal rotation is a co-current direction and the speed is increased up to several hundred km/s during the high confinement mode (H-mode) phase. This paper describes the experimental results of the toroidal rotation and momentum transport studies in the KSTAR plasmas.

2. Experimental results

Figure 1 shows a characteristic scaling for ohmic discharges without any auxiliary heating sources in KSTAR tokamak. The direction and magnitude of the core rotation strongly depends on the plasma current as shown in Fig. 1. The plasma current is in the range from 300 to 600 kA. Note that the (-) sign of the core V_φ means a counter-rotation direction, which indicates in the opposite direction to the plasma current. The core V_φ mostly showed in the counter-current direction and its value is decreasing to zero level with the plasma current is increasing. The maximum ion thermal Mach number defined as $M_i = V_\varphi/V_i$ for 300 kA is

reached up to 0.25.

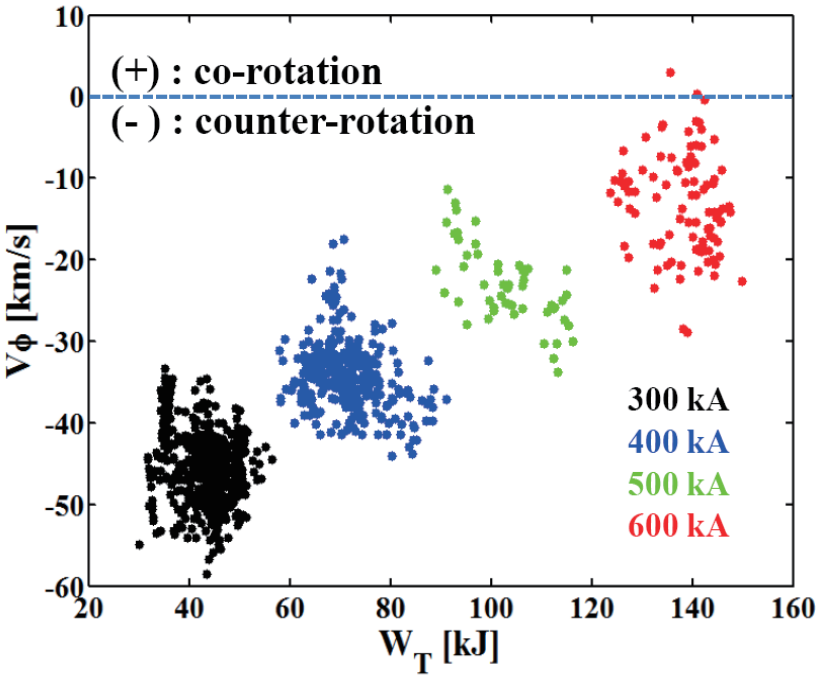

Fig. 1. Characteristic scaling for ohmic discharges.

The central ion thermal Mach number versus calculated beam torque in the neutral-beam injected H-mode plasmas is shown in Fig. 2. The maximum M_i has been measured up to 0.8, which is faster than any other tokamaks possibly attributable to lower TF error field and ripple [6].

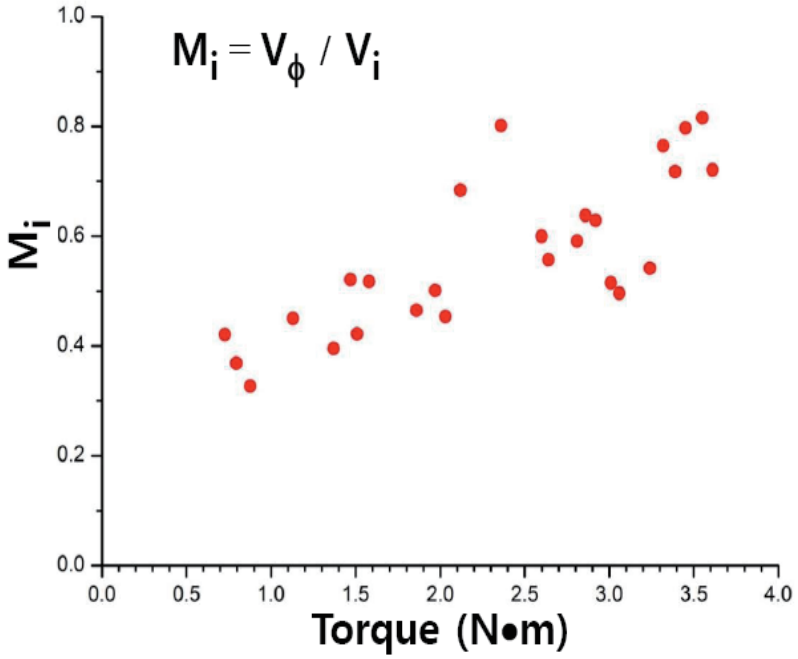

Fig. 2. Ion thermal Mach number vs. beam torque.

Figure 3 shows time traces of main plasma parameters with various auxiliary heating sources including NBI, ICRH and LHCD. The first ICRH in the L-mode plasma induces a

counter-rotation torque and the LHCD effect in the toroidal rotation is negligible since the applied power is not enough. The second ICRH injection results in the H-mode transition so that the toroidal rotation is mainly increased due to the better confinement.

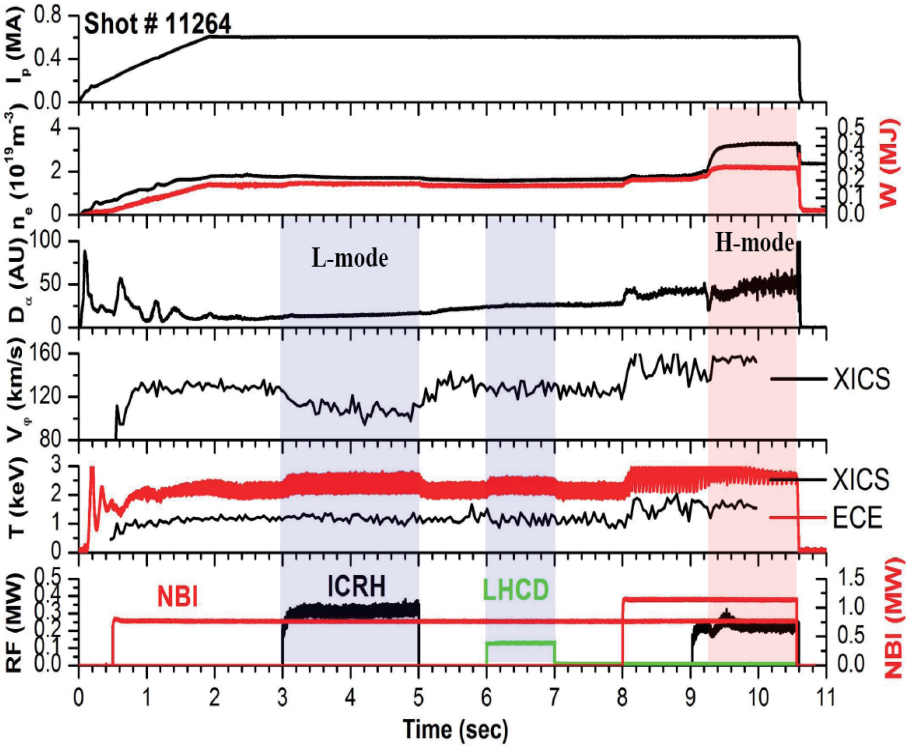

Fig. 3. Time traces for various heating sources.

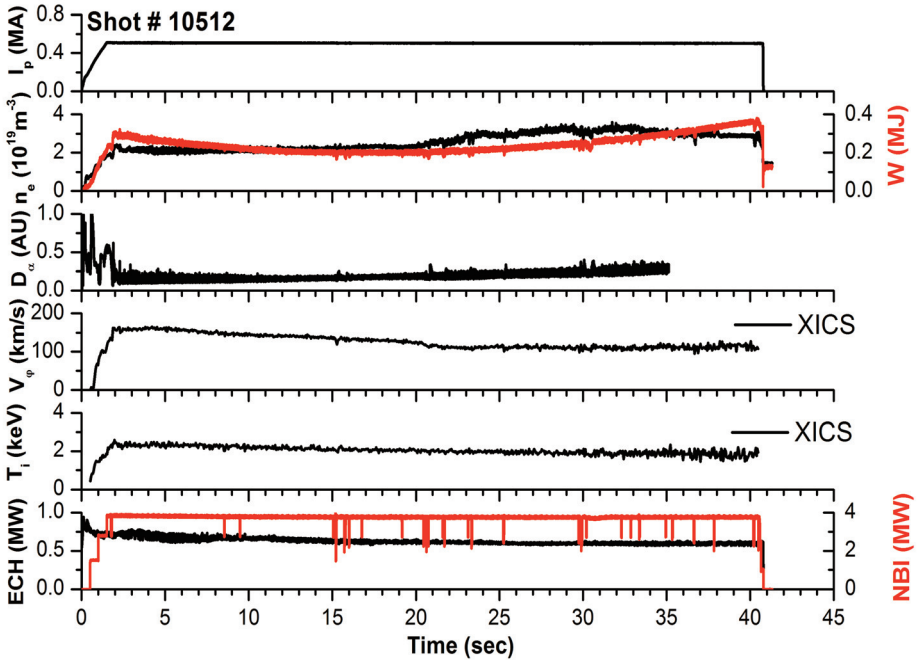

Fig. 4. Time traces for a long-pulse discharge.

Figure 4 shows temporal behaviour of the main plasma parameters for a long-pulse H-mode discharge with the plasma current of 0.5 MA. This discharge is a typical steady-state

operation without any sawtooth oscillations in KSTAR advanced tokamak scenario. The electron density and total stored energy are fairly constant except small changing at about 20 s, which is induced due to the divertor overheating. The core toroidal rotation and ion temperature from the XICS are successfully measured up to 40 seconds without any technical problems.

3. Summary

Toroidal rotation and momentum transport studies were investigated in KSTAR. The impurity toroidal rotation has been observed from various plasma discharges including a pure ohmic heating and neutral beam heated plasmas. In the ohmic plasmas, the direction and magnitude of the core rotation strongly depends on the plasma current, and the maximum core ion thermal Mach number is reached up to 0.25. In the neutral-beam injected H-mode plasmas, the central Mach number has been measured up to 0.8, which is faster than any other devices. Recently, the core toroidal rotation and ion temperature of a long-pulse plasma discharge are successfully measured up to 40 seconds.

Acknowledgement

This research was supported by Ministry of Science, ICT, and Future Planning under KSTAR project and was partly supported by the JSPS-NRF-NSFC A3 Foresight Program (NRF No. 2012K2A2A6000443).

References

[1] G. S. Lee et al., Nuclear Fusion **40**, 575 (2000).
[2] S. G. Lee et al., Rev. Sci. Instrum. **81**, 10E506 (2010).

[3] W. H. Ko et al., Rev. Sci. Instrum. **81**, 10D740 (2010).

[4] S. G. Lee et al., to be published in Fusion Sci. Tech. (Jan. 2016).

[5] J. Rice et al., Nuclear Fusion **3**, 421 (1997).

[6] Y. In et al., Nuclear Fusion **55** 043004 (2015).

Study of Plasma Toroidal Momentum Transport by Electrode Biasing in the J-TEXT Tokamak

Yue Sun, Z. P. Chen, G. Zhuang, L. Wang, H. Liu and Z. J. Wang

State Key Laboratory of Advanced Electromagnetic Engineering and Technology,
School of Electrical and Electronic Engineering,
Huazhong University of Science and Technology,
Wuhan 430074, People's Republic of China

Abstract

The toroidal momentum transport at the interior of plasma has been investigated by electrode biasing (EB) modulation in J-TEXT. The toroidal rotation (V_φ) of plasma is effectively modulated by EB in the experiments. The characteristics of V_φ perturbations, including the perturbation amplitude and phase delay, are fetched through sinusoidal-fittings, which are further comparatively studied under different modulation frequencies and amplitudes of EB. Moreover, the toroidal momentum transport coefficients, χ_φ and V_{conv}, are obtained in the region $r/a = 0.68 – 0.9$ by solving the toroidal momentum equation analytically. It is found that the values of the coefficients are significant at plasma edge, qualitatively consistent with the results on other devices; the convection velocity is always negative in the analyzed region, and reaches a maximum magnitude at around $r/a = 0.85$, suggesting the important pinch effect of toroidal momentum especially at the edge. Finally, the rotation difference between the impurity and main ions is discussed.

1. Introduction

It is widely accepted that toroidal rotation has beneficial roles on MHD stabilization [1,2] and confinement improvement [3,4]. By now, the underlying physics related to the toroidal rotation are still unclear, especially for the momentum transport. To investigate the momentum transport at the interior of plasma, where the momentum flux can hardly be measured directly, perturbative technique [5] is commonly employed to obtain the transport coefficients of toroidal momentum. Significant pinch term of toroidal momentum flux is widely observed on devices like JET [6], DIII-D [7], NSTX [8], JT-60U [9], etc. Comparisons show that the experimentally measured pinch velocity of toroidal momentum is in reasonable agreement with the existing theoretically predictions proposed by Hahm et al. and Peeters et al. However, the measured toroidal momentum diffusivity is found to be much larger than the neoclassical predictions, and is comparable in magnitude with the ion thermal diffusivity. To explain that, theories based on ion-temperature gradient driven turbulence are proposed and suggest that the momentum transport should be subjected to turbulent effects and are deeply coupled with the ion thermal transport. However, experiments on ASDEX-U shows that even in H-mode plasma where the ion thermal diffusivity is reduced to be close to the neoclassical level, the toroidal momentum

diffusivity is still highly anomalous and is larger than the neoclassical predictions by 1~2 orders of magnitude.

In our experiments, the toroidal momentum transport at the interior of plasma has been investigated by electrode biasing (EB) modulation in J-TEXT. The toroidal rotation of plasma is effectively modulated by EB. The characteristics of V_φ perturbations, including the perturbation amplitude and phase delay, are fetched through sinusoidal-fittings, which are further comparatively studied under different modulation frequencies and amplitudes of EB. The toroidal momentum transport coefficients, χ_φ and V_{conv}, are also obtained in the region r/a = 0.68 – 0.9 by solving the toroidal momentum equation analytically. It is found that the values of the coefficients are significant at plasma edge, qualitatively consistent with the results on other devices; the convection velocity is always negative in the analyzed region, and reaches a maximum magnitude at around r/a = 0.85, suggesting the important pinch effect of toroidal momentum especially at the edge.

2. Tungsten spectra of Zn-like XLV (W^{44+}) and CU-like XLVI (W^{45+})

The evolutions of toroidal rotations (V_φ) of the same EB modulation discharge (shot 1038057) are given in figure 1. Here, a positive V_φ corresponds to a co-I_p (parallel to plasma current) directed toroidal rotation. The edge V_φ of main ions (H^+) is measured by LMP, while the V_φ of CV ions at the interior of plasma (r/a < 0.9) is obtained through numerical inversion of the raw ERD signals. Together with that, the time-frequency spectrum of the Mirnov signals is also obtained to reveal the information of local plasma rotation. All these measurements indicate that toroidal rotation can be effectively modulated by EB not only at the boundary, but also at the interior region of plasma.

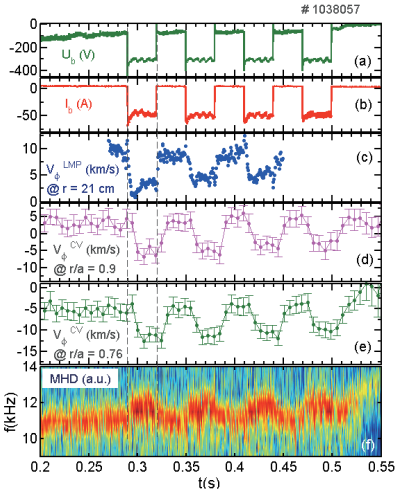

Fig. 1. Evolutions of (from up to bottom): bias voltage, bias current, toroidal rotation of main ions measured by LMP (at r = 21 cm), toroidal rotations of CV ions measured by ERD (at r/a = 0.9 and 0.76).

To quantify the characteristics of the perturbations, the evolutions of V_φ are fitted to the sinusoidal functions with the modulation frequency (see figure 2). Through the sinusoidal-fitting, both the amplitude and phase delay of V_φ perturbations can be fetched, as presented in figure 3. Here, the

phase delays of V_φ perturbations are relative to the phase of the bias current waveform. Comparison between the V_φ measurements of ERD shows that, the magnitude of V_φ perturbations is getting smaller while the phase delay is getting larger as the location moves in. This is consistent with the picture of momentum transport, since the momentum source of EB locates well at edge (r/a = 0.9 – 1).

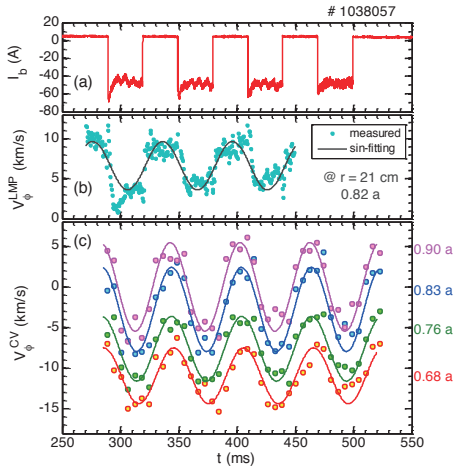

Fig. 2. Evolutions of (from top to bottom) bias current and toroidal rotations measured by LMP and ERD of the same discharge as Fig. 2 and 3. The evolutions of V_φ are fitted to the sinusoidal functions with the modulation frequency.

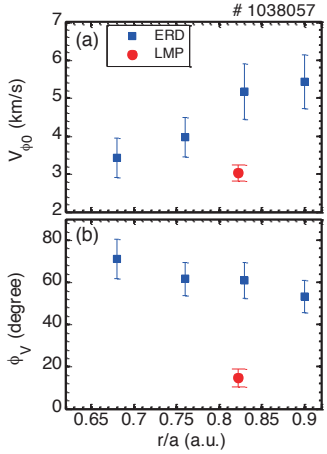

Fig. 3. Profiles of the magnitude and phase delay of V_φ perturbations of the same discharge as Fig. 3. The phase delays are relative to the phase of bias current waveform. Here, the errorbars only indicate the uncertainty induced by the sinusoidal function fittings.

Normally, the boundary is selected at the position r_0/a = 0 where momentum flux will not exist due to the symmetry, as done by the perturbative experiments on devices like JT-60U. However, in our experiments, the measurement of V_φ of CV ions is only available in the region r/a = 0.68 – 0.9. Therefore, we select the position r_0 = 0.68 a as the location of boundary. According to the results on other devices, the transport coefficients at this position should be non-zero, with the diffusivity χ_φ ~ 1 m^2/s and the convection velocity V_{conv} = -1 – -10 m/s. As a try, we set the boundary conditions as $\chi_\varphi(r_0)$ ~ 0 m^2/s and $V_{conv}(r_0)$ = 0 m/s firstly; the profiles of the transport coefficients are then obtained by using the profiles of n_e, $V_{\varphi 0}$ and Φ_V. It is found that transport coefficients are significant at plasma

edge, qualitatively consistent with the results on other devices. The convection velocity is always negative in the calculated region, and reach a maximum magnitude at around r/a = 0.85, indicating that the pinch effect of toroidal momentum is important especially at the edge. For a further step, cases with different boundary conditions ($\chi_\varphi(r_0)$ = 0, 1 m^2/s and $V_{conv}(r_0)$ = 0, -10 m/s, with r_0 = 0.68 a) are also studied, as shown in figure 4. The calculated profiles of the momentum transport coefficients are sensitive to the boundary conditions, but shear the similar tendency with radius. The profile of $\chi_\varphi(r)$ always increases with the radius in these cases, while $V_{conv}(r)$ always reaches its maximum magnitude at around r/a = 0.85. These results can provide a rough estimation of the toroidal momentum transport coefficients on J-TEXT as $\chi_\varphi \sim 1$ m^2/s and $V_{conv} \sim$ -10 m/s in the region r/a = 0.68 – 0.9.

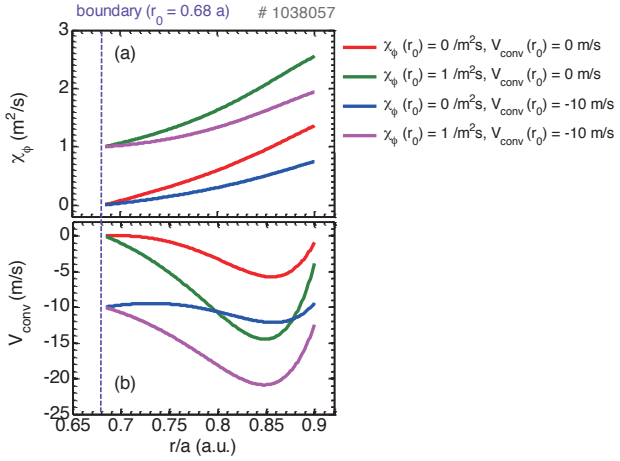

Fig. 4. The calculated toroidal momentum transport coefficients (i.e. the diffusivity χ_φ and convection velocity V_{conv}) of the same discharge as Fig. 3, with the boundary condition as χ_φ = 0, 1 m^2/s and V_{conv} = 0, -10 m/s respectively at r_0 = 0.68 a.

Acknowledgements

This work was partly supported by the JSPS-NRF-NSFC A3 Foresight Program in the field of Plasma Physics (NSFC: No.11261140328, NRF: No.2012K2A2A6000443). This work is also supported by the National Natural Science Foundation of China (Grant Nos. 10990214 and 11305070)

References:

[1] Garofalo A M *et al* 2002 *Phys. Rev Lett.* **89** 235001

[2] Politzer P A *et al* 2008 *Nucl. Fusion* **48** 075001

[3] Terry P W 2000 *Rev. Mod. Phys.* **72** 109

[4] de Vries P C *et al* 2009 *Nucl. Fusion* **49** 075007

[5] Jacchia A *et al* 1991 *Phys. Fluids B* **3** 3033

[6] Tala T *et al* 2009 *Phys. Rev. Lett.* **102** 075001

[7] Solomon W M *et al* 2009 *Nucl. Fusion* **49** 085005

[8] Solomon W M *et al* 2008 *Phys. Rev. Lett.* **101** 065004

[9] Yoshida M et al 2009 *Nucl. Fusion* **49** 115028

Investigation of the high density discharges on the J-TEXT Tokamak

G. Zhuang[1], P. Shi[1], J. Chen[1], L. Gao[1], Y. Liu[1]

[1]Huazhong University of Science and Technology, Wuhan, China

Abstract

To satisfy increasing demands on high-quality measurement of interior magnetic field in tokamak plasma, a far-infrared laser-based polarimeter-interferometer system has been developed on J-TEXT. With this system, high density disruption experiments have been performed on the J-TEXT tokamak to investigate the mechanism behind the density limit. Some interesting features of disruptions in high-density discharges are identified by carefully interpreting the measured polarimeter-interferometer data. During the density ramp-up phase of a high density discharge, asymmetry would occur on both electron density and at the High-Field-Side (HFS) edge ($r < -0.8a$) and extend gradually toward the center. Besides, a low-frequency (< 1kHz) density perturbation suddenly occurs at the HFS edge and also gradually propagates towards the core region. The disruption takes place when the asymmetry on electron density reaches the $q = 2/1$ resonant surface. Asymmetrical behaviors presented on reconstructed electron density and current density profiles provide a possible explanation for the high density disruption.

1. Introduction

Tokamak is regarded as one of the most promising candidates for future magnetic confined fusion reactor. A tokamak plasma is confined by magnetic field supplied by external magnetic coils and its self-inducing plasma current. The topology of magnetic field is closely related to the equilibrium and stability of the plasma, which means that the measurement of internal magnetic structure of plasma is of importance to conduct the tokamak physics research [1].

The laser-based Faraday-effect polarimetry, originally proposed in 1972 [2], is now becoming one of the most promising diagnostics for equilibrium magnetic field structure and its perturbation measurements. Recently, a high resolution polarimeter-interferometer system (POLARIS) based on three-wave technique has been built on J-TEXT tokamak [3-5] to study time evolution of electron density and magnetic perturbations, with high phase resolution ($<0.1^o$ for Faraday angle and $<1^o$ for line-integrated density at 50 kHz bandwidth), high temporal resolution (<1 μs), and high spatial resolution (15 mm minimum).

Based on the J-TEXT POLARIS, high density disruption experiments have been performed on J-TEXT tokamak and some interesting features of disruptions in high-density discharges are identified. The details will be presented n in Sec. 3.

2. The J-TEXT POLARIS

J-TEXT POLARIS based on three-wave technique uses three laser beams for simultaneous polarimetric and interferometric measurement. Two laser beams, namely L-beam and R-beam with counter-rotating circular-polarization, are collinearly aligned and propagated through plasma, while the

third laser beam with linear polarization serves as Local-oscillation (LO). Because of heterodyne measurement, frequencies of the three beams are slightly offset with no overlap among these three produced intermediate frequencies (IFs) (such as 1, 1.5, and 2.5 MHz). Each IF carries different plasma information, which can be isolated by band-pass filtering. Then the phase difference at each IF can be acquired by phase comparison with the signal provided by a reference mixer [6]. The laser frequency (694 GHz) is much larger than plasma frequency (~90 GHz) and electron cyclotron frequency (~56 GHz). Phase difference between L beam (or R beam) and LO beam is ϕ_L (or ϕ_R), while the Faraday effect depends on the phase difference between the L beam and R beam. Thus the Faraday angle α and line-integrated density ϕ can be described as $\alpha=(\phi_R-\phi_L)/2$ and $\phi=(\phi_R+\phi_L)/2$, respectively. At present, the J-TEXT POLARIS has a phase resolution less than 0.1^o and temporal resolution less than 10 μs [7], so it is capable of both polarimetric and interferometric measurements with high spatial and temporal resolutions.

The optical layout of the J-TEXT POLARIS is shown in Fig. 1. To cover the whole plasma cross-section (a = 0.25-0.29 m), the probe beams and LO beam (both 60 mm in diameter) are expanded by 10 times along the major radius direction using two pairs of parabolic mirrors, so the final size of both beams is 600 mm × 60 mm. The expanded probe beams propagate through the plasma, and is focused onto the linear detector array, while the LO beam is also sent to the array without passing through the plasma. Part of the probe beam without passing through plasma, shown in Fig. 1, is used as a reference aiming to eliminate the mechanical vibration.

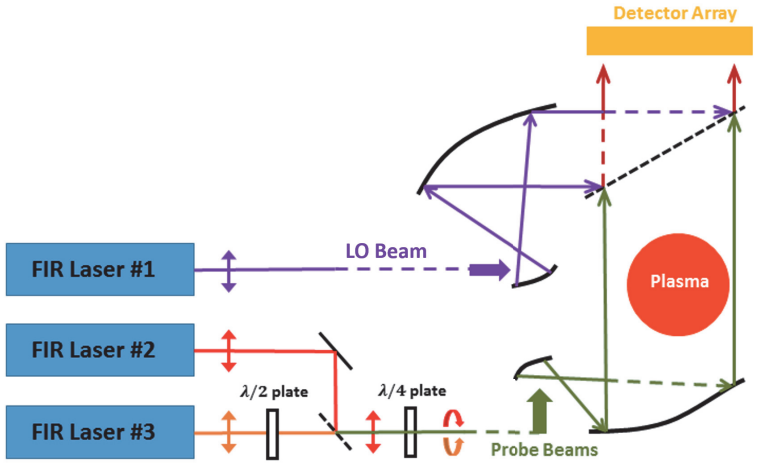

Fig. 1. Layout of J-TEXT POLARIS diagnostic.

3. High density experimental results

Recently, mechanisms of high-density disruption is under research on the J-TEXT. Up till now, some interesting features of high-density plasma disruptions are identified by the measured data supplied by POLARIS. In the density ramp-up phase, asymmetry phenomenon of electron density profiles would appear firstly at the outermost region x = -24 cm, be enhanced gradually and then spreads inward, as shown in Fig. 2(a). Asymmetry starts at the time when the ratio of line-averaged densities at -24 cm and 24 cm exceeds 1. Later on, it reaches x = -21 cm, as shown in Figs. 2(b) and 2(c). The maximum density at x = -24 cm can exceed twice of that at x = 24cm. Accompanying with the density asymmetry behavior, a low-frequency (<1 kHz) perturbation appears on electron density at the HFS edge and gradually propagates

towards the core region, as presented in Fig. 3. The discharge ends with a disruption when the density perturbations reach x = -18 cm (where q = 2 rational surface locates at x ~ -19cm confirmed by ERP calculation). The estimated electron density and current density profiles calculated with slice-and-stack method before the disruption are shown in Fig. 4, and the asymmetry behavior is clearly seen which is excited at 0.28s and x = -24 cm. The current density bump at the HFS edge begins to move inward at 0.32s. Synchronously the electron density bump and low frequency density perturbation also move inward, without evident changes on the LFS edge density. The observations suggest that the density ramp-up would lead to the edge plasma cooling and the edge pressure gradient steeping. Consequently asymmetry happening on electron density and current density profiles, and the low frequency density perturbations as well, would spread inward. Once it reaches the q=2 rational surface, the 2/1 mode is triggered and then the discharge is terminated by a disruption.

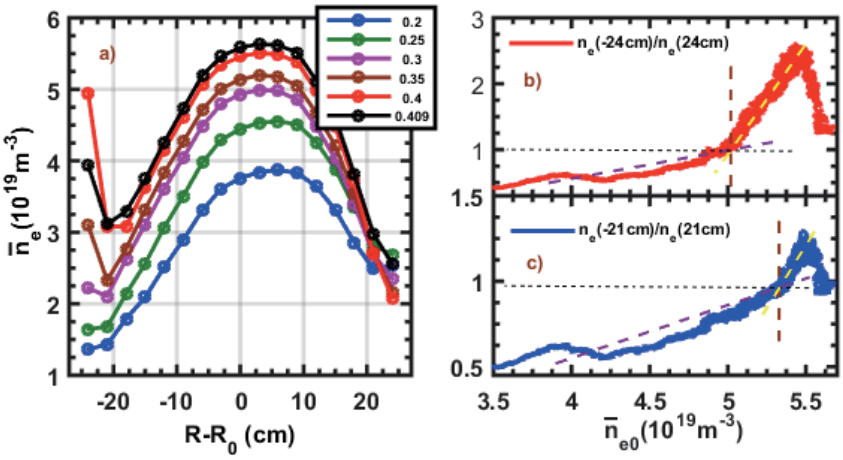

Fig. 2. (a) Profiles for line-averaged density measured by POLARIS; (b) and (c) the evolution of asymmetry at x = ±24cm and ±21cm with the central line-averaged density, respectively.

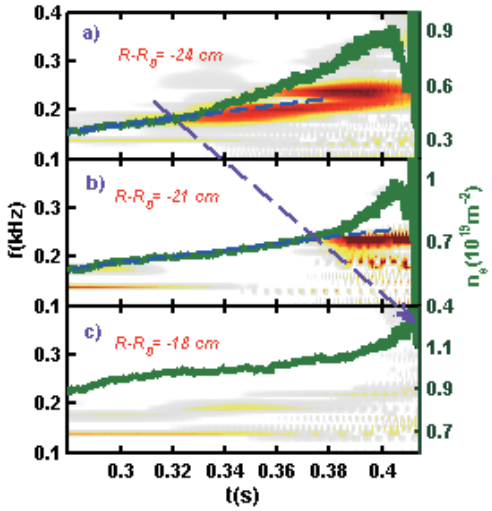

Fig. 3. (a),(b) and (c) Line-integral density and their spectra at -24cm, -21cm and -18 cm, respectively.

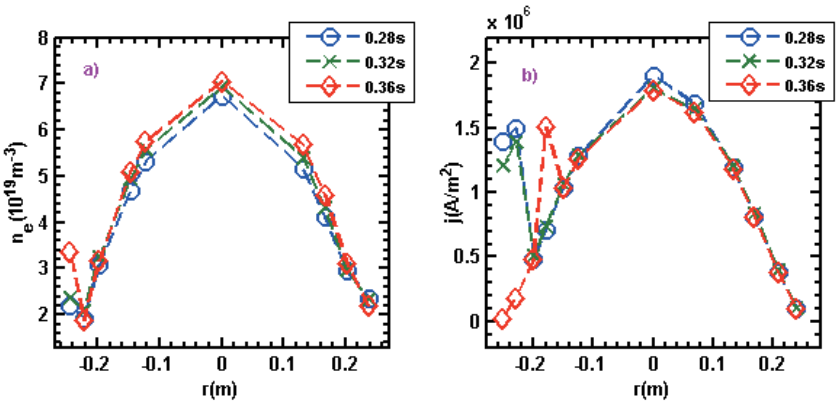

Fig. 4. (a) Estimated electron density profiles and (b) estimated electron current density profiles.

Acknowledgements

This work is supported by the ITER Project Funds of People's Republic of China: Contract Nos. 2013GB106001 and 2009GB107003, and partly supported by the JSPS-NRF-NSFC A3 Foresight Program in the field of Plasma Physics (NSFC No. 11261140328).

References

[1] A. J. H. Donné, et al., Nucl. Fusion 47 (2007) S337–S384.

[2] F. D. Marco and S. E. Segre, Plasma Phys. 14 (1972) 245.

[3] G. Zhuang, et al., Nucl. Fusion 53 (2013) 104014.

[4] J. Chen, G. Zhuang, Z. J. Wang, et al., Rev. Sci. Instrum. 83 (2012) 10E306.

[5] G. Zhuang, J. Chen, Q. Li, et al., J. Instrum. 8 (2013) C10019.

[6] Y. Jiang, D. L. Brower, L. Zeng, and J. Howard, Rev. Sci. Instrum. 68 (1997) 902.

[7] D. L. Brower, et al., Rev. Sci. Instrum. 74 (2003) 1534.

Observation of localized mode in the bad curvature region at the core-density-collapse event in the Large Helical Device

S. Ohdachi[1,2], K. Y. Watanabe[1], K. Tanaka[1], Y. Suzuki[1,2], Y. Takemura[1,2], S. Sakakibara[1,2], X. D. Du[1], T. Bando[2], Y. Narushima[1,2], R. Sakamoto[1,2], J. Miyazawa[1,2], G. Motojima[1], T. Morisaki[1] , and the LHD Experiment Group[1]

[1]National Institute for Fusion Science, 322-6, Oroshi-cho, Toki, Japan
[2]SOKENDAI (The graduate university for advanced studies), 322-6 Oroshi-cho, Toki, Japan

Abstract

The central beta of the super-dense-core (SDC) plasma in the Large Helical Device (LHD) is limited by a large scale MHD event called "core density collapse" (CDC). The detailed measurement of the spatial structure of the MHD activities reveals that new type of ballooning mode, quite localized in space and specifically destabilized in Heliotron devices, is the cause of the CDC. It is the first observation that the ballooning mode is destabilized in the global negative shear region by the 3D nature of the LHD magnetic field. It is effective to avoid the excitation of this mode for expanding high-density operational limit of the LHD.

1. Introduction

High-density operation is one possible reactor scenario of helical confinement system. In the SDC type discharges [1], the electron density higher than 10^{21} m^{-3} with toroidal magnetic field Bt = 2.5T is achieved in the LHD. It is much higher than the density in the equivalent Tokamak devices where the density limit is determined by the Greenwald limit. This is great advantage of the helical system. The SDC plasma is characterized by the fairly peaked density and pressure profiles. Fusion reactor with peaked density profile, similar to the SDC plasma, has many advantages. For example, since the fusion reaction rate is proportional to the density squared, the fusion reaction quite localized at the center of the plasma is anticipated. However, the central pressure or the central beta of SDC plasma is strongly limited by the CDC [2]. The central beta is reduced by as large as 50% by this collapse. The ballooning instabilities related with the 3D nature of the helical system, referred to high-n ballooning mode [3], is considered to be the cause of collapse. The stability of the ballooning mode is determined by the local magnetic properties, e.g., the local magnetic shear and the local magnetic curvature.

2. Ballooning mode and CDC precursor oscillations

In the Heliotron devices, it was predicted that the local magnetic shear can be reduced significantly around the local pressure gradient peak in the large negative global magnetic shear region when the

Shafranov-shift is large [3]. While the reduction of the local shear makes the ballooning mode unstable, the pressure gradient in the bad curvature region drives the mode. In the experiments, just before the CDC events, pre-cursor oscillations (f ~ 8 kHz) measured by the 80ch CO_2 laser imaging interferometer have been found only in the outboard side (Fig. 1). If the mode structure of the pre-cursor is localized around a flux tube (See, 3D image of the Fig. 2 (C)) connected to the outboard side of the horizontally elongated section (worst curvature region), two sharp peaks observed in the fluctuation profile shown in Fig. 2(B) can be understood; two peaks correspond to mode structure observation at two location marked by closed white circles p1 and p2 in the Fig. 2(C). A newly developed 2D SX detector array observing the bad curvature region shows that this pre-cursor like movement is aligned to the local magnetic field line (color pixels in Fig. 2 (C)). This observation also supports that the mode structure is quite localized to the local magnetic field line. Since the amplitude of the pre-cursors increase towards the collapse events, it is reasonable that high-n ballooning mode localized both in radially and poloidally triggers the CDC. Another reason we believe that the CDCs are caused by the high-n ballooning modes, they appears (shown by triangles in Fig. 2) where the ideal high-n ballooning modes become unstable [4] (upper right region of Fig. 4).

3. Operation for suppressing the CDC

In order to suppress the CDC for achieving higher central beta, control of the ballooning mode by the reduction of the Shafranov-shift and by the reduction of the pressure gradient at the bad curvature region is experimentally tested. Plasma shape control using quadrupole magnetic field is effective to reduce the shift and controls the appearance of the CDC [5]. This result can be explained by the stability of the high-n ballooning mode. In the relatively low magnetic field experiment (B_t = 1.5T), the pressure profile is broader than the profile with normal magnetic field B_t = 2.5T (Fig. 3). The operational regime is thereby expanded significantly with the condition of R_{ax0} = 3.75 m and B_t = 1.5T (purple symbols in Fig. 4). It is also consistent with the smaller growth rate predicted by Hn-Bal code with broader beta profile as observed in B_t = 1.5T experiments. The central beta has reached about 10%. It is highest central beta achieved in the LHD and is comparable to the maximum central beta recorded in B_t = 0.45T experiments. Therefore, the mitigation of the high-n ballooning mode is proved to be the key to achieve high central beta in high-density SDC type operation of the LHD.

References

[1] N. Ohyabu, et. al., Phys. Rev. Lett. **97**, 55002 (2006).

[2] H. Yamada, et. al., Plasma Phys. and Contr. Fusion **49**, B487 (2007).

[3] N. Nakajima, Physics of Plasmas **3**, 4545 (1996), **3**, 4556 (1996).

[4] S. Ohdachi, et. al., Contrib. Plasma Phys. **50**, 552 (2010).

[5] J. Miyazawa, et. al., Plasma Fusion. Res. **3**, S1047 (2008).

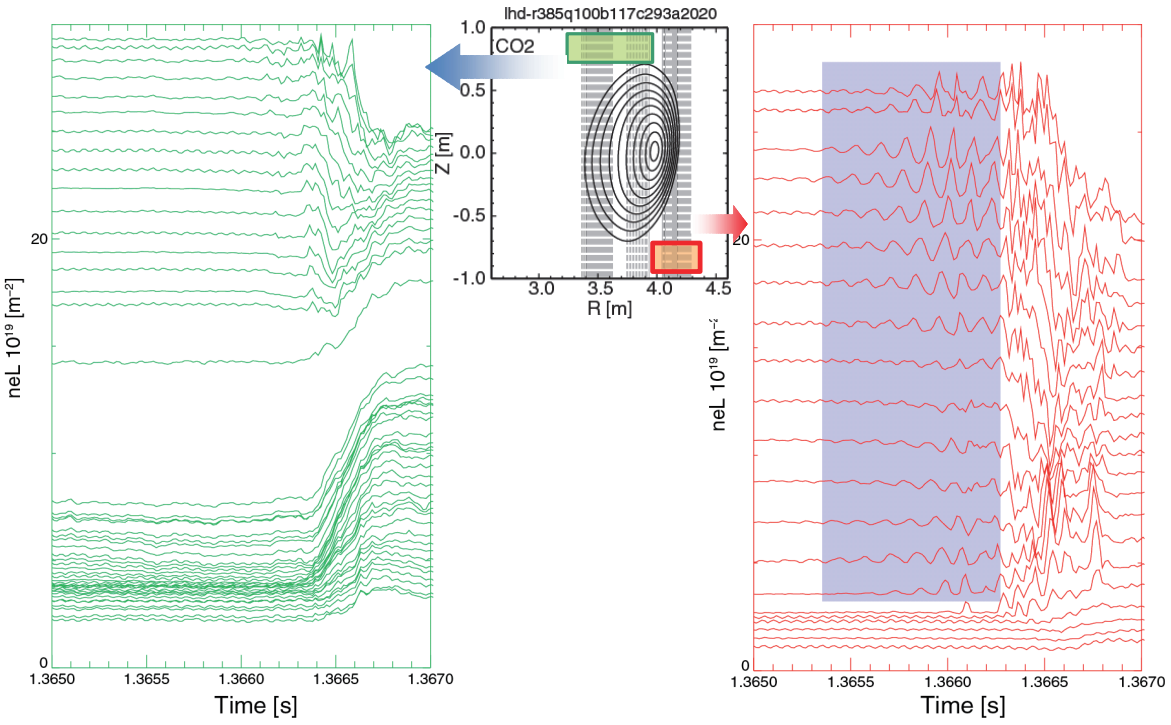

Fig. 1 Pre-cursor like oscillations observed by the 80ch CO2 imaging interferometer.

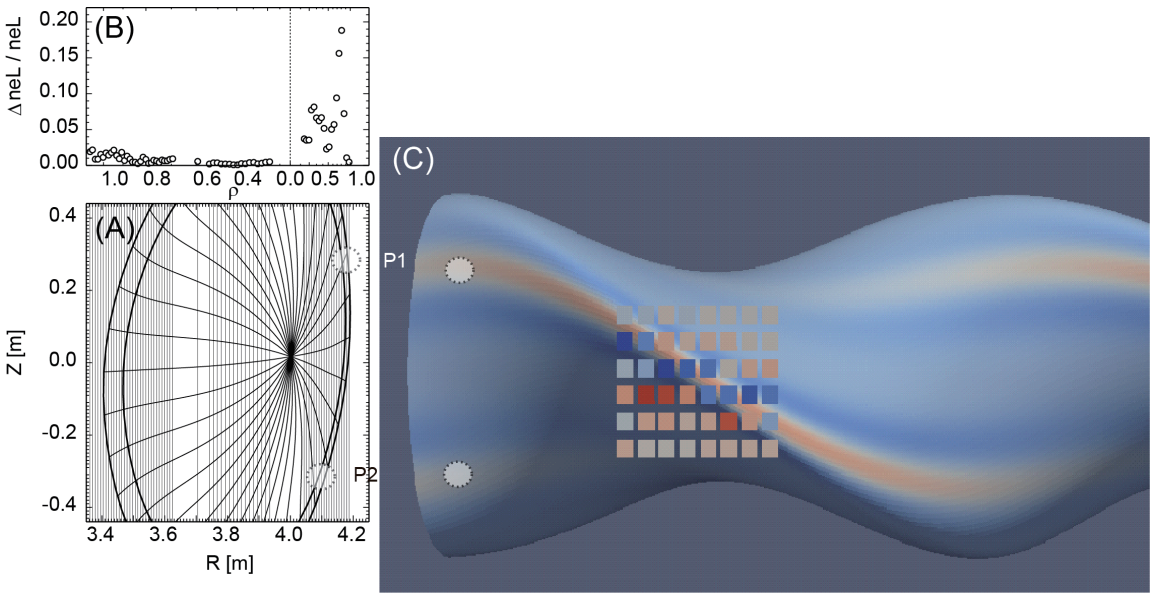

Fig. 2: Sightlines of CO_2 laser imaging interferometer (A), the line-integrated fluctuation profile in the pre-cursor phase (B) and hypothetical mode strucure drawn on the surface of the 3D image of LHD plasma (ρ ~0.8) together with the rapid change of the emission before the CDC, represented by color pixels, measured by 2D (6ch x 8ch) SX array (C) are shown.

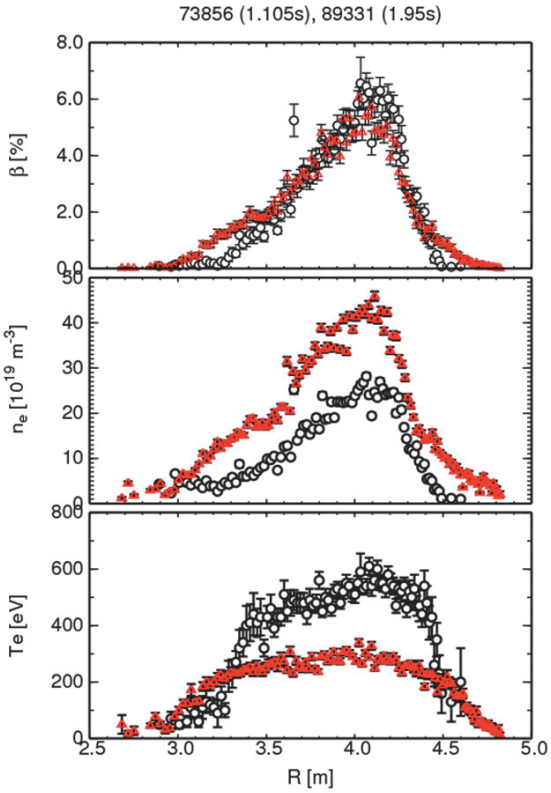

Fig. 3 Comparison of the beta profile with CDC(black) and without CDC(red).

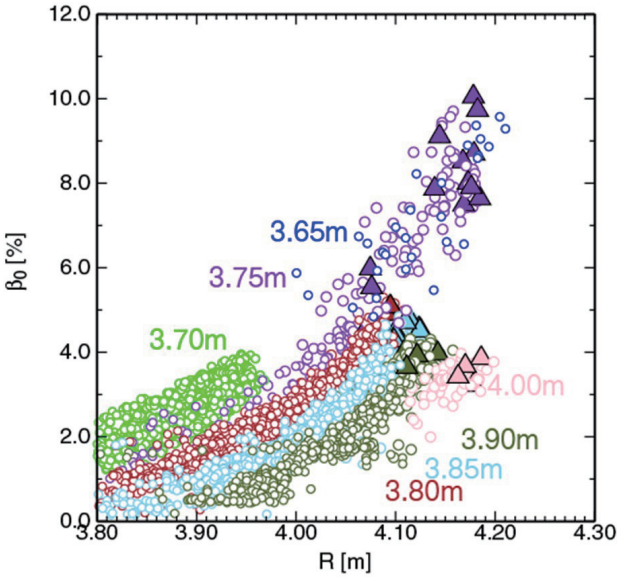

Fig. 4: The central beta as a function of the magnetic axis location is shown with different vacuum magnetic axis location R_{ax0}. B_t = 2.5T for R_{ax0} = 3.8-4.0m and B_t = 1.5T for R_{ax0} = 3.65m and 3.75m. Triangle symbols indicate the appearance of the CDC.

Quasi-snowflake discharge for heat flux reduction on EAST

B.J. Xiao[1,2], Z.P. Luo[1], J.G. Li[1,2], Y. Guo[1], Q.P. Yuan[1], L. Wang[1], J. Xu[1], G. Calabrò[3], R. Albanese[4], R. Ambrosino[4], G. De Tommasi[4], F. Crisanti[3], Y. Huang[1], Z. Xing[1], EAST Team and International Collaborators*

[1]*Institute of Plasma Physics, Chinese Academy of Sciences, Hefei, 230031, China*

[2]*School of Nuclear Science and Technology, University of Science and Technology of China, Hefei, 230026, China*

[3]*ENEA Unità Tecnica Fusione, C.R. Frascati, Via E. Fermi 45, 00044 Frascati, Roma, Italy*

[4] *CREATE, Universittà di Napoli Federico II, Universittà di Cassino and Universittà di Napoli Parthenope, Via Claudio 19, 80125, Napoli, Italy*

bjxiao@ipp.ac.cn

Abstract: Snowflake (SF) divertor configuration, is one of the attractive methods to spread heat load over divertor targets in tokamak because of enhanced scrape-off layer transport and increased plasma wetted area on divertor target. Exact SF for EAST is only possible at very low plasma current due to poloidal coil system limitation. However, we found an alternative way to operate EAST in a so called quasi-snowflake (QSF) or X-divertor configuration, characterized by two first-order nulls with primary null inside and secondary null outside the vacuum vessel. Both modeling and experiment showed this QSF can result in significant heat load reduction to divertor target In order to explore the plasma operation margin and effective heat load reduction under various plasma conditions and QSF shape parameters, we developed ISOFLUX/PEFIT shape feedback control algorithm. Simulation by tokamak simulation code for QSF isoflux control with a multi-input and multi-output controller confirmed its capability for QSF feedback control. In experiment, we firstly applied the control for QSF in a similar way to control the single null divertor configuration. But the significant different control gains are specially designed. Reproducible discharges have been obtained with stable and accurate plasma boundary control. The achieved stable configuration has considerable heat reduction on either L-mode or H-mode operation. Longest pulse QSF discharge has been reached up to 19 s sustained by LHW current drive.

1. Introduction

Heat and particle loads on the plasma facing components are one of the most serious challenging to be solved for the future tokamak fusion reactor [1,2]. One approach to handle the heat exhaust is to use alternative magnetic configurations, such as the snowflake divertor (SF) [3] and (super-)X-divertor [4,5]. The X-divertor places the second x-point near the plate, causing flared field lines there, which spreads the heat over a large area and increases the line connection length. The SF configuration is characterized by a second-order null (x-point) in the poloidal magnetic field, where both poloidal field and its spatial derivatives vanish. This splits the separatrix near the null into six segments: two of them enclose the confined plasma and four lead to the machine wall [6]. The poloidal cross-section of the obtained magnetic

* See the appendix of B. Wan, et al, Nucl. Fusion 55 (2015) 104015

flux surfaces with a hexagonal null-point has the appearance like a snowflake. Theoretical analyses indicate that the SF magnetic geometry leads to both higher power losses during scrape-off layer (SOL) transport and an increased plasma wetted area of the wall [7,8]. The former results from an increase in the connection length and the divertor volume, the latter from an increase in flux expansion and SOL width. The SF divertor discharge was first established on TCV [9], and later on NSTX [10] and DIIID [11].

EAST is constructed to be up-down symmetric, with the following main parameters [12]: major radius R=1.8m, minor radius a=0.45m, toroidal field B_T up to 3.5T, and plasma current I_p up to 1MA for highly elongated plasmas with an elongation κ=1.9. It can be operated in quite flexible plasma shapes with an elongation factor κ=1.5 ~ 2.0 and triangularity δ=0.3 ~ 0.6 for double null (DN) or single null (SN) divertor configurations. EAST equipped with 14 superconducting poloidal field (PF) coils for ohmic heating, ohmic current drive, plasma shaping and position control located outside the toroidal field coils [13]. It should be noted that PF7 and PF9 are permanent connected in series, so are PF8 and PF10. For the fast control of the vertical motion of the elongated plasma, a pair of inside coils (IC1 & IC2) in normal state are connected in anti-series and driven by a fast power supply. Exact SF for EAST is only possible at very low plasma current due to poloidal coil system limitation. However, we found an alternative way to operate EAST in a so called quasi-snowflake (QSF) or X-divertor configuration, characterized by two first-order nulls with primary null inside and secondary null outside the vacuum vessel.

2. EAST QSF discharge with ISOFLUX control

In EAST 2014 campaign, first plasma discharge in QSF configuration was achieved in ohmic discharges with only plasma position and current feedback control [14]. QSF plasma shape was achieved by using designated feed-forward coil current waveforms from simulation results. In these experiments the simplest form of plasma current and position (i.e. plasma centroid) control (RZI_p control) has been used [13].

In order to explore the plasma operation margin and effective heat load reduction under various plasma conditions and QSF shape parameters, plasma shape should be exactly controlled. We designed ISOFLUX/PEFIT [15] shape feedback control algorithm QSF shape control. Simulation by tokamak simulation code (TSC) for QSF shape control with multi-input and multi-output (MIMO) controller in ISOFLUX/PEFIT algorithm confirmed its capability for QSF shape-feedback control [16]. In EAST 2015 QSF dedicated experiment, we firstly applied the control for the QSF configuration in a similar way to the shape feedback for the conventional SN divertor configuration with significant controller tuning. In this new operation scenario, the plasma is controlled by RZIp algorithm until 2.7 s to form a desired QSF configuration with the designated feed-forward coil current waveforms. After 2.7s, the control transits to ISOFLUX/PEFIT shape feedback.

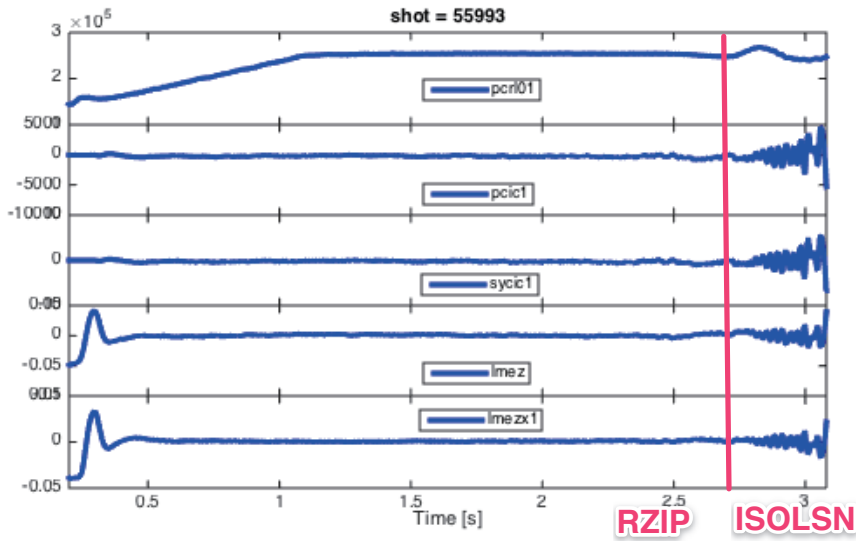

Fig. 1 ISOFLUX control test for QSF configuration, from top to bottom: plasma current (A), inner coil current (A), required current in inner coil (A), estimated vertical coordinate of plasma current center (m), estimated vertical coordinate of plasma current center for fast Z control (m).

1st attempt was to use the traditional single null controller in EAST PCS. The control results are shown in figure 1. We noticed that the plasma lasts 200 ms oscillation after transition to ISOFLUX control. This provides a room for the controller tuning. With the controller modification, reproducible well shape feedback controlled QSF discharges by this single null control (ISOLSN) algorithm. It can be seen there is bad plasma current control on shots 56429 and 56431, even the QSF discharge sustained to ramp down. Figure 3 shows the reconstructed plasma equilibrium shape for shot 56495 at four time stamps.

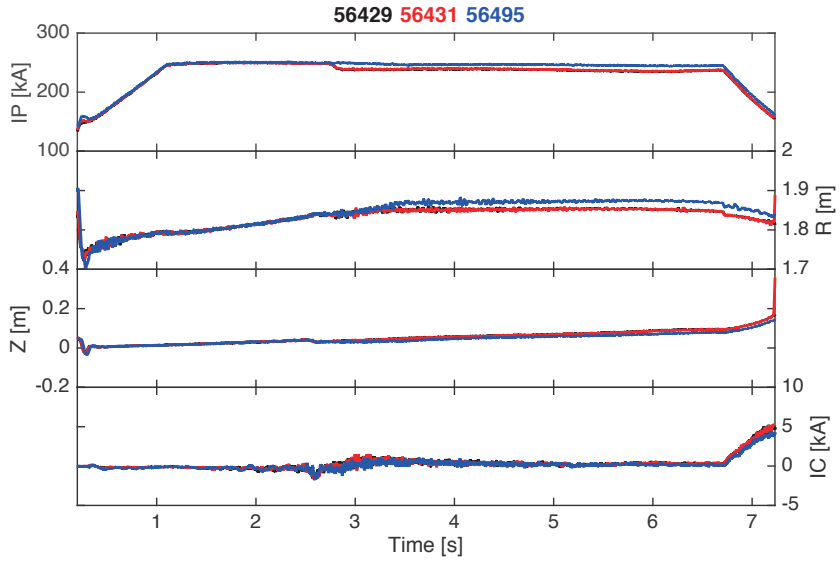

Fig. 2 QSF discharges with good ISOFLUX control, from top to bottom: plasma current (kA), estimated horizontal coordinate of plasma current center (m), estimated vertical coordinate of plasma current center (m), inner coil current (kA).

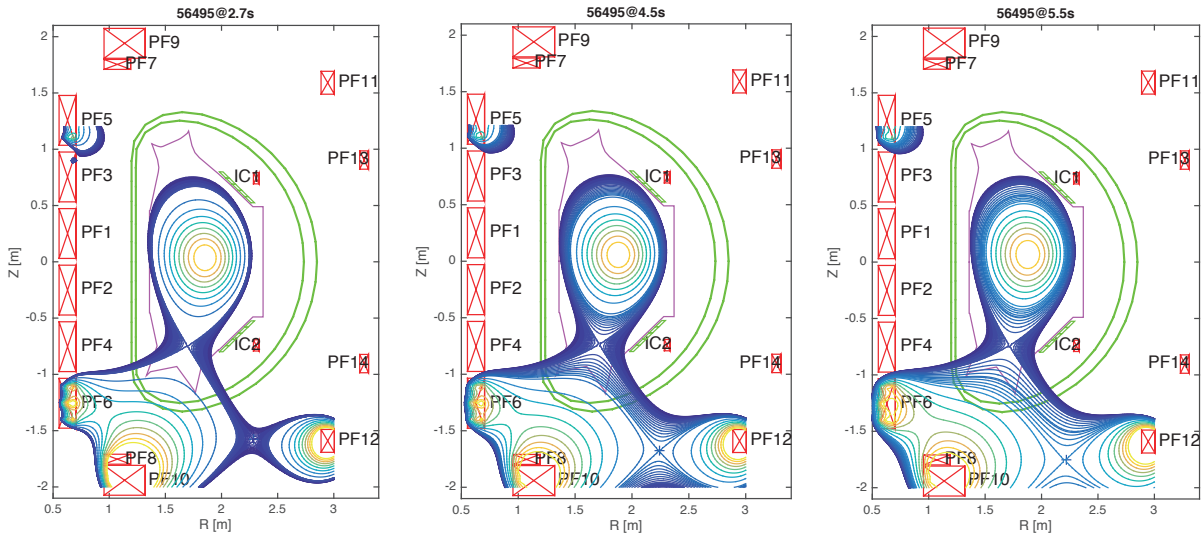

Fig. 3 Reconstructed plasma equilibrium shape for shot 56495.

As shown in Fig. 2 and Fig. 3, reproducible QSF discharges have been obtained with stable and accurate plasma boundary feedback control. In order to reach long-pulse QSF discharge, we need low hybrid wave current drive (LHW) for additional current drive. By simply adjusting the LHW antenna clearance and put some gas puff in front of the antenna to increase the boundary density, good wave coupling with plasma can be achieved. Figure 4 shows that the loop voltage can drop to nearly zero with 1 MW LHW @2.45 GH_z and 1 MW LHW @4.5 GH_z.

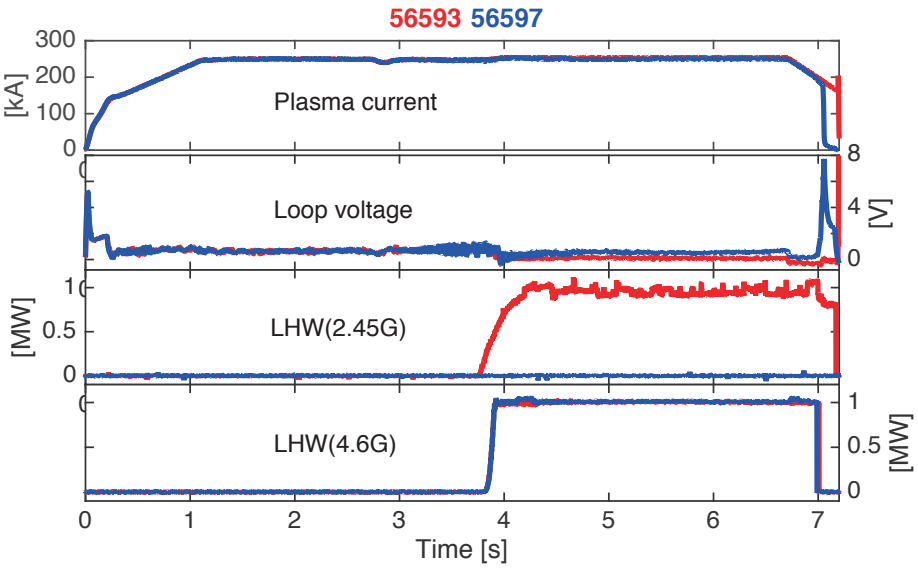

Fig. 4 QSF discharges with LHW, from top to bottom: plasma current (kA), loop voltage (V), 2.45 GH_z LHW (MW), 4.6GH_z LHW power (MW)

It should be noted that in shot 56597, QSF shape was controlled by ISOFLUX/PEFIT algorithm. The shape control error now comes from the parallel plasma equilibrium reconstruction code PEFIT running on GPU machine with real time data transformation

system based on reflective memory network [17] for EAST plasma control system. As shown in Fig. 4, the loop voltage can drop to 0 under the plasma conditions, which allow us to operate plasma in non-inductive current drive for long pulse or even steady-state. Figure 5 shows the longest QSF discharge up to 19 s sustained by LHW current drive.

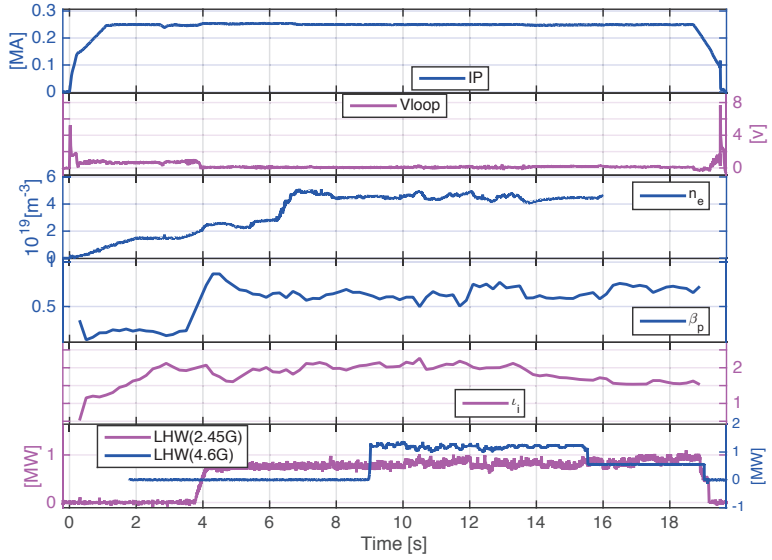

Fig. 5 Up to 19s long-pulse QSF discharges with LHW current drive, from top to bottom: plasma current (MA), loop voltage (V), line integral average density (m^{-3}), poloidal beta, internal inductance, 2.45G & 4.6G LHW power (MW)

After adding more power, we demonstrated H-mode operation for QSF shape. With 3.8MW neutral beam injection (NBI) and 1.7MW LHW power injection, the H-mode QSF discharge was also obtained, as shown in Fig. 6.

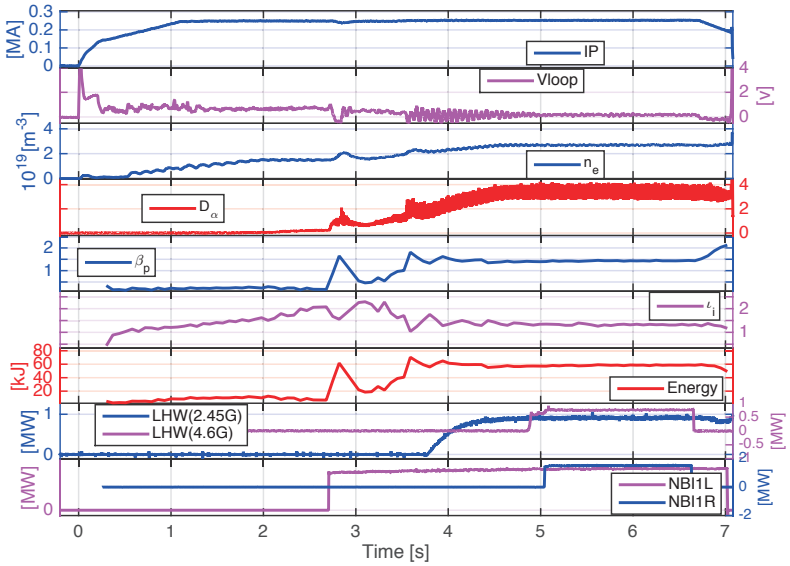

Fig. 6 QSF discharges in H-mode with LHW and NBI, from top to bottom: plasma current (MA), loop voltage (V), line integral average density (m^{-3}), D alpha (V), poloidal beta, internal inductance, plasma energy (kJ), 2.45G & 4.6G LHW power (MW), NBI power (MW)

3. Heat load analysis

In reference [14], two L-mode discharges in EAST 2014 campaign with similar input power, similar effective charge and electron average density, but with different configurations, SN and QSF was compared. The results confirm the predictions: the presence of a secondary null-point in QSF reduces B_p/B_{tot} in the divertor separatrix region, and this increases the connection length by ~30% and the flux expansion in the outer strike point (SP) region by a factor ~4. Reference 14 shows the comparison of the ion saturation current density measurement between SN and QSF. It observed the peak of the ion saturation current density was dropped once the QSF shape becomes stable, which indicates a possible heat flux reduction on plates.

Except the L-mode QSF discharge, the heat load analysis for H-mode QSF discharge in figures 7 and 8. Figure 7 shows the ion saturation current density for both SN (shot: 57237) and QSF (shot: 57239) H-mode discharge. In Fig. 8, the peak heat load was compared between LSN and QSF. It can be observed there is a significant peak heat load reduction in QSF shape compared to LSN. But it should be noted that the plasma current in LSN is 400 kA, where the plasma current in QSF is 250 kA. This may make this comparison a little bit unconvinced. More contrast experiment will be carried out in next campaign.

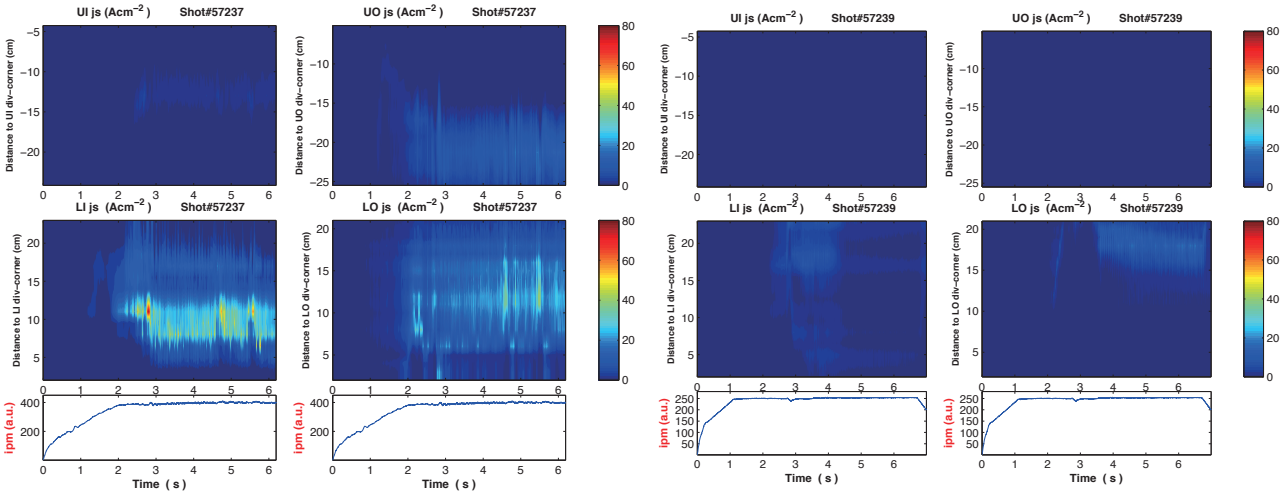

Fig. 7 Spatio-temporal profiles of ion saturation current density

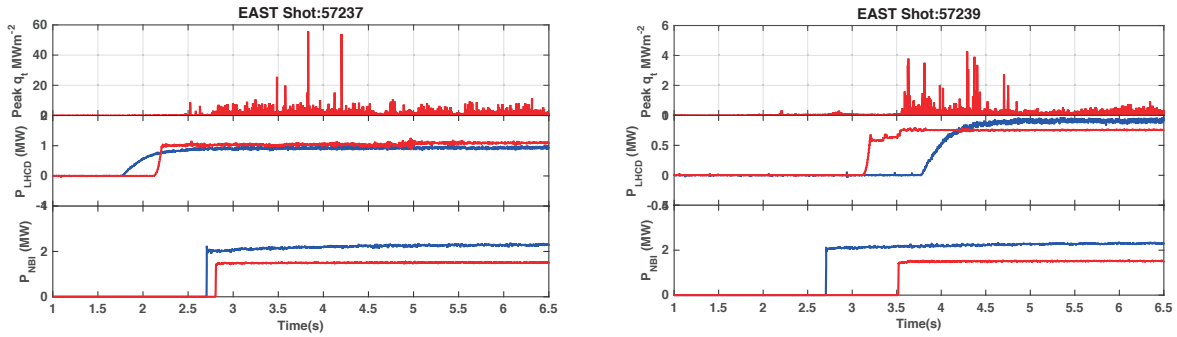

Fig. 8 Peak heat load comparison between LSN (57237) and QSF (57239)

4. Summary

In EAST 2015 campaign, the QSF discharges controlled by ISOFLUX with RTEFIT or PEFIT were demonstrated. The long-pulse up to 19 s in L-mode and H-mode QSF discharges were achieved. Although the flux expansion hasn't been optimized, the achieved stable QSF configuration shows the considerable heat load reduction on either L-mode and H-mode operation. In the next EAST campaign, the efforts will be devoted to more robust shape feedback control for various QSF shapes and extend the parameter operation margin. The opportunity for the plasma operation in long pulse and high parameters will be systematically explored.

Acknowledgments

This work is supported the National Magnetic Confinement Fusion Research Program of China under Grant No 2014GB103000, and the National Natural Science Foundation of China under Grant No. 11305216 and No. 11205191 and China-Japan-Korea A3 program.

Reference

[1] Loarte A. et al, 2007 Nucl. Fusion 47 S203
[2] Eich T. et al, 2011 Phys. Rev. Lett. 107 215001
[3] Ryutov D.D. 2007 Phys. Plasmas 14 064502
[4] Kotschereuther M. et al 2007 Phys. Plasmas 14 72502
[5] Valanju P.M. et al 2009 Phys. Plasmas 16 056110
[6] Vijvers W.A. et al 2014 Nucl. Fusion 54 023009
[7] Ryutov D.D. et al 2008 Phys. Plasmas 15 092501
[8] Ryutov D.D. et al 2014 Phys. Scr. 89 88002
[9] Piras F. et al 2009 Plasma Phys. Control. Fusion 51 055009
[10] Soukhanovskii V.A. et al 2011 J. Nucl. Mater. 415 S365-8
[11] Allen S. 2012 Proc. 24th Int. Conf. on Fusion Energy (San Diego, CA, 8-13 Oct. 2012)
[12] Wan Y. et al 2006 Overview progress and future plan of EAST project Proc. 21th Int. Conf. on Fusion Energy (Chengdu, China, 2006)
[13] Xiao B. J. et al 2008 Fusion Eng. Des. 83 181
[14] Calabro, G. et al 2015 Nucl. Fusion 55 083005
[15] Huang Y. et al 2016 Fusion Eng. Des. (to be published)
[16] Guo Y. et al 2015 Fusion Eng. Des. 101 101

A New Control Method of Edge MHD Stability in Tokamak Plasmas using Scrape Off Layer-Divertor Regions

K. Toi[1], H. Zushi[2] and S. Yamamoto[3]

[1] National Institute for Fusion Science, Toki, Gifu 509-5292, Japan

[2] Research Institute for Applied Mechanics, Kyushu University, Kasuga, Fukuoka 816-8580, Japan

[3] Institute of Advanced Energy, Kyoto University, Uji, Kyoto 611-0011, Japan

Abstract

This paper proposes an alternative method to generate magnetic perturbations (MPs) for edge localized mode (ELM) control by using SOL currents driven by electric biasing of toroidally segmented divertor targets. Two parameters are important for the MP generation: (1) length of the current path along the field line $L_{\parallel}$ and (2) magnitude of the current. The path length in collisionless SOL $L_{\parallel f}$ is estimated from the balance between the parallel free particle flow and the perpendicular one. In the collisional SOL, the length $L_{\parallel c}$ is expressed as $\sqrt{L_{\parallel f}\lambda_{ei}}$, where λ_{ei} is the mean free path. The safety factor q outside the separatrix in a tokamak plasma decreases rapidly from ∞ to ~ q_{95} at ρ~1.1 in the SOL (ρ: normalized minor radius). When the SOL currents flow having sufficiently long $L_{\parallel}$ and the phases among all segmented targets are adjusted, the current pattern is characterized by nearly resonant Fourier components having the toroidal mode number n specified by the biasing and the poloidal mode number $m \sim nq_{95}$. Thus driven SOL currents generate resonant magnetic perturbations (RMPs). The magnitude of the target current reaches ion saturation current or electron saturation current, depending on the polarity of the biasing voltage and the length $L_{\parallel}$. The RMP magnitude can reach above the required threshold for ELM control. Several critical issues of this new method are also discussed.

1. Introduction

In future fusion devices such as ITER, huge heat and particle load should be controlled appropriately by a divertor. The power to the divertor target plates P_{sep} is the sum of alpha power output Pα due to D-T reaction and an additional control power such as current drive P_{CD} with radiation power losses in SOL-divertor region P_{rad}, i.e., $P_{sep}=P\alpha + P_{CD} - P_{rad}$, and reaches about 100 MW in ITER [1]. The heat load q_{div} should be controlled down to the steady limit of 10 MW/m^2 and the transient limit of 20 MW/m^2 for avoiding melting and cracking of the tungsten targets [1]. A planned operation scenario of ITER is based on ELMy H-modes, where a part of the pedestal energy is often released to the divertor targets periodically by ELMs. The data base of the ELM impact on the pedestal show that the energy released by each ELM pulse ΔW_{ELM} increase with the decrease in the normalized collisionality ν^* as shown in Fig.1 [2]. In the ITER pedestal with ν^*~0.06, ΔW_{ELM}=20-30 MJ is inferred from the above data base. This energy loss is 20 to 40 times larger than the tolerable loss for divertor target lifetime.

ELM suppression and mitigation are attempted by using weak magnetic perturbations in many tokamaks [3] and in LHD [4]. Favorable results are obtained in these experiments, although the physics mechanisms of the ELM suppression and mitigation are not fully understood. Accordingly, a set of ELM control coil, so-called resonant magnetic perturbation (RMP) coils are planned to be installed inside the vacuum vessel for ELM control. The RMPs for ELM control are required to satisfy the following conditions: (1) $b_{mn}/B_t=(2\text{-}4)\times10^{-4}$ for the amplitude of the resonant Fourier component b_{mn} and the toroidal field B_t [5], and (2) localized perturbations only in the pedestal region to minimize the impacts on core plasma. The second condition requires the poloidal mode number m is much higher than unity, i.e., $m=nq_{95}>>1$ for $q_{95}=3-4$, where the toroidal mode number n is usually chosen $n=1$ to 4 for simplicity of the RMP coils. The use of /n/=1 RMPs needs a care of the effects on core plasma, in particular, coupling or destabilization of n=1 tearing mode and resistive wall mode which would be locked, although the /n/=1 RMPs are employed successfully to suppress or mitigate large ELMs without enhancing current driven MHD instabilities in KSTAR[6]. Effects of RMPs on core plasm are very sensitive to the plasma response, which is now actively investigated experimentally and theoretically. In most toroidal devices, the in-vessel RMP coils are employed for ELM control, except in JET and LHD where the coils are placed outside the vacuum vessel. The use of the in-vessel coils near long-pulse reactor grade plasmas is questionable. On the other hand, in the external coils placed outside the vessel a large ampere-turn is required because the coils are placed considerably away from the pedestal region. This requires massive mechanical structures to withstand large electromagnetic forces. For these reasons, we propose a new alternative method for ELM control of which method is based on an active use of scrape-off-layer (SOL) and divertor plasmas, in particular, SOL current. The SOL current flows along the open field lines in the SOL region. The currents induced by various causes are experimentally detected in several divertor tokamaks. The SOL current was first observed in JET, where the sheath potential differences in front of the targets due to power deposition asymmetry in inboard and outboard divertor targets dive the parallel current through thermoelectric effect [7]. Figure 2 shows the observed SOL current driven by thermoelectric effect in the AUG tokamak, where the current flows from the outer target to inner one [8]. Moreover, large SOL currents are also observed during type-I ELMs, exhibiting filament

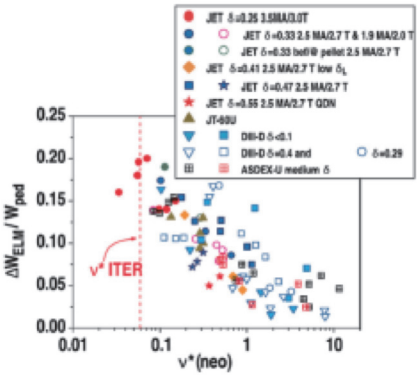

Fig.1 Energy released by an ELM pulse as a function of the normalized collisionality at the pedestal top [2]

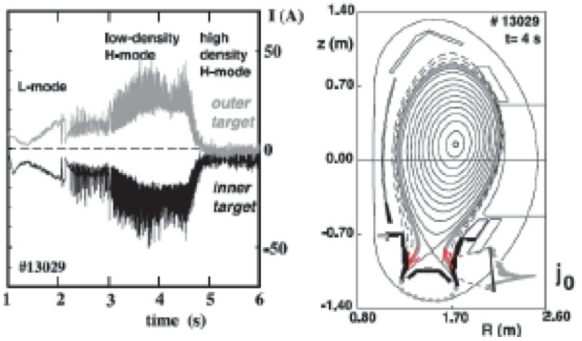

Fig.2 Time evolution of the SOL current induced by thermoelectric effects on AUG [81.

structures [9-11]. The large SOL currents form lobes near the X-point clearly. ELM control was done in the EAST tokamak using the SOL currents driven by lower hybrid waves (LHWs) [12]. This technique is interesting but very challenging toward the control of the LHW power deposition for the SOL current drive and hot spot problems under high power LHW.

2. Key parameters in a new control method by SOL current

In the method proposed here the currents are driven in the SOL along the open field lines by electric biasing of toroidally segmented divertor targets for the grounded vacuum vessel. This method was first motivated from the fact that helical field perturbations with the specified toroidal mode number *n* were successively generated by driving the currents along the field lines, of which currents are induced by electric biasing of toroidally separated large electrodes inserted just inside the last closed flux surface (LCFS)[13, 14]. Instead of the inserted large electrodes, we use the divertor target plates in the new method. In Fig.3(a), an example of the SOL current pattern is shown on the φ-θ plane, where the currents are driven by biasing both outboard and inboard side targets with P-N-P-N-P-N and N-P-N-P-N-P phasing

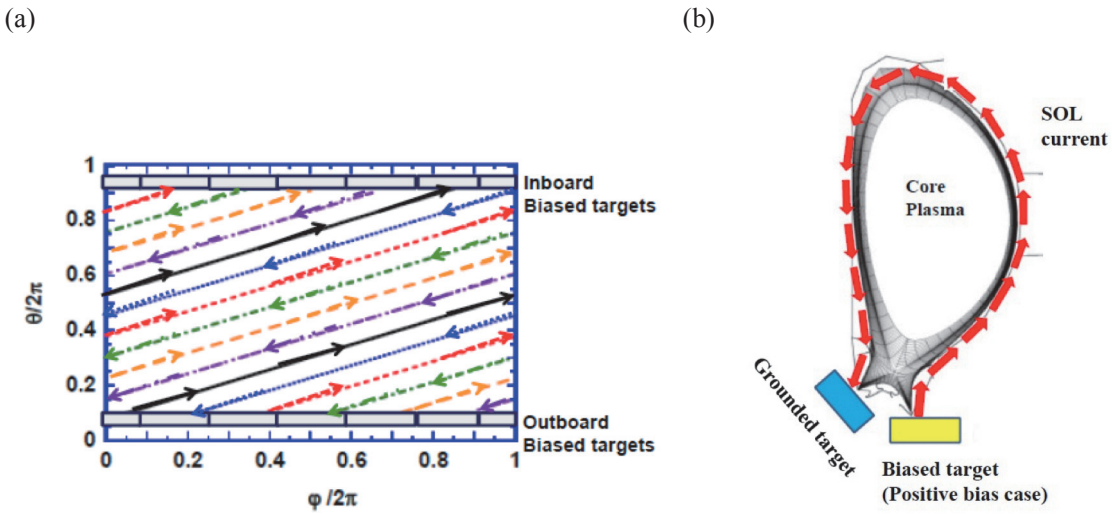

Fig.3 (a) An example of the SOL current pattern with P-N-P-N-P-N biasing (outboard side) and N-P-N-P-N-P biasing (inboard side). (b) Projection of the SOL currents launched from a P-biased target onto the poloidal cross section.

(N: negative, P:positive). In this example, it is assumed that the SOL currents flows connecting two outboard and inboard targets and no interference between neighboring SOL currents. The projection of the flowing path of the SOL current launched from a P-biased target onto the poloidal cross-section is schematically shown in Fig.3(a) for a single-null divertor configuration. The generation of magnetic perturbations such as RMPs by the SOL currents is governed by the following two key parameters: (1) length of the current path along the field line $L_{\parallel}$ and (2) magnitude of the current.

2.1 Estimation of the length of the flowing path of SOL current

The length of the current path in collisionless SOL ($L_{\parallel jf}$) is estimated from the balance

between the parallel free flow and the perpendicular flow for j-th charged particles, where $j=e$ and $j=i$ refer the electron and ion [15]. From the balance of the particle fluxes parallel and perpendicular to the magnetic field lines $A_{\parallel}\Gamma_{\parallel j} + A_{\perp}\Gamma_{\perp j} = 0$, the length of the SOL current is $L_{\parallel jf} = \frac{d^2 h v_{\parallel j}}{8(d+h)D_{\perp j}}$. Here, d is the effective radial width of the SOL current and h the toroidal projection length of the toroidal length of the biased target perpendicular to the field lines. The quantities $v_{\parallel j}$ and $D_{\perp j}$ are the thermal velocity and diffusion coefficient for j-th charged particles. The areas perpendicular and parallel to the field lines which collect the parallel and perpendicular flows respectively are expressed as $A_{\parallel}$ and $A_{\perp}$. Because of $v_{\parallel e} >> v_{\parallel i}$ and $D_{\perp e}=D_{\perp i}$, the path length of ion current driven by negative biasing is by a factor of $\sqrt{\frac{m_e}{m_i}}$ shorter than that of electron current driven by positive biasing, where m_e and m_i are respectively the mass of electron and ion. If plausible parameters d=0.03m, h=0.28m and $D_{\perp e}=D_{\perp i}$=0.2 m^2/s (~ 10D_{Bohm}: Bohm diffusion) with T_e=2 eV and B_t=5.2 T for biased divertor targets divided into 6 toroidal segments are assumed in an ITER-like device, $L_{\parallel ef}$=280 m for electron current and $L_{\parallel if}$=4.1 m for ion current in D-T plasma are predicted. The length of the field line connecting between the outboard and inboard targets of a single null divertor is ~$2\pi R q_{SOL}$, where q_{SOL} is the effective safety factor of the SOL. In an ITER like plasma of R=6.2 m and q_{SOL}=3.5, $L_{\parallel ef}$=280 m > $2\pi R q_{SOL}$ =136 m >> $L_{\parallel if}$=4.1 m for an assumed collisionless SOL. This result means that the SOL electron current filament having long length will act as "plasma coils" effectively. In a standard operation of ITER, however, the collisionless SOL is not the case. The ITER should be operated with detached divertor condition, for instance, in front of the divertor target plates $T_e=T_i$=2 eV and n_e=5x10^{20} m^{-3} are expected. For the condition, the SOL is no longer collisionless and is very collisional. That is, the mean free path of electrons or ions in the SOL λ_{ei} is estimated to be λ_{ei}~7x10^{-5} m << $2\pi R q_{SOL}$ < $L_{\parallel ef}$. In the collisional SOL, the length of the electron current filament is estimated as $L_{\parallel ec} = \sqrt{L_{\parallel ef}\lambda_{ei}}$, = 0.14 m [15]. In this situation, the SOL current would not act as "plasma coils" effectively. A generation method of RMPs in the situation is discussed in the next section.

2.2 Estimation of the magnitude of SOL current

The other key factor is how much SOL current is driven by the biasing of the divertor target plates. When the target is biased with negative voltage for the vacuum vessel, the maximum current extracted from the target reaches ion saturation current (density) i_{is}=0.61Ze$n_i\sqrt{\frac{T_e+T_i}{m_i}}$, when the magnitude of the biased voltage sufficiently exceeds ~3T_e where T_e is electron temperature at the ion sheath, where Z and n_i are the ion charge and ion density, respectively. On the other hand, when the target is biased by positive voltage of about (3~5)T_e, the current reaches electron saturation current (density) i_{es} where $i_{es}/i_{is}=\sqrt{\frac{m_i}{m_e}}$ >>1. From experimental data, $i_{es}/i_{is}=\sqrt{\frac{m_i}{m_e}}$ is not always true, but at least the ratio i_{es}/i_{is} is greater

than 10. As an example, if T_e=T_i=2 eV and n_e=5x10^{20} m^{-3} in front of the divertor target plates are assumed, i_{is}=0.6 MA/m^2 and i_{es}=6 MA/m^2 are obtained. The above-mentioned geometric parameters are assumed as d=0.03m, h=0.28m, each toroidal target segment can drive a current up to 5 kA for i_{is} and 50 kA for i_{es}, respectively. The SOL current layer locates fairly close to the pedestal top, for instance, the relative difference $\Delta\rho$ ($=\Delta r/\langle a\rangle$)=0.05, i.e., Δr~0.14 m for the averaged plasma minor radius $\langle a\rangle$=2.7 m so that the magnitude of magnetic perturbation generated the SOL currents would reach large value well above the required threshold for ELM control, i.e., b_{mn}/B_t=2-4x10^{-4} mentioned in [5]. The necessary magnitude can be obtained by appropriate control of applied basing voltage.

It should be noted that the current reaches up to the electron saturation current i_{es} by positive biasing if the current path $L_{\parallel}$ does not connect both biased outboard targets with grounded inboard targets. On the other hand, if $L_{\parallel}$ is much longer than the connection length of the field line the current is bounded up to i_{is} because of the divergence free of current density in the flux tube flows the SOL current.

3. Fourier spectra of SOL currents

It is important to investigate Fourier components of magnetic perturbations generated by the SOL currents in the φ - θ plane (φ and θ : toroidal and poloidal angles) on a certain flux surface. Here, for simplicity, we only calculate the Fourier spectra of the SOL current pattern as shown in Fig.3(a), since the Fourier components can generate almost similar those of generated magnetic perturbations. Before the calculation, we need information of the field line pitch or the safety factor extended outside LCFS. Figure 4 shows an example of the q-profile extended outside LCFS (ψ_N>1) as a function of the normalized poloidal flux ψ_N, where ψ_N=1 denotes the separatrix or LCFS [16]. As seen from Fig.4, the q-value in the SOL region (ψ_N>1) is close to that in the pedestal region just inside the LCFS, i.e., 0.9 < ψ_N < 1. It should be noted that the currents flow along the field lines in the SOL can intrinsically generate the Fourier components that resonate with the q-value in the pedestal region.

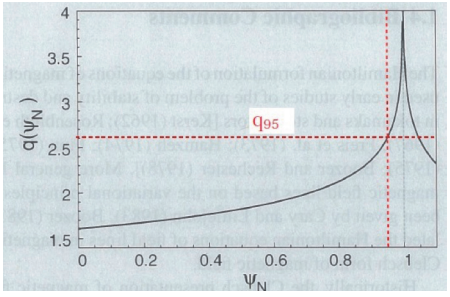

Fig.4 Safety factor q profile extended to the SOL region as a function of the normalized poloidal flux ψ_N [16].

Here, we calculate m and n Fourier spectra of the SOL current pattern. The SOL current pattern on the φ-θ plane in a collisionless SOL case is shown in Fig.5(a). The biased divertor targets are in the outboard side at $\theta/2\pi$=0.09 and the grounded inboard targets are at $\theta/2\pi$=0.92. Here, the simplest biasing scenario is adopted, that is, only outboard side targets are biased and the inboard ones are grounded, in contrast to that shown in Fig.3(a). Moreover, the SOL currents are assumed to be straight lines with a tilted angle corresponding to the q-value in the SOL, i.e., in this example q_{SOL}=3.5. The outboard targets for biasing is divided into 6 toroidal segments, for aiming at generation of n=3 magnetic perturbations. As discussed in the previous section, positive biasing is favorable for realizing long path length of the SOL

current $L_{\parallel}$ and large current carried by electrons. We discuss two typical cases, i.e., a collisionless SOL case relevant for attached divertor and a collisional case relevant for detached divertor.

As discussed in the previous subsection 2.1, a collisionless case $L_{\parallel}$ much longer than the connection length of the field line from the outboard target to the inboard one is shown in Fig.5 (a). Here, three target segments are positively biased and the targets between them are floated in a single null poloidal divertor

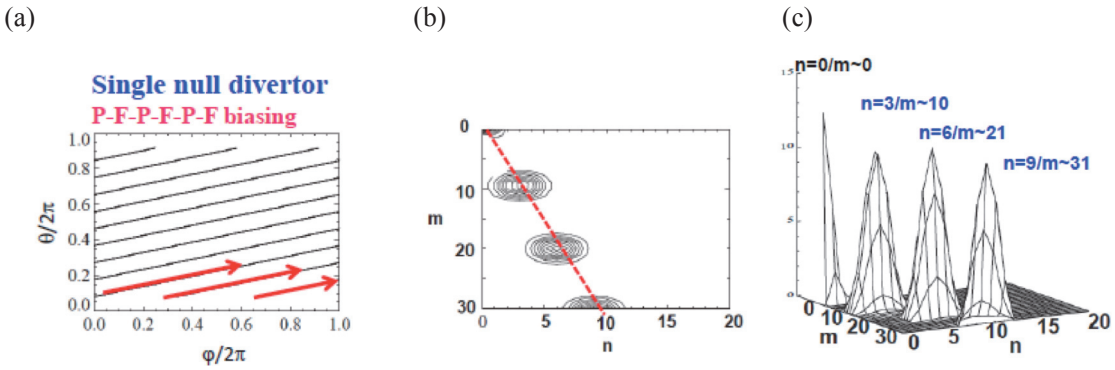

Fig.5 (a) SOL current pattern for n=3 RMP generation for a collisionless SOL case in a single-null divertor configuration, (b) Contour plot of the Fourier spectrum intensities of the current pattern on the m-n space, and (c) Surface plot of the m-n spectra. The broken line in Fig.(b) indicates the resonance of $m/n \sim q_{95}=3.5$.

configuration. No current flows through the floated targets. Figures 5(b) and (c) show the distributions of the Fourier spectra for *m* and *n* mode numbers. The spectra concentrate into the resonant components having $m/n \sim q_{95}$, although a small fraction of $m/n=0/0$ is generated. If the inboard targets are also positively biased and each SOL current does not any interference as shown in Fig. 3(a), the $m/n=0/0$ component can be removed and the all Fourier components become resonant ones. However, the interference of the currents launched from the outboard and inboard targets will be unavoidable. Note that more realistic SOL current pattern deviates from multi-straight lines due to toroidal effects. This tends to broaden the *m*-spectrum around the right resonant components. This may be favorable for introducing flexibility of generated magnetic perturbations for ELM control.

In a collisional case as discussed in previous subsection 2.1, the current path length is too short. I should be noted that the magnitude of currents flow each biased segmented target is large despite short $L_{\parallel}$. One possible way is to

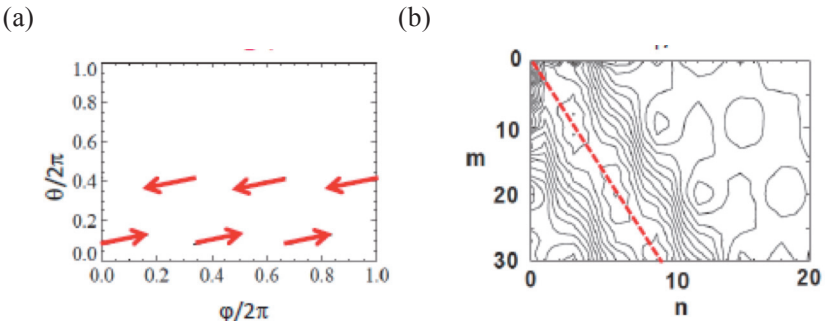

Fig.6 (a) Current patter simulates the currents of the feeders placed behind the divertor targets where the biasing pattern for the upper part is F-P-F-P-F-P and that of the lower part is P-F-P-F-P-F, (b) Contour plot of the Fourier spectra in the m-n space. The broken line in Fig. (b) indicates the resonance line of $m/n \sim q_{95}$.

arrange the feeder lines appropriately, for instance, behind the divertor baffles placed vertically in the divertor slot. In Fig.6(a), the equivalent current patter on the φ-θ plane is shown for the case that both upper and lower parts of the outboard divertor targets in a double null divertor configuration are positively biased as F-P-F-P-F-P phasing for the upper parts and P-F-P-F-P-F phasing for the lower ones. The feeders are placed with a tilted angle adjusted to q_{95}. This case also can generate resonant components mainly. However, this evaluation is very crude. More detailed design studies are needed to access the feasibility and are left for future work.

4. Discussions

In this section, the following key issues are briefly discussed: (1) heat removal and equalization of biased targets, (2) power input to SOL by the biasing, (3) phase interference among the SOL currents, (4) ion bombardment energy, (5) effects of SOL currents on cross-field heat and particle transport, and (6) others. For (1), the applied biasing voltage is at most ~100V for typical divertor conditions. Electrical insulation of the biasing targets against the vacuum vessel will be less than 200V. Both electrical insulation and heat conduction can be realized by Almina (Al_2O_3). This insulator has a special character for thermal conductivity. The thermal conductivity of Almina of 93% purity is nearly same as that of stainless steel SUS 304. Accordingly, heat deposited on the biased targets will be effectively transferred to heat sinks arranged behind the targets through thin coating of the high purity Almina. For (2), the power input by the biasing to each flux tube in the SOL connected to each biased target segment is ~ 2MW for assumed viasing voltage 200V and driven current 10 kA. Total power of all 6 target segments is at most 12 MW and is much less than the total power released from the plasma core P_{sep} ~ 100 MW. For (3), the phase interference among the biased targets may be minimized with a phasing pattern with a pair of P(positive) and F(floated), as shown in Figs. 5 and 6. It should be noted that thus generated RMPs may affect the SOL current magnitude and pattern considerably. This effect is highly nonlinear and should be investigated experimentally. For (4), positive biasing will minimize the ion bombardment energy, because the accelerating electric field is diminished by the biasing in front of the target. For (5), the SOL current flows along the field line will enhance radial heat and particle transport and may contribute to appreciable reduction of heat load with help of increase of the *e*-folding radial length. For (6), arcing among biased electrodes and plasma facing components (PFCs) grounded to the vacuum vessel may be induced because of generated potential differences among the targets and PFCs. This is an important issue to be studied experimentally. Triple Langmuire probe is often employed without suffering from any arcing events. This may provide us an insight for overcoming this problem.

5. Conclusion

A new method is proposed to generate RMPs by using SOL currents driven by toroidally segmented divertor target plates with specified phasing baising in a tokamak plasma. The feasibility is determined by two key parameters: the length of the SOL current along the open field lines and the magnitude of the current of the flux tube connecting with each biased target. A biasing pattern with several pairs of P(positive)-F(floated) phasing is most promising because of minimizing phase interference among SOL

current filaments and reducing ion bombard energy to the targets. Heat removal of biased target plates can be effectively performed through thin high purity Almina, ensuring ~200 V electrical insulation. This paper presents only preliminary discussions on the feasibility. Nevertheless, this method has high potentiality for ELM control and divetor heat handling with relatively simple setups, although more detailed design studies and experimental tests are strongly required.

Acknowledgements

This research is partly supported by the Grant-in-Aid for Challenging Exploratory Research from JSPS (No. 26630476) and the JSPS-NRF-NSFC A3 Foresight Program in the field of Plasma Physics (NSFC: No.11261140328, NRF: No.2012K2A2A6000443).

References

[1] A. Loarte et al., Chapter 4 in *the Progress in the ITER Physics Basis*, Nucl. Fusion **47** (2007) S203.

[2] A. Loarte et al., Plasma Phys. Control. Fusion **45**(2003) 1549 :

[3] A. Kirk et al., Plasma Phys. Control. Fusion **55** (2013) 124003.

[4] K. Toi et al., Nucl. Fusion **54** (2014) 033001.

[5] M.J. Schaffer et al., Nucl. Fusion **48** (2008) 024004.

[6] Y. M. Jeon et al., Phys. Rev. Lett. **109** (2012) 035004.

[7] P.J. Harbour et al., J. Nucl. Matter.**162-164** (1989) 236.

[8] A. Kallenbach et al., J. Nucl. Matter.**290-293** (2001) 639.

[9] A. Kirk et al., Phys. Rev. Lett. **96** (2006) 185001.

[10] H. Takahashi et al., Phys. Rev. Lett. **100** (2008) 205001.

[11] N. Vianello et al., Phys. Rev. Lett. **106** (2011) 125002.

[12] Y. Liang et al., Phys. Rev. Lett. **110** (2013) 235002.

[13] G. Matsunaga et al., Phys. Rev. Lett. **94** (2005) 225005.

[14] T. Ito et al., Phys. Plasmas **16** (2009) 092105.

[15] P.C. Stangeby, J. Phys. D: Appl. Phys. **18** (1985) 1547.

[16] S. Abdluaev, " *Magnetic stochasticity in magnetically confined fusion plasmas*", Springer, 2013.

Divertor leading edge experiments in KSTAR

Suk-Ho Hong on behalf of KSTAR team and collaborators

National Fusion Research Institute, Daejeon, Korea

Email: sukhhong@nfri.re.kr

This paper gives an overview of divertor leading edge experiments performed on KSTAR since 2014. Heat loads on the tungsten blocks were measured by divertor IR camera and compared with calculated results simulated by COMSOL. The results indicate that measured and calculated ones are consistent, and model can predict heat flux on the tungsten leading edge reasonably well.

1. Introduction

An important design issue for the ITER tungsten (W) divertor and in fact for all such components using metallic plasma-facing elements and which are exposed to high parallel power fluxes, is the question of surface shaping to avoid melting of leading edges. Inevitable engineering tolerances, especially with large scale, actively cooled systems, mean that misalignments, usually at the level of hundreds of microns, cannot be avoided. Surface shaping is expensive, especially when many tens of thousands of individual elements are involved, as in ITER. Recent experiments on JET cast some doubt on the power loading of extreme leading edges at glancing incidence [1], prompting the International Tokamak Physics Activity to launch a multi-machine effort to study leading edge physics in support of a shaping decision on ITER [2, 3, 4].

To study leading edge heat loads, we have designed and manufactured a series of multi-purpose, brazed W blocks based on tungsten (W), copper (Cu), and copper-chrome-zirconium alloy (CuCrZr). The blocks are mounted and assembled into graphite tiles installed on the central divertor of KSTAR. Depending on the plasma scenario, tungsten blocks were exposed directly to the plasma as the outer strike point, or remain inside the private flux region. The blocks were located within the line of sight of an infra-red (IR) camera system installed in an upper lateral port. The blocks are arranged in different groups, with toroidal gaps of 0.5 mm or 1 mm addressing specific issues: 1) leading edges caused by different shapes of blocks; 2) three different surface shapes, including toroidal chamfers similar to those envisaged for the ITER divertor; 3) two different block-to-block toroidal misalignments (±0.3 mm), simulating the worst case ITER engineering misalignment and 4) a variety of leading edge heights (0.3, 0.6, 1.0, and 2.0 mm), from the ITER worst case to heights even beyond the extreme value tested on JET. Adjustment of the outer divertor strike point position is used to deposit power on the different blocks in different discharges, but with emphasis in these first studies on studying power loading as a function of leading edge height. The measured power flux density on flat regions of the surrounding graphite tiles is used to obtain the parallel power flux, $q_{\parallel}$ impinging on the various W blocks.

The aim of the paper is to introduce divertor leading edge experiments performed in KSTAR since 2014. The paper is organized as follows. In section 2, we will describe the experimental setup. Block design for the experiments, diagnostics and modeling method are given. In section 3, results are briefly introduced. In section 4, a summary will be given.

2. Experimental Setup and thermal load analysis

Tungsten blocks of several different shapes and thickness were fabricated and installed at central divertor in 2014 as shown in Fig. 1. The base design is a conventional castellation of right angled square structure with 30 mm × 20 mm × 12 mm size: 5 mm tungsten, 13 mm CuCrZr base, and 2 mm pure cupper intermediate layer, with chamfer structure. Two other shapes are modification from this base design. One has rounded edge of radii of 3.4 mm and 1.7 mm, while the other has a double chamfer structure. Toroidal gap size is 0.5 mm or 1 mm. In 2016 campaign, tungsten blocks of several different heights were fabricated and installed at central divertor as shown in Fig. 2. In 2015 campaign, base design is a conventional castellation of right angled square structure with 30 mm × 20 mm × 12 mm size with a variety of leading edge heights (0.3, 0.6, 1.0, and 2.0 mm) with toroidal gap of 0.5 mm.

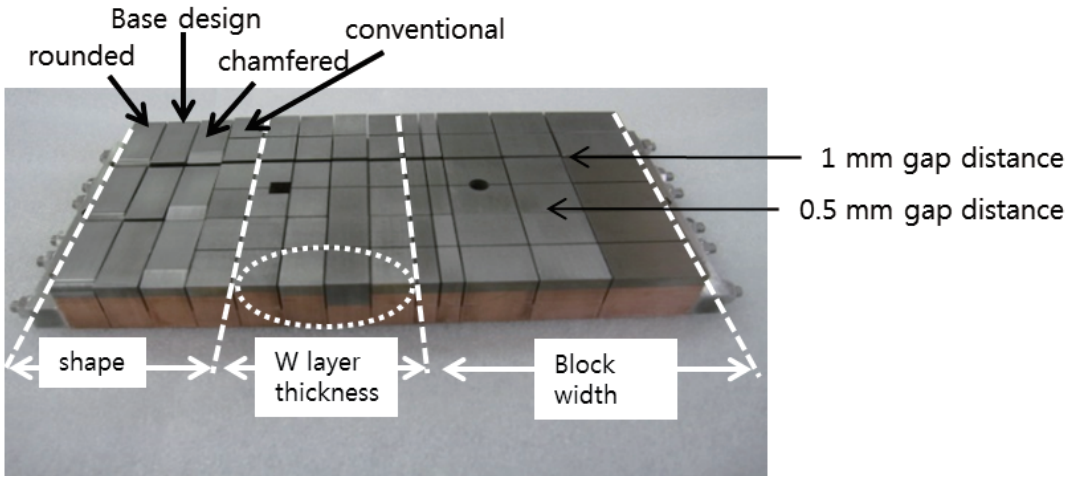

Fig. 1. Tungsten blocks for leading edge study in 2014 campaign.

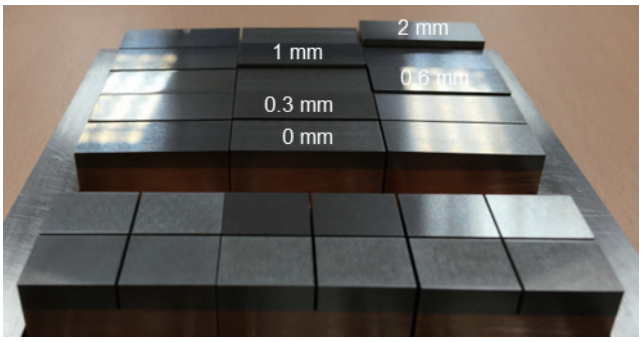

Fig. 2. Tungsten blocks for leading edge study in 2015 campaign.

The blocks were observed by an infra-red (IR) camera system from the top of the vacuum vessel as shown in Fig. 3. In 2014 campaign, the spatial resolution of the system is 1.2 mm/pixel and it is improved by zooming in lens system up to ~0.4 mm/pixel on the block surface in 2015 campaign.

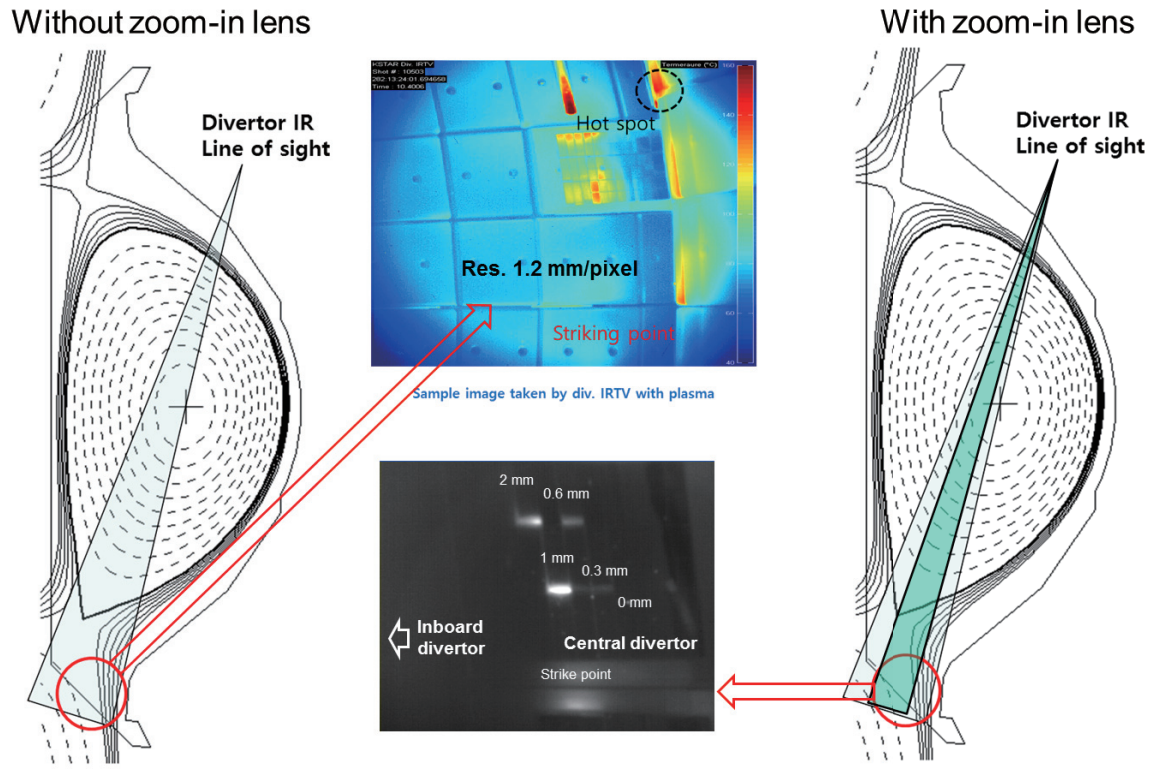

Fig. 3. Line of sight of divertor IR camera in 2014 and 2015 campaigns.

For the simulation of the thermal response of the blocks on the thermal loads, COMSOL modeling has been performed. Each block has been constructed and modeled separately. Typical heat flux on the blocks between 1-3 MW/m^2 is used for H-mode shots with type I ELMs. Angle of incident particles on divertor target at KSTAR depends on the poloidal position of the target in a range between 2 to 3 °, and we have chosen 3 °, which is the same as ITER case.

3. Results and discussion

Fig. 4. Shows an IR measurements during an ELMy H-mode (#11325). The IR image shows carbon tiles and tungsten blocks under heat load. The length of the plasma wetted area is about 30 mm with a peak heat flux on the divertor of 3 MW/m^2. Note that there is regular pattern on the heat flux that about half of the divertor tile in toroidal direction is shadowed. This shadow is caused by the edge of the tile and intrinsic misalignment. Graphite tiles installed on KSTAR has a rectangular shape with a dimension of 12 cm × 15 cm × 3 cm. The tiles are bolted onto the vacuum vessel by using a press bar at the center of the tile. Therefore, both edges of tile are about 2 mm higher than the height of the tile center, which makes shadow to the surface at the center. Assuming the toroidal symmetry, we can estimate the heat load on the tungsten blocks by comparing the heat flux on the carbon tiles (label A-B). In this case, the leading edges were exposed to a heat flux of 3 MW/m^2. Fig. 5 shows the measured IR intensity profiles of three different tungsten blocks with the results obtained by COMSOL simulation. Since the IR camera is not absolutely calibrated for tungsten surface, the intensity measured by IR camera is assumed to be proportional to the surface temperature.

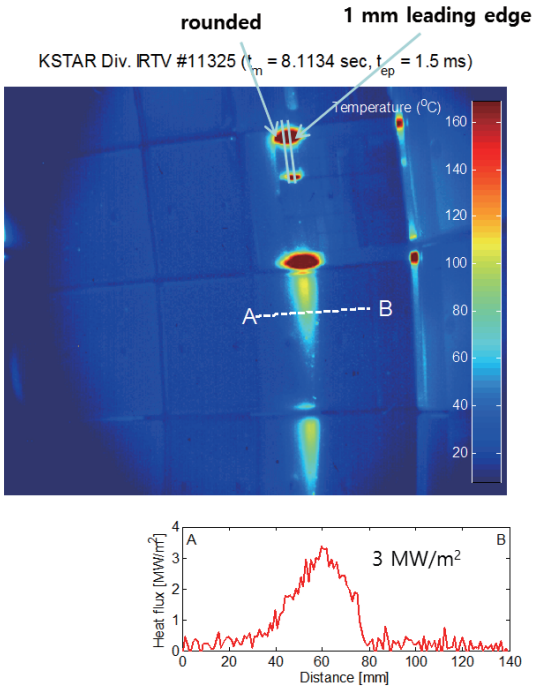

Fig. 4. An example of divertor IR measurement measurement during an ELMy H-mode. Line profile of heat flux profile is obtained between labels A and B.

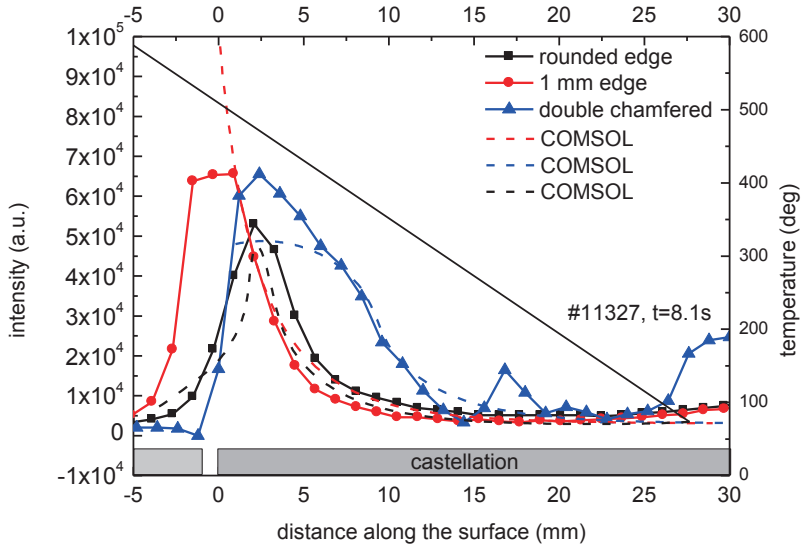

Fig. 5. the measured IR intensity profiles of three different tungsten blocks with the results obtained by COMSOL simulation (3 MW/m^2)

The temperature profiles obtained by COMSOL transient simulation and measured peak intensity matches very well with the calculation and show good agreement in shape. The results indicate that simple thermal analysis is very useful to predict heat load on castellated blocks with arbitrary shapes.

4. Summary

Heat loads on misaligned edges calculated by COMSOL simulation compared with measured ones by divertor IR in KSTAR are reported. Peak temperature of each block depends strongly on the shape of the block. The heat load patterns on the tungsten blocks calculated by COMSOL simulation show qualitatively good agreement with measured ones by IR camera: Simple analysis can be used to predict the heat load patterns on a PFC block for the first order estimation.

Acknowledgement

This research was supported by Ministry of Science, ICT, and Future Planning under KSTAR project and was partly supported by the JSPS-NRF-NSFC A3 Foresight Program in the field of Plasma Physics (NSFC: No.11261140328, NRF : No. 2012K2A2A6000443).

References

[1] G. F. Matthews et al., Phys. Scr. T128 (2007) 137
[2] M. Merola et al., Overview and status of ITER internal components, Fus. Eng. Des. 89 (2014) 890–895.
[3] S.-H. Hong et al., Fus. Eng. Des. 89 (2014) 1704.
[4] R. A. Pitts et al., Physics basis and design of the ITER plasma-facing components, J. Nucl. Mater. 415 (2011) S957–S964.

Evaluation of divertor fluxes from electric probe measurements during ELMy H-modes in KSTAR

Jun-Gyo Bak[1], Heung-Su Kim[1], Min-Keun Bae[2], Kyu-Sun Chung[2] , Suk-Ho Hong[1]

[1]National Fusion Research Institute, Daejeon, Korea
[2]Hanyang University, Seoul, Korea

Email : jgbak@nfri.re.kr

The characteristics of the divertor particle and heat fluxes are investigated from the electric probe measurements during ELM bursts in ELMy H-mode plasmas with the lower single null (LSN) configuration in Korea Superconducting Tokamak Advanced Research (KSTAR). The divertor heat fluxes in inter and intra ELM periods become 3 and 1.5 times higher, respectively, as the neutral beam (NB) power increases from 1.7 MW to 4.4 MW. It is found that the peak amplitude of the divertor flux during an ELM burst obtained near the outer strike point (OSP) decreases up to about 20 % as the ELM frequency increases by a factor of ~ 6.5 due to the ELM mitigation and the plasma shaping, which is similar to the trend of the amplitude versus the frequency of the ELM observed in other tokamaks. The ELMs are mitigated by using several methods as magnetic perturbation (MP) field, supersonic molecular beam injection (SMBI) and electron cyclotron heating (ECH) at the edge region. In this work, results from the experimental investigations of particle and heat fluxes during ELM bursts from the electric probe measurements at the divertor region are presented.

1. Introduction

The edge localized modes (ELMs) in H-mode discharges increase the scrape-off layer (SOL) plasma and produce burst-like particle fluxes on the divertor targets which are about ten times larger than the stationary particle flux between ELMs [1]. The large transient divertor heat pulses due to the ELMs (especially, type-I giant ELMs) would be potentially an impact on the divertor design of the next-step high power tokamak such as ITER because the maximum power load on the divertor target, as a critical design parameter in the ITER, should be less than 10 MW m^{-2} [2] due to the thermal engineering limitation in the material. The activities on the ELM control have been carried out for reducing the divertor heat flux due to the ELM in several tokamaks such as experiments for investigating effect of plasma shaping on the ELM behavior [1,3] and for ELM mitigations by using methods as magnetic perturbation (MP) field [1,4], supersonic molecular beam injection (SMBI) [5] and electron cyclotron heating (ECH) [1,6] at the edge region.

Figure 1 shows the divertor probes (DPs) used for the evaluation of heat and particle fluxes at the divertor region in the Korea Superconducting Tokamak Advanced Research (KSTAR).

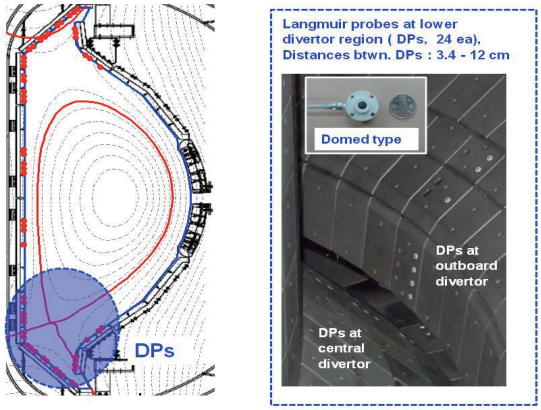

Fig. 1. Langmuir probes at the divertor region in KSTAR.

The DPs consists of a fixed edge Langmuir probe array (ELPA) with 40 single probes and 2 triple probes at the lower divertor region. The divertor particle fluxes were evaluated from the DP measurements

for the estimate of heat flux on the divertor by using an electron temperature measured with a fast reciprocating Langmuir probe assembly (FRLPA) [7] at the outboard mid-plane, as the SOL region, in the KSTAR tokamak. From the experimental campaign of 2014, the electron temperatures, obtained from the triple probe measurements near and far from an outer strike point (OSP) at lower outboard divertor region, were able to be used for evaluating the divertor heat flux. After the H-mode plasmas were routinely produced in the KSTAR tokamak, the investigations of divertor heat flux are needed to evaluate the power load on the divertor target in ELMy H-mode discharges because the heating power have been gradually increased for high plasma performance in the KSTAR tokamak. Thus, the initial investigation of the particle and heat fluxes at the divertor region was carried out from the DP measurement during ELMy H-mode plasmas. In this paper, preliminary results from the experimental investigations of peaked divertor particle and heat fluxes during ELM bursts in ELMy H-mode discharges are presented in Sec. 2. Finally, the summary is described in Sec. 3.

2. Divertor particle and heat fluxes

The particle fluxes were evaluated by using the relation of $\Gamma_{div} = I_{is}/(eS)\ sin\alpha$ from ion saturation current I_{is} measured with the DPs at the outer divertor region in ELMy H-mode discharges under the lower single null (LSN) configuration. Where S is an effective area of each divertor probe, and α is the angle between the magnetic field and the divertor target surface. The value of α was assumed as 5°. Heat flux can be obtained from $q_{div} = \gamma kT_e\Gamma_{div}$ where kT_e and γ are electron temperature and sheath transmission coefficient at divertor region, respectively. The averaged value of γ was theoretically predicted as ~ 7 from various models for case of $kT_e \sim kT_i$ [8]. The experimental values of γ were reported as 6 – 7 in ASDEX-U, TdeV and Alcator-C-mod [9-10]. Here, we assumed as γ =7 in the evaluation of the heat flux with some uncertainty. We used two values of kT_e measured by using triple probes near and far from the outer strike point (OSP) in the outer divertor region as mentioned in Ref.11.

2.1. Dependence of divertor heat flux on neutral beam power

The spatiotemporal profile of heat flux on outer divertor target illustrated by the S-axis is shown in Fig. 2(a). The divertor heat fluxes in the inter and intra ELM periods are mostly loaded near the OSP.

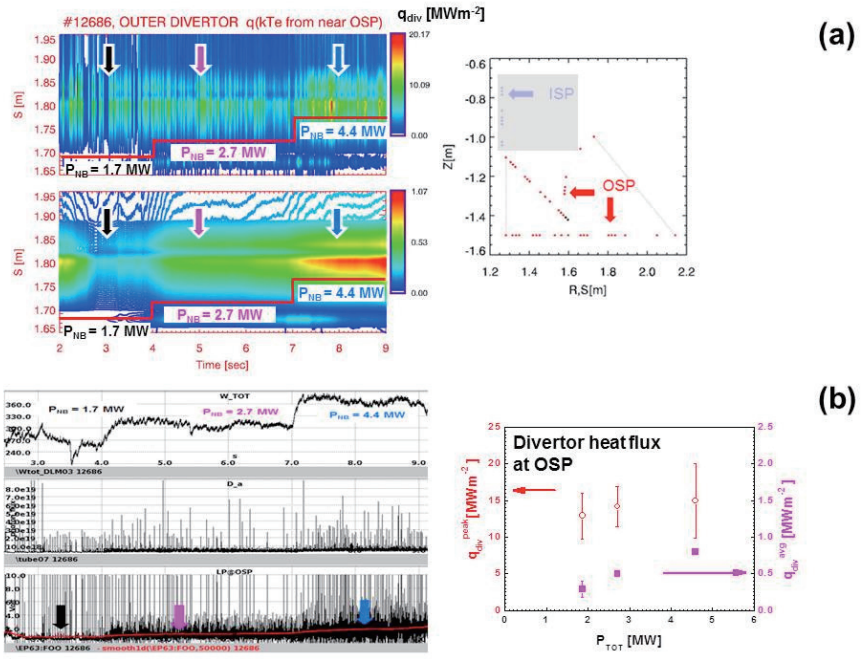

Fig. 2. (a) Contour plot of heat flux at outer divertor region as a function of time and distance from a reference location (R =1.261 m) to each probe (in the S-axis) for three different NB powers: left upper and lower illustrate $q_{div}^{peak} + q_{div}^{avg}$ and only q_{div}^{avg}, respectively, together with divertor probes in the RZ and RS coordinates, and (b) time evolution of stored energy, D_α and I_{isat} at the OSP, together with heat fluxes vs. total power (NB plus ohmic powers). Here, B_T=1.6 T, I_p = 0.6 MA and ohmic power was 0.1- 0.2 MW.

The stored energies W_{TOT} for three different neutral beam (NB) power are 0.28 ± 0.01 MJ for 1.7 MW (2.5s - 3.5s), 0.31 ± 0.01 MJ for 2.7 MW (5.0 - 6.5s) and 0.37 ± 0.01 MJ for 4.4 MW (7.5 - 8.5s) as shown in Fig. 2(b). The peaked heat fluxes during ELM bursts q_{div}^{peak} at the OSP are 12.9 ± 3.1 MWm^{-2}, 14.2 ± 2.7 MW m^{-2}, and 14.9 ± 5.1 MWm^{-2}, and the mean values of the heat flux in the inter-ELM period q_{div}^{avg} are 0.29 ± 0.11 MWm^{-2}, 0.50 ± 0.01 MW m^{-2}, and 0.80 ± 0.02 MWm^{-2} for the three different NB powers. The heat fluxes in the inter ELM phases were almost equal to the averaged values of the heat flux that were 0.18 ± 0.25 MWm^{-2}, 0.50 ± 0.35 MW m^{-2}, and 0.76 ± 0.48 MWm^{-2} obtained in three different time ranges. The values of divertor heat fluxes in the inter-ELM phase (stationary state) were quite low, and was about two order of magnitude smaller than the transient values (during ELM bursts). Thus, we investigated the peaked divertor fluxes in the ELM phases during plasma discharges as mentioned below.

2.2. ELM amplitude and peaked divertor heat flux versus ELM frequency

In ELMy H-modes, it was found that there was the correlation between the ELM amplitude and frequency as reported in other tokamaks [1]. The ELM amplitude, which is defined as the energy drop during an ELM burst normalized to the stored energy W_{ELM} / W_{TOT}, decreases up to about 20 % as the ELM frequency f_{ELM} increases within ranges of plasma parameters as shown in Fig. 3(a). Mostly, the trends of W_{ELM} / W_{TOT} $\propto 1/f_{ELM}$ can be observed for the range of $f_{ELM} \leq 250$ Hz as type I ELM. The peak amplitudes of the divertor heat flux q_{div}^{peak} near an OSP during the ELM bursts decrease as the magnitude of f_{ELM} is increased as shown in Fig. 3(b). The inverse proportion between the divertor fluxes and ELM frequency was clearly observed in case that f_{ELM} was less than 250 Hz, which was quite similar with the trend of W_{ELM} / W_{TOT} versus f_{ELM}. The experimental investigations of the inverse proportion between the divertor fluxes and ELM frequency due to plasma shaping and the ELM mitigation were presented in the following subsections. Here, the neutral beam (NB) was a major heating for achieving H-modes, and its power P_{NB} was 1.65 ~ 5.33 MW. Plasma density n_e was 0.7 ~ 8.0 × 10^{19} m^{-3}. The ELM frequency was obtained from the search method of local maximums in the smoothed D_α signal (smoothing with 10 points).

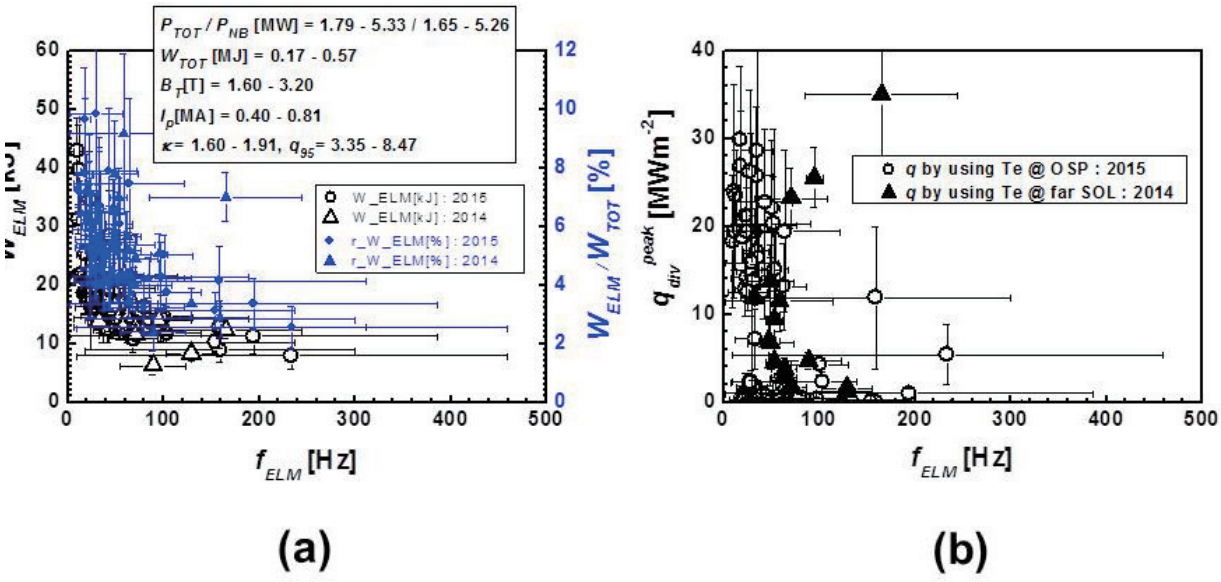

Fig. 3. (a) Stored energy drop W_{ELM} (in black color) and W_{ELM}/W_{TOT} (in blue color) and (b) peaked divertor heat flux q_{div}^{peak} during an ELM versus ELM frequency. Here, two figures show data obtained in the experimental campaigns of 2014 and 2015

2.3. Effect of plasma shape and current on magnitude of peaked divertor flux during ELM bursts

The plasma elongation κ, as one of plasma shaping parameters, increases from 1.81 to 1.92 in the time range of 2.0 - 3.0 s (I_p = 0.63 MA, B_T = 2.0 T), and the safety factor q_{95} also becomes higher as from 4.96

to 5.76 as shown in Fig. 4(a). It is found that f_{ELM} increases from 32 ± 8 Hz to 62 ± 20 Hz and the peaked value of divertor particle flux near the OSP during ELMs Γ_{div}^{peak} decreases from 0.20 ± 0.02 × 10^{23} $m^{-2}s^{-1}$ to 0.12 ± 0.03 × 10^{23} $m^{-2}s^{-1}$ due to the increase of κ. The energy drop due to the ELM normalized to the stored energy W_{ELM} / W_{TOT} decreases from 5.3 ± 0.6 % to 3.1 ± 0.7 % while the stored energy W_{TOT} is nearly constant as ~ 0.26 MJ. The behavior is similar to the experimental result reported in the DIII-D [3].

The value of I_p increases from 0.8 MA to 1.0 MA in the time range of 6.0 - 7.8 s (B_T = 2.7 T), and n_e (W_{TOT}) becomes higher as from ~ 3 to ~ 7 × 10^{19} m^{-3} (from 0.42 to 0.57 MJ) as shown in Fig. 4(b). It is found that f_{ELM} decreases from 51 ± 13 Hz to 33 ± 4 Hz and Γ_{div}^{peak} slightly increases from 0.29 ± 0.02 × 10^{23} $m^{-2}s^{-1}$ to 0.37 ± 0.10 × 10^{23} $m^{-2}s^{-1}$ due to the increase of I_p. Here, the magnitude of the ELM W_{ELM} / W_{TOT} increases from 3.3 ± 0.4 % to 3.7 ± 0.5%. The values of κ was 1.70 ~ 1.77 and q_{95} decreased from 5.4 ± 0.1 to 4.7 ± 0.1.

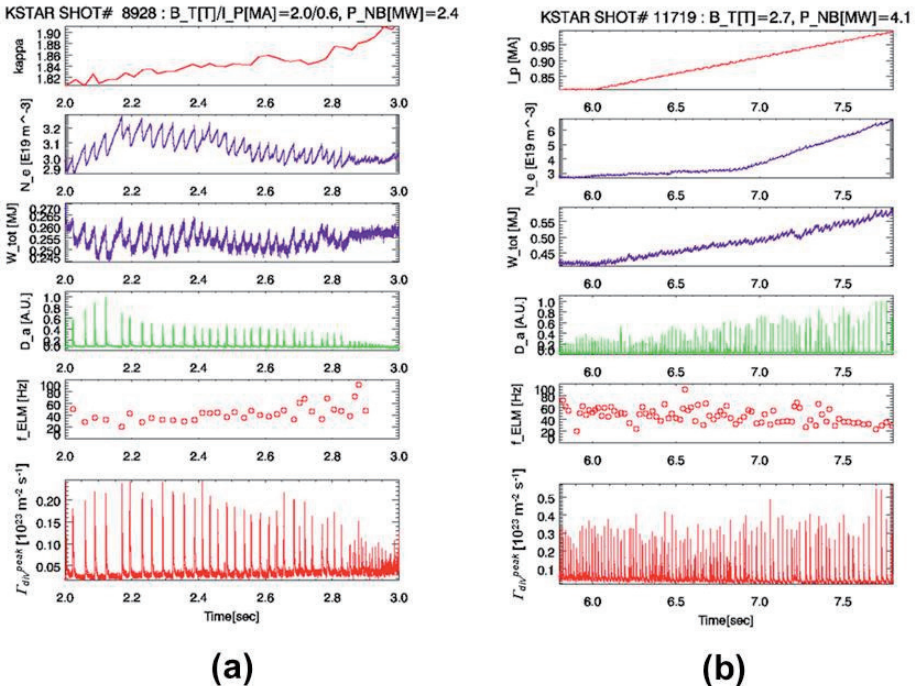

Fig. 4. (a) Time evolution of plasma parameters during a plasma shaping: elongation, plasma density, stored energy, $D\alpha$, f_{ELM} and divertor particle flux near the OSP (from top to bottom), and (b) Time evolution of plasma parameters as increasing plasma current: plasma current, plasma density, stored energy, D_{α}, f_{ELM} and divertor particle flux near the OSP (from top to bottom). Here, two figures are from Figs. 4 and 5 in Ref. 12.

2.4. Effect of magnetic perturbation at the edge on magnitude of peaked divertor flux during ELM bursts

The ELM size is reduced as f_{ELM} rises when the ELM is mitigated due to magnetic perturation (MP) field produced by the resonant magnetic perturbation (RMP) coils (top, middle and bottom) [13] as shown in Fig. 5(a). The MP field (n = 2) with a two-step waveform is applied to the plasma edge region in the time range of 2.0 - 6.0 s (I_p = 0.68 MA, B_T = 1.8 T). Here, the MP field by top and bottom RMP coils was activated from 3.0 s and the MP field by all RMP coils was ON from 5.0s. The ELM mitigation is more effective for higher MP field. The value of W_{TOT} decreases from ~ 0.35 MJ to ~ 0.25 MJ and the density pump-out (from 6 × 10^{19} m^{-3} to 4.4 × 10^{19} m^{-3}) during the MP field. f_{ELM} increases from ~ 20 Hz up to ~ 135 Hz and Γ_{div}^{peak} decreases from 1.2 × 10^{22} m^{-2} s^{-1} to 0.55 × 10^{22} m^{-2} s^{-1} when the MP field is 'ON' as shown in Fig. 5(a). W_{ELM} / W_{TOT} decreases from 4.1 % to 1.1 %.

The ELM is mitigated when the MP field with a step waveform (with n = 1 and 90° phasing) is applied to the plasma edge region in the time range of 3.0 - 5.0 s (I_p = 0.5 MA, B_T = 2.0 T) as shown in Fig. 5(b).

The MP field was produced by all of RMP coils. It is found that f_{ELM} rises from 57 ± 34 Hz to 90 ± 18 Hz and the peaked value of divertor heat flux near the OSP during ELMs q_{div}^{peak} decreases from 7.9 ± 4.1 MWm^{-2} to 3.3 ± 1.5 MWm^{-2} due to the MP field. The value of W_{ELM} / W_{TOT} is reduced from 5.4 ± 1.6 % to 4.8 ± 1.0 %. In addition, W_{TOT} decreases from 0.32 ± 0.01 MJ to 0.22 ± 0.01 MJ and there is the density pump-out (from ~ 2×10^{19} m^{-3} to ~ 0.6×10^{19} m^{-3}) in the phase of the ELM mitigation due to the MP field. When the MP field is turned off, the values of three parameters are recovered again such as W_{ELM} / W_{TOT}= 6.3 ± 1.8 %. f_{ELM} = 50 ± 36 Hz and q_{div}^{peak} = 5.8 ± 2.7 MWm^{-2}. Here, the values of κ and q_{95} were 1.70 ~ 1.95 and 6.35 ~ 7.30, respectively. For n=1 MP field, the similar trend was also observed when only middle RMP coil was activated.

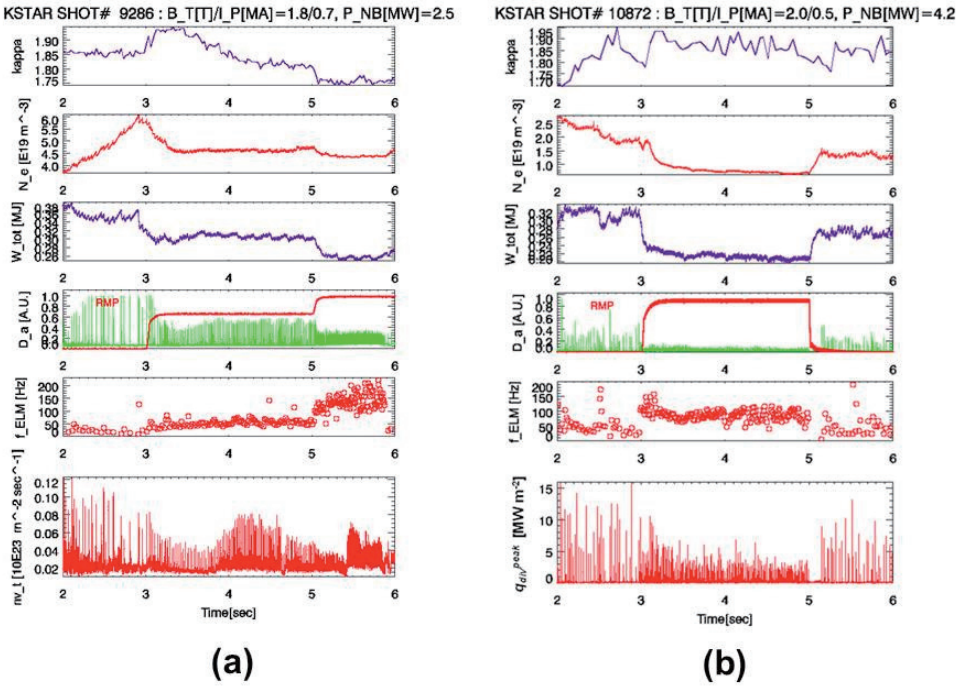

Fig. 5. Time evolutions of plasma parameters during (a) two-stepped MP fields at the edge by RMP coils (n=2 all coils from 5.0 s) and (b) one pulsed MP fields by RMP coils (n=1 all coils, 90 phasing): elongation, plasma density, stored energy, D_α with MP field, f_{ELM} and divertor heat flux near the OSP (from top to bottom). Here, Fig. 5(b) is from Fig. 6 in Ref. 12.

2.5. Effects of SMBI and ECH on magnitude of peaked divertor flux during ELM bursts

The ELM is mitigated when three SMBIs (time duration: ~ 8 ms, ~ 2ms, ~ 3ms) are applied to the plasma edge region in the time range of 6.05 - 6.4 s (I_p = 0.4 MA, B_T = 1.9 T) as shown in Fig. 6(a). It is found that f_{ELM} rises from 80 ± 20 Hz to 188 ± 49 Hz and q_{div}^{peak} decreases from 2.7 ± 1.3 MWm^{-2} to 1.0 ± 0.6 MWm^{-2} after three SMBIs. The value of W_{ELM} / W_{TOT} decreases from 5.9 ± 1.0 % to 4.3 ± 0.8 %, and W_{TOT} slightly decreases from ~ 0.16 MJ to ~ 0.15 MJ due to the SMBI. Here, both values of κ and q_{95} decrease from ~ 1.9 to ~ 1.8 and from ~ 7.8 to ~ 6.8, respectively. In addition, the ELM is mitigated and f_{ELM} becomes faster when D_2 gas was puffed to the divertor region in the time range of 7.5 - 9.5 s (I_p = 0.6 MA, B_T = 1.5 T) as shown in Fig. 6. It is found that f_{ELM} rises from 33 ± 14 Hz to 283 ± 83 Hz and q_{div}^{peak} decreases from 6.9 ± 3.2 MWm^{-2} to 0.3 ± 0.2 MWm^{-2} due to the gas-puff. The value of W_{ELM} / W_{TOT} decreases from 5.4 ± 1.6 % to 1.8 ± 0.4 % and W_{TOT} also decreases from 0.34 ± 0.01 MJ to ~ 0.28 MJ. Here, the values of κ decreased from ~1.9 to ~ 1.8 and q_{95} was 4.0 ~ 4.3.

The ELM is mitigated and f_{ELM} increases by the application of the ECH (170 GHz, P_{ECH}= ~ 0.8 MW) as shown in Fig. 6(b). The ECH is applied from 6.5 s during a plasma discharge (I_p = 0.5 MA, B_T = 2.4 T). It is found that f_{ELM} becomes from 80 ± 24 Hz to 110 ± 19 Hz and q_{div}^{peak} slightly decreases from 4.3 ± 1.5 MWm^{-2} to 3.7 ± 1.5 MWm^{-2} due to the ECH. The value of W_{ELM} / W_{TOT} slightly decreases from 6.3 ± 0.9 %

to 5.7 ± 0.9 % and W_{TOT} increases from ~ 0.21 MJ to ~ 0.22 MJ. Here, the values of κ and q_{95} were ~ 1.8 and ~ 7.0, respectively. It was thought that the ELM mitigation was weak because most of P_{ECH} might be deposited inside the plasma edge. It was reported that the ELM mitigation was clearly observed as the ECH beam was moved towards the plasma separatrix in the TCV [6].

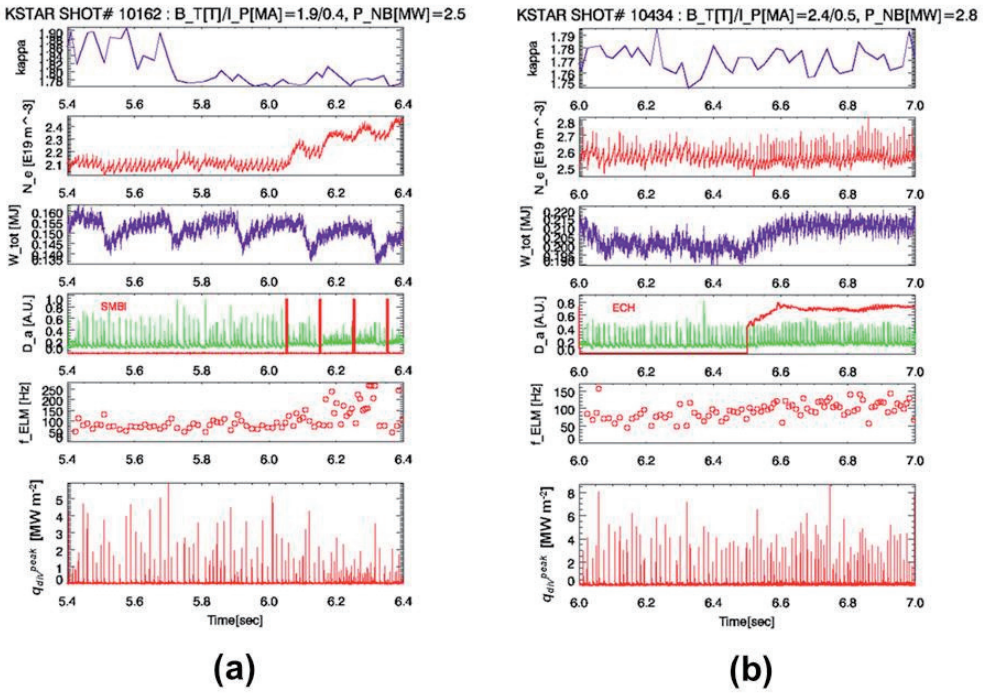

Fig. 6. (a) Time evolution of plasma parameters during SMBI at the edge,: elongation, plasma density, stored energy, D_α with SMBI, f_{ELM} and divertor heat flux near the OSP (from top to bottom) and (b) Time evolution of plasma parameters during ECH inside the edge region: elongation, plasma density, stored energy, D_α with ECH waveform, f_{ELM} and divertor heat flux near the OSP (from top to bottom). Here, two figures are from Figs. 8 and 10 in Ref. 12.

3. Summary

In ELMy H-modes, the divertor heat fluxes in inter and intra ELM periods become 3 and 1.5 times higher, respectively, as the neutral beam (NB) power increases from 1.7 MW to 4.4 MW. There was relation between the ELM amplitude and the ELM frequency as $W_{ELM}/W_{TOT} \propto 1/f_{ELM}$, and W_{ELM}/W_{TOT} decreased up to ~ 20 % as the ELM frequency f_{ELM} increases in the range of $f_{ELM} \leq 250$ Hz. From the experimental investigation of the divertor particle and heat fluxes during ELM bursts due to the plasma shaping and the ELM mitigations in the KSTAR tokamak, it was found that the peak amplitude of particle flux near the OSP Γ_{div}^{peak} decreased up to 60 % when the plasma elongation κ, a factor of the plasma shaping, increased from 1.81 to 1.92. Similar trends of the peak amplitude of divertor fluxes during an ELM phase were also observed in the ELM mitigations due to the MP field, the SMBI and the ECH as following: the peak amplitude decreased up to about 37 - 86 % as f_{ELM} increased by a factor of 1.4 – 2.4. The trend was more clearly shown in the ELM mitigation due to the MP field and the SMBI, comparing with the cases of the ECH. In addition, it was observed that q_{div}^{peak} increased up to ~ 130 % when plasma current I_p increased from 0.8 MA to 1.0 MA. Finally, it could be estimated that particle flux towards the main wall was two orders of magnitude smaller than the divertor particle flux.

Further investigation of the heat flux will be required to estimate how much transient power will be loaded on the divertor target during ELM burst and to understand how the power load will be able to be reduced by using methods for the ELM mitigation. In addition, the study of the ELM effect on the profile of the fluxes from electric probe and infra-red camera measurements in the divertor and SOL regions will be also carried out to understand the edge particle transport during ELMs in tokamaks.

Acknowledgements

This research was supported by Ministry of Science, ICT, and Future Planning under KSTAR project contract, and was partly supported by the JSPS-NRF-NSFC A3 Foresight Program in the field of Plasma Physics (NSFC: No. 11261140328, NRF: No. 2012K2A2A6000443).

References

[1] D.N. Hill, *Journal of Nuclear Materials*, 241-243 (1997) 182.
[2] J. Linke, *Transaction of Fusion. Science and Technology*, 49 (2006) 455.
[3] T. Ozeki, et al., *Nuclear Fusion*, 30 (1990) 1425.
[4] Y. Liang, et al., *Plasma & Fusion Research*, 5 (2010) S2018.
[5] J. Cheng, et al., *Journal of Nuclear Materials*, 438 (2013) S1200.
[6] J.X. Rossel, et al., *Nuclear Fusion*, 52 (2012) 032004.
[7] J.G. Bak, et al., *Contributions to Plasma Physics*, 53 (2013) 69.
[8] P.C. Stangeby and G.M. McCracken, Nucl. Fusion 30 (1990) 1225.
[9] C.S. Pitcher and P.C. Stangeby, Plasma Phys. Control. Fusion 39 (1997) 779
[10] B. LaBombard et al., Phys. Plasmas 2 (1995) 2242.
[11] H.S. Kim, J.G. Bak et al., submitted to Fusion Eng, Design
[12] J.G. Bak et al., submitted to Fusion Eng, Design
[13] Y. M. Jeon, et al., *Phys. Rev. Lett.*, 109(2012) 035004.

The Symplectic Particle-in-cell Simulation of Nonlinear X-B Mode Conversion

Jian Liu[1], Hong Qin[1], Jianyuan Xiao[1]

[1]Department of Modern Physics and School of Nuclear Science and Technology,
University of Science and Technology of China, Hefei, Anhui 230026, China

Abstract

The nonlinear mode conversion of extraordinary waves in non-uniform magnetized plasmas is studied using the variational symplectic particle-in-cell simulation. The accuracy of the nonlinear simulation is guaranteed by the long-term accuracy and conservativeness of the symplectic algorithm. The spectra of the electromagnetic wave, the evolution of the wave reflectivity, the energy deposition profile, and the parameter-dependent properties of radio-frequency waves during the nonlinear mode conversion are investigated. It is illustrated that nonlinear effects evidently change the consequences of the radio-frequency injection into the magnetized plasmas. The evolutions of the rf wave reflectivity and the energy deposition are observed, while the self-interaction of the Bernstein waves and mode excitations are involved. Even for waves weak in magnitude, nonlinear effects also become significant after long-playing wave injections, which are common in the real rf wave heating and current drive operations.

1. Introduction

Radio-frequency (rf) wave injection plays an important role in auxiliary heating and current drive for modern magnetic confinement fusion devices [1-4]. A typical method for rf wave injection into some over-dense plasmas, where the plasma frequency ω_{pe} is much larger than the electron cyclotron frequencyω_{ce}, is to excite the electron Bernstein waves (EBWs). Two different ideas are commonly used for coupling rf power to EBWs, i.e., the ordinary-extraordinary-Bernstein (O-X-B) and extraordinary-Bernstein (X-B) mode conversion. The O-X-B scheme is usually used for the electron Bernstein wave current drive (EBCD) in spherical tokamaks (ST), where the electron cyclotron resonance current drive (ECCD) method is incapable [4,5]. The X-B scheme requires steeper plasma density profile, which is also available in some STs [6-9]. During the X-B mode conversion, the electromagnetic wave is initially injected into the plasma, perpendicularly to the background magnetic field, and propagates as an extraordinary (X) wave within the plasma. When the X wave reaches the cutoff location, where the local right-handed cutoff frequency ω_R is equal to the frequency of the incident wave ω, part of the energy of the incident wave penetrates the cutoff layer and continues propagating as EBWs. The X-B conversion will be significantly enhanced if the electron density gradient becomes large appropriately.

The linear X-B mode conversion can be theoretically investigated using the cold plasma model [10, 11]. In this model, the kinetic effects of the electrons are neglected. At the same time, the ions offer a positive charged background. The linear theory predicts that the reflectivity of the injected wave is a constant.

The cold plasma assumption is only accurate enough when the wave length is much larger than the electron gyroradius. As the electron temperature increasing, the kinetic effect becomes significant and

should be taken into account. The kinetic theory of mode conversion is so complicated that the analytical solution is unreachable except for some particular cases. On the other hand, the linear condition no longer holds for large-amplitude or long-term wave evolution. In modern magnetic confinement devices, the power of the rf wave injection is so large that the nonlinear effects cannot be neglected. The nonlinear effects during the propagation of Bernstein waves have been directly observed in some experiments. Those nonlinear effects can vary the reflectivity during the wave injection, which is different from the prediction of linear theory. The simulation study on the nonlinear physics of rf waves in plasmas has bloomed into an attractive research field. However, the analytical and numerical study on nonlinear rf waves are severely constrained by the existing mathematical and algorithmic tools.

Containing both kinetic and nonlinear effects, the first-principle particle simulation is regarded as a necessary and powerful tool for dealing with the nonlinear rf wave physics. Different aspects of the X-B mode conversion have lately been investigated using gyro-kinetic particle-in-cell (PIC) codes. For nonlinear mode conversions, where the timescale of the mode conversion is much larger than the periods of the rf waves, the long-term simulation is inevitably required. Since the number of time steps in a long-term simulation is large, the coherent accumulation of the numerical error from each time step turns out to be the most serious difficulty. To ensure the reliability of the simulation results, the long-term numerical accuracy and stability should be guaranteed. To overcome the difficulty, a newly developed variational symplectic PIC method is employed in this paper to study the nonlinear X-B mode conversion. The symplectic PIC algorithm bounds the global numerical error for an arbitrary long time by preserving the symplectic structure of the original Lagrangian system. Its long-term accuracy, stability, and conservativeness has been theoretically discussed and practically verified.

Suffering no accumulation of the global energy errors, the symplectic PIC method shows its unparalleled advantage in the long-term simulation research and provides accurate nonlinear simulation results. In the simulation of nonlinear rf mode conversion, it is illustrated that the nonlinear effects evidently change the consequences of the rf wave injection into the magnetized plasmas. The wave reflectivity, which is regarded as a constant value in linear theory, varies in the nonlinear mode conversion process. The evolutions of the rf wave reflectivity and the energy deposition are observed, while the self-interaction of the Bernstein waves and mode excitations are involved. The spectra of the electromagnetic wave, the energy deposition profile, and the parameter-dependent properties of radio-frequency waves during the nonlinear mode conversion are also investigated. It is found that even for waves weak in magnitude, nonlinear effects become significant after long-playing wave injections as well. When simulating rf waves with small amplitudes, the nonlinear phenomena becomes obvious after more than several hundred wave periods. New modes are excited during a sufficient long time even if the amplitude of incident wave is small. To study the parameter-dependent properties of the nonlinear X-B conversion, we compare the rf wave injection procedures with different electron temperatures, amplitudes of injection waves, and plasma density gradients, respectively. It is discovered that a lower electron temperature can enhance the reflectivity. Meanwhile the dependence of the reflectivity on the plasma density gradient is sensitive.

2. The model of X-B conversion and the symplectic PIC method

To have a clear visual of the nonlinear X-B mode conversion, the evolution of $E_y(x, t)$ is investigated. The amplitude of the wave source E_1 is set to 1.0 *MV/m*, and the temperature of electrons is set to 57.6eV. The evolution of E_y in different time intervals are recorded as contour plots in Fig. 1, where the horizontal axis is the location x and the vertical axis is the time t. At the beginning of the wave injection, the mode conversion structure forms in a short time. and the reflection is stable.

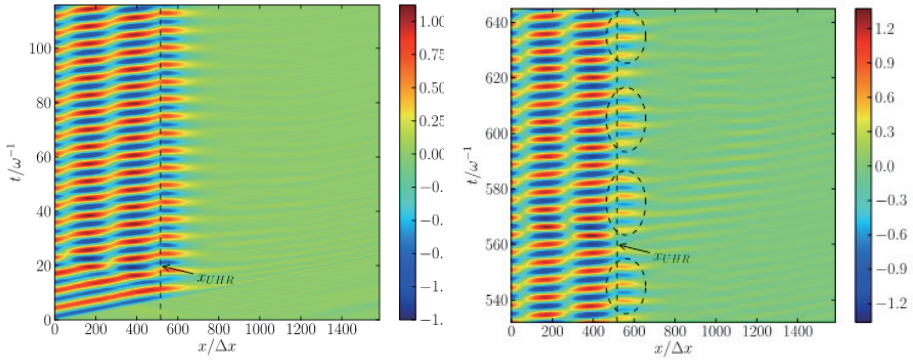

Fig.1 The contours of $\mathbf{E_y}(x,t)$ in te time interval [0, 115/ω] and [530/ω, 645/ω].

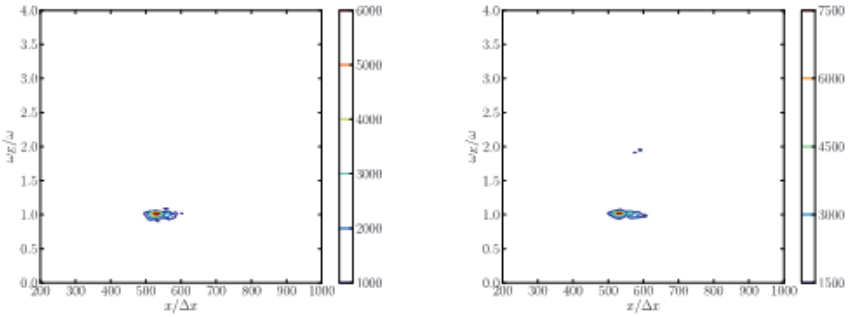

(a) $[0, 174/\omega]$ (b) $[116/\omega, 290/\omega]$

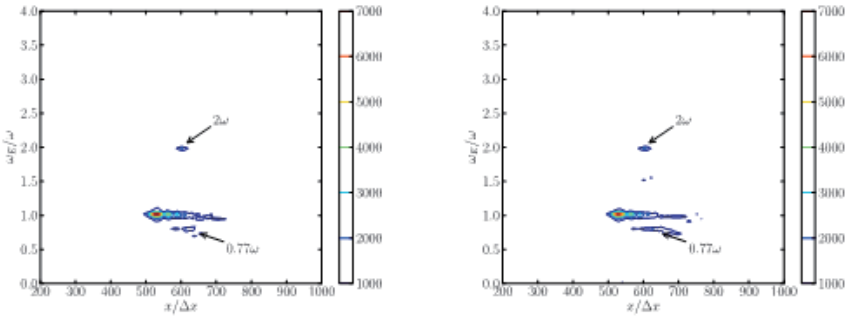

(c) $[290/\omega, 464/\omega]$ (d) $[406/\omega, 580/\omega]$

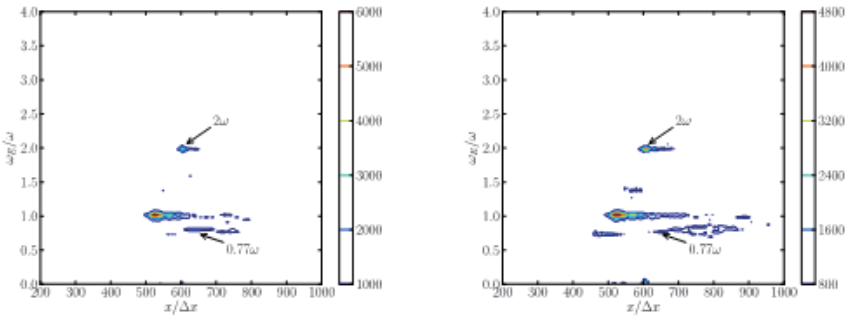

(e) $[580/\omega, 754/\omega]$ (f) $[812/\omega, 986/\omega]$

Fig.2 The evolution of time spectra of $\mathbf{E_x}(x,t)$ during the X-B mode conversion. Here $\mathbf{E_1 = 1.0MV/m}$, $\mathbf{n_r = 380}$, $\mathbf{x}$ is in [240Δl, 960Δl] and the interval of t is marked in each caption of the subfigures. We can see that after about 116/ω the wave with frequency 2ω occurs, and after 290/ω the wave with frequency 0.77ω occurs

After about 100 periods, the wave structure becomes unstable, which is marked by dashed ellipses. This unstable wave structure implicates that the nonlinear phenomenon happens during the X-B mode conversion. So the spectrum of electric field will be focused next.

One major difference between linear and nonlinear processes is that during the nonlinear process the system will generate extra modes with frequencies other than the frequency of wave source. During the mode conversion the evolution of time spectrum of E_x is recorded, and the results are shown in Fig. 2.

In the initial stage of wave injection, there only exists the wave with frequency ω. After about $116/\omega$, the electrostatic wave propagates to the position at $x \sim 608\Delta x$, where a mode with the frequency 2ω appears. Then the component of the second harmonic mode becomes stronger, meanwhile another mode with the frequency $\omega' = 0.77\omega$ appears. Compared with subfigures in Fig. 2, we can see that the mode with frequency ω' is divided into two packets when propagating. The generation of the mode with frequency 2ω can be explained as the result of self-interaction of Bernstein wave. This second harmonic generation (SHG) of Bernstein wave has been studied previously. Then the wave with frequency $\omega' = 0.77\omega$ s generated near the location where the SHG of Bernstein wave happens, which implicates that the generation of the wave with frequency ω' is closely related to the SHG of Bernstein wave. According to the parametric decay instability (PDI) theory, there should be a another wave with frequencyω'', which satisfies $2\omega - \omega' = \omega''$.

4. Discussions

In last section an increasing reflectivity phenomenon during the mode conversion process is discovered. To make sure this phenomenon is not caused by different number marker particles, we changed the maximum number of marker particles per grid to 2000 and repeated the simulation.

The parameters are the same as we used in last simulation, and the amplitude of incident wave E_1 is also set to 1.0MV/m. The results show the fact that this phenomenon is not effected much by number marker particles per grid.

In another hand, the influence of different grid size Δl and time step Δt are also tested, and in all these simulations the new mode generation phenomenon and the increasing behavior of reflectivity are found. So the influence of numerical approximation can be almost ruled out.

To summarize our work, the variational symplectic PIC scheme has been adopted to simulate the nonlinear X-B mode conversion. The conservation of symplectic structure guarantees this algorithm can generate more convincible results than the traditional ones. The detailed work shows that when the amplitude of incident wave is sufficient large, the amplitude will increase during the mode conversion, and modes with frequencies other than ω may be generated. Even for wave with small amplitudes the reflectivity changes significantly when time is sufficiently long. In the meantime we found that the energy deposition happens within a wide spatial range of the plasma. The simulation also suggests that a higher electron temperature can improve the efficiency of energy conversion. Moreover, the sensitive correlation between density gradient and reflectivity are verified.

In this paper only X-B mode conversion is discussed. For future plan, the simulation on mode conversion of other waves, such as lower hybrid wave (LHW) and ion cyclotron wave (ICW), will be

processed. In those cases, the numerical simulation can help decide the optimal parameters for the heating or current drive devices, and predicts the nonlinear effects in the plasma when the high power wave is injected.

Acknowledgements

This research is supported by JSPS-NRF-NSFC A3 Foresight Program (NSFC-11261140328), National Magnetic Confinement Fusion Energy Research Project (2015GB111003, 2014GB124005), National Natural Science Foundation of China (NSFC-11575185, 11575186, 11305171), the CAS Program for Inter-disciplinary Collaboration Team, and the Geo-Algorithmic Plasma Simulator (GAPS) Project.

References

[1] K. Ushigusa, T. Imai, Y. Ikeda, O. Naito, K. Uehara, H. Yoshida, H. Kubo, et al. , Nucl. Fusion 29, 1052 (1989).

[2] Z. Lianmin, S. Jiafang, L. Fukun, J. Hua, W. Mao, L. Liang, W. Xiaojie, and X. Handong, Plasma Sci. Technol. 12, 118 (2010).

[3] D. Start, J. Jacquinot, V. Bergeaud, V. Bhatnagar, G. Cottrell, S. Clement, L. Eriksson, A. Fasoli, A. Gondhalekar, C. Gormezano, et al., Phys. Rev. Lett. 80, 4681 (1998).

[4] H. Laqua, V. Erckmann, H. Hartfub, H. Laqua, et al. , Phys. Rev. Lett. 78, 3467 (1997).

[5] R. Cairns and C. Lashmore-Davies, Phys. Plasmas 7, 4126 (2000).

[6] H. Kuehl, Phys. Rev. 154, 124 (1967).

[7] A. Ram and S. D. Schultz, Phys. Plasmas 7, 4084 (2000).

[8] B. Jones, P. Efthimion, G. Taylor, T. Munsat, J. Wilson, J. Hosea, R. Kaita, R. Majeski, R. Maingi, S. Shiraiwa, et al., Phys. Rev. Lett. 90, 165001 (2003).

[9] S. Shiraiwa, K. Hanada, M. Hasegawa, H. Idei, H. Kasahara, O. Mitarai, K. Nakamura, N. Nishino, H. Nozato, M. Sakamoto, et al., Phys. Rev. Lett. 96, 185003 (2006).

[10] K. G. Budden, The propagation of radio waves: the theory of radio waves of low power in the ionosphere and magnetosphere (Cambridge University Press, 1988) pp. 596-602.

[11] A. Ram, A. Bers, S. Schultz, and V. Fuchs, Phys. Plasmas 3, 1976 (1996).

Secular Full-orbit Dynamics of Runaway Electrons in Tokamak and Neoclassical Pitch-angle Scattering

Yulei Wang[1], Jian Liu[1], Hong Qin[1]

[1]Department of Modern Physics and School of Nuclear Science and Technology,
University of Science and Technology of China, Hefei, Anhui 230026, China

Abstract

It is discovered that the tokamak field geometry generates a pitch-angle scattering effect for runaway electrons. This neoclassical pitch-angle scattering is much stronger than the collisional scattering and invalidates the gyro-center model for runaway electrons. As a result, the energy limit of runaway electrons is found to be larger than the prediction of the gyro-center model and to depend heavily on the background magnetic field.

1. Introduction

Runaway electrons in a tokamak are energetic particles accelerated by the electric field. They cannot be braked by the collisional drag [1]. A large amount of runaway electrons are produced in tokamaks during fast shutdowns, disruptions [2–15], or aggressive current drive [16]. The massive energy carried by runaway beams poses great danger to plasma-facing components [17–20]. Understanding the physics of runaway electrons in toroidal field configurations is thus critical. The dynamics of runaway electrons involves different timescales spanning 11 orders of magnitude, which brings difficulties to both analytical and numerical studies. Gyro-center model is often applied to tackle the multi-scale problem by averaging out the fast gyro-motion and has produced fruitful results [21–29]. According to the gyro-center model, the magnetic moment of runaway electron is an adiabatic invariant, and the parallel momentum increases due to the work by the loop electric field. There is no channel of momentum transfer from the parallel to the perpendicular direction, except for the collision with background plasmas. In general, the collisional effect is rather weak for charged particles with high velocities [25]. For a typical runaway electron, the collision time is $\tau_{col} \sim 0.5s$, which is much longer than the gyro-period T_{ce} ($\sim 10^{-10}s$) and the transit period T_{tr} ($\sim 10^{-8}$). When the collisional effect can be neglected, the perpendicular momentum will monotonically decrease due to the synchrotron radiation of the gyro-motion [25], and parallel momentum will monotonically increase to its maximum limit until the electric field acceleration is finally balanced by the radiation dissipation. The pitch-angle scattering due to collisions will transfer a small amount of energy from the parallel direction to the perpendicular direction. This small collisional effect keeps the runaway electrons energetic in the perpendicular direction, but does not modify the energy limit in the parallel direction by much. The gyro-center model predicts that the energy limit of runaway electrons does not depend on collisions and the magnitude of background magnetic field [21].

Contrary to the common wisdom, our analysis shows that the gyro-center model is not valid for runaway electrons. This is because they move with the speed of light in the parallel direction, the local

magnetic field they see changes by a large amount during one gyro-period. Therefore, the basic assumption for the gyro-center model, i.e., the magnetic field is approximately constant in one gyro-period, breaks down. In fact, the magnetic moment μ is no longer an adiabatic invariant. Similar non-conservation of μ has been observed in the presence of magnetic turbulence with wavelength comparable to the gyro-radius [30, 31].

In this proceeding, we abandon the gyro-center model and study the multi-timescale runaway dynamics by numerically solving the dynamical equations of runaway electrons directly in the six-dimensional phase space. Long-term simulation results confirm that the gyro-center model is indeed invalid, see Fig. 1. More than one hundred billion time steps are required in the simulation. To eliminate the coherent accumulation of numerical errors from each time step, which is usually a show-stopper for long-term simulations, we utilize the newly developed volume-preserving algorithm (VPA) for relativistic particles [32]. The VPA can guarantee the long-term accuracy by preserving the phase-space volume of the original physical system. Its long-term conservativeness and stability have been verified.

Taking the advantage of the VPA method, we discovered that there exists a new pitch-angle scattering mechanism, which transfers momentum of runaway electrons between the parallel and perpendicular directions. It arises from the full orbit dynamics in the toroidal geometry of a tokamak, hence the name of neoclassical scattering. The neoclassical pitch-angle scattering process is about a million times faster than the collisional pitch-angle scattering, resulting in a rapid transfer of the parallel momentum, gained from the loop electric field, to the perpendicular direction. As an important result, the simulation study indicates a new energy limit for runaway electrons, which is higher than the result from the gyro-center model and varies with the magnitude of the background magnetic field. This unexpected neoclassical pitch-angle scattering effect for runaway electrons and its important consequence are briefly discussed in this proceeding.

2. The physical model

When focusing on the long-term dynamics of runaway electrons in a tokamak, we take into account the background magnetic field, the loop electric field, and the electromagnetic radiation. The dynamical equations of runaway electrons are

$$\frac{d\mathbf{x}}{dt} = \mathbf{v}\,, \tag{1}$$

$$\frac{d\mathbf{p}}{dt} = -e(\mathbf{E} + \mathbf{v} \times \mathbf{B}) + \mathbf{F}_R\,, \tag{2}$$

$$\mathbf{p} = \gamma m_0 \mathbf{v}\,, \tag{3}$$

where $\mathbf{x}$, $\mathbf{v}$, $\mathbf{p}$ denote the position, velocity and mechanical momentum of a runaway electron, e denotes the unit charge, m_0 is the rest mass of electron, $\mathbf{E}$ and $\mathbf{B}$ are the electric and magnetic field, and the Lorentz factor γ is defined as

$$\gamma = \sqrt{1 + \mathrm{p}^2/\mathrm{m}_0^2\mathrm{c}^2}\,, \tag{4}$$

The effective electromagnetic radiation drag force $\mathbf{F}_R$ is

$$\mathbf{F}_R = -P_R \frac{\mathbf{v}}{v^2}, \tag{5}$$

where P_R is the radiation power determined by [33]

$$P_R = \frac{q_e^2}{6\pi\epsilon_0 c}\gamma^2\left[\left(\frac{\mathbf{a}}{c}\right)^2 - \left(\frac{\mathbf{v}}{c}\times\frac{\mathbf{a}}{c}\right)^2\right]. \tag{6}$$

Here, ϵ_0 is the permittivity in vacuum, c is the speed of light in vacuum, and $\mathbf{a} = d\mathbf{v}/dt$ denotes the acceleration.

As a model, the background magnetic field and inductive electric field are set to be

$$B = \frac{B_0 R_0}{R}\mathbf{e}_\xi - \frac{B_0\sqrt{(R-R_0)^2+z^2}}{qR}\mathbf{e}_\theta, \tag{7}$$

$$E = \frac{E_l R_0}{R}\mathbf{e}_\xi, \tag{8}$$

Where $R = \sqrt{x^2+y^2}, \xi$, and z are radial distance, azimuth, and height of the cylindrical coordinate system respectively, $\mathbf{e}_\xi$ and $\mathbf{e}_\theta$ are the unit vectors along toroidal and poloidal directions, and q denotes safety factor. Without loss of generality, we use the parameters of EAST [34]. The major radius is $R_0 = 1.7\,m$, the safety factor is $q = 2$, the central magnetic field is $B_0 = 3\,T$, and the loop electric field is $E_l = 0.2\,V/m$. The initial parallel and perpendicular momentum of a typical runaway electron are set to be $p_{\|0} = 5\,m_0 c$ and $p_{\perp 0} = 1\,m_0 c$, and the initial position is $R = 1.8\,m$ and $\xi = z = 0$. The time-step of simulation is set to $\Delta t = 1.9\times10^{-12}s$, which is about 1% of the gyro-period.

3. Results

The failure of gyro-center model can be show clearly from Fig. 1 which shows the single relative increment of local magnetic field. The magnetic field changes about 30% after 1.7s, which of course breaks the assumptions of gyro-center theory.

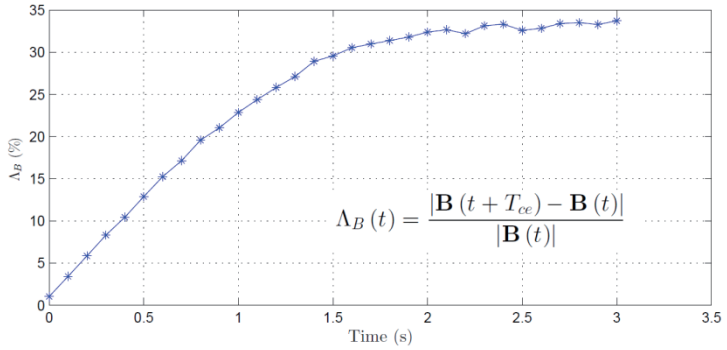

Fig.1 The change ratio of background magnetic field Λ_B during one gyro-period at different time of a runaway dynamics.

Figure 2 shows the evolution of momentum which looks very different from the results of gyro-center theory. The failure of gyro-center theory causes the neoclassical scattering which rises from the toroidal geometry and results in the strong oscillation of momentum.

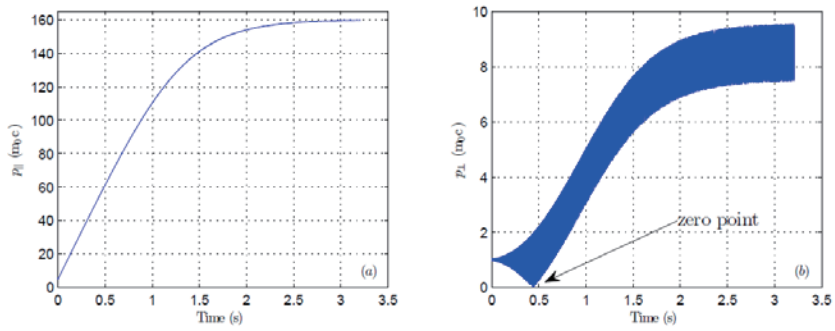

Fig. 2 The evolution of (a) parallel momentum and (b) perpendicular momentum of a runaway electron. The initial position of the electron is at $R = 1.8$ m, $\xi = z = 0$, and the initial momentum is $p_{\parallel} = 5\ \mathrm{m_0c}$ and $p_{\perp} = 1\mathrm{m_0c}$. The center magnetic field is $B_0 = 3$ Tand the loop electric field is $E_l = 0.2\mathrm{V/m}$.

Figure 3 plots the behavior of energy limit under different electric and magnetic field. For the case of $B_0 = 1$ T, our energy limit is about 20% higher than the result of gyro-center theory, because more energy is transferred to the perpendicular direction through the neoclassical pitch-angle scattering. If the magnetic field is extremely strong, the gyro-center approximation model will be valid, and our energy limit curve will recover the gyro-center result.

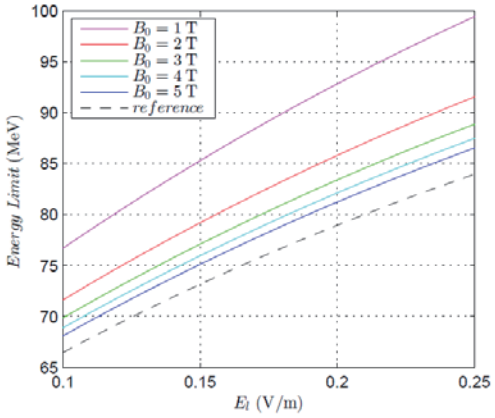

Fig.3 Plots of energy limit versus loop electric field E_l. The black dashed curve corresponds to the energy limit curve predicted by gyro-center model [21], where collisional effect is ignorable. The solid curves correspond to energy limits with different magnetic field intensities. The loop electric field is set to be radially uniform in order to compare with the gyro-center model.

Acknowledgements

This research is supported by JSPS-NRF-NSFC A3 Foresight Program (NSFC-11261140328), National Magnetic Confinement Fusion Energy Research Project (2015GB111003, 2014GB124005), National Natural Science Foundation of China (NSFC-11575185, 11575186, 11305171), the CAS Program for Inter-disciplinary Collaboration Team, and the Geo-Algorithmic Plasma Simulator (GAPS) Project.

References

[1] H. Dreicer, Phys. Rev. 115, 238 (1959).

[2] R. Yoshino, T. Kondoh, Y. Neyatani, et al., Plasma Phys. Control.Fusion 39, 313 (1997).

[3] R. Jaspers, N. L. Cardozo, F. Schuller, et al., Nucl.Fusion 36, 367 (1996).

[4] P. Helander, L.-G.Eriksson, and F. Andersson, Phys. Plasmas 7, 4106 (2000).
[5] P. Helander, L. Eriksson, and F. Andersson, Plasma Phys. Contr. Fusion 44, B247 (2002).
[6] T. Fülop, H. Smith, and G. Pokol, Phys. Plasmas 16, 022502 (2009).
[7] R. Gill, B. Alper, A. Edwards, et al., Nucl.Fusion 40, 163 (2000).
[8] R. Jaspers, K. Finken, G. Mank, et al., Nucl.Fusion 33, 1775 (1993).
[9] R. Nygren, T. Lutz, D. Walsh, et al., J. Nucl.Mater.241, 522 (1997).
[10] P. Parks, M. Rosenbluth, and S. Putvinski, Phys. Plasmas 6, 2523 (1999).
[11] M. Rosenbluth and S. Putvinski, Nucl. Fusion 37, 1355 (1997).
[12] R. Yoshino and S. Tokuda, Nucl. Fusion 40, 1293 (2000).
[13] H. Tamai, R. Yoshino, S. Tokuda, et al., Nucl.Fusion 42, 290 (2002).
[14] M. Lehnen, S. Bozhenkov, S. Abdullaev, et al., Phys. Rev. Lett.100, 255003 (2008).
[15] K. Finken, S. Abdullaev, M. Jakubowski, et al., Nucl.Fusion 47, 91 (2007).
[16] N. J. Fisch, Rev. Mod. Phys. 59, 175 (1987).
[17] H.-W. Bartels, Fusion Eng. Des. 23, 323 (1994).
[18] T. Kawamura, H. Obayashi, and A. Miyahara, Fusion Eng. Des. 9, 39 (1989).
[19] H. Bolt, A. Miyahara, M. Miyake, et al., J. Nucl.Mater.151, 48 (1987).
[20] R. Jaspers, N. L. Cardozo, A. Donne, et al., Rev. Sci. Instrum.72, 466 (2001).
[21] J. Martín-Solís, J. Alvarez, R. Sánchez, et al., Phys. Plasmas 5, 2370 (1998).
[22] J. Martín-Solís, B. Esposito, R. Sánchez, et al., Phys. Plasmas 6, 238 (1999).
[23] J. Liu, H. Qin, N. J. Fisch, et al., Phys. Plasmas 21, 064503 (2014).
[24] M. Bakhtiari, G. Kramer, M. Takechi, et al., Phys. Plasmas 12, 102503 (2005).
[25] X. Guan, H. Qin, and N. J. Fisch, Phys. Plasmas 17, 092502 (2010).
[26] H. Qin, X. Guan, and N. J. Fisch, Report No. PPPL-4639, Princeton Plasma Physics Laboratory (PPPL), Princeton, NJ (United States) (2011).
[27] G. Papp, M. Drevlak, T. Fülop, et al., Nucl.Fusion 51, 043004 (2011).
[28] J. Rax, N. Fisch, and L. Laurent, Plasma Phys. Contr. Fusion 35, B129 (1993).
[29] F. Andersson, P. Helander, and L.-G.Eriksson, Phys. Plasmas 8, 5221 (2001).
[30] S. Dalena, A. Greco, A. Rappazzo, et al., Physical Review E 86, 016402 (2012).
[31] S. Dalena, A. Rappazzo, P. Dmitruk, et al., Astrophys. J. 783, 143 (2014).
[32] R. Zhang, J. Liu, H. Qin, et al., Phys. Plasmas 22, 044501 (2015).
[33] J. D. Jackson, Classical electrodynamics, vol. 3 (Wiley New York etc., 1962).
[34] S. Wu, Fusion Eng. Des. 82, 463 (2007).

Statistical analysis of non-diffusive transport in the linear device NAGDIS-II

H.Tanaka[1,2] and Ohno lab group[3]

[1]National Institute for Fusion Science, Toki 509-5292, Gifu, Japan
[2]SOKENDAI (Department of Fusion Science), Toki 509-5292, Gifu, Japan
[3]Graduate School of Engineering, Nagoya University, Nagoya 464-8603, Aichi, Japan

Abstract

We have investigated non-diffusive edge plasma transport in the linear device NAGDIS-II. For this purpose, in this study, two-dimensional motions perpendicular to the magnetic field were extracted by the spatiotemporal analysis of a multiset of simultaneously measured fluctuations and a fast imaging camera used in the detached divertor condition. As a result, spiral-shape structure rotating to the **E** × **B** drift direction was identified.

1. Introduction

In the edge region of the fusion devices, blobby plasma transport is a well-known phenomenon as one of the typical non-diffusive plasma transports. This transport is mostly observed in the scrape-off layer (SOL) in tokamak devices. Blobs forming a filament structure along the magnetic field [1] effect on the SOL density profile, parallel flow, recycling process, impurity transport, and so on. Blobs have high density compared with that in the background SOL plasma. Therefore, when a blob passes through the Langmuir probe electrode, a positive spike of the ion saturation current is observed. Normally, blobs are propagated toward the low-field side direction due to the **E** × **B** drift with the internal electric field **E** inside the blob and the toroidal magnetic field **B** [2]. On the other hand, in the linear plasma devices, there are no gradient and curvature of the magnetic field; however, similar cross-field transports were reported [3, 4, 5]. This transport mechanism is supposed as the centrifugal force or the neutral wind effect [6]. Surely there are some of differences in between the tokamaks and linear devices, comparison and universal understanding of the cross-field transport are important for the magnetic confinement fusion in addition to the plasma physics.

In the linear plasma device NAGDIS-II (**NAG**oya **DI**vertor plasma **S**imulator – **II**) [7], a number of positive spikes were observed in the ion saturation current fluctuation measured at periphery outside the plasma column. In this study, we are focusing on the two-dimensional (2D) measurements perpendicular to the magnetic field, because 1D measurement cannot distinguish radial and azimuthal motions, causing some wrong interpretations. In order to extract the 2D behaviors of coherent plasma structures in NAGDIS-II, we employed two methods: the spatiotemporal correlation analysis of a multiset of two-position fluctuations in a steady-state discharge and the proper orthogonal decomposition (POD) analysis of a 2D movie obtained by a fast imaging camera in the detached divertor condition.

2. Experimental setup in the linear plasma device NAGDIS-II

Figure 1(a) shows the schematic top view of NAGDIS-II. This linear device has the open magnetic field geometry and can generate high-density plasmas in a steady state. An Intermediate electrode with diameter of 20 mm is located between a cathode and a hollow anode. By increasing the neutral gas pressure in the divertor test region, the plasma detached condition is obtained. In order to extract the 2D behaviors, we prepared two types of the experimental setup [8].

Firstly, we employed spatiotemporal correlation analysis for a multiset data obtained by two Langmuir probe tips. As shown in Fig.1(b), one probe tip was fixed at the horizontal position 10 mm away from the center of the plasma column. The other probe was moved horizontally (x) and vertically (y) at a position ranging from x = 0 mm to 40 mm and from y = -20 mm to 20 mm, respectively, with a spatial resolution of 2 mm. The ion saturation current I_{sat} was measured at each position with a sampling frequency of 1 MHz.

Next, we have directly measured by the 2D motion by a fast imaging camera. A viewing port made of quartz glass was installed at the end of a vacuum vessel. In order to reduce a large amount of heat load from the plasma column into the viewing port, detached plasma was generated. The sampling frequency was 30,000 frame/s, and the number of pixels was 128 × 256, corresponding to an observation area of approximately 54 × 108 mm^2.

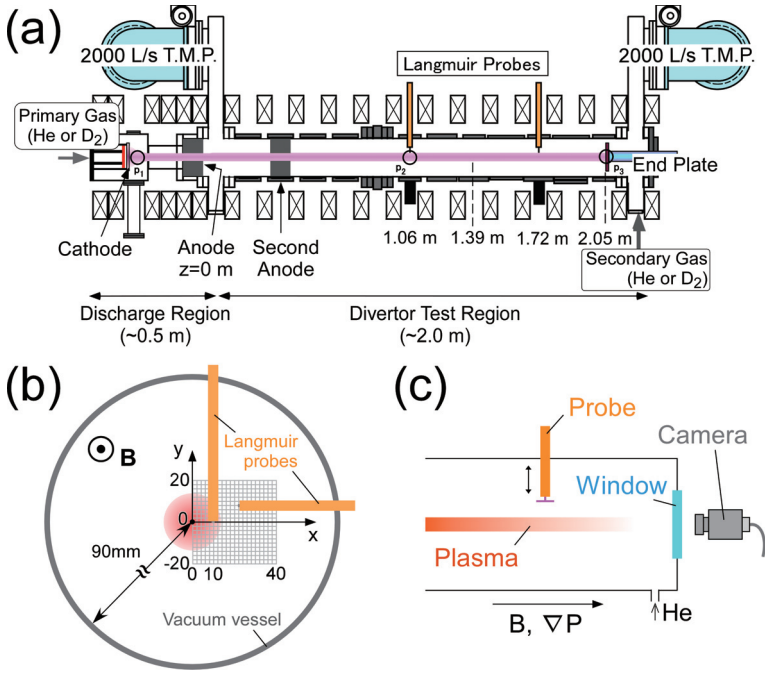

Fig.1 (a) Top view of NAGDIS-II [7]. (b) Schematic of two-positon probe measurement [8]. One probe inserted from the top is fixed. Another probe inserted from the side moves on the grid points. (c) Experimental setup of the fast imaging camera measurement [8].

3. Extraction of 2D behaviors

2D spatiotemporal correlation function between two-position signals, $I(x_i, t)$ and $I(x_j, t)$, was defined by

$$C_{ij}(\tau) = \left\langle \tilde{I}(x_i, t)\tilde{I}(x_j, t+\tau) \right\rangle, \quad (1)$$

where ~ indicates a fluctuation component that is obtained by subtracting the mean <>. In this study, x_i was fixed and x_j was moved on grid points in Fig.1 (b); then, we used a band-passed components, $I_f(x_i, t)$, instead of $I(x_i, t)$. Figure 2 shows the 2D spatiotemporal correlation function with a band-pass filter of 28 kHz < f < 38 kHz, which contains a spectral peak of $I(x_i, t)$. It can be found that a spiral-shape structure rotates toward the anti-clockwise direction which corresponds to the **E** × **B** drift direction.

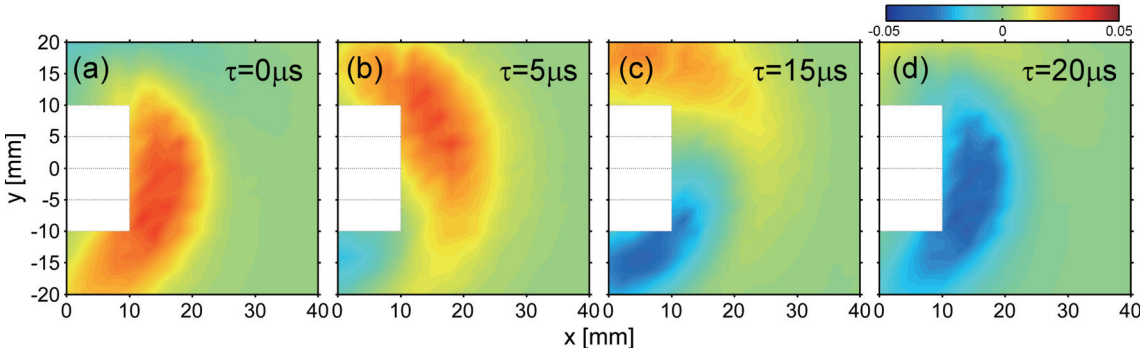

Fig.2 Spatiotemporal correlation functions at (a) τ = 0, (b) 5, (c) 10, and (d) 15 μs.

Figure 3 shows the 2D snapshots captured with a fast imaging camera in the detached divertor condition, as shown in Fig.1(c). These images show that spiral-shape coherent structures appeared discontinuously around the plasma column. In addition, the structures rotate in the E × B drift direction. The fundamental mode number is evaluated as m = 1 by applying the POD method [8], as shown in Fig.4. The fundamental component of the spiral structure was found to be rotating as a rigid body at a frequency of f ~ 3.3 kHz by Fourier analysis.

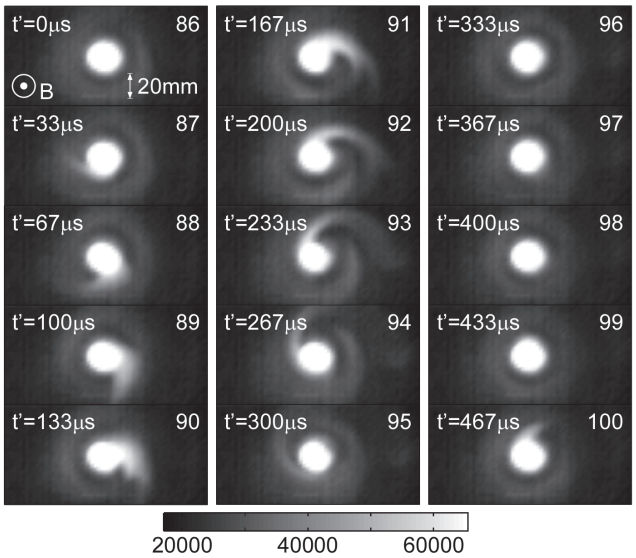

Fig.3 Successive snapshots captured by the fast imaging camera [9].

4. Summary

We have clarified 2D motions of coherent plasma structures in NAGDIS-II. Spatiotemporal

correlation technique was employed for a multiset of two-position fluctuations. Fast imaging camera measurement was carried out and the POD method was applied to analyze the mode behaviors. It was found that the spiral-shape structure dominantly appear in the edge region of NAGDIS-II.

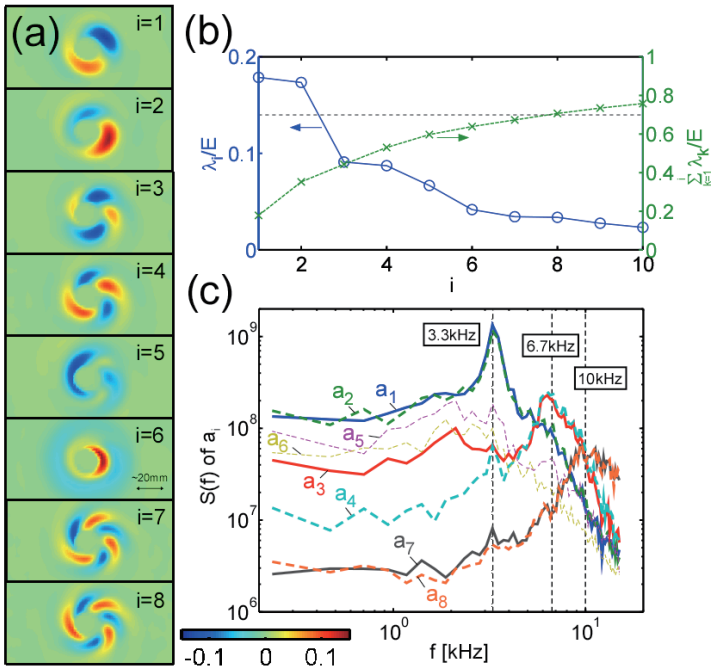

Fig.4 (a) The orthonormal bases for the space of mode numbers i = 1–8, (b) the ratio between the eigenvalue of mode i and energy, λ_i/E (circles) and its summation between k = 1 to i (squares). (c) The power spectra of the orthogonal bases for time $a_i(t)$ [8].

Acknowledgements

This research was supported by KAKENHI (19360413, 10J00024, 23860064) and NIFS/NINS under the project of Formation of International Network for Scientific Collaborations. This work was partly supported by the JSPS-NRF-NSFC A3 Foresight Program in the field of Plasma Physics (NSFC: No.11261140328, NRF: No.2012K2A2A6000443).

References

[1] R.J. Maqueda, G.A. Wurden, S. Zweben, et al., Rev. Sci. Instrum. **72** (2001) 931.

[2] S.I. Krasheninnikov, Phys. Lett. A **283** (2001) 368.

[3] G.Y. Antar, G. Counsell, Y. Yu, et al., Phys. Plasmas **10** (2003) 419.

[4] T. A. Carter, Phys. Plasmas **13** (2006) 010701.

[5] N. Ohno, K. Furuta, and S. Takamura, J. Plasma Fusion Res. **80** (2004) 275.

[6] S.I. Krasheninnikov and A.I. Smolyakov, Phys. Plasmas **10** (2003) 3020.

[7] N. Ohno, D. Nishijima, S. Takamura, et al., Nucl. Fusion **41** (2001) 1055.

[8] H. Tanaka, N. Ohno, Y. Tsuji, et al., Contrib. Plasma Phys.**50** (2010) 256.

[9] H. Tanaka, N. Ohno, Y. Tsuji, et al., Contrib. Plasma Phys.**52** (2012) 424.

Atomic data and modeling for tungsten ion spectra

D.Kato[1,2], H.A. Sakaue[1], I. Murakami[1,2], M. Goto[1,2], T. Oishi[1,2],S. Morita[1,2], K. Fujii[3], N. Nakamura[4], X.-B. Ding[5], and C.-Z. Dong[5]

[1]National Institute for Fusion Science, Toki 509-5292, Gifu, Japan
[2]Deptertment of Fusion Science, SOKENDAI, Toki 509-5292, Gifu, Japan
[3]Graduate School of Engineering, Kyoto University, Kyoto615-8540, Japan
[4]Institue for Laser Science, The University of Electro-Communications, Tokyo 182-8585, Japan
[5]Colledge of Phys. and Electronic Eng., Northwest Normal University, Lanzhou, 730070, China

Abstract

A magnetic-dipole (M1) line emission of the ground state W^{27+} is observed at the Large-Helical-Device (LHD). A collisional-radiative model is constructed to synthesize vertical profiles of the M1 line intensity on a horizontally elongated poloidal cross section of the LHD. The present model includes effects of proton collision and ionization excitation from W^{26+}. Collision rate coefficients of protons become larger than those of electrons at temperature of 800 eV or higher. The collision rate coefficients dominate over the M1 transition rate at the density of 10^{13} cm^{-3}. The spatial distribution of the M1 line intensity shows a peak at about 1 keV where the fractional ion abundance of W^{27+} becomes maximum. Strong enhancement of the M1 line intensity by proton collision is predicted.

1. Introduction

Tungsten, which is used as divertor materials in ITER, will cause serious radiation loss once it accumulates in the plasma core because it is not fully ionized even in the ITER with Te = 15 - 20 keV. It is, therefore, necessary for the stable operation of ITER to study the influx and edge transport of the tungsten ion. Usage of visible line emission of the tungsten ion is useful because the radiation shielding of detectors is not necessary by using optical fibers. However, the knowledge on visible lines of the tungsten from fusion experiments has been extremely limited to neutral atoms and ions in low charge states. The magnetic-dipole (M1) line from ground state highly-charged tungsten ions in the visible and near-UV ranges have been observed by using electron-beam-ion-traps (EBITs) [1-5] and the Large-Helical-Device (LHD) with tungsten pellet injection [6,7] (Table 1). These M1 lines are useful for measurements of ion temperature, rotation velocity and ion density of tungsten ions in edge plasmas including Scrape-Off Layer (SOL) and divertor regions of ITER. Such visible M1 lines can be investigated in the LHD because the LHD discharge is entirely stable for substantial amount of tungsten density exhibiting no MHD instabilities.

2. Observation of near-UV M1 line emission from W^{27+} inLHD

Tungsten was introduced into the LHD plasmas by injecting a polyethylene pellet (0.6 mm long and 0.6 mm diameter) containing a tungsten wire. Size of the tungsten wire is 0.15 mm in diameter and 0.6 mm

in length from which the number of tungsten atoms in the pelletis estimated to be 6.6×10^{17}. Line emission was observed at 44 lines of sight along the horizontal axis of a horizontally elongated poloidal cross section of the LHD.Figure 1 shows an emission line spectrum in 330 – 340 nm and the vertical profile of each line intensity. In the figure, emission linesfrom tungsten ions are indicated by allows with wavelength values (nm) determined by fitting each line profile to the Gaussian distribution function. The line at 337.7 nm is identified as the M1 line of W^{27+} in the ground state due to transition between two fine-structure levels: $4f_{5/2}$ (the lower level) and $4f_{7/2}$ (the upper level). The wavelength value coincides with that measured by means of an EBIT [3] (Table 1).

3. Atomic model for M1 line emission from W^{27+} in the ground state

A collisional-radiative (CR) model is developed to analyze the vertical profile of the M1 line of W^{27+}. HULLAC code [8] is used to generate atomic data (energy levels, radiative transition rates, electron collision strengths). Proton collision effects are included in the model approximating proton collision strengths as mass scaled electron collision strengths. Ionization excitation from W^{26+} is also taken into account.In ionizing plasmas, fractional populations of excited levels n_k are obtained by solving the quasi-stationary state equation,

$$0 = \sum_{j\neq k}\left(n_e C^e_{kj} + n_p C^p_{kj}\right)n^{(q)}_j + \sum_{j>k} A_{kj} n^{(q)}_j + n_e \sum_j S^{q-1\to q}_{kj} n^{(q-1)}_j \, n_{q-1}/n_q$$
$$- \left[\sum_{j\neq k}\left(n_e C^e_{jk} + n_p C^p_{jk}\right) + n_e S^{q\to q+1}_k + \sum_{j<k} A_{jk}\right] n^{(q)}_k$$

where n_e and n_p are electron and proton densities, respectively, C^e_{kj} and C^p_{kj} (de-)excitation rate coefficients by electron and proton collisions, respectively, $S^{q\to q+1}_k$ ionization rate coefficients by electron collisions, A_{kj} transition rates, and n_q fractional ion abundances of W^{q+}. Figure 2 shows the (de-)excitation rate coefficients between the ground-term fine-structure levels of W^{27+}. It is noted that the rate coefficients are calculated assuming the Maxwellian velocity distribution of electrons and protons with an identical temperature ($T_e = T_p$). The rate coefficients of protons are larger than those of electrons at temperatures of 800 eV or higher. In the figure, rate coefficients of the M1 transition between the two levelsare also indicated by dotted linesfor electron densities of 10^{13} cm^{-3} and 10^{11} cm^{-3}. The collision rates of 10^{13} cm^{-3} are larger than the M1 transition rate at temperatures of 1 keV or higher. Fractional ion abundances of W^{q+} are calculated using ionization and recombination rate coefficients: S_q and α_q, respectively.

$$\frac{1}{n_e}\frac{dn_q}{dt} = -\left(S_q + \alpha_q\right)n_q + S_{q-1}n_{q-1} + \alpha_{q+1}n_{q+1}$$

Uncertainty in the rate coefficients [9,10] causes significantly different results (Fig. 3). The discrepancy is small for W^{27+} whose fractional abundance has a maximum around 1 keV.

4. Vertical profile of the M1 line intensity

Figure 4 shows a 2D plot of the M1 line intensity distribution as a function of electron temperature and density. The intensity is calculatedusing the emissivity $\varepsilon_{ij}^{(q)} = A_{ij} n_j^{(q)}(T_e, n_e)/n_e$and the fractional ion abundance at a given temperature and a density,

$$I_{ij}(T_e, n_e) = n_e \varepsilon_{ij}^{(q)} n_q + n_e \varepsilon_{ij}^{(q-1)} n_{q-1}$$

wherethe second term represents contribution of the ionization excitation from W^{26+}. The distribution shows a peak at about 1 keV where the fractional ion abundance of W^{27+} becomes maximum. The peak temperature decreases slightly as the density increases. The intensity profile is primarily determined by the fractional ion abundance of W^{27+}.Vertical profiles of the M1 line intensity are obtained by integrating spatial distributions of the intensity along the horizontal axis of a horizontally elongated poloidal cross section. In the present study, the spatial distribution is assumed to be uniform at a constant effective minor radius r_{eff}. Figure 5 shows the spatial distribution of the M1 line intensity on the poloidal cross section and the vertical profile for a measured electron temperature profile$T_e(r_{\mathrm{eff}})$and a density profile$n_e(r_{\mathrm{eff}})$ shown in Fig. 6.The radial distributionshows a maximum at $r_{\mathrm{eff}} \sim 0.35$ m, and correspondingly the vertical profile has two peaks at$Z \sim \pm 0.2$ m, respectively. Proton collision effects increase the M1 intensity remarkably, whereas the increase by the ionization excitation from W^{26+} is less significant.

Table 1 List of magnetic-dipole lines of W^{q+} measured by means of electron-beam-ion-traps (EBITs) [1-4].

q+	IP (keV)	Wavelength (nm)	Transition
26+	0.7844	333.748(9)	$4f^2\ {}^3F_4 \rightarrow {}^3F_3$
		335.758(11)	$4f^2\ {}^3F_4 \rightarrow {}^1G_4$
		389.433(12) 389.41(6) 389.35(3)	$4f^2\ {}^3H_5 \rightarrow {}^3H_4$
27+	0.8334	337.743(26)	$4f\ {}^2F_{7/2} \rightarrow {}^2F_{5/2}$
28+	0.8814	344.588(33)	$4d^9 4f\ (5/2,5/2)_3 \rightarrow (5/2,7/2)_4$
52+	4.709	362.67(2) 362.713(10) 362.6(2)	$3d^4\ {}^5D_3 \rightarrow {}^5D_4$

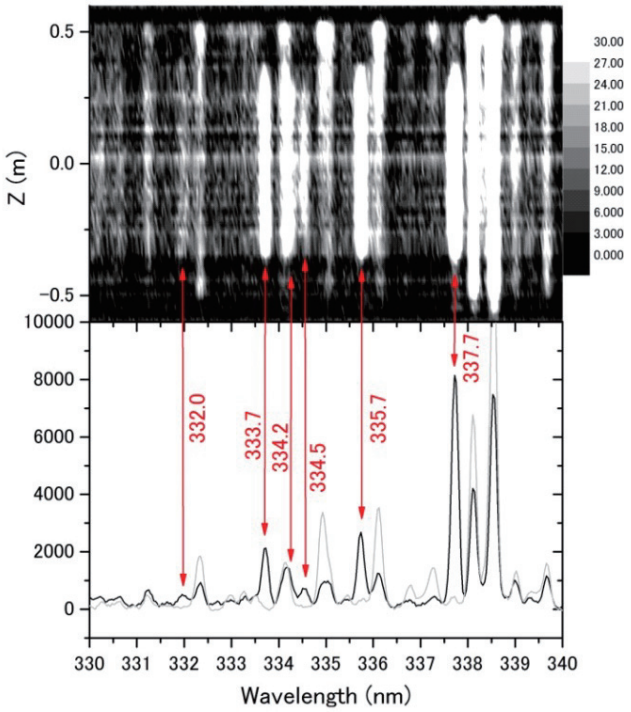

Fig.1 Emission line spectrum in 330 - 340 nm measured at the LHD (shotno. 121534).Solid line indicatesthe spectrum measured after tungsten injection (t = 4.1 – 4.138 s), andlight gray the spectrum measured before the tungsten injection. The upper panel shows vertical profiles of line-integrated intensities of the lines along the horizontal axis of a horizontally elongated poloidal cross section.Red arrows indicate emission lines from tungsten ions. Numbers are the central wavelengths in nm.

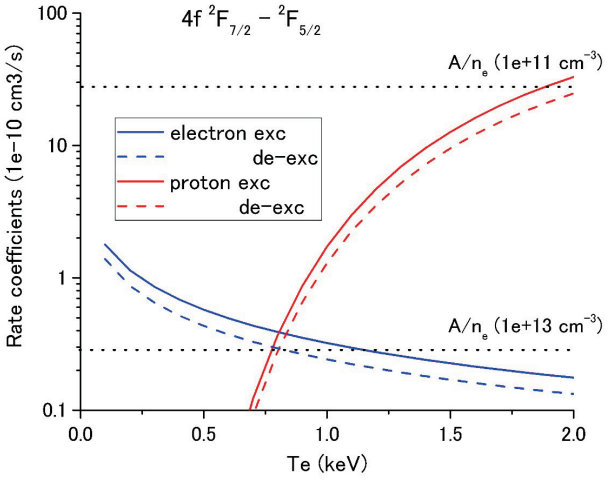

Fig.2 Collisional excitation and de-excitation rate coefficients between ground state fine-structure levels of W^{27+}. Solid lines stand for excitation and dashed lines for de-excitation. Dotted lines are rate coefficients of M1 transition between the fine-structure levels for electron densities of 10^{13} and 10^{11} cm^{-3}, respectively.

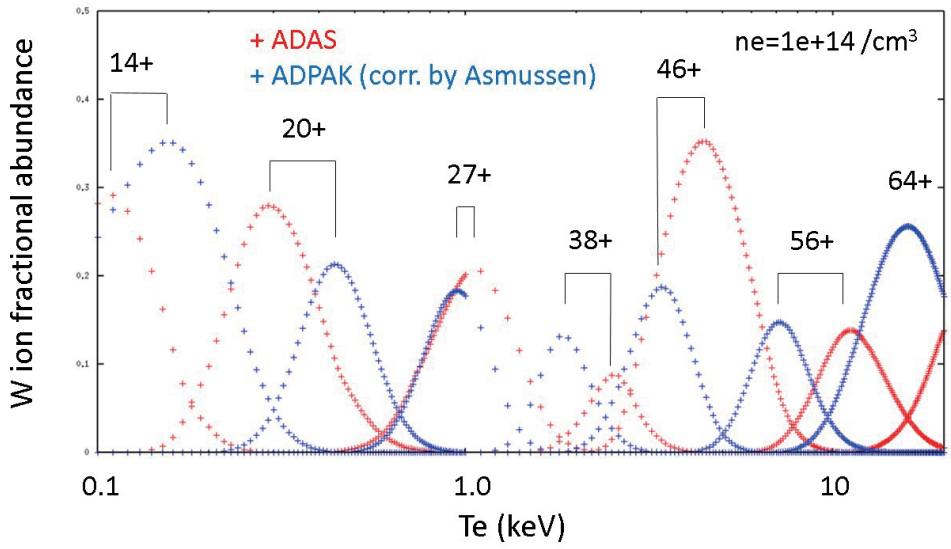

Fig.3 Fractional ion abundances of W^{q+} at $n_e = 10^{14}\text{cm}^{-3}$. Two sets of ionization and recombination rate coefficients (ADAS [9] and modified ADPAK [10]) are used in the present calculation.

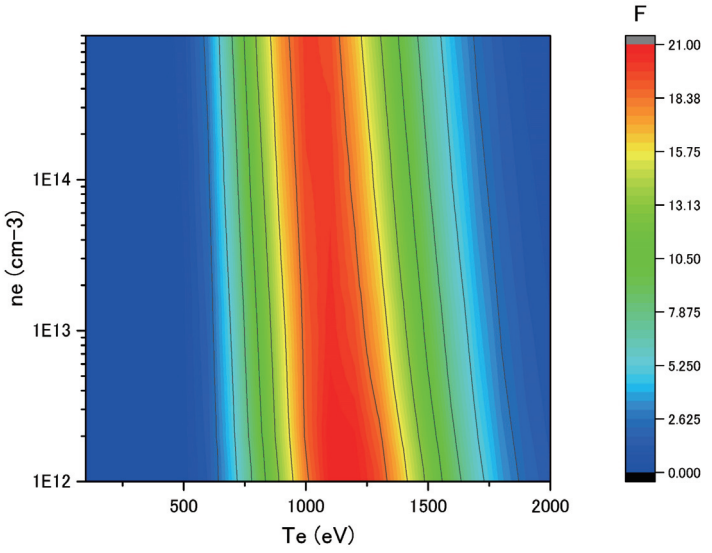

Fig.4 2D plot of M1 line intensity distribution as a function of electron temperature and density.

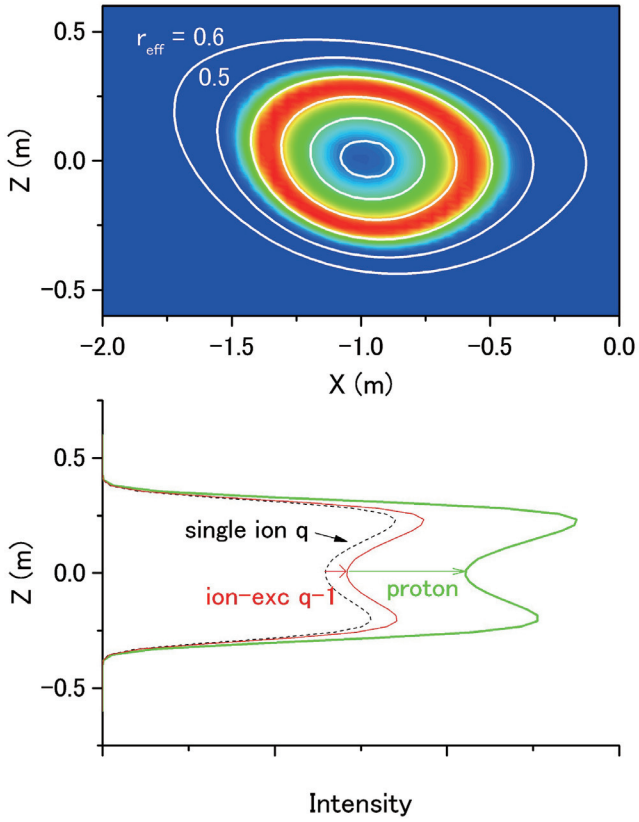

Fig.5 Upper) Radial distribution of M1 line intensity on a horizontally elongated poloidal cross section of the LHD, and Lower) vertical profile of the line-integrated intensity along the horizontal axis.

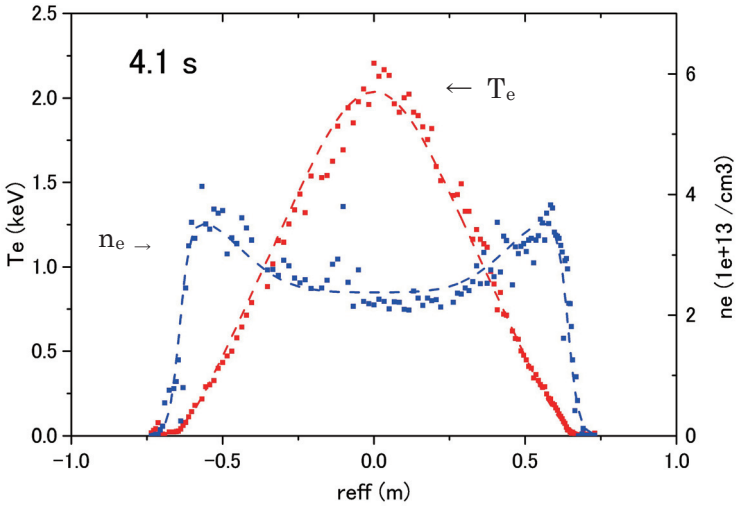

Fig.6 Radial profiles of electron temperature and density measured by Thomson scattering.

Acknowledgements

This work was partly supported by the JSPS-NRF-NSFC A3 Foresight Program in the field of Plasma Physics (NSFC: No.11261140328, NRF: No.2012K2A2A6000443). DK is grateful to KAKENHI (15H04235).

References

[1] H. Watanabe et al., Phys. Rev. A **63**(2001) 042513; Can. J. Phys. **90**(2012) 197.

[2] A. Komatsu et al., Phys. Scr. **T144**(2011) 014012;Plasma and Fusion Res.: Rapid Commun.**7**(2012) 1201158.

[3] Z. Fei et al., Phys. Rev. A **86**(2012) 062501.

[4] M. Qiu et al., J. Phy. B: At. Mol. Opt. Phys.**47**(2014) 175002.

[5] Y. Kobayashi et al., Phys. Rev. A **92** (2015) 022510.

[6] D. Kato et al., Phys. Scr. **T156** (2013) 014081.

[7] K. Fujii et al., Phys. Scr., in press.

[8] A.Bar-Shalom, M.Klapisch and J.Oreg, J.Quant.Spectr.Radiant.Trans. **71** (2001) 169.

[9]The Atomic Data and Analysis Structure(ADAS) http://open.adas.ac.uk/.

[10] K. Asmussen et al., Nucl. Fusion **38**(1998) 967.

Study of impurity radiation in attached and detached plasmas of LHD

H.M.Zhang[1], S.Morita[1,2], T.Oishi[1,2], I.Murakami[1,2], M.Goto[1,2], X.L.Huang[2] and Y.Liu[1]

[1]SOKENDAI (Graduate University for Advanced Studies), Toki 509-5292, Gifu, Japan
[2]National Institute for Fusion Science, Toki 509-5292, Gifu, Japan

Abstract

Detached plasma has been successfully achieved with use of m/n=1/1 resonant magnetic perturbation (RMP) coils in Large Helical Device (LHD) without any additional impurity gas puffing. Study of the impurity radiation is then important to clarify the physical mechanism triggering the RMP-assisted detachment. Resonance lines of CIII (977.02 Å, $2s2p - 2s^2$), CIV (1548.2 Å, 2p – 2s), CV (40.27 Å, $1s2p - 1s^2$) and CVI (33.73 Å, 2p – 1s) measured by vacuum ultraviolet (VUV) and extreme ultraviolet (EUV) spectrometers are used to estimate the radiation power from C^{2+} – C^{5+} ions because carbon is the most abundant impurity element in LHD. For this purpose the spectral intensity from the VUV spectrometer is absolutely calibrated using the EUV spectrometer from which the intensity has been already calibrated. The partial carbon radiation at each ionization stage of C^{2+} to C^{5+} ions, $P_{rad}(C^{q+})$, can be estimated for attached and detached plasmas by calculating a ratio of the partial carbon radiation to the resonance line based on ADAS atomic code. It is found that the radiation from C^{3+} ions existing near radial location of $\iota/2\pi = 1$ in the ergodic layer increases up to 40% of the total radiation loss and becomes a dominant origin to trigger the detached plasma, while the carbon radiation is negligibly small in the attached plasma.

1. Introduction

Steady operation of the detached plasma has been achieved without additional impurity gas puffing in LHD by forming m/n = 1/1 magnetic island at $\iota/2\pi = 1$ in the ergodic layer with RMP coils [1]. Carbon released from graphite divertor plates is a dominant intrinsic impurity in high-density LHD discharges [2]. Then, it seems that the carbon radiation during the plasma detachment is also important for the effective edge plasma cooling triggering the detachment. In LHD, C^{2+} and C^{3+} ions with low ionization energies (E_i = 48, 65 eV) are located near the outer boundary in the ergodic layer, whereas C^{4+} and C^{5+} ions with relatively high ionization energies (E_i = 392, 490eV) are located near the last closed flux surface (LCFS) [2]. In the RMP-assisted plasma detachment, therefore, it is very interesting to compare the radiation power from C^{2+} and C^{3+} ions located outside $\iota/2\pi = 1$ with that from C^{4+} and C^{5+} ions located inside $\iota/2\pi = 1$.

The partial radiation power at each ionization stage in carbon ions of C^{2+} to C^{5+}, $P_{rad}(C^{q+})$, is analyzed from line intensities of CIII – CVI resonance transitions which can be measured with extreme ultraviolet (EUV: 10 – 500 Å) and vacuum ultraviolet (VUV: 300 – 2400 Å) spectrometers. Intensity ratios of the $P_{rad}(C^{q+})$ to the resonance line can be useful to estimate the $P_{rad}(C^{q+})$. For its purpose the electron temperature at the radial location where the carbon ion exists has to be evaluated because the intensity ratio is sensitive to the electron temperature. In addition, spectral intensity has to be absolutely calibrated, in

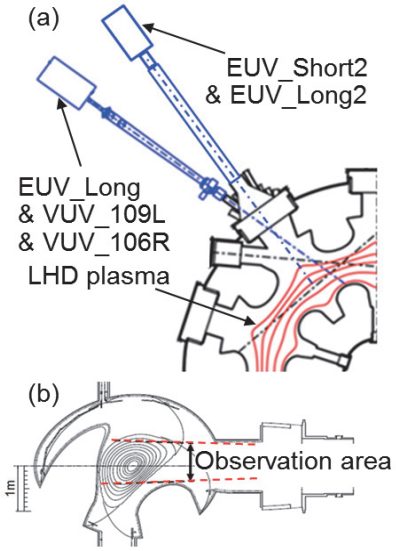

Fig. 1 (a) Schematic view of space-resolved EUV and VUV spectrometers (EUV_Short2 and EUV_Long2) and high-time-resolution EUV and VUV spectrometers (EUV_Long, VUV_109L and VUV_106R) and (b) observation area of EUV_Long, VUV_109L and VUV_106R.

particular, for the VUV spectrometer. Thus, the P_{rad} (C^{q+}) analyzed with the intensity ratio are compared between attached and detached plasmas.

2. Experimental setup

In LHD, the m/n = 1/1 magnetic island formed by the RMP coil system was originally used for the local island divertor experiment to realize an efficient particle exhaust. The O-point of the m/n = 1/1 magnetic island is then positioned in the outboard side of horizontally elongated plasma cross section at #6-O or #7-O toroidal section. In the present study it is called 6-O or 7-O island configuration. Since the detached plasma is realized at the magnetic axis position of R_{ax} = 3.90 m, the m/n = 1/1 island is located in the ergodic layer due to the low edge rotational transform.

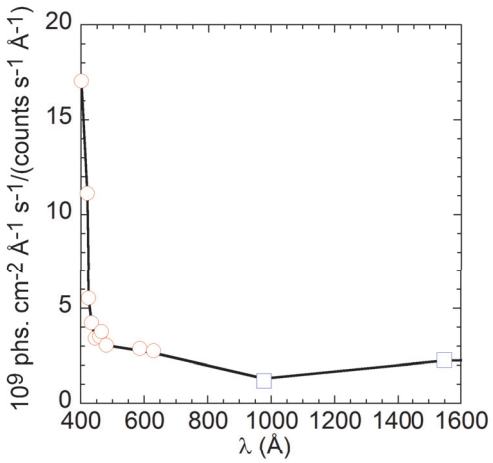

Fig. 2 Absolute intensity calibration factor of VUV_109L and VUV_106R in the wavelength range of 400–1600 Å.

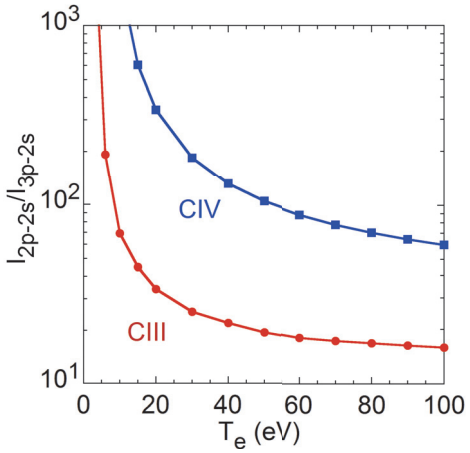

Fig. 3 Intensity ratios of CIII (977.02 Å/386.2 Å) and CIV (1548.2 Å/312.4 Å).

The EUV and VUV spectrometers are installed on #10-O diagnostic port of LHD, as shown in Fig.1 (a). In the present study, two EUV spectrometers named EUV_Short (10-100 Å) and EUV_Long (50-650 Å) and two 20 cm normal incidence VUV spectrometers named VUV_109L (300-1000 Å) and VUV_106R (970-1900 Å) are used for simultaneous high-time resolution measurement (5ms) of carbon resonance lines, i.e. CIII (977.02 Å, $2s2p - 2s^2$), CIV (1548.2 Å, 2p – 2s), CV (40.27Å, $1s2p - 1s^2$) and CVI (33.73 Å, 2p – 1s) [3,4]. Two space-resolved EUV spectrometers named EUV_Short2 and EUV_Long2 are used for simultaneous vertical profile measurement of CIII (386.2 Å), CIV (384.17 Å), CV (40.27 Å) and CVI (33.73 Å) in the range of $-0.6 \leq Z \leq 0.6$ m with a time resolution of 100 ms [5–7]. The EUV_Long, VUV_109L and VUV_106R have a similar observation range, as shown in Fig. 1 (b).

3. Calibration of VUV spectrometers

In order to obtain absolute intensity of CIII and CIV resonance lines two VUV spectrometers of VUV_109L and VUV_106R have to be calibrated. The wavelength ranges of EUV_Long and VUV_109L are overlapped between 400 and 650 Å. Since the spectral intensity of EUV_Long has been already calibrated on the basis of profile measurement of bremsstrahlung in previous studies [3,8], the spectral intensity of VUV_109L can be easily calibrated by directly comparing the same spectrum from both spectrometers in the same wavelength range of 400 – 650 Å. The result is plotted in Fig. 2 with open circles.

In order to calibrate the intensity of VUV spectra in longer wavelength range, e.g. 650 – 1600 Å, the intensity ratio method is applied. Two intensity ratios of CIII (977.02 Å/386.2 Å, 2p – 2s/3p – 2s) and CIV (1548.2 Å/312.4 Å, 2p – 2s/3p – 2s) are calculated with ADAS atomic code as a function of electron temperature [9]. Here, the absolute intensities of CIII (386.2 Å) and CIV (312.4 Å) are obtained with EUV_Long spectrometer.

The electron temperature at radial location where the C^{2+} – C^{5+} ions exist is determined by analyzing the vertical profile of CIII – CVI emissions, as shown in Fig.4. The vertical profiles of CIII (386.2 Å), CIV (384.02 Å), CV (40.27 Å) and CVI (33.73 Å) are simultaneously observed with EUV_Long2 and

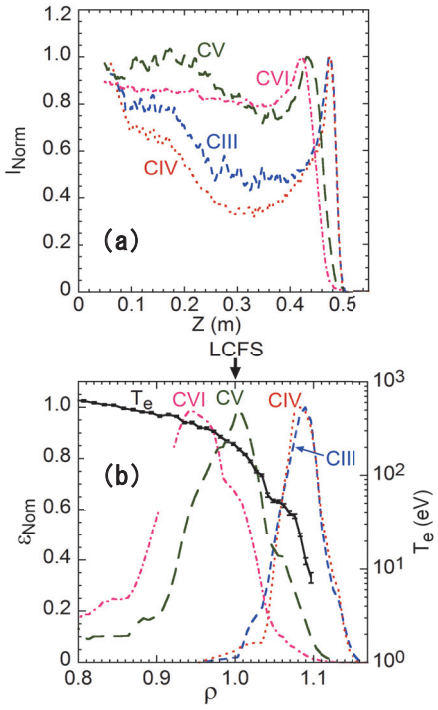

Fig. 4 (a) Normalized chord-integrated vertical profiles of CIII (386.2 Å), CIV (384.02 Å), CV (40.27 Å) and CVI (33.73 Å) and (b) Normalized local emissivity profiles of CIII to CVI and T_e profile as a function of minor radius.

EUV_Short2. The result is plotted in Fig. 4 (a). A sharp peak appears in the vertical profile at 0.4 < Z < 0.5 m because the chord length passing through the edge plasma is very long at the top edge in horizontally elongated plasma cross section. The intensity in CIII – CVI profiles is normalized at each edge peak. Local emissivity profiles of CIII – CVI are obtained by reconstructing the measured profiles as function of minor radius, ρ, with calculation of magnetic surfaces. The result is plotted in Fig. 4 (b). The emissivity profile is also normalized at each peak value. In the same figure T_e profile measured by Thomson scattering system is also plotted. Then, the electron temperature at radial locations of C^{2+} – C^{5+} ions is determined from the peak position in the CIII – CIV emissivity profile, i.e. 15 eV for C^{2+}, 20 eV for C^{3+}, 210 eV for C^{4+} and 360 eV for C^{5+}.

The intensity ratio in Fig. 3 is determined with electron temperatures mentioned above. Thus, the spectral intensities from VUV_109L and VUV_106R spectrometers can be absolutely calibrated at wavelengths of 977.02 Å and 1548.2 Å based on the absolute intensities of CIII (386.2 Å) and CIV (312.4 Å) and the intensity ratio. The result obtained from the intensity ratio method is shown in Fig. 2 with open squares. Finally, the analyzed calibration factor is fitted with a smooth curve in the wavelength range of 400 – 1600 Å, as shown in Fig. 2 with solid line.

4. Estimation of partial radiation P_{rad} (C^{q+})

Radiation power of the resonance transition generally occupies a considerably large part in the radiation power from impurity ions in certain ionization stage. Therefore, the P_{rad} (C^{2+}), P_{rad} (C^{3+}), P_{rad}

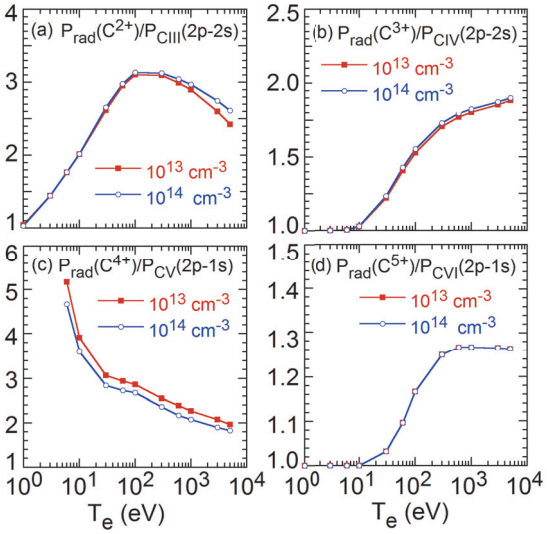

Fig. 5 Ratios of partial carbon radiation power at each ionization stage to radiation power of resonance line: (a) P_{rad} (C^{2+})/P_{CIII} (2p-2s), (b) P_{rad} (C^{3+})/P_{CIV} (2p-2s), (c) P_{rad} (C^{4+})/P_{CV} (2p-1s) and (d) P_{rad} (C^{5+})/P_{CVI} (2p-1s).

(C^{4+}) and P_{rad} (C^{5+}) can be evaluated from the resonance lines of CIII (977.02 Å), CIV (1548.2 Å), CV (40.27 Å) and CVI (33.73 Å), respectively. The ratio of P_{rad} (C^{q+}) to resonance line intensity is calculated using ADAS atomic code. The results are shown in Figs. 5 (a) – (d) as a function of electron temperature with parameter of electron density. Since the ratio is practically insensitive to n_e as seen in the figure, the contribution of n_e can be neglected in the present analysis. As the value of T_e for each ionization stage of carbon ions is already determined from the profile analysis done in Fig. 4 (b), the P_{rad} (C^{q+}) can be estimated from the intensity ratio in Fig. 5.

5. P_{rad} (C^{q+}) in attached and detached plasmas

The partial carbon radiation of P_{rad} (C^{2+}) to P_{rad} (C^{5+}) is analyzed for attached and detached plasmas. Figure 6 shows a comparison of discharge waveform between attached (Figs. 6 (a) – (f)) and detached (Figs. 6 (g) – (l)) plasmas. These two discharges are operated at magnetic axis position of R_{ax} = 3.90 m and heated by negative-ion-source based NBIs. The total radiation loss, P_{rad}, shows similar values for both plasmas, i.e. 20 – 25% to the port-through NBI power, P_{NBI}. In the attached plasma the line-averaged electron density is maintained constantly (~5×10^{13} cm^{-3}) during t = 4 – 8 s with P_{rad} = 1400 kW. The contribution of P_{rad} (C^{2+}) and P_{rad} (C^{4+}) to P_{rad} is less than 1%, while P_{rad} (C^{3+})/P_{rad} and P_{rad} (C^{5+})/P_{rad} are 8% and 2%, respectively.

In the discharge with detached plasma, the m/n = 1/1 island is formed in the ergodic layer and the O-point of the island is located at the outboard side of #6 toroidal section. With increase in the electron density, the plasma detachment occurs at t = 5.0 s, as shown in Figs. 6 (g) – (l). The electron density starts to increase after appearance of the detachment at t = 5.0 s, but it is saturated at t = 6.0 s. The plasma detachment is steadily maintained at high density of $n_e = 12\times10^{13}$ cm^{-3} during t = 6 – 8 s until the end of NBI pulse. The radiation loss also reaches the maximum value of P_{rad} = 1700 kW. Compared with the attached plasma, it is found that the P_{rad} (C^{2+})/P_{rad} and P_{rad} (C^{3+})/P_{rad} significantly increase to 3% and 40%

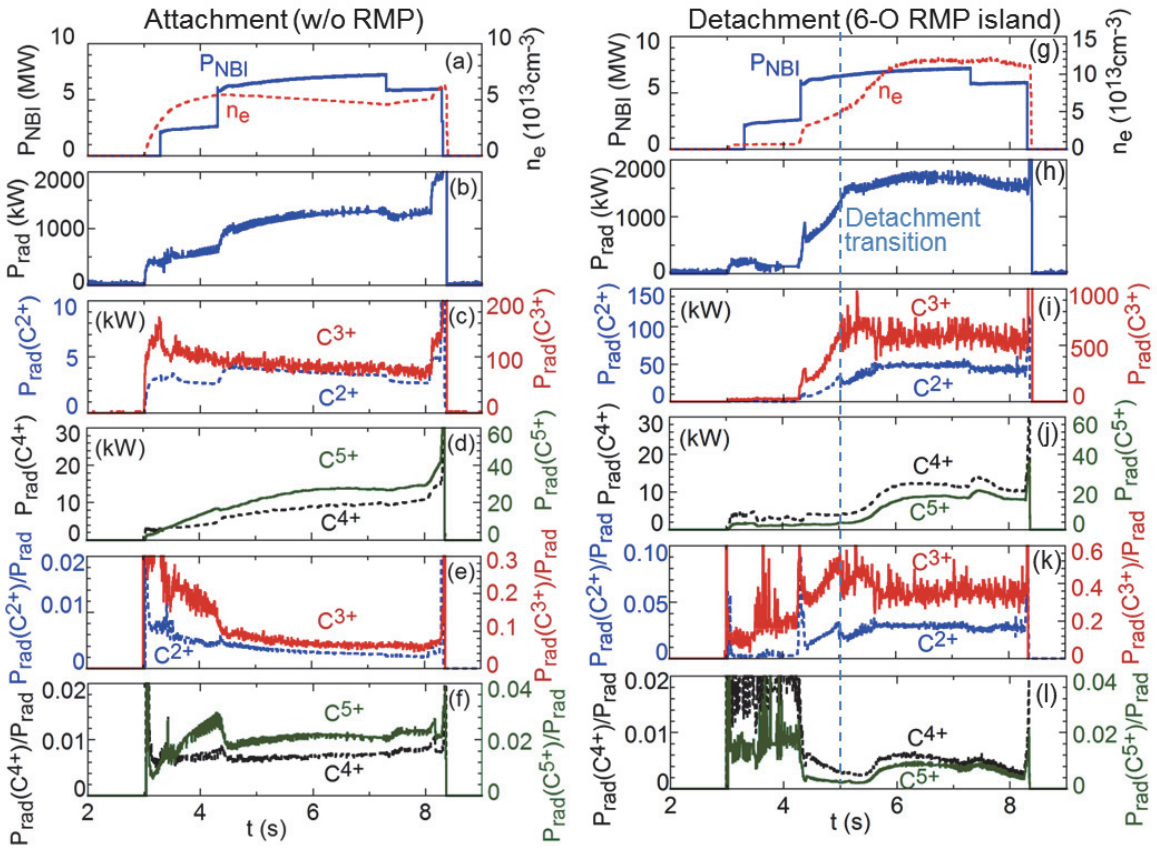

Fig. 6 Time behaviors of (a) NBI port-through power and line-averaged electron density, (b) total radiation loss (P_{rad}), partial carbon radiation power of (c) P_{rad} (C^{2+}) and P_{rad} (C^{3+}) and (d) P_{rad} (C^{4+}) and P_{rad} (C^{5+}) and ratios of P_{rad} (C^{q+}) to P_{rad} of (e) P_{rad} (C^{2+})/P_{rad} and P_{rad} (C^{3+})/P_{rad} and (f) P_{rad} (C^{4+})/P_{rad} and P_{rad} (C^{5+})/P_{rad} in the attached plasma without RMP. Graphs of (g) - (l) indicate time behaviors from detached plasma with 6-O RMP island in the same meaning as graphs (a) - (f).

during the detachment phase, whereas the increment of P_{rad} is only 300 kW. In contrast, the P_{rad} (C^{4+})/P_{rad} and P_{rad} (C^{5+})/P_{rad} do not change so much compared to the attached plasma.

The drastic increase in P_{rad} (C^{2+}) and P_{rad} (C^{3+}) during the detachment phase is very clear from the present analysis. The P_{rad} (C^{3+}) expresses a dominant portion in the total carbon radiation in the detached plasma. Therefore, it is concluded that the edge transport of C^{2+} and C^{3+} ions locating near m/n = 1/1 island is changed by external supply of the RMP field. In addition, the carbon transport near LCFS is not affected by the supplied RMP field because the P_{rad} (C^{4+}) and P_{rad} (C^{5+}) do not change at all in both discharges with attachment and detachment.

6. Summary

The partial carbon radiation of C^{2+} – C^{5+} ions has been estimated for attached and detached plasmas by analyzing the intensity of CIII – CVI resonance lines. It is found that the P_{rad} (C^{3+}) is much stronger than P_{rad} (C^{2+}), P_{rad} (C^{4+}) and P_{rad} (C^{5+}) in both the attached and detached plasmas. The P_{rad} (C^{3+}) is much increased in the detached plasma with 6-O island, i.e. 40% to P_{rad}, while P_{rad} (C^{3+}) indicates only 8% to P_{rad} in the attached plasma. The P_{rad} (C^{3+}) is therefore thought to be the dominant origin for triggering the

RMP-assisted detached plasma in LHD.

Acknowledgements

The authors thank all members of the LHD experimental group for their technical support. This work was partially carried out under the LHD project financial support (NIFS14ULPP010). This work was also partly supported by the JSPS KAKENHI Grant Number 23340183 and JSPS-NRF-NSFC A3 Foresight Program in the field of Plasma Physics (NSFC: No.11261140328, NRF: No. 2012K2A2A6000443).

References

[1]. M. Kobayashi, et al., Phys. Plasmas **17**, 056111 (2010).

[2]. M. B. Chowdhuri, et al., Phys. Plasmas **16**, 062502 (2009).

[3]. M. B. Chowdhuri, et al., Rev. Sci. Instrum. **78**, 023501 (2007) and Erratum: **84,** 109901 (2013).

[4]. T. Oishi, et al., Plasma Fusion Res. **10**, 3402031 (2015).

[5]. C. F. Dong, et al., Rev. Sci. Instrum. **81**, 033107 (2010).

[6]. H. M. Zhang, et al., Jpn. J. Appl. Phys. **54**, 086101 (2015).

[7]. X. L. Huang, et al., Rev. Sci. Instrum. **85**, 043511 (2014).

[8]. C. F. Dong, et al., Rev. Sci. Instrum. **82**, 113102 (2011).

[9]. H. P. Summers, JET-IR **06**, (1994).

Effects of force balance on impurity transport in the stochastic layer of LHD in comparison with EUV emission measurements

S. Y. Dai[1,2 *], M. Kobayashi[1,3], G. Kawamura[1], S. Morita[1,3], T. Oishi[1,3], H. M. Zhang[3], Y. Feng[4], Y. Suzuki[1,3] and the LHD experiment group[1]

[1] National Institute for Fusion Science, Toki 509-5292, Japan

[2] Key Laboratory of Materials Modification by Laser, Ion and Electron Beams (Ministry of Education), School of Physics and Optoelectronic Technology, Dalian University of Technology, Dalian 116024, PR China

[3] SOKENDAI (The Graduate University for Advanced Studies), Toki 509-5292, Japan

[4] Max-Planck-Institute für Plasmaphysik, D-17491 Greifswald, Germany

Abstract

The transport properties and line emissions of the intrinsic carbon in the stochastic layer of the Large Helical Device have been investigated with the three-dimensional edge transport code EMC3-EIRENE. The simulations of impurity transport and emissivity have been performed to study the dedicated experiment in which the carbon emission distributions are measured by a space-resolved EUV spectrometer system. A discrepancy of the CIV impurity emission between the measurement and simulation is obtained, which is studied with the variation of the ion thermal force and friction force in the impurity transport model. An enhanced ion thermal force or a reduced friction force in the modelling can increase the CIV impurity emission at the inboard X-point region.

1. Introduction

The transport behavior of impurities in the edge plasma is one of the most critical issues for the operation and performance of the fusion devices. In the Large Helical Device (LHD), the complicated three-dimensional (3D) structure of the stochastic magnetic field in the edge region leads to the impurity transport characteristics being quite different from that in tokamaks with 2D magnetic configuration. The transport properties of edge impurity are investigated in LHD by using a space-resolved extreme ultraviolet (EUV) spectrometer system [1-2]. In the present work, the 3D edge transport code EMC3-EIRENE [3-4] is used to study the transport behavior and line emissions of the intrinsic carbon in the stochastic layer of LHD. Recently, the development of the computational grid for the divertor leg regions of LHD has been achieved [5], which results in a good description of the plasma and impurity transport in the divertor leg regions of LHD.

2. Results and discussion

The trajectories of the inboard and outboard X-point regions are indicated with blue dotted lines and magenta solid lines in Fig. 1 (a), respectively. It can be seen that the CIV impurity emission is stronger for the inboard X-point region compared to the outboard one as shown in Fig. 1 (a). Figure 1 (b) shows the 2D distributions of CIV impurity emissions by EMC3-EIRENE modelling for the default case. Figure 1 (b) shows that the CIV impurity emission for the outboard X-point region is stronger between the magenta solid lines compared to the inboard one between the blue dotted lines. Here, a clear discrepancy of the CIV line emission pattern can be seen between the measurement and simulation.

2.1 The effect of the ion thermal force on CIV line emission

First, two important definitions are introduced for studying the difference between the experiment and modelling. The line emission ratio is defined as the ratio of the integrated value of the outboard X-point region emission (between the magenta solid lines in Fig. 1 (b)) to that of the inboard X-point region emission (between the blue dotted lines in Fig. 1 (b)). This line emission ratio can well describe the distribution pattern of inboard and outboard emissions quantitatively. The absolute line emission of CIV impurity is integrated over the area in Fig. 1, which can be used to make a rigorous quantitative comparison with the total intensity of CIV impurity emission measured in the experiment.

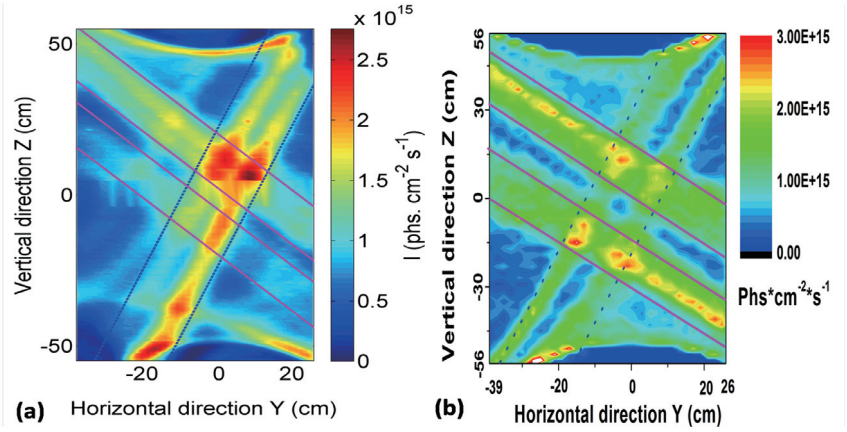

Fig. 1 2D distributions of CIV impurity emissions obtained from the experiment (a) and EMC3-EIRENE simulation (b).

Figure 2 shows the line emission ratios and integration values of CIV impurity emission as a function of the ion thermal force ratio. The ion thermal force ratio is defined as the changed value of the ion thermal force over the default value used in the impurity transport model [6]. The experimentally measured line emission ratio between in- and out-board regions and total integrated intensity of CIV impurity emission as shown in Fig. 2 (a) and (b) are 0.85 and 6.56×10^{18} Photons s^{-1}, respectively. For the default case of the simulations (the magenta values in *x* axis), the calculated line emission ratio and absolute CIV impurity emission are 1.14 and 7.54×10^{18} Phs s^{-1}, respectively. The reduction of the ion thermal force does not

change the line emission ratio and integration value of CIV impurity emission as shown in Fig. 2. The line emission ratio decreases and the absolute CIV impurity emission increases as increasing the ion thermal force more than four times larger. The CIV impurity mainly accumulates in the divertor leg regions for the inboard side of the torus and in the X-point region for the outboard side, respectively. The increase of the ion thermal force results in a stronger divertor leg leakage of C^{3+} impurity to X-point region for the inboard side. Hence, the CIV impurity emission from inboard region increases and the line emission ratio of outboard region to inboard region reduces accordingly. However, the absolute emission increases greatly and becomes much larger than the experimental value. A lower sputtering coefficient in simulations may lead to a good agreement with the experimental measurement of absolute emission at around $FiG_{changed}/FiG_{default}$ = 6~8. However, the use of about 6~8 times enhanced force seems too large compared to the default value used in the impurity transport model.

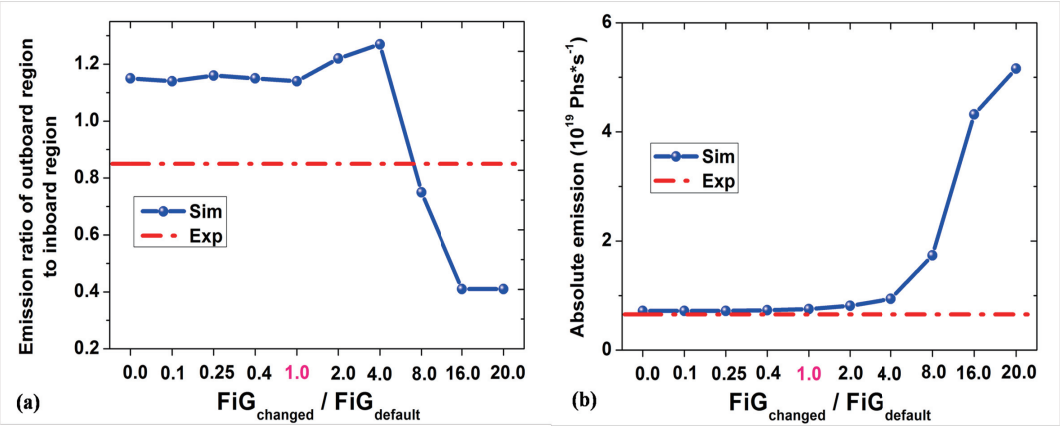

Fig. 2 The line emission ratios (a) and integration values (b) of CIV impurity emission as a function of the ion thermal force ratio. Here, the FiG is the ion thermal force.

2.2 The effect of the friction force on CIV line emission

The background plasma flow is usually directed towards the target plate, which will lead to the suppression of divertor leakage of impurities by friction force. The effect of the friction force is investigated in Fig. 3 which presents the line emission ratios and integration values of CIV impurity emission as a function of the friction force ratio. The friction force ratio is defined as the changed value of the friction force over the default value used in the impurity transport model [6]. The line emission ratios and integration values of CIV impurity emission do not change with increasing the friction in Fig. 3, which indicates that the plasma edge for the default case is in the friction force dominated case. The line emission ratio shows a good agreement with the experimental result when the friction force reduces by a factor of 8. However, the case that the good agreement is obtained by 8 times lower friction force exceeds the expected range compared to the value used in Ref. [6].

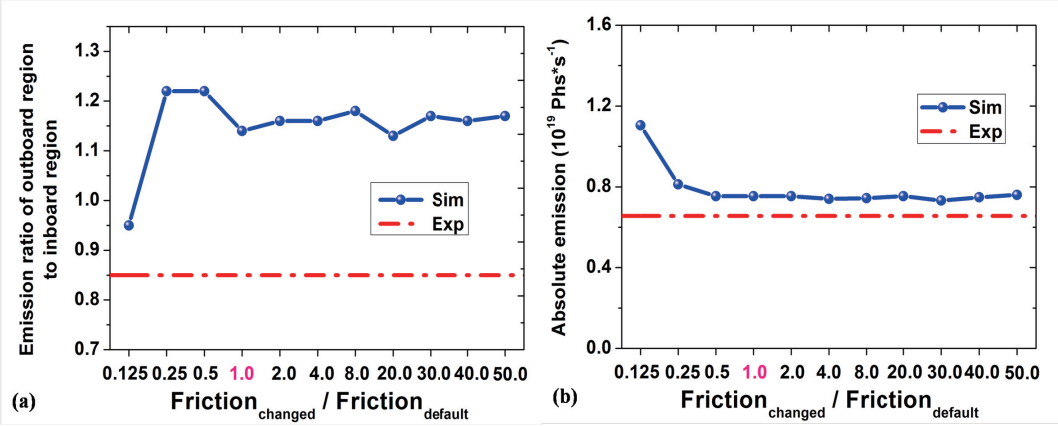

Fig. 3 The line emission ratios (a) and integration values (b) of CIV impurity emission as a function of the friction force ratio.

3. Summary and outlook

The 3D edge transport code EMC3-EIRENE is used to investigate the transport properties and line emissions of the impurity in the stochastic layer of LHD. The 2D distribution of CIV line emission is simulated and compared with the emission distribution measured by a space-resolved EUV spectrometer system. For the default case of the simulations, the 2D distribution pattern of CIV impurity emissions by EMC3-EIRENE modelling shows a deviation from the experimental measurement. The effects of the ion thermal force and friction force have been studied to check their influences on the CIV line emissions. A more comprehensive study of impurity source distribution at the first wall is foreseen in the future. The contribution of the first wall impurity source perhaps plays an important role to determine the distribution pattern and absolute intensity of CIV impurity emission.

Acknowledgements

This work was partly supported by the JSPS-NRF-NSFC A3 Foresight Program in the field of Plasma Physics (NSFC: No.11261140328, NRF: No.2012K2A2A6000443).

References

[1] S. Morita, et al., J. Nucl. Mater. 463, 644-648 (2015).

[2] H. M. Zhang, et al., Plasma. Fus. Res. 10, 3402038 (2015).

[3] Y. Feng, et al., Contrib. Plasma Phys. 44, 57 (2004).

[4] D. Reiter, et al., Nucl. Fusion 47, 172 (2005).

[5] G. Kawamura, et al, Contrib. Plasma Phys. 54 (4-6), 437-441 (2014).

[6] P. C. Stangeby. 2000 The Plasma Boundary of Magnetic Fusion Devices (Bristol: Institute of Physics Publishing).

Plasma behaviors during minor disruption with 2/1 locked mode on J-TEXT

Y. Liu[1], G. Zhuang[3], S. Morita[1,2], J. Chen[3], L. Gao[3] and Q.M. Hu[3]

[1]SOKENDAI (Graduate University for Advanced Studies), Toki 509-5292, Gifu, Japan

[2]National Institute for Fusion Science, Toki 509-5292, Gifu, Japan

[3]Huazhong University of Science and Technology, Wuhan, China

Abstract

Minor disruptions investigated on J-TEXT tokamak are caused by 2/1 mode locking with RMP coils set to 2/1 mode. The transport process of electrons is monitored by three-wave polarimeter-interferometer system (POLARIS), with temporal resolution 1μs and phase resolution 0.1^{o}. According to electron transport, the minor disruption is divided into 4 phase to study. From the time evolution of electron density perturbation profile, it is obvious that a surface exists, the electrons are transported from inner side of which to outer side, indicating the contact of 1/1 and 2/1 two existing magnetic island. After that, rapid loss of electrons has been observed. When the number of total electrons reaches its minimum value, it keeps unchanged with almost fixed shape for ~ 0.16 ms, implying that an inward force existing eliminates the outward velocity of electrons. Then plasma discharge starts to recover from minor disruption and comes to a new equilibrium.

1. Introduction

The earliest tokamak experiments exhibits major disruptions which terminates the plasma discharge, and these have been observed in all subsequent tokamaks. It is a major issue for the stable operation of a tokamak due to its highly damaging effect. Owing to the fast plasma current decay, electric fields are induced which produce eddy currents in wall components, leading to enormous $\mathbf{j}\times\mathbf{B}$ forces [1, 2]. Damage caused by these forces greatly determines the lifetime of plasma facing components [3, 4]. Another effect of the disruption is the instant deposition of the stored plasma energy on the vacuum inner wall or limiter [5]. If the heat deposits vacuum inner wall or limiter, these parts may be damaged by cracking or melting. The last effect is about the increased electric fields during disruptions. The electrons exposed to these fields are accelerated and reach dramatically high energy, which could produce substantial damage [6]. And suppression of runaway electrons is also studied in many fusion devices [7-11]. So it should be avoided in fusion devices expected to attain the high confinement times needed for future fusion reactions. Detailed experimental studies of disruptions have been made in many machines and the operating conditions leading to disruption have also been investigated [12-14]. Until now, many development processes of disruptions have been proposed [15-18]. It is widely accepted that a disruption is often accompanied by precursor modes, in particular those at q=1, q=1.5, and q=2 surfaces. At present, it is unclear whether the modes are growing such that the overlap criterion is always fulfilled and the plasma interior becomes ergodic. After this initiation phase, the proper disruption sets in with a negative loop voltage spike and the plasma current decay phase. The sudden loss of plasma energy occurs at the time of the negative spike in the loop voltage.

This energy loss appears at plasma facing components as enhanced heat flux. It can lead to a release of impurities from the walls, which then cool the plasma and accelerate the decay phase [19]. Most important, details of particle transport from core region to that outside of plasma region is not well understood. Recently, three-wave polarimeter-interferometer system (POLARIS) had been established on J-TEXT tokamak, which offers huge convenience to study the particle transport during disruption caused by locking mode. Because of irreversibility and serious of major disruption, our studies focus on minor disruption. On the other hand, it is very important to understand the mechanism of plasma discharge recovering from minor disruption, which is helpful to avoid and mitigate the occurrence of major disruption.

The rest of this paper is organized as follows: J-TEXT POLARIS and related diagnostic systems are introduced in section 2. In section 3, the plasma behavior presented on line-integrated density during minor disruption is shown. Finally, summary is given in section 4, respectively.

2. Experimental setup

The Joint-TEXT (J-TEXT) tokamak is a conventional device with an iron core. It has a major radius R_0=105 cm and a minor radius r=25-29 cm with a movable titanium-carbide coated graphite limiter. The main parameters of a typical J-TEXT discharge are center-line toroidal field $B_T \sim 2.0$ T, plasma current I_p= 200 kA lasting for 400ms, plasma densities $n_e = (1\text{-}10) \times 10^{19}$ m-3, and electron temperature $T_e \sim 1$ keV [20]. Recently, a three-wave polarimeter-interferometer system (POLARIS) had been installed on this tokamak with three wave technique, in which three laser beams in 432 μm with slight frequency shifts (~1 MHz) are used for detection. Two of the laser beams propagating through plasma cross-section as probe beams are counter-rotating circular-polarization and collinear, offering information of Faraday angle, while the third beam is served as local oscillation to gives phase of line-integral density. In this system the probe beams have been expanded by parabolic mirrors to cover the whole plasma cross section. The expanded probe beams propagate through the plasma vertically and received by a multi-chord mixer array (17 chords with 0.03 m chord spacing from 0.81m to 1.29 m, as shown in Fig.1), offering simultaneous measurements of Faraday angle, and line-integrated density profile along the major radius of tokamak. The temporal resolution of the system could reach 1μs, while the phase resolution of the system is less than 0.1° [21]. Besides, a poloidal Mirnov array consisting of 24 2D Mirnov pickup coils and a toroidal Mirnov array consisting of 8 pickup coils are used to detect the magnetic perturbations produced by rotating magnetic island. The hard x-ray (HXR) spectrum is detected by NaI scintillator in the energy range 0.5-5 MeV, which is about 5 m away from the torus [22]. A 16-channel heterodyne electron cyclotron emission (ECE) radiometer had been developed, which is used to measure the electron temperature profile during minor disruption [23]. Lately, J-TEXT has been equipped with two sets of saddle coils. One set is installed outside the vacuum vessel and generates static RMP (named static RMP or SRMP), and another set is installed inside the vacuum vessel, which can generate either static or rotating RMP (named dynamic RMP or DRMP). In order to study the particle transport during minor disruption, static RMP is applied in this experiment. A resonant and dominant m/n = 2/1 component of radial magnetic field b_r of strength 0.54 gauss/kA is generated at plasma edge, r = a. Here, m and n are the poloidal and toroidal mode number,

respectively [24,25].

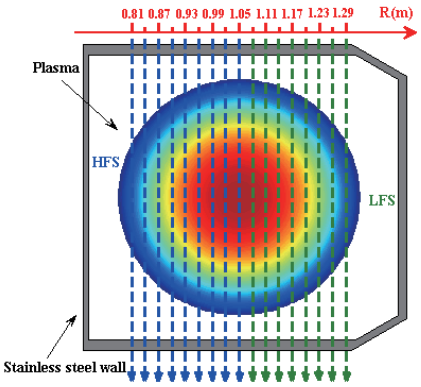

Fig.1. 17 chords of POLARIS with 0.03 m chord spacing from 0.81 m to 1.29 m.

3. Experimental observations

A typical experimental observation of minor disruption with discharge finally terminated by a major disruption is shot 1039746, with minor radius r = 26.5cm, plasma current I_p = 185 kA, toroidal magnetic field B_t = 1.75 T, safety factor at the edge of plasma region q_a = 2.9, and central line-averaged density n_e = 1.21 × 10^{19} m^{-3}. More important, occurrences of MHD activities have a good repeatability under this discharge condition. Mirnov signal, line-averaged electron density at x = 0 and -24 cm, HXR, ECE and Hα signal are given in Figs. 2(a)-2(f), respectively. An m/n = 2/1 tearing mode is formed at about 0.072 s during the increase phase of plasma current, with rotation frequency ~5 kHz. The static RMP is applied at 0.3 s with increase slop 10 kA/s lasting for about 0.2 s. After RMP is applied, the rotation frequency changes. Along with enhancement of coil current of RMPs, the rotation frequency decreases to 1.1 kHz at about 0.432 s with present b_r = 0.71 gauss at plasma edge, and ceases rotation immediately with corresponding Mirnov signal shown in Fig. 2(a). When magnetic island is locked, central line-averaged density starts to grow up and lasts for 10 ms about 5.2% increases. Then five continuous minor disruptions occur with no obvious perturbation observed on plasma current and x displacement, which shown on central line-averaged density signal are five sudden drops about 3.1% and recover rapidly as shown in Fig. 2(b). Whereas five positive pulses are observed on line-averaged density at x = -24 cm, as presented in Fig. 2(c). It indicates that particles emerging out from the core region, during minor disruptions. On the other hand, five abrupt changes appear on HXR, ECE and Hα signals, consistent with those occur on central line-averaged density, as shown in Figs. 2(d)-2(f). Observing the intensity of five positive pulses on HXR in Fig .2(d), it is obvious that the pulse intensity becomes smaller and smaller along with time evolution, and the fifth one is hardly found out but exists. Meanwhile the mean value of hard-x ray signal also becomes smaller and smaller. This implies that the amount of energetic particles is less and less, maybe resulting from most of energetic particles having already run away from plasma region during last minor disruption. The effect of five minor disruptions on ECE signal is presented in Fig. 2(e). As well known, the

measure position of ECE signal depends on the strength of toroidal field, and the probe position of signal is at R = 0.9662 m which could not cover q=2 resonant surface under this toroidal field. The electron temperature at the position shows five sharp drops, but come back to a new equilibrium in a few milliseconds which is slower than that presented on central line-averaged density signal. In Fig. 2(f), the five abrupt increases of Hα agree well with signals mentioned above with telling that the collision frequency between thermal electrons and hydrogen atoms increase dramatically during these five minor disruptions, proving that energy and particles emerging from core region have five periods of abrupt increase and rapid recover.

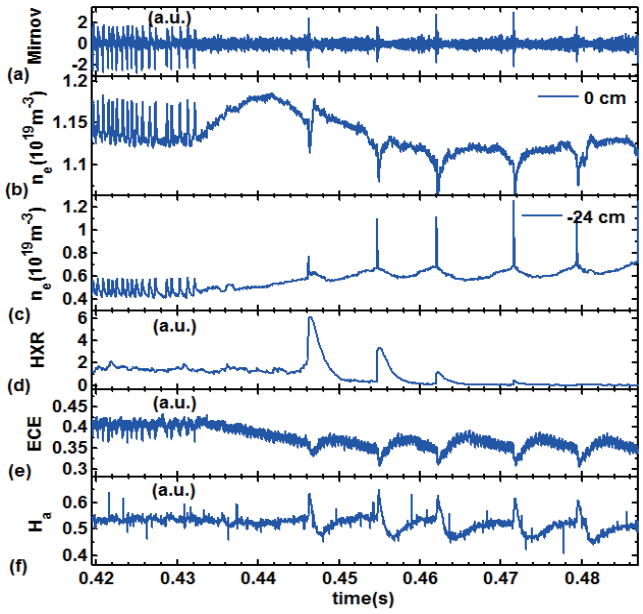

Fig.2. (a) Mirnov signal, line-averaged electron density at (b) x = 0 and (c) -24 cm, (d) HXR, (e) ECE and (f) Hα signals.

The temporal and spatial distribution of 17 chords line-integral density provided by POLARIS covering 100% of plasma cross section, with impact parameter x = 0.24 m, 0.21 m, 0.18 m, 0.15 m, 0.12 m, 0.09 m, 0.06 m, 0.03 m, 0, -0.03 m, -0.06 m, -0.09 m, -0.12 m, -0.15 m, -0.18 m, -0.21 m, -0.24 m (0 denotes the position of major radius and positive value corresponds to low field side), is shown in Fig. 3(a). It is obvious that total number of electrons present a sharp decrease during minor disruption. More information could be found in minor disruptions with appropriate magnification. The line-integrated density at core region and LFS decreases obviously, but an abrupt positive perturbation exists at the edge of high field side during every minor disruption which happens much earlier, as presented in Fig. 3(b)-3(f). To study the particle transport process during minor disruption, detail information of minor disruption provided by POLARIS is shown in Fig. 4.The line-integrated density begins to change at 0.5512s, as shown in Fig. 4(a), and then line-integrated density shows an obvious decrease at x ~ -0.1m and 0.15m. At about 0.55141s, the total number of electrons arrives at its minimum value with keeping unchanged for about 0.16ms as shown in Fig. 4(b). Then it starts to increase, and larger than former one at the termination of minor disruption. So

the minor disruption could be divided into four phases.

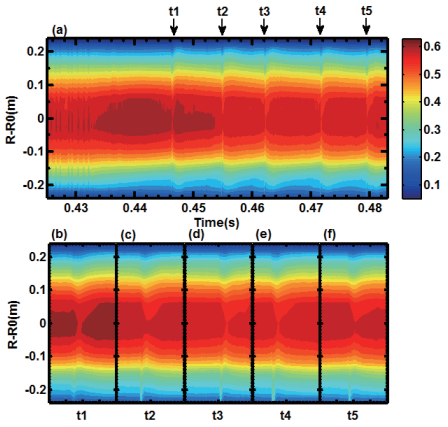

Fig.3. Spatial evolutions of (a) line-integrated electron density and (b)-(f) during every minor disruption for 2ms in Fig. 2.

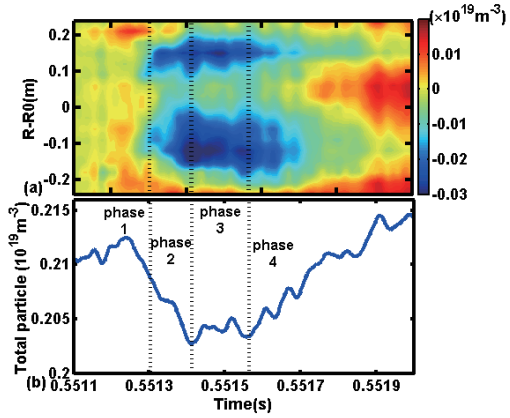

Fig.4.(a) Spatial structure of line-integrated density and (b) total number of electrons as a function of time.

To study the particle transport process during minor disruption, detail information of minor disruption provided by POLARIS is shown in Fig. 3, which is the time-evolution and spatial structure of perturbation of line-integrated density, defined as $n(r,t) - n(r,t_0)$ ($n(r,t_0)$ is the 17 chords line-integrated density at 0.5511s, and $n(r,t)$ is the density distribution during minor disruption).The line-integrated density begins to change at 0.5512s, as shown in Fig. 4(a), after that line-integrated density shows an obvious decrease at x ~ -0.1m and 0.16 m. At about 0.55141 s, the number of total electrons arrives at its minimum value with keeping almost constant for about 0.16 ms as shown in Fig. 4(b). Then it starts to increase, and larger than that before minor disruption at the termination of minor disruption. So the minor disruption could be divided into four phases.

Resulting from the distribution of line-integrated density starting to change at t = 0.5512 s, the density perturbation is redefined with $n(r,t) - n(r,t_0)$. During phase 1, the number of total electrons in the whole plasma cross section almost keeps constant before almost 0.5513 s, as shown in Fig. 4(b). However, the distribution of electron density is always changing during this phase, which is shown in Fig. 5(a).

Observing from the density perturbation distribution along major radius direction, it is obvious that electron density at -0.1 m and 0.1 m decreases rapidly with time, but electron density at the edge of low field side and high field side grow up, with almost no change occurs at about -0.16 m and 0.19 m, lasting for about 0.1ms. It obviously reveals that the electrons flow from inner region to outer region, indicating the electron density profile becomes more and more flat, and electron density gradient at the edge becomes larger and larger, varying with time. Then the number of total electrons starts to decrease lasting for about 0.11 ms, and the minimum value is about 95% of mean value, corresponding temporal evolution of electron density perturbation is shown in Fig. 5(b), in which whole electron density profile shows a decrease. When total number of electrons reaches its minimum values, it keeps constant for about 0.16 ms with density perturbation profiles unchanged. Then total number of electrons begins to rise at 0.55157 s lasting for about 0.43 ms, while the density perturbation profiles still keep almost fixed. After the minor disruption, it is found that the density at -0.24 m is larger than former one, but the electron density values at -0.1 m and 0.2 m are still less than that before minor disruption. It means the electron density profile is flatter than that at 0.5512 s.

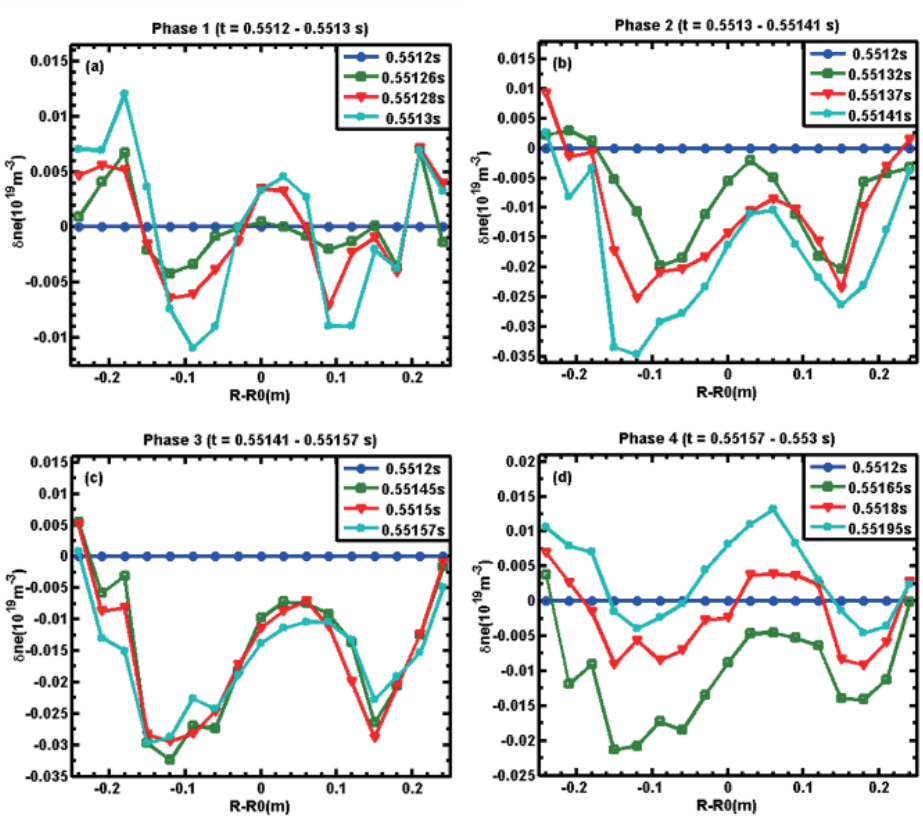

Fig.5. Distribution of line-integrated density perturbations at 0.5512s during (a) phase 1, (b) phase 2, (c) phase 3 and (d) phase 4.

4. Summary

During minor disruption, the particle transport process is well observed by POLARIS, due to its high spatial and temporal resolution. The electron density shows a redistribution at the plasma edge during phase 1, total number of electrons keeps constant. The electron density shows a decrease in whole plasma cross-section with unchanged density profile during phase 2. At the end of phase 2, the total number of electrons arrives at its minimum value, about 95% of mean value. Then it keeps constant for 0.16ms with fixed density profile during phase 3. According to Ware-pinch formula, the inward velocity should largely rise. Due to electron temperature at the edge continuously drops, the collision frequency increases gradually. So the inward velocity rises, resulting from increase of edge resistance and E_{φ}. Then plasma discharge begins to restore from minor disruption. Besides, minor disruption is also clearly observed on AXUV, SXR, H_{α}, CIII, HXR, V_{loop} signals. Due to the ability for clear observation of electron density behaviors during minor disruption, the particle transport and electron density distribution under magnetic island configuration during minor disruption will be studied in the future.

Acknowledgements

The authors would like to thank Prof. Zhuang Ge, Dr. Hu Qiming and all the engineers and technicians on J-TEXT for their support and assistance to the project. This work is supported by the ITER Project Funds of People's Republic of China: Contract Nos. 2013GB106001 and 2009GB107003, and partly supported by the JSPS-NRFNSFC A3 Foresight Program in the field of Plasma Physics（NSFC No. 11261140328).

References

[1] F.B. Marcus, F. Hofmann, S.C. Jardin, et al., Nucl. Fusion **30**1990 1511.

[2] B.J. Merrill and S.C. Jardin J. Nucl. Mater.**145** (1987) 881-885.

[3] F. Engelmann, M. Chazalon, M.F.A. Harrison, et al., J. Nucl. Mater. **145** (1987) 154-164.

[4] G. Federici, C.H. Skinner, J.N. Brooks, et al., Nucl. Fusion **41** (2001) 1967.

[5] K.H. Finken, W.Y. Baek, K.H. Dippel, et al., Nucl. Fusion **32** (1992) 915.

[6] M.N. Rosenbluth and S.V. Putvinski, Nucl. Fusion **37** (1997) 1355.

[7] M. Lehnen, S.A. Bozhenkov, S.S. Abdullaev, et al., Phys.Rev.lett.**100** (2008) 255003.

[8] S.A. Bozhenkov, M. Lehnen, K.H. Finken, et al., Plasma phys.Control.Fusion **50** (2008) 105007.

[9] P. Helander, L.G. Eriksson and F. Andersson, Phys. Plasmas **7** (2000) 4106-4111.

[10] D.G. Whyte, T.C. Jernigan, D.A. Humphreys, et al., Phys.Rev.Lett.**89** (2002) 055001.

[11] V.V. Plyusnin, V. Riccardo, R. Jaspers, et al., Nucl. Fusion **46** (2006) 277.

[12] M. Greenwald, J.L. Terry, S.M. Wolfe, et al., Nucl. Fusion **28** (1988) 2199.

[13] M.Murakami, J.D.Callen and L.A.Berry,Nucl. Fusion **16**(1976) 347.

[14] R.S. Granetz, Phys. Rev. Lett.**49** (1982) 658.

[15] R.B. White, D.A. Monticello, M.N. Rosenbluth, et al., Phys. Fluids **20**(1977) 800.

[16] R.B. White, D.A. Monticello and M.N. Rosenbluth, Phys. Rev. Lett.**39** (1977) 1618.

[17] B. Carreras, B.V. Waddell, H.R. Hicks, et al., Phys. Rev. A**18** (1978) 2732.

[18] D.C. Robinson and K. McGuire, Nucl. Fusion **19** (1979) 115.

[19] D.J. Ward and J.A. Wesson, Nucl. Fusion **32** (1992) 1117.

[20] G. Zhuang, K.W. Gentle, P. Diamond, et al., Nucl. Fusion **55** (2015) 104003.

[21] J. Chen, G. Zhuang, Q. Li, et al., Rev. Sci.Instrum.**85** (2014) 11D303.

[22] D.W. Huang, Z.Y. Chen, Y.H. Luo, et al., Rev. Sci.Instrum.**85** (2014) 11D845.

[23] Z.J. Yang, P.E. Phillips, G. Zhuang, et al., Rev. Sci.Instrum.**83** (2012) 10E313.

[24] B. Rao, G. Wang, Y.H. Ding, et al., Fusion Eng. Des.**89** (2014) 378-384.

[25] B. Rao, G. Zhuang, M. Zhang, et al., IEEE Trans.Appl.Supercond.**22** (2012) 4201804.

Development of VUV camera system on the EAST tokamak

Z.J. Wang[1, 2], X. GAO[1,2], S.Ohdachi[3], T.F.MING [2], X.D. DU [3]

[1]University of Science and Technology of China (USTC), Hefei, China
[2]Institute for Plasma Physics, Chinese Academic Sciences (ASIPP), Hefei, China
[3]National Institute for Fusion Science (NIFS), Toki, Japan

Abstract

A tangentially viewing vacuum ultraviolet (VUV) imaging system is proposed on the Experimental Advanced Superconducting Tokamak (EAST), which aims at providing the temporal evolution of the two-dimensional (2D) spatial structures by measuring the edge plasma emission (including the pedestal region). With this diagnostic, the properties of heat and impurity transport can be studied as well under a specific experiment condition, such as heat modulation, pellet injection. In general, the mode number can be distinguished directly from the raw images obtained by a tangential view [1]. In addition, a 2D measurement with both high temporal and spatial resolutions can be realized through a single high speed-camera, which successfully avoids the constraint of space. However, there is no intrinsic tangential port for diagnostics on EAST, which is different with the case on the large helical device (LHD) [2]. And, the port is very long due to the superconducting structures on EAST. Therefore, a unique design for the optics is required to realize a tangential view and satisfy the request of temporal and spatial resolutions. In this work, two proposals are investigated, that is a Schwarzschild telescope plus a fold mirror, and the other is based on a single aspheric mirror. The performance of these two proposals is compared with a phantom calculation, including the image quality, estimation of spatial resolutions and noise levels, etc.

1. Introduction

In H-mode operation a transport is formed at the edge of the plasma, and this leads to steep pressure and current density gradients that are subject to instability. Each burst of instability causes a reduction in density and temperature in the outer zone of the plasma, and the periodic behavior constitutes a relaxation oscillation. A fall in the density and temperature across the plasma radius is also observed and existence of ELMs (edge localized modes) causes some deterioration of confinement through the time averaged reduction of the transport barrier. The explanation of ELMs is not clear. It is perhaps not surprising that the increase in edge gradients in H-modes leads to instability, but no unequivocal identification of the type of instability has been made. ELMs present a serious problem for tokamaks. The large heat pulses which these ELMs release would cause serious damages with ELMs of reduced amplitude have reduced confinement. From the previous researches, it is clearly that the electron temperature in pedestal region is about 100 eV. Based on the edge plasma parameters on EAST, strong C VI line emission from the pedestal region can be expected. With tangentially viewing 2D imaging system, full coverage on the poloidal plane could be obtained. In order to investigate the edge plasma activities, a high-speed tangentially viewing vacuum ultraviolet (VUV) imaging system is developed on EAST.

2. Schematic view of the VUV Camera

In LHD, a high-speed vacuum ultraviolet (VUV) telescope system is being developed to investigate edge plasma activities [2, 3]. The construction starts from 2008, and the upgrade has been made at 2010. And the system has been transferred to the tangential port (6T). The high-speed VUV telescope system

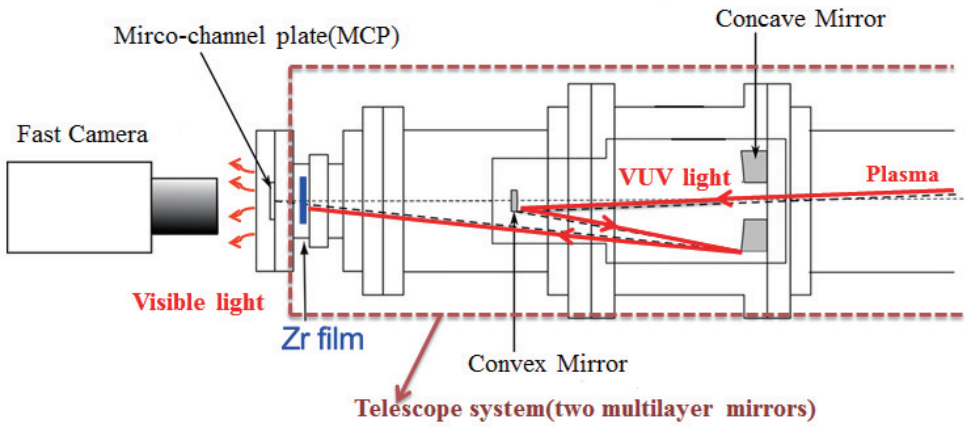

Figure 1: Schematic of the high-speed VUV telescope system on LHD

consists of three parts: a telescope composed by a set of multi-layer mirrors, a micro-channel plate (MCP) and a visible imaging high-speed camera. Fig.1 shows the schematic diagram of the VUV telescope imaging system. Photons are reflected by the telescope system, then images at the phosphor plate of the MCP. Eventually, these visible images are recorded by the high-speed camera. A telescope system is adopted in the optical system because larger solid anger can be realized. Consequently, more photons are collected than that with a simple pin-hole camera system. The telescope system consists of two multi-layer mirrors, i.e. a convex mirror and a concave mirror, where the curvatures are 144.5 mm and 390 mm, respectively. The focus length of the optical configuration is about 7 meters.

3. Installation for EAST tokamak

Tangential view is not available in the superconducting Tokamak like EAST because of the thick coil cooling structure. Luckily, by inserting a 'folding' mirror, semi-tangential view will be possible.

We adopt an inverse Schwarz child type telescope plus a fold mirror to realize a 2D tangentially viewing imaging system on EAST. The telescope and fold mirror are installed inside the vacuum chamber. Proposal for the optical design is shown in Fig. 2. Multilayer mirrors (also-called multilayer interference coatings) are interference optical system, and the maximum reflection is expected by the constructive interference. They are formed by depositing alternating layers of two materials with different refractive indices that form long-term stable interfaces. Typically, the two materials are alternating high and low atomic number in order to maximize the difference in electron density. The requirements of optical design are shown in the table.

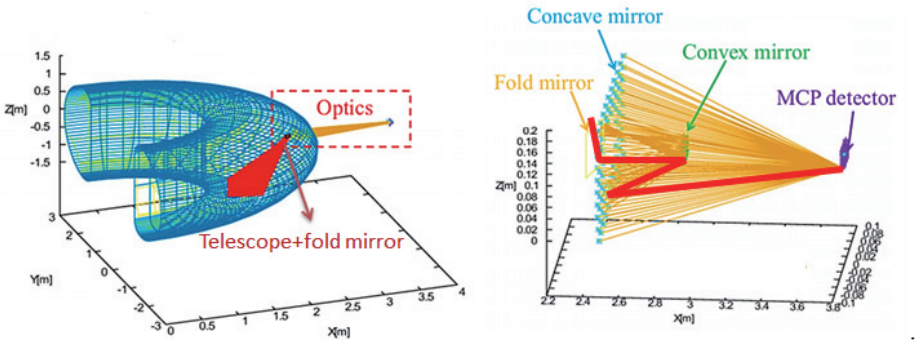

Figure 2: Proposal for the optical design

Requirements of optical design				
Magnification factor	Object distance	Viewing field	Mirror size	Pixel size
0.1	2.5 - 5m	most area of the target plane	180mm	28μm

4. Synthetic image studies

In order to perform the tomographic reconstruction/generation of synthetic line-integrated measurement, the geometry matrix, which contains the geometry information of the diagnostic system, should be constructed. In the case of tangentially viewing imaging system, it is a three-dimensional problem. And it becomes more complex for the tangentially viewing VUV imaging system due to the complex twisted plasma shape.

Since the imaging data are line-integrated measurement, developments of certain techniques for data analysis are required to obtain the information of the local emissivity. A new method is proposed to construct the so-called geometry matrix for a tangentially viewing imaging system. The geometry matrix links the local emissivity and line-integrated measurement. The basic idea is to convert the three-dimensional problem to be a two-dimensional one by project the sightlines onto a target plane. And the equilibrium code named EFIT is employed. With EFIT code, the magnetic field lines can be traced with finite beta. And the traces of magnetic field line which localizes outside the last closed flux surface (LCFS) can also be obtained with EFIT. Synthetic images can be made after the construction of geometry matrix. Consequently, the local emissivity can be estimated by comparing the assumed emission profile and line-integrated images. In addition, computed tomographic reconstruction is another common method to estimate the local information from line-integrated measurement. Several algorithms, such as Phillips-Tikhonov method, maximum entropy method, have been investigated in this article for the computed tomographic reconstruction.

Given a 2D emission profile E(x, y), the i^{th} nonlocal measurement can be described by:

$$I_i = \iint S_i(x,y)E(x,y)\,dx\,dy$$

Here, Si(x, y) is the nominal weight function describing the geometry of the diagnostics. For the normal array measurement, a straight sight line can be parameterized by the signed distance p to a chosen origin (x_0, y_0) and an angle θ with the x-axis. Here, $S_i(x, y)$ is the nominal weight function describing the geometry of the diagnostics. We simulate with different m numbers. Simulation results show that the synthetic images are sensitive to the emission, especially for fluctuations with high poloidal mode number. Figure 3 is the Assumed profiles corresponding synthetic images with different M numbers.

5. Summary and outlook

The VUV imaging system is composed of a telescope made of Mo/Si multilayer mirrors, micro-channel plate (MCP) and a high-speed visible CMOS camera. With Mo/Si mirrors, VUV photons with a wavelength of 13.5 nm can be selectively measured. A telescope optics rather than pin-hole optical system is selected; the solid angle of the mirror viewed from the plasma is much larger than the solid angle of a pin-hole system.

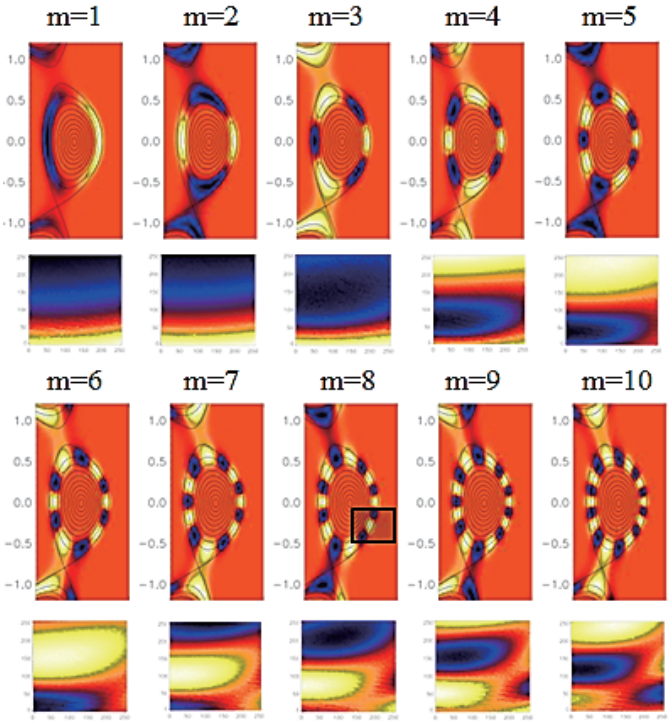

Figure 3: Assumed profiles corresponding synthetic images with different M numbers.

By measuring the CVI line emission around 13.5 nm, ELMs activities are directly visualized by this device. Additionally, since the time evolution of line emission of C VI is selectively measured, it is possible to carry out carbon impurity transport study with this imaging system. Phantom test based on an EFIT equilibrium was performed to estimate the performance of the optical design. It shows that the proposal can realize an acceptable coverage on the target plane, and synthetic images are sensitive to the emission profiles. Further optimization on the geometric parameters are undergoing to improve the image quality, spatial resolution of the system.

This work was partly supported by the JSPS-NRF-NSFC A3 Foresight Program in the field of Plasma Physics (NSFC: No.11261140328, NRF: No.2012K2A2A6000443).

References

[1] T.F. Ming, S. Ohdachi, Y. Suzuki and LHD Experiment Group. Plasma and Fusion Research, Vol 6, 2406120 (2011)

[2] T.F. Ming, S. Ohdachi, S. Sakakibara, and Y. Suzuki. Rev. Sci. In strum. 83, 10E513 (2012)

[3] Masaki TAKEUCHI, Satoshi OHDACHI, and LHD experimental group. Development of a high-speed VUV camera system for 2-dimensional imaging of edge turbulent structure in the LHD. Plasma and Fusion Research, 5(1):S1037, 2010.

Acknowledgements

This work was partly supported by the JSPS-NRF-NSFC A3 Foresight Program in the field of Plasma Physics (NSFC: No.11261140328, NRF: No.2012K2A2A6000443).

Program of A3 Seminar
(1-4 December 2015, Gotemba, Japan)

30 November 2015 (Monday)
Registration: evening

1 December (Tuesday)

Session 1 (Opening & Category: III & young persons) Chair: S.Ohdachi	08:30	**Shigeru MORITA** (NIFS)	Opening
	08:40	**Mitsutaka ISOBE** (NIFS)	Recent progress of fast-ion loss detector project in magnetic confinement fusion devices in Japan
	09:05	**Jungmin JO** (SNU)	14.1 MeV d-t neutron measurement results in KSTAR deuterium plasma
	09:30	**Jun-Young KIM** (UST)	Fast ion loss associated with RMP penetration
	09:55	**Liqun HU** (ASIPP)	Some key technique on plasma diagnostics in Tokamak reactor nuclear environment
Coffee Break 10:20-10:35			
Session 2 (Category: I) Chair: L.Q.Hu	10:35	**Sangwook JUNG** (NFRI)	ECH and ECCD experimental results of KSTAR in 2015
	11:00	**Bojiang DING** (ASIPP)	LHCD study toward to high performance plasma
	11:25	**Xiaoquan JI** (SWIP)	Integrated real-time control of magnetic islands by ECRH on the HL-2A tokamak
	11:50	**Katsuyoshi TSUMORI** (NIFS)	Preparation and improvement for NBI system to LHD deuterium experiment
Lunch Break12:15-13:40			
Session 3 (Category: I & IIa) Chair: M.Isobe	13:40	**YoungMu JEON** (NFRI)	Improved plasma equilibrium control by using a newly developed, self-proven controller design method
	14:05	**Sonjong WANG** (NFRI)	Experimental results of helicon wave coupling in KSTAR plasmas
	14:30	**Tetsutarou OISHI** (NIFS)	Flow velocity and ion temperature of carbon impurities measured using VUV spectroscopy in the ergodic layer of LHD
	14:55	**Shigeru MORITA** (NIFS)	Edge particle confinement at low edge temperature in low input power discharges
Coffee Break 15:20-15:35			
Session 4 (Category: I & IIa) Chair: S.H.Hong	15:35	**Naoko ASHIKAWA** (NIFS)	In-vessel fuel retention and removal on tungsten in EAST and KSTAR
	16:00	**Junling CHEN** (ASIPP)	Key issues of plasma surface interactions in EAST
	16:25	**Zhengying CUI** (SWIP)	Impurity transport study with Al and Ne injection in the HL-2A ECRH plasma
	16:50	**Xianli HUANG** (NIFS)	Comparison of impurity transport among different LHD configurations based on radial profiles of Fe n=3-2 Lα transition array

2 December (Wednesday)			
Session 5 (Category: IIb & IV) Chair: B.J.Xiao	08:30	**Nong XIANG** (ASIPP)	(Title not decided)
	08:55	**Hao WANG** (NIFS)	Simulations of energetic particle driven geodesic acoustic mode in 3-dimensional LHD equilibrium
	09:20	**Xiaodi DU** (NIFS)	Resistive interchange modes destabilised by helically trapped energetic ions in a helical plasma
	09:45	**Jayhyun KIM** (NFRI)	Locked mode stabilization by applying non-axisymmetric field
Coffee Break 10:10– 10:30			
Session 6 (Category: IV) Chair: K.Toi	10:30	**Hyun-Seok KIM** (NFRI)	Validation of plasma response model for real-time q profile control in KSTAR
	10:55	**Sang Gon LEE** (NFRI)	Toroidal rotation and momentum transport studies in KSTAR
	11:20	**Zhipeng CHEN** (HUST)	Plasma rotation and moment transport in tokamak
Lunch 11:45-13:30			
Session 7 (Category: I & IIb) Chair: S.Morita	13:30	**Yasuhiko TAKEIRI** (NIFS)	Welcome speech
	13:40	**Baonian WAN** (ASIPP)	Some key technique in plasma physics
	14:05	**Ge ZHUANG** (NUST)	Investigation of high density disruptions in the J-TEXT tokamak
	14:30	**Yeong-Kook OH** (NFRI)	Result of KSTAR 2015 operation
	14:55	**Satoshi OHDACHI** (NIFS)	Observation of localized mode in the bad curvature region at the core-density-collapse event in the Large Helical Device
Coffee Break & Seminar Photo 15:10– 15:40			
Session 8 (Category: IIa & IIb) Chair: J.H.Kim	15:40	**Bingjia XIAO** (ASIPP)	Control of quasi-snowflake divertor plasma shape
	16:05	**Kazuo TOI** (NIFS)	A new control method of edge MHD stability in toroidal plasmas using SOL-divertor region
	16:30	**Suk-Ho HONG** (NFRI)	Divertor leading edge experiments in KSTAR
	16:55	**Jun-Gyo BAK** (NFRI)	Evaluation of divertor fluxes from electric measurements during ELMy H-modes in KSTAR

3 December (Thursday)			
Session 9 (Category: IIa & IV) Chair: N. Xiang	08:30	**Jian LIU** (USTC)	Theory and Simulation of runaway electrons in tokamaks
	08:55	**Yulei WANG** (USTC)	Theory and Simulation of runaway electrons in tokamaks
	09:20	**Hirohiko TANAKA** (NIFS)	Statistical analysis of non-diffusive transport in the linear device NAGDIS-II
	09:45	**Daiji KATO** (NIFS)	Atomic data and modeling for tungsten ion spectra
Coffee Break 10:10 - 10:30			
Session 10 (Category: young persons) Chair: Y.K. Oh	10:30	**Hongming ZHANG** (NIFS)	Study of impurity radiation in attached and detached plasmas of LHD
	10:55	**Shuyu DAI** (NIFS)	EMC3-EIRENE modelling of edge impurity transport in the stochastic layer of LHD compared with EUV emission measurements
	11:20	**Yang LIU** (NIFS)	Study of plasma behavior during minor disruption based on J-TEXT POLARIS
	11:45	**S.Morita** (NIFS)	Summary reports, closing and others
Lunch Break 12:20 - 14:30			
Session 11 Discussions on A3 program Chair: S. Morita L.Q. Hu Y.K. Oh	14:00-17:00 Discussions on next seminar and workshop plans Education of young scientists Discussion on coordinator meeting Discussion on annual report of A3 collaboration Discussion on web site of A3 collaboration Discussions on machine operation schedules Discussions on new toroidal devices Discussion on budget and administrative works "Some key issues in international cooperation among institutes" by Sha WU, H. HOSOKAWA, M. ASAI et al.		

4 December (Friday)	
Session 12 Discussions on A3 collaboration Chair: S. Morita L.Q. Hu Y.K. Oh	09:00-12:00 Plenary meeting on future collaboration at each category for A3 Foresight Program on Critical Physics Issues Specific to Steady State Sustainment of High-Performance Plasmas **Category I:** Steady state sustainment of magnetic configurations (Current drive and profile control) **Category II:** Edge and divertor plasma control Category IIa: Transport of edge and divertor plasmas Category IIb: Stability of edge plasma **Category III:** Confinement of alpha particles (Interaction of energetic particle and bulk plasma) **Category IV:** Theory and simulation 13:30-17:00 Individual discussion on personnel exchange Individual discussion on hardware construction and operation of diagnostics and heating devices Individual discussion on device operation and machine time Discussions on on-going and future studies in A3 collaboration Discussions with PHD students, Post-doctoral researchers and young scientists Discussion on post-A3 program

(END)

List of participants of A3 Foresight Program Workshop in Gotemba

No.	Nation	Name	Affiliation
1	Japan	Shigeru MORITA	NIFS
2	Japan	Tetsutarou OISHI	NIFS
3	Japan	Naoko ASHIKAWA	NIFS
4	Japan	Mitsutaka ISOBE	NIFS
5	Japan	Hao WANG	NIFS
6	Japan	Daiji KATO	NIFS
7	Japan	Hirohiko TANAKA	NIFS
8	Japan	Kazuo TOI	NIFS
9	Japan	Yang LIU	NIFS
10	Japan	Katsuyoshi TSUMORI	NIFS
11	Japan	Xiaodi DU	NIFS
12	Japan	Xianli HUANG	NIFS
13	Japan	Hongming ZHANG	NIFS
14	Japan	Shuyu DAI	NIFS
15	Japan	Sangwook JUNG	NFRI
16	Korea	Yeong-Kook OH	NFRI
17	Korea	Suk-Ho HONG	NFRI
18	Korea	Jun-Gyo BAK	NFRI
19	Korea	YoungMu JEON	NFRI
20	Korea	Sang Gon LEE	NFRI
21	Korea	Jayhyun KIM	NFRI
22	Korea	Sonjong WANG	NFRI
23	Korea	Sangwook JUNG	NFRI
24	Korea	Jun-Young KIM	UST
25	Korea	Jungmin JO	SNU
26	Korea	Junling CHEN	ASIPP
27	China	Zhipeng CHEN	HUST
28	China	Bojiang DING	ASIPP
29	China	Liqun HU	ASIPP
30	China	Jian LIU	USTC
31	China	Baonian WAN	ASIPP
32	China	Sha WU	ASIPP
33	China	Nong XIANG	ASIPP
34	China	Bingjia XIAO	ASIPP
35	China	Yulei WANG	USTC
36	China	Ge ZHUANG	HUST
37	China	Zhengying CUI	SWIP
38	China	Xiaoquan JI	SWIP
39	China	WANG Zhijun	ASIPP
40	China	Satoshi OHDACHI	NIFS
41	Japan	Yasuhiko TAKEIRI	NIFS
42	Japan	Makoto ASAI	NIFS
43	Japan	HOSOKAWA Hideo	NIFS
44	China	Z.J.Wang	ASIPP